

University of Kentucky

UKnowledge

University of Kentucky Doctoral Dissertations

Graduate School

2011

STEEL BEAMS STRENGTHENED WITH ULTRA HIGH MODULUS CFRP LAMINATES

Nisal Abheetha Peiris

University of Kentucky, abheetha@yahoo.com

[Right click to open a feedback form in a new tab to let us know how this document benefits you.](#)

Recommended Citation

Peiris, Nisal Abheetha, "STEEL BEAMS STRENGTHENED WITH ULTRA HIGH MODULUS CFRP LAMINATES" (2011). *University of Kentucky Doctoral Dissertations*. 204.
https://uknowledge.uky.edu/gradschool_diss/204

This Dissertation is brought to you for free and open access by the Graduate School at UKnowledge. It has been accepted for inclusion in University of Kentucky Doctoral Dissertations by an authorized administrator of UKnowledge. For more information, please contact UKnowledge@lsv.uky.edu.

ABSTRACT OF DISSERTATION

Nisal Abheetha Peiris

The Graduate School
University of Kentucky

2011

STEEL BEAMS STRENGTHENED WITH ULTRA HIGH MODULUS
CFRP LAMINATES

ABSTRACT OF DISSERTATION

A dissertation submitted in partial fulfillment of the
requirements for the degree of Doctor of Philosophy in the
College of Engineering
at the University of Kentucky

By
Nisal Abheetha Peiris

Lexington, Kentucky

Director: Dr. Issam Elias Harik, Professor of Civil Engineering

Lexington, Kentucky

2011

Copyright © Nisal Abheetha Peiris 2011

ABSTRACT OF DISSERTATION

STEEL BEAMS STRENGTHENED WITH ULTRA HIGH MODULUS CFRP LAMINATES

Advanced composites have become one of the most popular methods of repairing and/or strengthening civil infrastructure in the past couple of decades. While the use of Fiber Reinforced Polymer laminates and sheets for the repair and strengthening of reinforced concrete structures is well established, research on the application of FRP composites to steel structures has been limited. The use of FRP material for the repair and rehabilitation of steel members has numerous benefits over the traditional methods of bolting or welding of steel plates. Carbon FRPs (CFRPs) have been preferred over other FRP material for strengthening of steel structures since CFRPs tend to possess higher stiffness. The emergence of high modulus CFRP plates, with an elastic modulus higher than that of steel, enables researchers to achieve substantial load transfer in steel beams before the steel yields.

This research investigates both analytically and experimentally, the bond characteristics between ultra high modulus CFRP strengthened steel members and the flexural behavior of these members. A series of double strap joint tests with two different CFRP strip widths are carried out to evaluate the development length of the bond. Both ultra high modulus and normal modulus CFRP laminates are used to compare strengthened member performance. Steel plates reinforced with CFRP laminates on both sides are loaded in tension to evaluate the load transfer characteristics. Debonding under flexural loads is

also studied for ultra high modulus CFRP strengthened steel girders. Flexural tests are carried out under 4-point bending on several small scale wide flange beams. This study also introduces the novel ultra high modulus CFRP plate strip panels for strengthening of steel bridge girders. The first field application of ultra high modulus CFRP laminates in strengthening steel bridge girders in the United States is also carried out as part of the research. Full scale load tests carried out before and after the strengthening are utilized to measure the degree of strengthening achieved and checked against the expected results. A finite element model is developed and calibrated using data obtained from the field testing of the bridge. The model is then used to evaluate the behavior of the bridge under different conditions before and after the strengthening process.

KEYWORDS: Carbon Fiber Plates, Adhesive, Steel Beams, Bond Behavior, Bridge Strengthening

Nisal Abheetha Peiris

Student's Signature

06-27-2011

Date

STEEL BEAMS STRENGTHENED WITH ULTRA HIGH MODULUS
CFRP LAMINATES

By

Nisal Abheetha Peiris

Dr. Issam E. Harik
Director of Dissertation

Dr. Kamyar C. Mahboub
Director of Graduate Studies

06-27-2011
Date

DISSERTATION

Nisal Abheetha Peiris

The Graduate School
University of Kentucky

2011

STEEL BEAMS STRENGTHENED WITH ULTRA HIGH MODULUS
CFRP LAMINATES

DISSERTATION

A dissertation submitted in partial fulfillment of the
requirements for the degree of Doctor of Philosophy in the
College of Engineering
at the University of Kentucky

By
Nisal Abheetha Peiris

Lexington, Kentucky

Director: Dr. Issam Elias Harik, Professor of Civil Engineering

Lexington, Kentucky

2011

Copyright © Nisal Abheetha Peiris 2011

To my parents.....

ACKNOWLEDGMENTS

This dissertation would not be possible without the guidance of my advisor Dr. Issam Harik. He offered me the opportunity to study at the University of Kentucky and guided and supported this research. I'm thankful for his insightful comments, encouragement and criticism, and for not accepting anything other than my best.

The suggestions and assistance provided by my advisory committee members, Dr. Hans Gesund, Dr. George Blandford, Dr. Brad Davis, and Dr. Tingwen Wu were much appreciated.

None of the experimental work included in this research would be possible without the support of numerous individuals. The laboratory testing would not have been a reality, without the contributions from my colleague, Mr. Drew Thompson. A special thank you goes to my colleague Mr. Ryan Studer and Mr. Gene Yates of the Department of Civil Engineering for their assistance in the laboratory testing.

The bridge testing was feasible because of the support received by members of the Kentucky Transportation Center. I'm grateful to Mr. Clark Graves, Mr. Brad Rister, Dr. Charlie Sun, Mr. Dan Eaton, Mr. Jamie Creech, Mr. Jared Fairchild, Mr. Timothy Jones and Mr. Richard Reitenour for the many hours spent underneath the bridge.

I'm thankful to Mrs. Shelia Williams for her administrative assistance and Miss. Dora Van Zee for her assistance in the preparation of this dissertation. The time and effort put into reviewing the dissertation by my colleague, Dr. Michael Davidson is also appreciated.

The financial funding received from the Graduate School, Department of Civil Engineering and the Kentucky Transportation Center was invaluable for me to undertake this endeavor.

TABLE OF CONTENTS

Acknowledgments.....	iii	
List of Tables.....	vi	
List of Figures.....	viii	
Chapter 1	INTRODUCTION	
1.1	Steel Strengthening with Fiber Reinforced Polymer (FRP)	1
1.2	State-of-the-art on ultra high modulus CFRP strengthened steel structures	3
1.3	Field Applications	5
1.4	Research Objectives	7
1.5	Research Significance	7
1.6	Organization of Dissertation	8
Chapter 2	BOND AND FLEXURAL BEHAVIOR TESTS	
2.1	Introduction	11
2.2	Double Strap Joint Tests	15
2.3	Doubly Reinforced Steel Plate Tests	37
2.4	Steel beam tests	47
Chapter 3	ANALYTICAL AND FINITE ELEMENT ANALYSIS OF BOND	
3.1	Introduction	62
3.2	Double Strap Joint	66
3.3	Doubly Reinforced Steel Plate	84
3.4	Steel beams	99
Chapter 4	PRELIMINARY ANALYSIS AND LOAD RATING OF KY32 BRIDGE	
4.1	Introduction	114
4.2	KY32 Bridge	114

4.3	Simple Beam Analysis	117
4.4	Post Installed Shear Studs	118
4.5	Finite Element Beam Analysis of Shear Stud Distribution	119
4.6	Load Rating of KY32 Bridge	123
Chapter 5	EXPERIMENTAL BRIDGE GIRDER STRENGTHENING WITH UHM CFRP	
5.1	Introduction	132
5.2	Rebar Location	135
5.3	Drilling and Installing Shear Studs	137
5.4	Application of ultra high modulus CFRP	142
5.5	Bridge Instrumentation and Load Tests	149
5.6	Load Test Results	159
Chapter 6	FINITE ELEMENT ANALYSIS AND PARAMETRIC STUDY OF BRIDGE	
6.1	Introduction	169
6.2	KY 32 Bridge Finite Element Analysis	170
6.3	Load Rating Using Finite Element Analysis	186
6.4	Parametric Study of KY 32 Bridge	189
Chapter 7	CONCLUSIONS AND RECOMMENDATIONS	
7.1	Summary and Conclusions	193
7.2	Future Work	199
Appendix A		203
Appendix B		244
References		275
Vita		284

LIST OF TABLES

Table 1.1	Classification of CFRP	2
Table 1.2	Reported bridge retrofit using CFRP around the world	6
Table 2.1	CFRP Material Properties	20
Table 2.2	Adhesive Epoxy Material Properties	22
Table 2.3	Normal modulus 5 mm (0.2 in) wide specimen test results	26
Table 2.4	Normal modulus 10 mm (0.4 in) wide specimen test results	27
Table 2.5	Ultra high modulus 5 mm (0.2 in) wide specimen test results	28
Table 2.6	Ultra high modulus 10 mm (0.4 in) wide specimen test results	29
Table 4.1	Different Truck Types for Load Rating	124
Table 4.2a	Truck Weight Analysis according to AASHTO guidelines (Non-Composite bridge – prior to retrofit) – Metric Units	130
Table 4.2b	Truck Weight Analysis according to AASHTO guidelines (Non-Composite bridge – prior to retrofit) – Customary US Units	130
Table 4.3a	Truck Weight Analysis according to AASHTO guidelines (Partially Composite bridge – after retrofit) – Metric Units	131
Table 4.3b	Truck Weight Analysis according to AASHTO guidelines (Partially Composite bridge – after retrofit) – Customary US Units	131
Table 5.1	Truck tire loads	158
Table 6.1a	Truck Weight Analysis using data from calibrated finite element model (Non-Composite bridge – prior to retrofit) – Metric Units	187

Table 6.1b	Truck Weight Analysis using data from calibrated finite element model (Non-Composite bridge – prior to retrofit) – Customary US Units	187
Table 6.2a	Truck Weight Analysis using data from calibrated finite element model (Composite bridge – after retrofit) – Metric Units	188
Table 6.2b	Truck Weight Analysis using data from calibrated finite element model (Composite bridge – after retrofit) – Customary US Units	188

LIST OF FIGURES

Fig. 2.1	Double Strap Joint Specimen Dimensions	15
Fig. 2.2	Specimen Preparation	17
Fig. 2.3	Steel coupon test	18
Fig. 2.4	CFRP tensile test	19
Fig. 2.5	Tensile stress-strain relationship for CFRP laminates	20
Fig. 2.6	Observed rupture of CFRP laminates	21
Fig. 2.7	Failure of Epoxy coupons	22
Fig. 2.8	Double Strap Joint Specimen Gage Layout	23
Fig. 2.9	Tensile testing of double strap joint specimen	25
Fig. 2.10	Typical steel-epoxy interface debonding seen in normal modulus CFRP	30
Fig. 2.11	Typical combined steel-epoxy interface debonding and CFRP delamination seen in normal modulus CFRP	30
Fig. 2.12	Typical CFRP delamination seen in normal modulus CFRP	31
Fig. 2.13	Typical combined steel-epoxy debonding and CFRP delamination seen in ultra high modulus CFRP	32
Fig. 2.14	Typical CFRP delamination seen in ultra high modulus CFRP	32
Fig. 2.15	Typical CFRP rupture seen in high modulus CFRP	32
Fig. 2.16	Failure load variation with bond length for NM 5 mm (0.2 in) specimens	33
Fig. 2.17	Failure load variation with bond length for NM 10 mm (0.4 in) specimens	33
Fig. 2.18	Failure load variation with bond length for UHM 5 mm (0.2 in) specimens	34

Fig. 2.19	Failure load variation with bond length for UHM 10 mm (0.4 in) specimens	34
Fig. 2.20	Average failure load per unit width	35
Fig. 2.21	Strain variation along bond length for NM 10-75B specimens	36
Fig. 2.22	Strain variation along bond length for UHM 10-75B specimens	37
Fig. 2.23	Doubly Reinforced Steel Plate Specimen Dimensions	38
Fig. 2.24	Doubly Reinforced Steel Plate Specimen Gage Layout	39
Fig. 2.25	Doubly Reinforced Steel Plate with attached Strain Gages	40
Fig. 2.26	Testing of Doubly Reinforced Steel Plate Specimen	40
Fig. 2.27	Debonding locations on normal modulus CFRP specimens	41
Fig. 2.28	Debonding observed in doubly reinforced steel specimens	42
Fig. 2.29	Debonding location on ultra high modulus CFRP specimens	42
Fig. 2.30	Strain variation at center of the laminates	43
Fig. 2.31	Strain variation along specimen centerline at 44.4 kN (10 kip)	44
Fig. 2.32	Strain in steel plate	45
Fig. 2.33	Shear stress distribution at 44.4 kN (10 kip)	46
Fig. 2.34	Dimensions of W10x22 and C7x9.8 composite section	47
Fig. 2.35	Beam and laminate dimensions in elevation	48
Fig. 2.36	Adjoining strip panels with ‘finger’ joint	48
Fig. 2.37	Dimensions and layout of strip panels	49
Fig. 2.38	Strain gage layout on steel beams	51
Fig. 2.39	Beam testing setup	52

Fig. 2.40	Beam being tested	53
Fig. 2.41	Load vs. mid span displacement	54
Fig. 2.42	Steel strain on top of bottom flange	54
Fig. 2.43	Rupture of full width laminate	55
Fig. 2.44	Flexural strain and shear stress in full width laminate	56
Fig. 2.45	Debonding at mid span ‘finger’ joint	58
Fig. 2.46	Flexural strain and shear stress in primary 10 mm (0.4 in) strip panel	59
Fig. 2.47	Flexural strain and shear stress in secondary 10 mm (0.4 in) strip panel	60
Fig. 3.1	Analytical and experimental results for NM 5 mm (0.2 in) specimens	69
Fig. 3.2	Analytical and experimental results for NM 10 mm (0.4 in) specimens	69
Fig. 3.3	Analytical and experimental results for UHM 5 mm (0.2 in) specimens	70
Fig. 3.4	Analytical and experimental results for UHM 10 mm (0.4 in) specimens	70
Fig. 3.5	Hart-Smith model for laminate joints of different Young’s modulus	71
Fig. 3.6	Hart-Smith model for laminate joints with different adhesive thickness	72
Fig. 3.7	75 mm bond finite element model	74
Fig. 3.8	Tensile strains along bond for 10 mm (0.4 in) wide normal modulus specimens	76
Fig. 3.9	Tensile strains along bond for 10 mm (0.4 in) wide ultra high modulus specimens	77

Fig. 3.10	Shear and Von Mises stress at initiation of failure in adhesive	79
Fig. 3.11	Typical failure in adhesive seen in longer bond lengths	80
Fig. 3.12	Ultimate failure of bond	80
Fig. 3.13	Finite element and experimental results for NM 5 mm (0.2 in) specimens	81
Fig. 3.14	Finite element and experimental results for NM 10 mm (0.4 in) specimens	81
Fig. 3.15	Finite element and experimental results for UHM 5 mm (0.2 in) specimens	82
Fig. 3.16	Finite element and experimental results for UHM 10 mm (0.4 in) specimens	82
Fig. 3.17	Doubly reinforced plate	85
Fig. 3.18	Tensile stress distribution- NM specimens at 44.5 kN (10 kip)	87
Fig. 3.19	Shear stress distribution- NM specimens at 44.5 kN (10 kip)	87
Fig. 3.20	Tensile stress distribution- UHM specimens at 44.5 kN (10 kip)	88
Fig. 3.21	Shear stress distribution- UHM specimens at 44.5 kN (10 kip)	88
Fig. 3.22	Tensile stress distribution variation due to outer adherend modulus	89
Fig. 3.23	Shear stress distribution variation due to outer adherend modulus	90
Fig. 3.24	FEA and experimental results for NM laminate tensile stress- 22.2 kN (5 kip)	93
Fig. 3.25	FEA and experimental results for NM laminate tensile stress- 44.5 kN (10 kip)	93
Fig. 3.26	FEA and experimental results for UHM laminate tensile stress- 22.2 kN (5 kip)	94
Fig. 3.27	FEA and experimental results for UHM laminate tensile stress-44.5 kN (10 kip)	94

Fig. 3.28	FEA and experimental results for NM laminate shear stress- 44.5 kN (10 kip)	96
Fig. 3.29	FEA and experimental results for UHM laminate shear stress-44.5 kN (10 kip)	96
Fig. 3.30	Shear distribution in NM CFRP doubly reinforced steel plate	97
Fig. 3.31	Failure of adhesive layer in NM CFRP doubly reinforced steel plate	98
Fig. 3.32	Bonded laminate on beam soffit	100
Fig. 3.33	Analytical and experimental shear stress distribution	101
Fig. 3.34	Shear stress variation with tensile modulus of laminate	102
Fig. 3.35	Finite element beam model	106
Fig. 3.36	Load deflection relation for control beam	106
Fig. 3.37	Load deflection relation for full width laminate strengthened beam	107
Fig. 3.38	Load deflection relation for 10 mm (0.4 in) strip panel strengthened beam	107
Fig. 3.39	Strain distribution in control beam	108
Fig. 3.40	Strain distribution in full width laminate strengthened beam	109
Fig. 3.41	Strain distribution in 10 mm (0.4 in) strip panel strengthened beam	109
Fig. 3.42	Tensile stress distribution in laminate edge at failure	110
Fig. 3.43	Shear stresses at the strip panel joint with layered shell elements	111
Fig. 3.44	Tensile stresses at the strip panel joint at 311.4 kN (70 kip)	112
Fig. 3.45	Tensile stresses in the strip panel finger joint model to match beam stresses	112
Fig. 3.46	Shear stress distribution in the 10 mm (0.4 in) strip panel	113

Fig. 4.1	KY 32 over Lytles Creek Bridge in Scott County, KY	115
Fig. 4.2	Layout of KY32 Bridge	116
Fig. 4.3	FEA model for Composite 1-1-2-7ft stud spacing girder	121
Fig. 4.4	Load-deflection curves for different shear stud layouts	122
Fig. 4.5	Strain profiles and plastic stress distribution for positive bending	127
Fig. 5.1	Stages in the repair and testing of KY 32 Bridge	134
Fig. 5.2	Locating rebars on the top and bottom of the KY32 Bridge	135
Fig. 5.3	Layout of top and bottom rebar mat	136
Fig. 5.4	ASTM 193 B7 threaded rod and nut	137
Fig. 5.5	Shear connector location on girders	138
Fig. 5.6	Shear connector placement	138
Fig. 5.7	Drilling rig fixed to the bottom flange	139
Fig. 5.8	Drilling through the bottom flange into the concrete deck	139
Fig. 5.9	Inserting of adhesive into drilled hole	140
Fig. 5.10	Inserting threaded rod with twisting motion	140
Fig. 5.11	Threaded rods held in place during curing	141
Fig. 5.12	Tightening of nut to specified torque	141
Fig. 5.13	Temporary platform and enclosing for grit blasting	142
Fig. 5.14	UHM CFRP laminate placement on bottom flange	143
Fig. 5.15	Layout of UHM CFRP laminates on each girder	144
Fig. 5.16	Sanding laminate edges to obtain reverse taper	145

Fig. 5.17	Tapered laminate edges	145
Fig. 5.18	Application of epoxy on to the top surface of the laminate	146
Fig. 5.19	Spreading of epoxy with V-notch trowel	147
Fig. 5.20	Placing laminate on the top flange	148
Fig. 5.21	Clamping both top and bottom laminates	148
Fig. 5.22	Laminates on bottom flange before and after painting	149
Fig. 5.23	Reusable strain gage and LVDT positions on KY32 Bridge	151
Fig. 5.24	Attaching reusable strain gages	152
Fig. 5.25	Wire mounted weights hung above LVDT locations on girder G3	152
Fig. 5.26	Instrumentation under the bridge at all four location	153
Fig. 5.27	Data acquisition to laptop computer via two signal conditioners	153
Fig. 5.28	Location of strain gages on laminates	154
Fig. 5.29	Attached strain gages on the two bottom laminates on girder G3	156
Fig. 5.30	Separate data acquisition system and laptop for laminate strain data	156
Fig. 5.31	Load test truck dimensions	157
Fig. 5.32	Load position on deck at mid span	157
Fig. 5.33	Displacement perpendicular to direction of traffic at mid-span – before retrofit	160
Fig. 5.34	Strain profile on center girder (G3) and edge girder (G1) at mid-span – before retrofit.	161
Fig. 5.35	Displacement perpendicular to direction of traffic at mid-span under HS20 truck load – before and after installing shear studs	163
Fig. 5.36	Displacement along direction of traffic under HS20 truck load – before and after installing shear studs	163

Fig. 5.37	Strain profile on center girder (G3) at mid-span under HS20 truck load – before and after installing shear studs	164
Fig. 5.38	Displacement perpendicular to direction of traffic at mid-span under HS20 truck load – before and after application of UHM CFRP laminates	166
Fig. 5.39	Displacement along direction of traffic under HS20 truck load – before and after application of UHM CFRP laminates	166
Fig. 5.40	Strain profile on center girder (G3) at mid-span under HS20 truck load – before and after application of UHM CFRP laminates	167
Fig. 5.41	Strain profile in the UHM CFRP laminates on the center girder (G3) under an HS20 truck load	168
Fig. 6.1	Load-slip relation for shear connectors	172
Fig. 6.2	Concrete Stress-Strain curve	174
Fig. 6.3	3-D Bridge model	176
Fig. 6.4	Displacement along the direction of traffic – before retrofit.	176
Fig. 6.5	Displacement perpendicular to direction of traffic at mid-span – before retrofit	177
Fig. 6.6	Strain profile on center girder (G3) and edge girder (G1) at mid-span – before retrofit	178
Fig. 6.7	Displacement along the direction of traffic – after post installing shear studs	179
Fig. 6.8	Displacement perpendicular to direction of traffic at mid-span – after post installing shear studs	179
Fig. 6.9	Strain profile on center girder (G3) and edge girder (G1) at mid-span – after post installing shear studs	180
Fig. 6.10	Steel girder model with epoxy and CFRP layer	181
Fig. 6.11	Displacement along the direction of traffic – after laminate application	182

Fig. 6.12	Displacement perpendicular to direction of traffic at mid-span – after laminate application	182
Fig. 6.13	Strain profile on center girder (G3) and edge girder (G1) at mid-span – after laminate application	183
Fig. 6.14	Displacement along the direction of traffic under HS20 truck load	184
Fig. 6.15	Displacement perpendicular to direction of traffic at mid-span under HS20 truck load	185
Fig. 6.16	Strain profile on center girder (G3) and edge girder (G1) at mid-span – after laminate application	186
Fig. 6.17	Displacement perpendicular to direction of traffic at mid-span – at each stage of strengthening with different laminate thicknesses	189
Fig. 6.18	Displacement perpendicular to direction of traffic at mid-span – theoretical simple support without barrier wall and friction forces	191
Fig. 6.19	Displacement perpendicular to direction of traffic at mid-span – theoretical simple support non-composite bridge strengthening	192

CHAPTER 1

INTRODUCTION

1.1 Steel Strengthening with Fiber Reinforced Polymer (FRP)

Advanced composites have become one of the most popular methods of repairing and/or strengthening civil infrastructure in the past couple of decades. The use of Fiber Reinforced Polymer (FRP) laminates plates and fabric for the repair and strengthening of reinforced concrete structures is well established with design guidelines in the form of ACI 440-02 (ACI Committee 440, 2002) and European fib bulletin 14 (fib Task group 9.3, 2001). Research on the application of FRP composites to steel structures has been limited. This is quite significant considering that more than 52% of the 72,524 structurally deficient bridges listed in the National Bridge Inventory (NBI) for 2007 by the Federal Highway Administration (FHWA) have steel superstructures (FHWA 2007).

The use of FRP material for the repair and rehabilitation of steel members hold numerous benefits over the traditional methods of bolting or welding of steel plates. FRP materials have the benefits of high strength to weight ratio, corrosion resistance, can be adhesively bonded, and have a stiffness comparable to that of steel. Project costs are reduced due to low transportation and handling costs as well as low application, and labor costs. As compared to traditional repair methods, FRP is less disruptive to regular service during the repair process. Furthermore, repairs that employ FRP contribute minimal additional dead load to the structure. Bonded FRP strengthening also creates less stress concentration as compared to mechanical fastening. While FRP repairs have also proven to have better fatigue performance compared to welded cover plates (Bocciarelli et al. 2009(b)), concern over environmental durability and galvanic corrosion exists (Lenwari et al. 2006).

Carbon FRPs (CFRPs) have been used heavily among other FRP materials for strengthening of steel structures, primarily because CFRP materials have relatively higher stiffness. CFRP laminates for application on steel structures are available as pultruded

plates, as preimpregnated (prepreg) sheets and as non-impregnated sheets (Hollaway and Cadei 2002). Pultruded plates are typically bonded to the steel using a two part epoxy adhesive, while prepregs can be bonded the same way or with a compatible adhesive film. The layup of non-impregnated laminate sheets, though common in concrete strengthening, is typically not used for steel strengthening as the fiber volume fraction, orientation, and other mechanical properties of the final composite are heavily dependent upon the quality of the application process.

The elastic modulus of commonly used CFRP plates varies from 150 – 450 GPa (21.76 x 10⁶ - 65.27 x 10⁶ psi) (Zhao and Zhang 2007). Depending on the modulus of the CFRP material researchers have used terms such as “normal modulus”, “high modulus” and “ultra high modulus” to categorize laminates. Given that no universally accepted classification system currently exists, the following categorization based on multiples of the modulus of steel, given in Table 1.1 is proposed and adopted in this dissertation.

Table 1.1: Classification of CFRP

Laminate Category	Modulus Relative to Steel	Modulus / GPa (ksi)
Low Modulus	$E_{CFRP} \leq 0.5E_{Steel}$	< 100 (14,500)
Normal/Intermediate Modulus	$0.5E_{Steel} \leq E_{CFRP} \leq E_{Steel}$	100 – 200 (14,500 – 29,000)
High Modulus	$E_{Steel} \leq E_{CFRP} \leq 2E_{Steel}$	200-400 (29,000 – 58,000)
Ultra High Modulus	$E_{CFRP} \geq 2E_{Steel}$	> 400 (58,000)

1.2 State-of-the-art on ultra high modulus CFRP strengthened steel structures

Most research literature available at present on strengthening of steel structures has mainly focused on normal modulus CFRP. A review by Hollaway and Cadei (2002) addressed some primary issues regarding the use of FRP in strengthening steel structures such as adhesive bond with reference to surface preparation and durability; force transfer between adherents and adhesive; and, in-service properties of FRP and impact damage. Zhao and Zhang (2007) conducted a review on FRP strengthened steel structures covering topics such as bond between steel and CFRP, strengthening of steel hollow section members, and fatigue crack propagation in FRP-steel members.

Previous research carried out on CFRP strengthening of steel structures has concentrated mostly on issues such as bond, bond strength (Hildebrand 1994; Täljsten 1997; Smith and Teng 2001; Benachour et al. 2008; Deng et al. 2004; Lenwari et al. 2006; Fawzia et al. 2006; Photiou et al. 2006; Bocciarelli et al. 2009(a)), bond length (Schnerch et al. 2006; Nozaka 2005(a); Nozaka 2005(b); Deng et al. 2004; Liu et al. 2005(b)), fatigue performance (Tavakkolizadeh and Saadatmanesh 2003(a); Liu et al. 2005(a); Bocciarelli et al. 2009(b)), and flexural performance (Schnerch and Rizkalla 2008, Lenwari et al. 2005; Tavakkolizadeh and Saadatmanesh 2003(b)). Several field applications of CFRP plates in strengthening actual bridge girders have been documented with excellent results (Miller et al. 2001; Hollaway and Cadei 2002; Phares et al. 2003; Moy and Bloodworth 2007). Several design guidelines for the use of FRP in strengthening steel have already been developed in the United Kingdom (Moy 2001; Cadei et al. 2004), Italy (CNR-DT 202/2005), and Schnerch et al. (2007) have introduced a design guide for use in the United States.

In numerous laboratory experiments normal modulus CFRP plates have been used successfully to strengthen concrete/steel-steel composite girders (Tavakkolizadeh and Saadatmanesh 2003(b); Lenwari et al. 2005; Al-Saidy et al. 2004; Fam et al. 2009; Aly and El-Hacha 2009). Applications involving wide flange beams have been limited due to findings of negligible increases in elastic stiffness. In order for a significant amount of

load transfer to occur, and for the effective use of CFRP material, the steel needs to yield in compression; the thickness of the CFRP plates need to be increased considerably; or, the distance between the bottom flange and CFRP plate needs to be increased by the insertion of some additional material (Schnerch and Rizkalla 2008). Given the difficulties of achieving these behaviors using normal modulus CFRP laminates, limited research has been carried out on strengthening of steel structures with CFRP, as compared to CFRP strengthening of concrete structures.

The emergence of high modulus CFRP plates, with an elastic modulus higher than that of steel, enables researchers to achieve substantial load transfer in steel beams before the steel yields. The failure modes for normal modulus CFRP bonded steel systems include failure at the steel/CFRP-adhesive interface, cohesive failure of adhesive, CFRP delamination and CFRP rupture (Zhao and Zhang 2007). But the failure mode for high modulus and ultra high modulus CFRP has been found to be mostly CFRP rupture (Zhao and Zhang 2007; Schnersch and Rizkalla 2008). This has been attributed to the lower rupture strain of high modulus CFRP as well as reduced normal (or peeling) stresses on the adhesive at the ends due to thinner CFRP plates required for a particular strengthening level.

Since applying laminates to non-composite steel beams generally acts to slightly increase the beam stiffness while shifting the neutral axis towards the laminate, the most efficient use of laminates is achieved when they are employed to strengthen concrete-steel composite bridge girders. However strengthening of damaged girders, as well as improving fatigue resistance, can be achieved even on non-composite beams. Full scale beam tests conducted by Dawood et al. (2007) and Schnersch and Rizkalla (2008) showed that significant service level stiffness increases as well as service load increases can be achieved by using ultra high modulus CFRP.

1.3 Field Applications

While CFRP laminates have been used in strengthening concrete bridge girders for over two decades, the field application of CFRP to steel girders has been limited. Hollaway and Cadei (2002) present several field applications of normal modulus CFRP in several bridges in the United Kingdom. These include the Hythe bridge over the Thames river in Oxfordshire, Slattocks Canal bridge in Rochdale, Bow Road Bridge in East London, and the Bid bridge in Kent. Normal modulus CFRP plates with a modulus of 112 GPa (16,240 ksi) were employed in strengthening two bridges in Delaware. The first bridge, 1-704 bridge on I-95 over Christina creek, had a single girder strengthened (Miller et al. 2001), while the second bridge, the Ashland bridge on State Route 82 over Red Clay creek had CFRP strips applied to two floor beams (Chacon et al. 2004). Normal modulus CFRP laminates were also effectively used in a bridge on State highway 92 in Pottawattamie County, Iowa where the laminates were applied on all girders in the positive moment regions, while up to three layers of laminates were applied to some girders to evaluate the effect of stacking laminates (Phares et al. 2003).

Table 1.2 lists the bridges around the world where CFRP has been used as the method of retrofit. High modulus CFRP laminates have been used to strengthen a couple of bridges in the United Kingdom. The Acton railway bridge in London was strengthened using CFRP plates with modulus of 310 GPa (44,950 ksi) to improve the fatigue resistance of secondary girders (Moy and Bloodworth 2007). The King Street cast iron railway bridge in Mold was strengthened using high modulus CFRP and GFRP laminate with an elastic modulus of 360 GPa (52,200 ksi). The Takiguchi Bridge in Tokyo, Japan is the only field application of ultra high modulus (UHM) CFRP laminates known to the author. The bridge girders were strengthened with 4 mm (0.1575 in) thick ultra high modulus laminates. The laminates were stacked along the bottom of the tension flange to create a maximum laminate thickness of 14 mm (0.55 in) at mid span.

Table 1.2: Reported bridge retrofit using CFRP around the world

Bridge	Location	Laminate Type (Modulus)	Date
Takiguchi Bridge	Tokyo (Japan)	Ultra High modulus CFRP plate (Modulus 450 GPa /65250 ksi)	2008
Acton Bridge	London Underground (England)	High modulus CFRP plates (Modulus 310 GPa /44950 ksi)	2000
King Street Bridge	Mold, Flintshire (England)	High modulus CFRP + GFRP plates (Modulus 360 GPa /52200 ksi)	2000
1-704 Bridge on I- 95 over Christina Creek	Newark, Delaware (USA)	CFRP plate (Modulus 112 GPa /16240 ksi)	2000
Ashland Bridge on State Rt. 82 over Red Clay Creek	Northern Delaware (USA)	CFRP plate (Modulus 112 GPa /16240 ksi)	2002
7838.5S092 Bridge on State Highway 92	Pottawattamie county,Iowa (USA)	CFRP plates (Modulus 138 GPa /20000ksi)	2003
Hythe Bridge over the Thames River	Oxfordshire (England)	CFRP plates (Modulus 160 GPa /23200 ksi)	1999
Slattocks Canal Bridge	Rochdale (England)	CFRP plates (Modulus unknown)	2000
Bow Road Bridge	East London (England)	CFRP plates (Modulus unknown)	unknown
Bid Bridge	Kent (England)	CFRP plates (Modulus unknown)	unknown

1.4 Research Objectives

The objective of this research is to investigate, both analytically and experimentally, the bond characteristics between ultra high modulus CFRP strengthened steel members and the flexural behavior of these members.

1.5 Research Significance

The proposed research constitutes one of the first experimental and analytical evaluations of bond stresses between ultra high modulus CFRP plates and steel. The bond characteristics of ultra high modulus CFRP strengthened steel are still not fully understood. Some studies on bond behavior carried out on normal modulus CFRP have been extended to higher modulus FRP with the aid of parametric studies (Deng et al. 2004). The flexural behavior of ultra high modulus CFRP strengthened steel beams have been experimentally evaluated by Schnerch and Rizkalla (2008).

The study also hopes to introduce the novel ultra high modulus CFRP plate strip panels, developed at the University of Kentucky, for strengthening of steel bridge girders. Although generally more economical than other repair methods, one of the drawbacks in the application of CFRP plates for flexural strengthening of bridge girders has been the man power required to attach continuous laminate plates along the entire lengths of bridge girders. The difficulty of application increases in proportion to bridge length, as well as the degree of accessibility to the underside of the bridge superstructure. When required, construction of scaffolding along the length of bridges can be time consuming and costly.

Splicing of CFRP plates can provide an economical alternative where individual workers can carry out the strengthening process on a single boom truck or scaffolding, significantly reducing labor and equipment costs. Few studies have been reported on the viability of lap splicing of CFRP plates for concrete beams (Yang and Nanni 2002; Stalling and Porter 2003), although in one study, Schnerch and Rizkalla (2008) evaluated

the effectiveness of lap splices for composite concrete deck-steel girders. The present guidelines require the splice plate to be at least 800mm (31.5 in.) long to prevent premature debonding (Schnerch et al. 2007). The laminate strips are to be mounted on a fabric/wire mesh designed to keep the required spacing between strips while facilitating the handling of handling several strips at once. The length of each segment/panel is to be approximately 1.5 m (5 ft.) or less, allowing for individual workers to handle and mount sections on to the bottoms of girders.

The first field application of ultra high modulus CFRP laminates on steel bridge girders in the United States will also be carried out as part of the proposed research. While UHM CFRP laminates have been used to strengthen a bridge in Japan (Table 1.2), the process of application and the effectiveness of the retrofit are not well documented. The current study aims to evaluate the practicality of UHM CFRP application in the field. The performance of the strengthened bridge is also analyzed by measuring strain and deflection data at preselected locations on the bridge, both before and after retrofit.

1.6 Organization of Dissertation

In order to achieve the objective of this research, it was divided into two phases, laboratory investigation and field investigation, with each phase consisting of respective experimental and analytical components.

- **Laboratory Investigation of Bond Characteristics between Steel and High Modulus CFRP.**

A comprehensive stress analysis of the interfacial stresses between steel and ultra high modulus CFRP is not available in current literature. Some experimental data is available by Schnerch et al. (2004) on the performance of double strap joints for different resins and layup processes. Single lap shear tests have been recommended for CFRP plates to evaluate the bond characteristics (Zhao and Zhang 2007), but due to application of load onto the FRP plate, and possibility of misalignment of loading, most researchers prefer the simplicity of the double strap joint. In the current study,

a series of double strap joint tests with two different CFRP strip widths are carried out to evaluate the development length of the bond. Both ultra high modulus and normal modulus CFRP laminates are used to compare performance. Steel plates reinforced with CFRP laminates on both sides are loaded in tension to evaluate load transfer characteristics. Debonding under flexural loads is also studied for ultra high modulus CFRP strengthened steel girders. Flexural tests are carried out under 4-point bending on several small scale wide flange beams and the potential of using strips as splices instead of lap splices is investigated. Also, debonding of both non-segmented and selected spliced panels of ultra high modulus CFRP plate arrangements are tested.

The experimental data are further complemented with data obtained from finite element analysis (FEA). Closed form analytical solutions available for the evaluation of shear stresses in plates as well as beams are assessed for practical applicability with ultra high modulus CFRP laminates. Material tests conducted on steel, normal and ultra high modulus CFRP and the adhesive are carried out to verify manufacturer specifications. Material properties measured during these tests are included in the FEA to account for non-linear material behavior. The commercial finite element program ANSYS is used to perform three dimensional non-linear analysis (ANSYS 2009).

- **Field Investigation of High Modulus CFRP Strengthened Steel Bridge**

While several field applications of normal modulus CFRP plates in strengthening actual bridge girders have been documented (Miller et al. 2001; Hollaway and Cadei 2002; Phares et al. 2003; Moy and Bloodworth 2007), none have been documented using ultra high modulus CFRP. The KY32 Bridge over Lytles creek in Scott County, KY is strengthened using high modulus CFRP laminates. Full scale load test data measured before and after the strengthening are utilized to measure the degree of strengthening achieved and checked against the expected results.

A finite element model is developed and calibrated using data obtained from the field testing of the bridge. The model is then used to evaluate the behavior of the bridge under different load positions before and after the strengthening process.

A summary of the contents of the next chapters is as follows:

- Chapter 2: An overview of current research of the bond between steel and CFRP as well as developments in steel beam strengthening with CFRP is given in this chapter. Laboratory testing, completed as part of the current study, in evaluating the development length and other bond characteristics is also detailed. Testing procedures and results for double lap shear, doubly reinforced steel plates in tension, and small scale steel beams strengthened with CFRP plates are also presented.
- Chapter 3: Numerical and Finite Element Analyses (FEA) performed on the laboratory test specimens are presented in this chapter. Analytical results are compared to the experimental measurements.
- Chapter 4: An overview of the KY32 bridge as well as the preliminary analysis and load rating performed are detailed in this chapter.
- Chapter 5: A detailed description of the strengthening of the KY32 Bridge in Scott County is given in this chapter. Field-measured load test results in the form of deflections and strains at each stage of strengthening are also included.
- Chapter 6: The FEA of the KY32 Bridge is presented in this chapter. The results are compared with the field test results and a parametric study into different laminate thicknesses and support conditions is also carried out.
- Chapter 7: The final chapter summarizes the present research and provides suggestions for future work.

CHAPTER 2

BOND AND FLEXURAL BEHAVIOR TESTS

2.1 Introduction

Bonding of plates to the surfaces of steel and concrete beams has proved to be an effective method in strengthening as well as increasing the service life of many engineering structures. Although this method of repair requires the adhesive joint to have adequate strength, the design of such joints is rarely encountered in engineering construction. Historically plate bonding in civil engineering has been confined mostly to steel plates bonded to steel beams. However, fiber reinforced polymer (FRP) composite materials, especially carbon fiber reinforced polymer (CFRP), initially developed in the aerospace and automobile industry, have become popular among civil engineers in strengthening applications that require high corrosion resistance. Strengthening of steel beams with CFRP composite plates has not been as widespread as retrofitting of reinforced concrete beams. One important reason for this is the relatively high, innate strength and stiffness of steel which makes it a very difficult material to strengthen. Only with the arrival of CFRP material with a modulus at least comparable to or greater than that of steel has the strengthening of steel beams with CFRP plates become more viable. Even with ultra high modulus CFRP laminates, which have a tensile modulus more than twice that of steel, the weakest link in the plate bonding process is still the bond between the steel and CFRP.

A comprehensive experimental study of the interfacial stresses between steel and ultra high modulus CFRP is not available in current literature. Most studies conducted have focused on the bond between steel and normal modulus CFRP laminates. Zhao and Zhang (2007) summarize several different testing methods used by researchers to evaluate bond behavior. Research carried out by Xia and Teng (2005) evaluated the bond behavior of normal modulus CFRP laminate plates utilizing single lap shear joints, while Fawzia et al. (2006) tested layered CFRP sheets in double lap strap joints. Al-Emrani and Kliger (2006) evaluated the bond of four different laminates from normal modulus to

high modulus, while Miller et al. (2001) evaluated the force transfer between steel and normal modulus CFRP; both of these studies used CFRP doubly reinforced steel plate specimens for experimentation. El Damatty and Abushagur (2003) used shear lap tests to evaluate bond between CFRP sheets and steel. Colombi and Poggi (2005) tested normal modulus CFRP laminates using both doubly reinforced steel plates as well as double strap joint specimens. Experimental data are available by Schnerch et al. (2004) on the performance of ultra high modulus double strap joints for different resins and layup processes. Findings from Schnerch et al. (2004) were useful in the selection of epoxy for the current research.

While single lap shear tests have been recommended for CFRP plates to evaluate the bond characteristics (Zhao and Zhang 2007), due to application of load onto the FRP plate and the possibility of loading misalignment, most researchers prefer the double strap joint for its simplicity. In the current research, bond is evaluated using both doubly reinforced steel specimens and double strap joint specimens. As stated in Colombi and Poggi (2006), the first type (doubly reinforced) represents steel members strengthened with laminates, while the second type (double strap joint) represents a repaired section of steel with partially or fully developed crack. A series of double strap joint tests with two different CFRP strip widths are carried out to evaluate the development length of the bond. Both ultra high modulus and normal modulus CFRP laminates are used to compare performance. Steel plates reinforced with CFRP laminates on both sides (doubly reinforced) are loaded in tension to evaluate the load transfer characteristics.

FRP strengthened steel beams have been reported to undergo various modes of failure. Steel beams can fail in shear, lateral torsional buckling, yielding in flexure or compression (top or bottom flange), etc. When a steel member's failure is dominated by tensile yielding, CFRP laminates can be used to increase its capacity. Flexural failure due to either crushing of concrete (in composite beams) or yielding of steel in compression or rupture of FRP laminate in tension has been reported (Hollaway and Cadei 2002; Schnerch and Rizkalla 2008; Tavakkolizadeh and Saadatmanesh 2003(b)). Local failure is defined as the peeling or debonding of FRP laminates at locations of high stress

concentrations. In order to understand and model the debonding failures in FRP strengthened beams, it is first necessary to understand the interfacial behavior between the FRP and the substrate. The strength of these joints is governed by stress concentrations which occur in the vicinity of geometric discontinuities (Stratford and Cadei 2006). The geometric discontinuities include bond defects, discontinuities in the substrate such as cracks, and steps in the strengthening plate which include the end of the plate. Since FRP plates were initially used in strengthening reinforced concrete beams, most of the research on bond behavior of FRP and substrate has been oriented towards FRP-concrete interface.

Tavakkolizadeh and Saadatmanesh (2003(b)), Nozaka et al. (2005(a)) and Colombi and Poggi (2006) experimentally tested normal modulus CFRP plate strengthened steel girders. Lenwari et al. (2005) used CFRP laminates with an elastic modulus of 300 GPa (43500 ksi) to strengthen steel beams. Photiou et al. (2006), Fam et al (2009) and Linghoff et al. (2009) tested multiple beams strengthened with laminates of varying elastic modulus, all less than 330 GPa (47900 ksi). The local failure modes for normal modulus CFRP bonded steel systems include failure at the steel/CFRP-adhesive interface, cohesive failure of adhesive; and, CFRP delamination and CFRP rupture (Zhao and Zhang 2007). However, the failure mode for high modulus and ultra high modulus CFRP has been found most commonly to be rupture (Zhao and Zhang 2007; Schnerch and Rizkalla 2008). This phenomenon has been attributed to the lower rupture strain of high modulus CFRP as well as reduced normal (or peeling) stresses on the adhesive at the ends due to thinner CFRP plates required for a particular strengthening level. Schnerch and Rizkalla (2008) performed some of the earliest beam tests to evaluate the flexural performance of ultra high modulus CFRP laminates in strengthening steel beams. Schnerch and Rizkalla (2008) as well as Dawood et al. (2009) also evaluated the viability of lap splicing of CFRP laminates.

The ultra high modulus CFRP laminates used in this study are produced using unidirectional fiber orientation bonded together by the resin matrix. The carbon fibers make up approximately 71% of the volume of the laminate. The tensile strength of the

individual carbon fiber is approximately 2600 MPa (377 ksi). The tensile strength of the laminate is primarily dependent on the strength of the fibers while its compressive strength is primarily dependent on the compressive strength of the resin matrix. Consequently, CFRP laminates are primarily used to strengthen the tension side/flange of structural members.

In order to further the state of the art, debonding under flexural loads is investigated in the current study for ultra high modulus CFRP strengthened steel girders. Flexural tests are carried out under 4-point bending on several small scale wide flange beams. The potential of using 1.2 m (4 ft) long strip panels, instead of lap splices, to achieve load transfer is investigated. The debonding of both non-segmented and the proposed strip panel type splice panels of ultra high modulus CFRP plate arrangements is evaluated both experimentally and analytically.

2.2 Double Strap Joint Tests

The primary objective of the double strap joint specimen test is to evaluate the bond length required to achieve full load transfer between the steel and CFRP. In order to facilitate comparison between the strip panel splices proposed as a method of splicing flexural members, as well as to replicate actual field applications where the laminate would have a smaller width than the base steel, 5 mm (0.2 in) and 10 mm (0.4 in) wide strips are used in the testing. Both normal and ultra high modulus CFRP laminates are tested to evaluate differences in development length and ultimate joint load.

2.2.1 Double Strap Joint Specimens

Two 50 mm (2 in) wide, 4.8 mm (0.19 in) thick steel plates were positioned to achieve 1 mm (0.039 in) gap between the short edges as shown in Fig. 2.1. The steel surface where the laminate is applied was ground and cleaned with solvent prior to the application. Both the normal modulus and ultra high modulus laminates were 1.2 mm (0.047 in) thick.

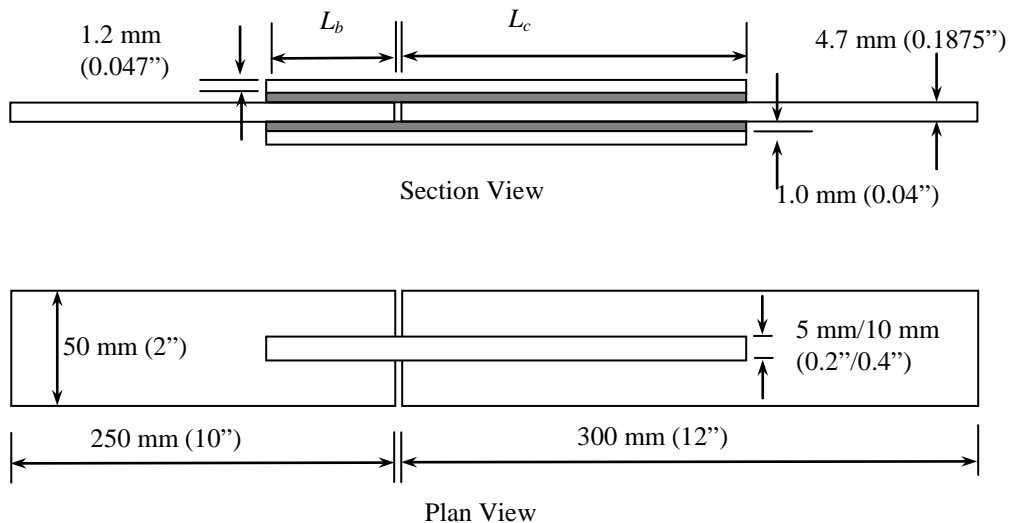


Fig. 2.1: Double Strap Joint Specimen Dimensions

The normal modulus laminate were manufactured to be 100 mm (4 in) wide, and the ultra high modulus laminates were manufactured to be 50 mm (2 in) wide. The laminates were shear cut to the required lengths and widths using a mechanical shear. The ultra high modulus laminates were manufactured with a peel-ply to prevent any damage or contamination to the surface. Additionally the laminate surface was manufactured with a roughened profile for better bonding. In contrast, the normal modulus laminates did not have rough profiles or a peel plies. Therefore the normal modulus laminates were cleaned with Acetone before the application of epoxy.

The two part epoxy was applied onto the laminates using the manufacturer specified dispenser gun. The epoxy was spread using a small v-notched trowel (Fig. 2.2 (a)) to obtain a triangular profile and also to spread the epoxy evenly along the laminate. The laminates were then placed along the centerline on the top surface of the two steel plates at pre-marked locations, which designated the required bond length (L_b in Fig. 2.1). The laminates were then gently pressed onto the steel surface using a roller as shown in Fig. 2.2 (b). After laminate placement and rolling, the expected final thickness of the epoxy was 1 mm (0.039 in). However, due to the small width of the specimens, no spacers were placed to obtain the expected thickness. Once the laminates were applied on one side, the specimens were allowed to cure for at least two days before the procedure was repeated on the other side of the specimen. The specimens were mounted on wooden frames when installing the laminates on the other side to prevent accidental forces being applied to the already mounted laminates. Once both laminates were installed, the specimens were further cured for a minimum of 14 days at room temperature. A small uniform pressure was applied onto the laminates during the first two days of curing. Consequently, the final measured thickness of the epoxy was found to be between 0.6 mm - 0.7 mm (0.0236 in - 0.275 in).

A total of 52 specimens were prepared and tested. Bond lengths (L_b) of 12.5 mm (0.5 in), 25 mm (1 in), 37.5 mm (1.5 in), 50 mm (2 in), 75 mm (3 in) and 100 mm (4 in) were tested for both normal modulus and ultra high modulus laminates. For most bond lengths both 5 mm (0.2 in) and 10 mm (0.4 in) wide CFRP specimens were tested with two

specimens each for each width. Some ultra high modulus laminates were not tested at shorter bond lengths, but instead were tested at extended bond lengths of 125 mm (5 in) and 150 mm (6 in) for both the 5 mm (0.2 in) and 10 mm (0.4 in) widths. Also, a bond length of 175 mm (7 in) was used in testing of the 10 mm (0.4 in) wide laminate. The control side length (L_c) was kept at 150 mm (6 in) for bond lengths (L_b) less than 100 mm (4 in) and was increased to 200 mm (8 in) for all other bond lengths.



(a) Spreading epoxy on laminate



(b) Pressing on to steel surface with roller

Fig. 2.2: Specimen preparation

2.2.2 Material Properties

All materials used in the experiments were tested to ascertain the corresponding mechanical material properties. The material tests were carried out in accordance with relevant ASTM specifications.

2.2.2.1 Steel

The steel plates used in the test were classified as ASTM A36 steel. Tensile tests were performed on coupons made according to ASTM E8M-09 specifications. The average yield strength of the steel plates was found to be 409.7 MPa (59.4 ksi), with an ultimate strength of 470.2 MPa (68.18 ksi). The Young's modulus was not evaluated and was taken as 200 GPa (29000 ksi). Fig. 2.3 depicts one of the steel coupons (Fig. 2.3(a)) and the tensile test configuration (Fig. 2.3(b)).



(a) Steel coupon



(b) Tensile test

Fig. 2.3: Steel coupon test

2.2.2.2 CFRP Laminates

The normal modulus CFRP laminates used in the experiments were Sika CarboDur S1012, produced by Sika Corporation. The ultra high modulus laminates were ePLATE HM512, distributed by Mitsubishi Plastics Composites America, Inc. Tensile tests on the laminates were performed according to ASTM 3039-00 guidelines. Strain gages were attached to the specimens in directions both parallel and perpendicular to the loading direction. The specimens were 381 mm (15 in) long and 25 mm (1 in) wide with a gage length of 229 mm (9 in). Aluminum tabs 75 mm (3 in) long were attached to both ends for gripping (Fig. 2.4(a)). The tensile test in progress is shown in Fig. 2.4(b). Five ultra high modulus and three normal modulus specimens were tested. The average of the evaluated material properties are given in Table 2.1.



(a) CFRP specimen



(b) Tensile test

Fig. 2.4: CFRP tensile test

Table 2.1: CFRP Material Properties

Laminate Category	Tensile Modulus		Tensile Strength		Ultimate Tensile Strain
	GPa	ksi	MPa	ksi	
Normal Modulus	187	27017	2979	432	0.01808
Ultra High Modulus	514	74586	1923	279	0.00332

Stress-strain relationship for one normal modulus and one ultra high modulus laminate specimens is shown in Fig. 2.5. Ultimate tensile strains are slightly more than the recorded values as some strain gages were damaged prior to failure of the specimens. Both laminate types failed in rupture, although the normal modulus laminates showed a relatively more ‘explosive’ type of failure (Fig. 2.6(a)), compared to the ultra high modulus laminates, which split into smaller pieces as depicted in Fig. 2.6(b).

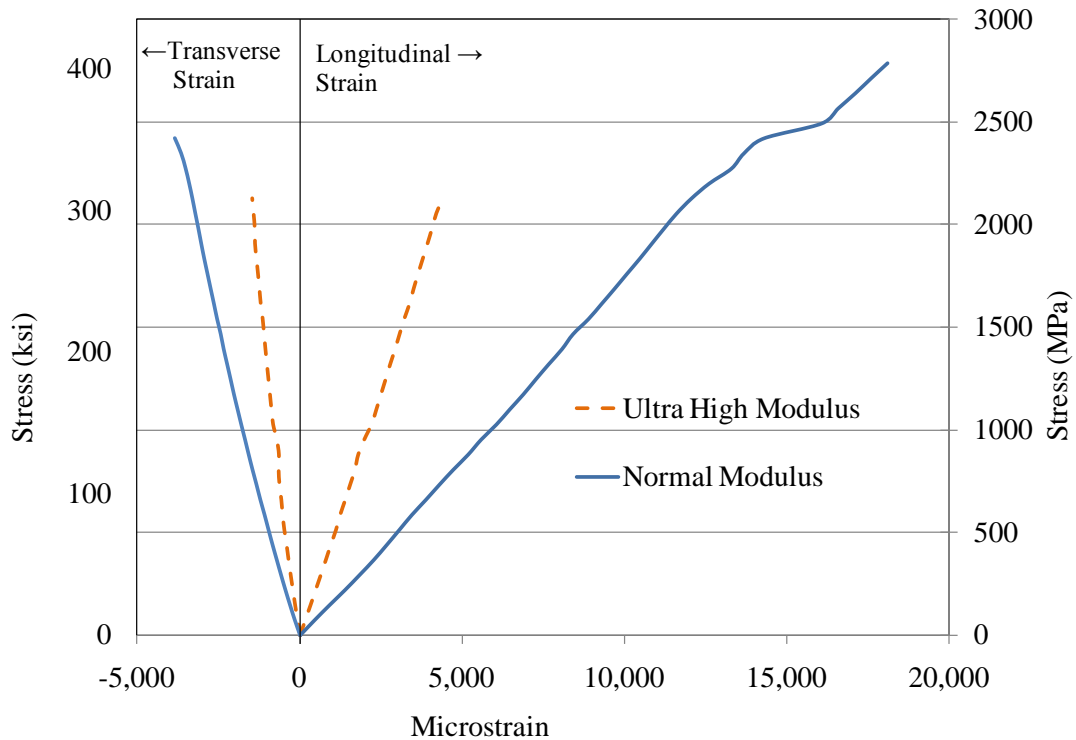


Fig. 2.5: Tensile stress-strain relationship for CFRP laminates



(a) Normal modulus CFRP



(b) Ultra high modulus CFRP

Fig. 2.6: Observed rupture of CFRP laminates

2.2.2.3 Adhesive Epoxy

The two part epoxy used was Spabond 345 produced by SP-High Modulus, the marine business of the Gurit Corporation. The selection of the epoxy was based on research conducted by Shnerch (2005) on different epoxy types for use with ultra high modulus CFRP. The tensile testing of the epoxy adhesive was done according to ASTM D638-08 specifications. Epoxy coupons 13 mm (0.5 in) wide and 5 mm (0.2 in) thick were prepared and tested. The ultimate failure was brittle as shown in Fig. 2.7. The evaluated material properties are given in Table 2.2.



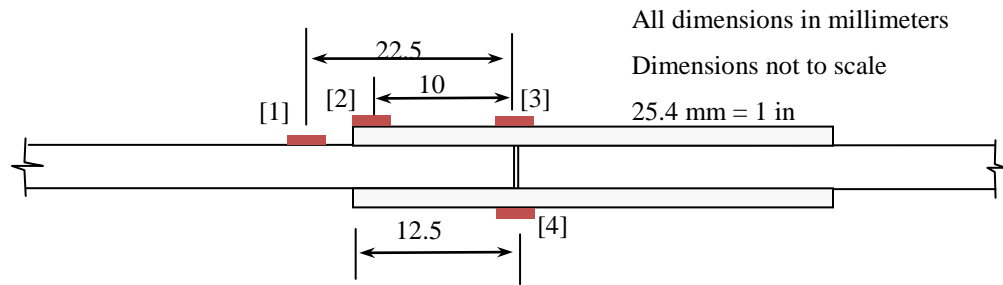
Fig. 2.7: Failure of Epoxy coupons

Table 2.2: Adhesive Epoxy Material Properties

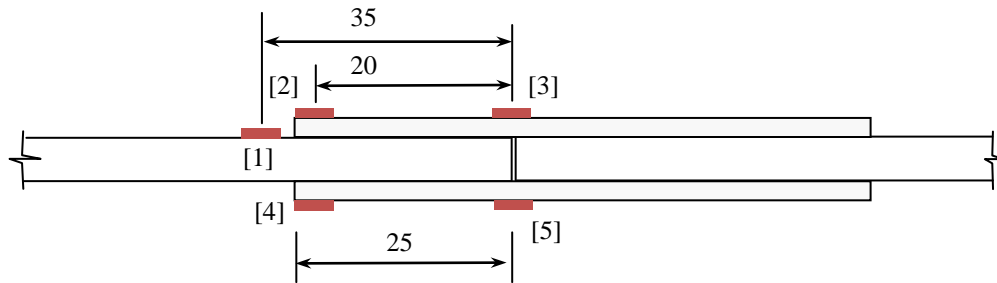
Tensile Modulus		Tensile Strength		Ultimate Tensile Strain
MPa	ksi	MPa	ksi	
3007	436	34.6	5.02	0.0132

2.2.3 Instrumentation and Testing

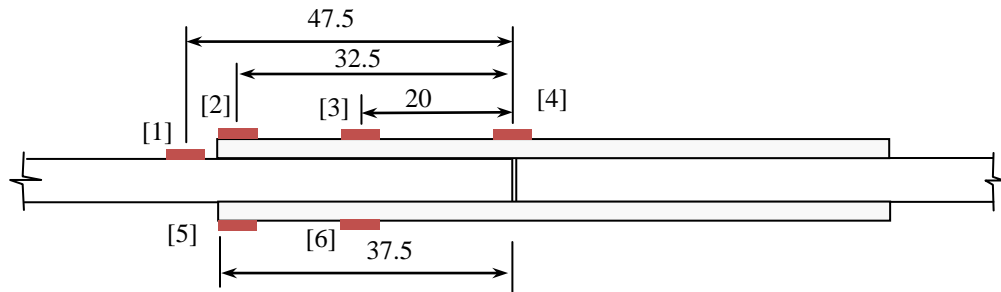
The double strap joint specimens were instrumented with foil type electrical resistance strain gages along the bond length center line. The surface profiles on the ultra high modulus CFRP laminates were sanded down to obtain level yet rough surface characteristics. Similarly, the normal modulus CFRP laminates were sanded for bonding to the gages. The number of gages attached to the laminate varied depending on the length of the bond. Gages were attached on both sides of the bond to facilitate identification of potential unbalances in the loading. Gage numbering and distances from the gap to each gage are illustrated in Fig. 2.8. The specimens were tested in a universal tensile testing machine at a strain rate of 1.25 mm/min (0.05 in/min). The strain gages were connected to a data acquisition system and the strain data were collected through a laptop computer. A representative test setup for the specimens is shown in Fig. 2.9.



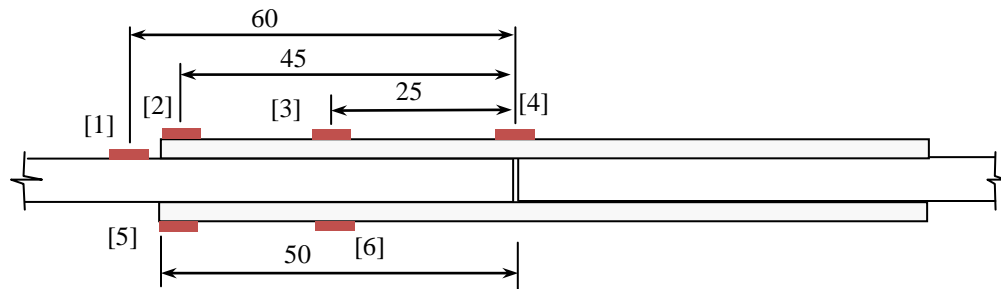
(a) 12.5 mm (0.5 in) Specimen



(b) 25 mm (1 in) Specimen

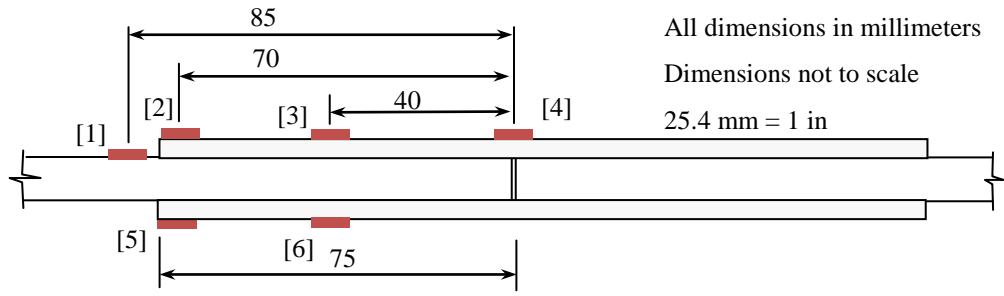


(c) 37.5 mm (1.5 in) Specimen



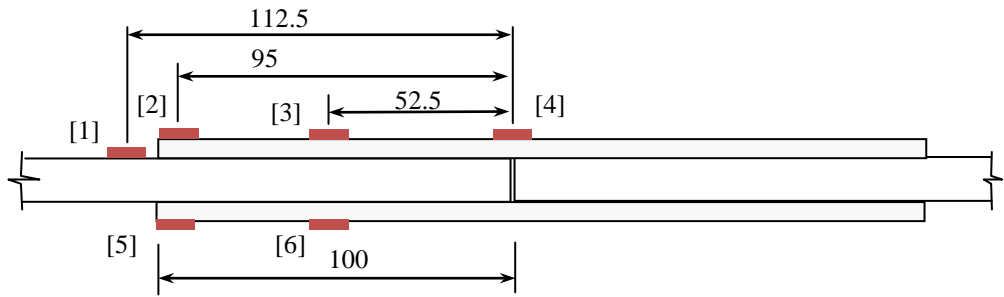
(d) 50 mm (2 in) Specimen

Fig. 2.8: Double Strap Joint Specimen Gage Layout

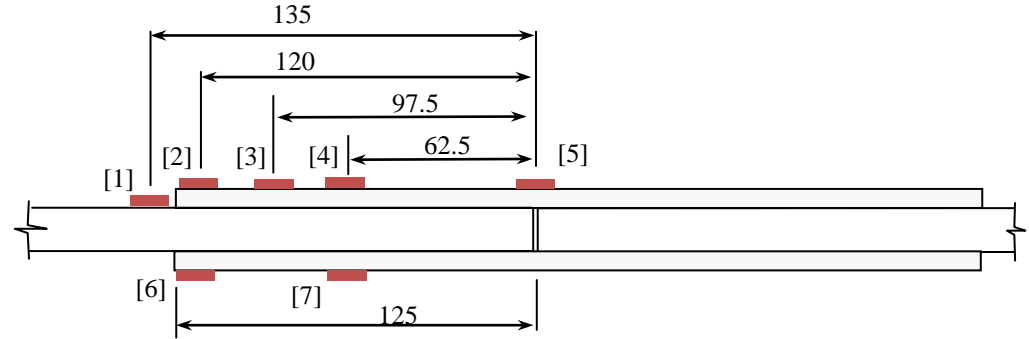


All dimensions in millimeters
 Dimensions not to scale
 25.4 mm = 1 in

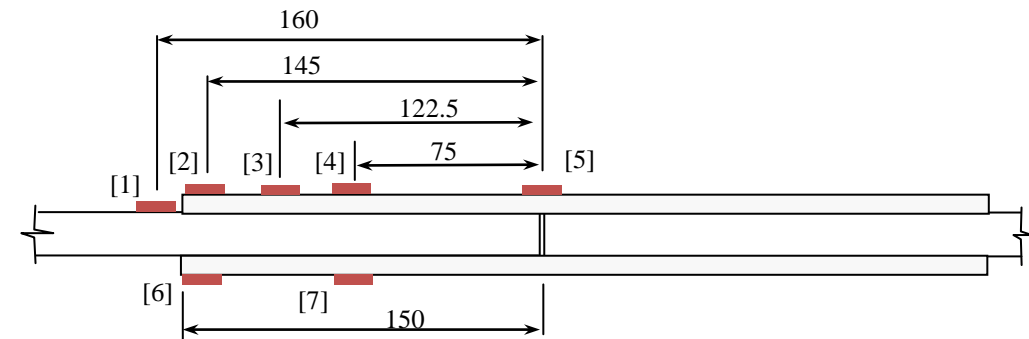
(e) 75 mm (3 in) Specimen



(f) 100 mm (4 in) Specimen

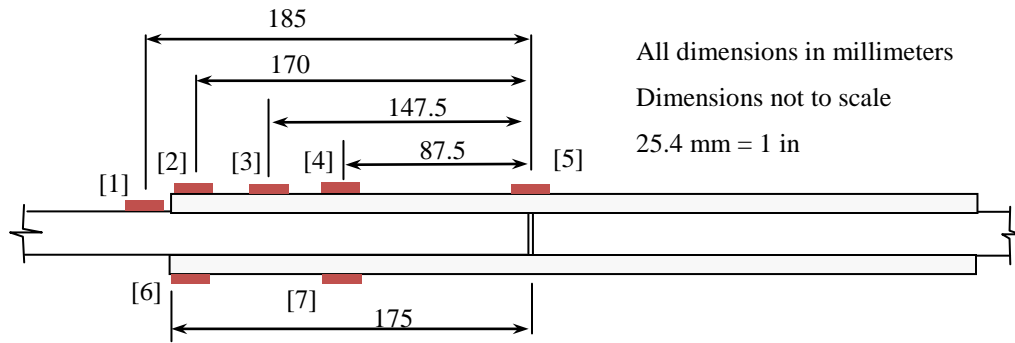


(g) 125 mm (5 in) Specimen



(h) 150 mm (6 in) Specimen

Fig. 2.8: Double Strap Joint Specimen Gauge Layout (Continued)



(i) 175 mm (7 in) Specimen

Fig. 2.8: Double Strap Joint Specimen Gage Layout (Continued)



Fig. 2.9: Tensile testing of double strap joint specimen

2.2.4 Test Results

The recorded failure load and observed mode of failure for normal modulus CFRP is provided in Table 2.3 and Table 2.4.

Table 2.3: Normal modulus 5mm (0.2 in) wide specimen test results

Specimen ID	Bond Length		Failure Load		Failure Mode
	mm	in	N	lbf	
NM5-12.5A	12.5	0.5	2282	513	Steel-adhesive interface debonding
NM5-12.5B	12.5	0.5	2980	670	Steel-adhesive interface debonding
NM5-25A	25	1	7758	1744	Steel-adhesive interface debonding
NM5-25B	25	1	7838	1762	Steel-adhesive interface debonding
NM5-37.5A	37.5	1.5	8296	1865	Steel-adhesive interface debonding
NM5-37.5B	37.5	1.5	8479	1906	Steel-adhesive interface debonding CFRP delamination
NM5-50A	50	2	11895	2674	Steel-adhesive interface debonding CFRP delamination
NM5-50B	50	2	10414	2341	Steel-adhesive interface debonding CFRP delamination
NM5-75A	75	3	7046	1584	CFRP delamination
NM5-75B	75	3	12433	2795	CFRP delamination
NM5-100A	100	4	10988	2470	CFRP delamination
NM5-100B	100	4	11419	2567	Steel-adhesive interface debonding CFRP delamination

Table 2.4: Normal modulus 10mm (0.4 in) wide specimen test results

Specimen ID	Bond Length		Failure Load		Failure Mode
	mm	in	N	lbf	
NM10-12.5A	12.5	0.5	7878	1771	Steel-adhesive interface debonding
NM10-12.5B	12.5	0.5	8821	1983	Steel-adhesive interface debonding
NM10-25A	25	1	15214	3420	Steel-adhesive interface debonding
NM10-25B	25	1	12162	2734	Steel-adhesive interface debonding
NM10-37.5A	37.5	1.5	20262	4555	Steel-adhesive interface debonding
NM10-37.5B	37.5	1.5	21966	4938	Steel-adhesive interface debonding CFRP delamination
NM10-50A	50	2	19800	4451	CFRP delamination
NM10-50B	50	2	18341	4123	CFRP delamination
NM10-75A	75	3	22669	5096	Steel-adhesive interface debonding CFRP delamination
NM10-75B	75	3	35778	8043	CFRP delamination
NM10-100A	100	4	20881	4694	CFRP delamination
NM10-100B	100	4	20983	4717	CFRP delamination

As listed in Table 2.3 and Table 2.4, the first letters of the specimen ID denote the modulus of CFRP (NM for normal modulus and UHM for ultra high modulus). Numbers immediately following the letters indicate the width of the laminate. The second part of the identification includes the bond length and repetition. For example, UHM5-50A would represent the ultra high modulus 5 mm (0.2 in) wide, 50 mm (2 in) bond length specimen, with the final ‘A’ representing the first of two specimens tested.. The double

strap joint test results for the ultra high modulus laminates are provided in Table 2.5 and Table 2.6.

Table 2.5: Ultra high modulus 5mm (0.2 in) wide specimen test results

Specimen ID	Bond Length		Failure Load		Failure Mode
	mm	in	N	lbf	
UHM5-25A	25	1	4159	935	Steel-adhesive interface debonding CFRP delamination
UHM5-37.5A	37.5	1.5	12153	2732	Steel-adhesive interface debonding CFRP delamination
UHM5-37.5B	37.5	1.5	6090	1369	Steel-adhesive interface debonding CFRP delamination
UHM5-50A	50	2	13243	2977	Steel-adhesive interface debonding CFRP delamination
UHM5-50B	50	2	14266	3207	Steel-adhesive interface debonding CFRP delamination
UHM5-75A	75	3	16419	3961	Steel-adhesive interface debonding CFRP delamination
UHM5-75B	75	3	22989	5168	CFRP rupture
UHM5-100A	100	4	8310	1868	Steel-adhesive interface debonding CFRP delamination
UHM5-100B	100	4	14235	3200	Steel-adhesive interface debonding CFRP delamination
UHM5-125A	125	5	18754	4216	CFRP rupture CFRP delamination
UHM5-125B	125	5	18470	4152	CFRP delamination
UHM5-150A	150	6	14257	3205	CFRP rupture CFRP delamination
UHM5-150B	150	6	16886	3796	CFRP rupture

Table 2.6: Ultra high modulus 10mm (0.4 in) wide specimen test results

Specimen ID	Bond Length		Failure Load		Failure Mode
	mm	in	N	lbf	
UHM10-12.5A	12.5	0.5	4693	1055	Steel-adhesive interface debonding CFRP delamination
UHM10-25A	25	1	12616	2836	Steel-adhesive interface debonding CFRP delamination
UHM10-37.5A	37.5	1.5	11481	2581	Steel-adhesive interface debonding CFRP delamination
UHM10-37.5B	37.5	1.5	21366	4803	CFRP delamination
UHM10-50A	50	2	25423	5715	CFRP delamination
UHM10-50B	50	2	24875	5592	Steel-adhesive interface debonding CFRP delamination
UHM10-75A	75	3	32331	7268	CFRP rupture CFRP delamination
UHM10-75B	75	3	29213	6567	CFRP delamination
UHM10-100A	100	4	46259	10399	CFRP rupture
UHM10-100B	100	4	25672	8779	CFRP rupture
UHM10-125A	125	5	22731	5110	CFRP delamination
UHM10-125B	125	5	21499	4833	Steel-adhesive interface debonding
UHM10-150A	150	6	36739	8259	CFRP rupture CFRP delamination
UHM10-150B	150	6	32064	7208	CFRP rupture
UHM10-175A	175	7	28523	6412	CFRP rupture

Three types of failure, observed during the testing of the normal modulus laminate specimens, are presented in Fig. 2.10 through Fig. 2.12. Specifically, steel-adhesive layer debonding seen in normal modulus CFRP double strap joint specimen failure is shown in Fig. 2.10. Combined steel-adhesive debonding with delamination within the CFRP laminate is shown in Fig. 2.11. Also complete CFRP delamination is seen in Fig. 2.12.



Fig. 2.10: Typical steel-epoxy interface debonding seen in normal modulus CFRP



Fig. 2.11: Typical combined steel-epoxy interface debonding and CFRP delamination seen in normal modulus CFRP



Fig. 2.12: Typical CFRP delamination seen in normal modulus CFRP

During the normal modulus CFRP laminate testing, debonding was observed at shorter bond lengths while delamination within the CFRP laminate was observed at longer bond lengths. In some instances, steel-epoxy interface debonding was observed on one side, while CFRP delamination occurred on the other side. In the ultra high modulus CFRP laminate specimens, failure due exclusively to debonding between steel and epoxy on both sides was not observed. While at shorter bond lengths, debonding still occurred, some degree of delamination was always present. Typical failures observed in the ultra high modulus laminates are presented in Fig. 2.13 through Fig. 2.15. The ultra high modulus CFRP laminates generally failed in rupture for longer bond lengths. For a number of cases, the exact failure mechanism was unclear because the two sides would undergo different modes of failure.

In order to evaluate the bond length, the failure load is plotted against the bond length for normal modulus CFRP in Figs. 2.16 and 2.17. Similar plots are shown for UHM CFRP in Figs. 2.18 and 2.19. The development length for normal modulus CFRP laminates is approximately 50 mm (2 in), for the ultra high modulus CFRP laminates the development length is approximately 75 mm (3 in). The test data is compared with existing bond models in the next chapter.



Fig. 2.13: Typical combined steel-epoxy debonding and CFRP delamination seen in ultra high modulus CFRP



Fig. 2.14: Typical CFRP delamination seen in ultra high modulus CFRP



Fig. 2.15: Typical CFRP rupture seen in ultra high modulus CFRP

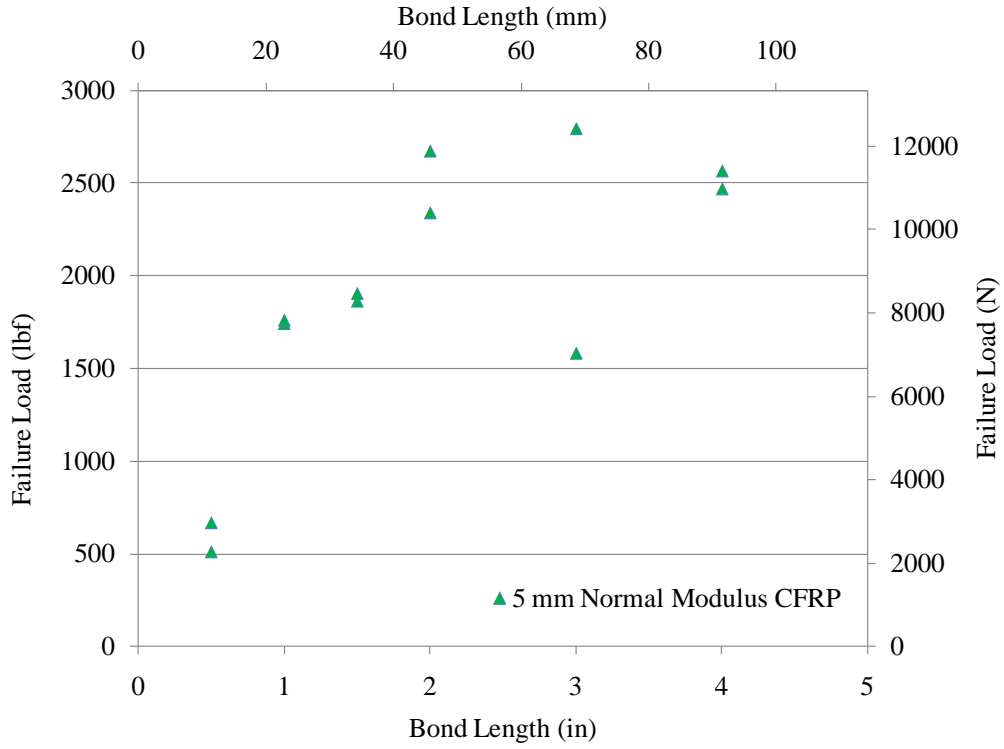


Fig. 2.16: Failure load variation with bond length for NM 5 mm (0.2 in) specimens

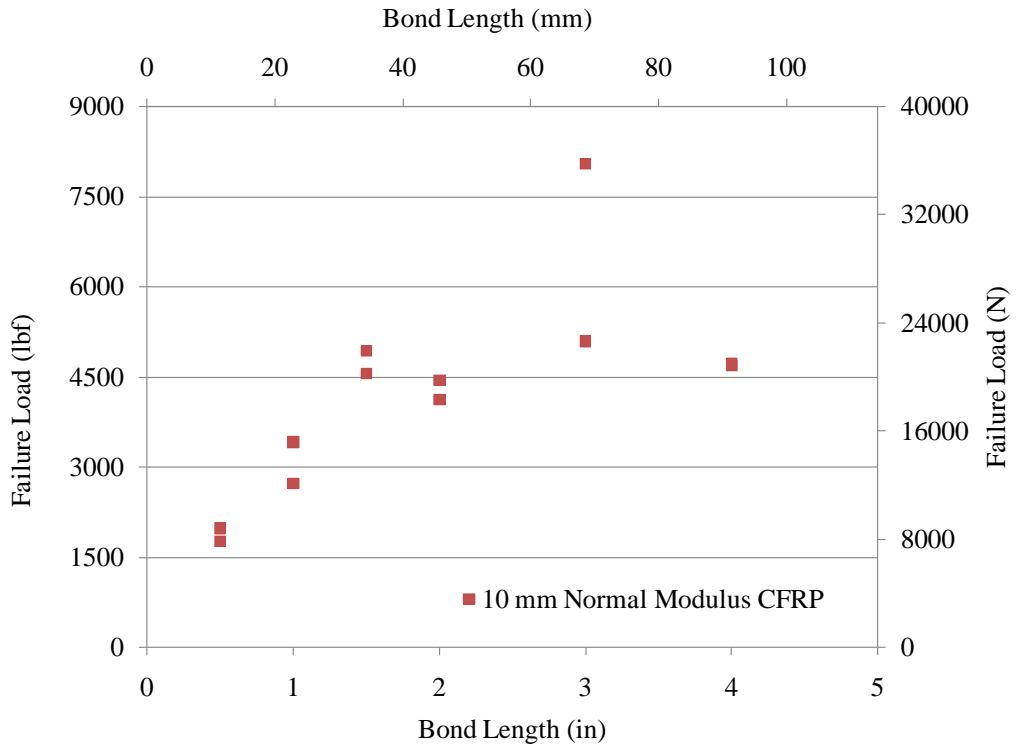


Fig. 2.17: Failure load variation with bond length for NM 10 mm (0.4 in) specimens

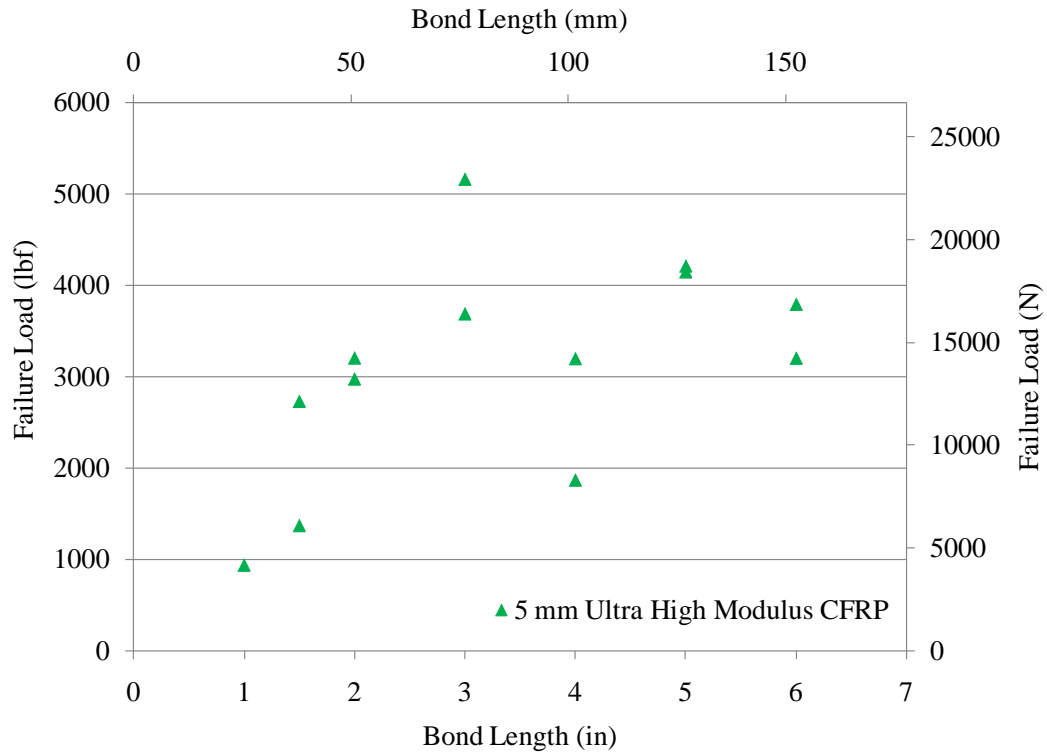


Fig. 2.18: Failure load variation with bond length for UHM 5 mm (0.2 in) specimens

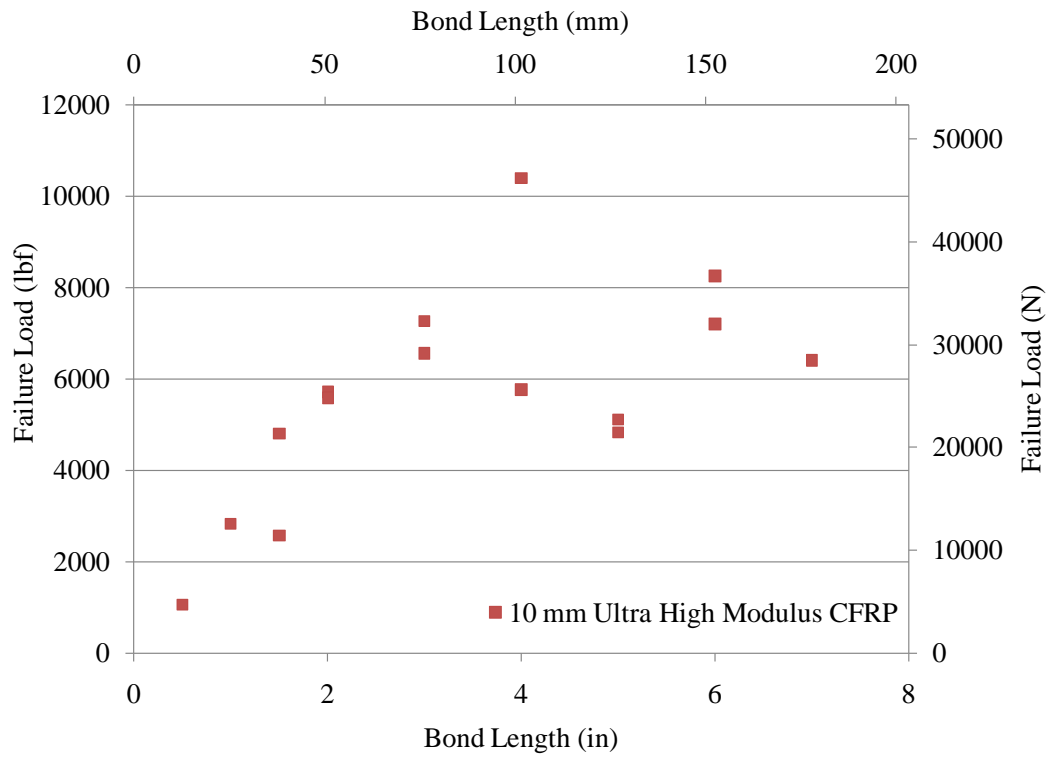


Fig. 2.19: Failure load variation with bond length for UHM 10 mm (0.4 in) specimens

In order to facilitate comparisons between the normal modulus and ultra high modulus laminates, the average failure load per unit width of laminate is plotted with respect to each bond length in Fig. 2.20. The development length for each laminate type is estimated as the bond length beyond which no further increase in load carrying capacity is observed, despite further increases in bond length. Accordingly, the development length for the normal modulus CFRP is found to be approximately 41 mm (1.6 in), while for the ultra high modulus CFRP, the development length is 64 mm (2.5 in). The bond strengths for the normal modulus and ultra high modulus laminates are approximately 2.1 kN/mm (12 kip/in), and 3.0 kN/mm(17 kip/in), respectively.

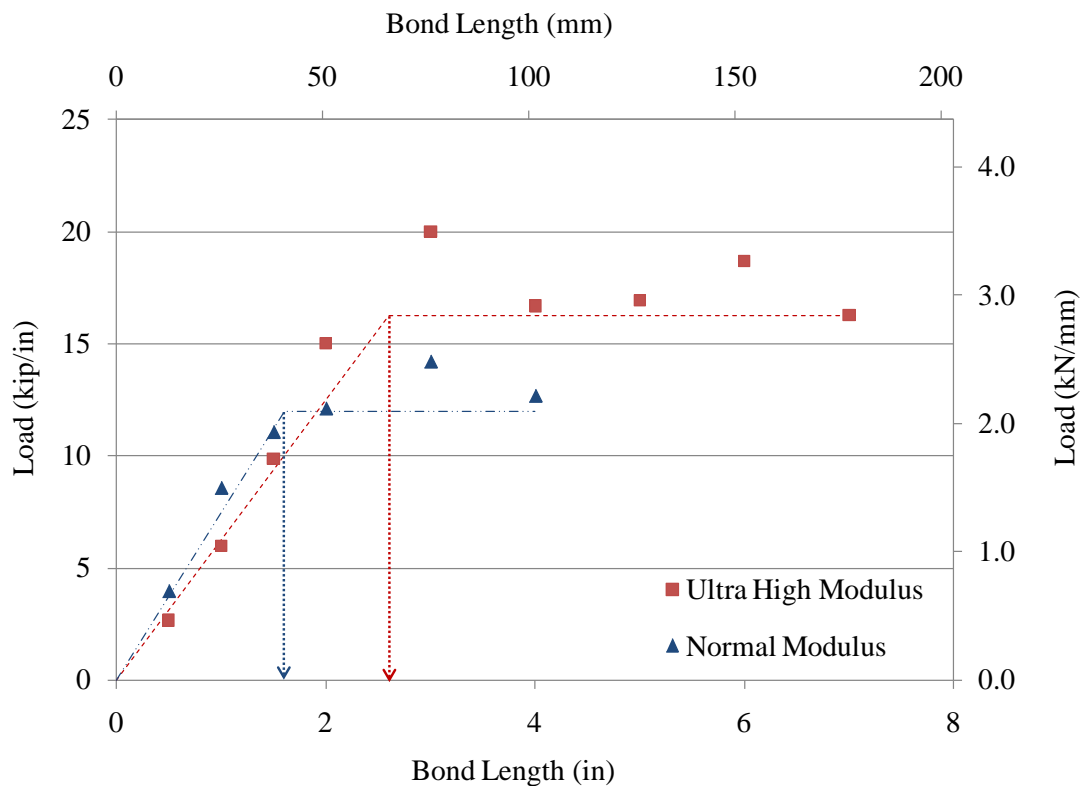


Fig. 2.20: Average failure load per unit width

The average shear strength of the epoxy is calculated using test results for the shorter bond length specimens of the normal modulus CFRP laminates, which failed in debonding between the steel and adhesive interface. Accordingly, the shear strength is found by dividing the failure load by the measured bond area. The average shear strength is calculated to be 27 MPa (3.9 ksi).

The strain variation for the NM 10-75B specimen along the length of the bond is shown in Fig. 2.21. While this specimen had the largest failure load among the 10 mm (0.4 in) wide normal modulus CFRP laminates tested, the maximum strain observed just before failure (0.008486) is less than half of the average ultimate strain observed during material testing (0.01808) for laminate in tension. The relatively smaller failure strains explain the lack of observed rupture failures for the normal modulus laminate specimens. The strain variation for the same bond length of 75 mm (3 in) is shown in Fig. 2.22, for the ultra high modulus CFRP laminate. The strain observed just before rupture in the ultra high modulus specimen was 0.00283. Although this strain is less than the average ultimate strain of 0.00332, observed in the material tensile tests, it is greater than the guaranteed ultimate strain provided by the manufacturer (0.00268). Strain results for the tested specimens are provided in Appendix A.

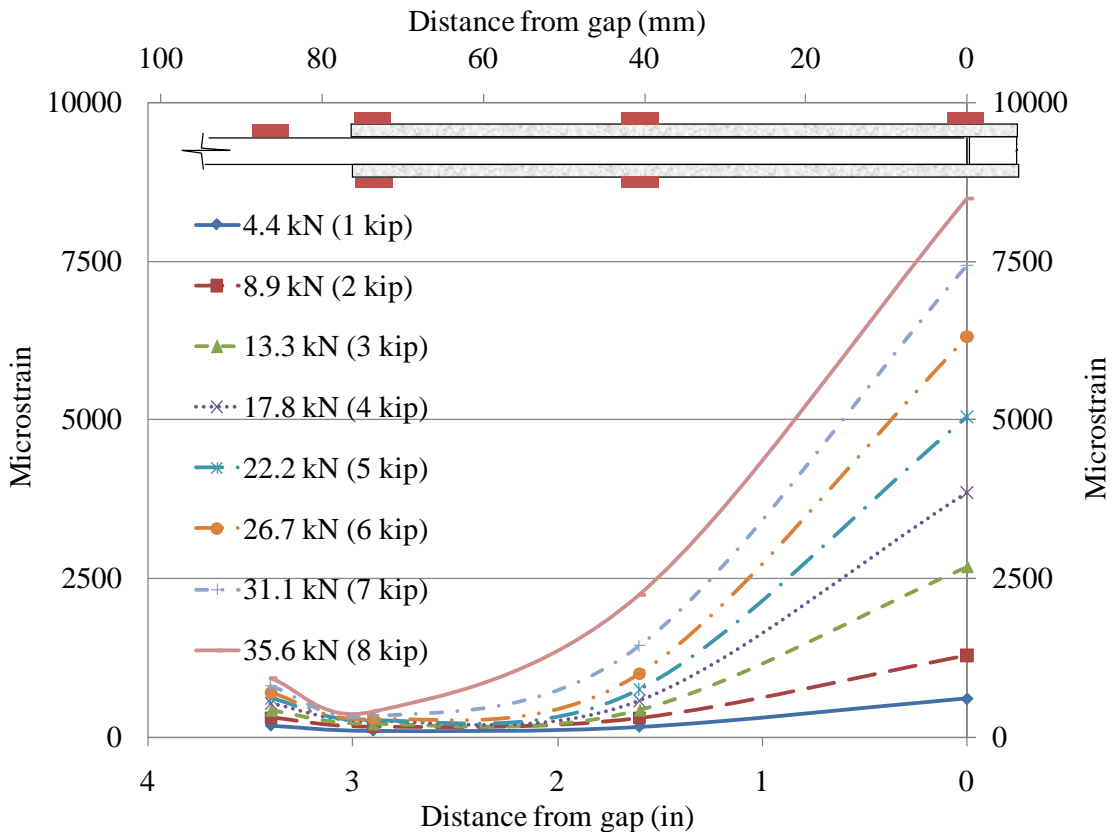


Fig. 2.21: Strain variation along bond length for NM 10-75B specimens

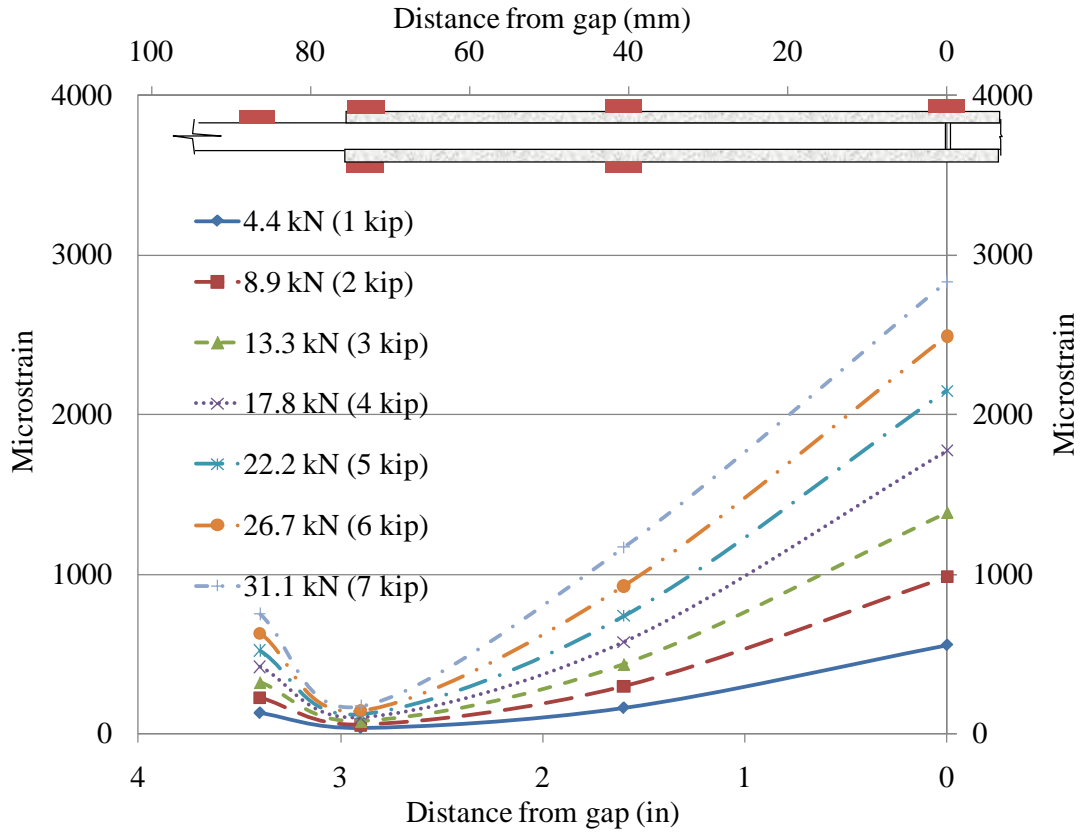


Fig. 2.22: Strain variation along bond length for UHM 10-75B specimens

2.3 Doubly Reinforced Steel Plate Tests

Doubly reinforced steel plate specimens were made and tested to evaluate load transfer between the steel and CFRP. Also these specimens were used to determine common failure modes. Both normal and ultra high modulus CFRP laminates were tested to evaluate the effect of increased tensile modulus in the laminates.

2.3.1 Doubly Reinforced Steel Plate Specimens

A 50 mm (2 in) wide, 4.8 mm (0.1875 in) thick, and 610 mm (24 in) long steel plate is used as the reinforced plate. The top and bottom steel surfaces where the laminate is applied was ground and cleaned with solvent before application of laminates. The applied

laminates were 25 mm (1 in) wide, 1.2 mm (0.047 in) thick, and 381 mm (15 in) long as shown in Fig. 2.23.

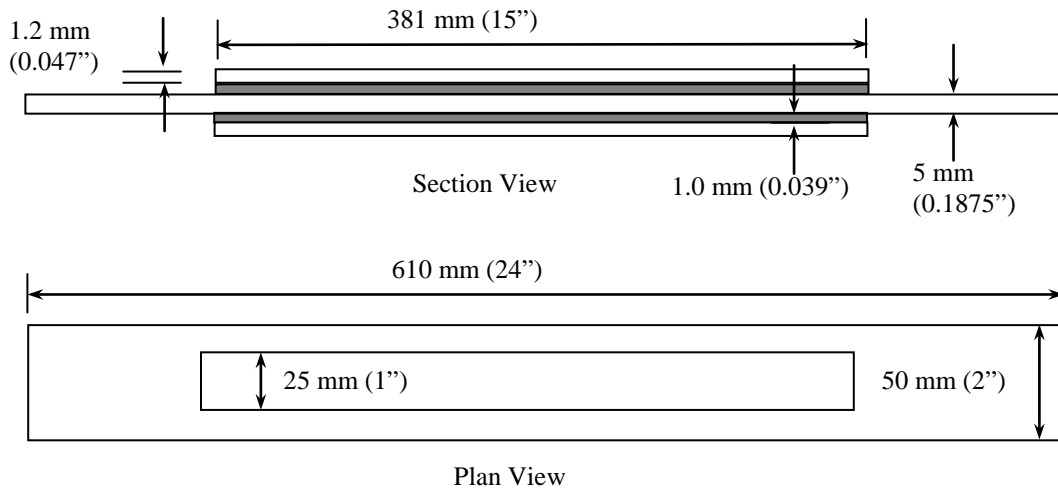


Fig. 2.23: Doubly Reinforced Steel Plate Specimen Dimensions

The normal modulus laminate were manufactured to be 100 mm (4 in) wide, and the ultra high modulus laminates were produced to be 50 mm (2 in) wide. The laminates were shear cut to the required lengths and widths using a mechanical shear. Similar to the double strap joint specimens, the normal modulus laminates were cleaned with Acetone before application of epoxy. The ultra high modulus laminates had a peel ply, and therefore, no cleaning was required. The two part epoxy was applied to the laminates using the manufacturer specified dispenser gun and spread using a small v-notched trowel to obtain a triangular profile. The laminates were then placed on the top surface of the steel plate, along the plate centerline. Subsequently the laminates were gently pressed onto the steel surface using a roller. After the laminates were applied to one side, the specimens were allowed to cure for at least two days before the procedure was repeated on the other side of the specimen. Once both laminates were setup the specimens were further cured for a minimum of 14 days at room temperature. Small uniform pressure was applied to the laminates during the first two days of curing, for both sides of the specimen. While 1 mm (0.04 in) was the design adhesive epoxy thickness the average thickness of the final specimens was found to be 1.2 mm (0.05 in). Six specimens were prepared and tested; three normal modulus specimens and three ultra high modulus specimens.

2.3.2 Material Properties

The same materials used in the double strap joint specimens were used to make the doubly reinforced steel plate specimens. Complete details of the experiments carried out to evaluate the mechanical material properties can be found in section 2.2.2.

2.3.3 Instrumentation and Testing

Similar to the double strap joint specimens, the doubly reinforced steel plate specimens were instrumented with foil type electrical resistance strain gages along the bond center line. The surface profiles of the ultra high modulus CFRP laminates were sanded down to obtain level yet rough surfaces. Similarly, the normal modulus CFRP laminates were sanded to obtain rough surfaces for bonding to the gages. Gages were attached on one side of the bond, while a single gage was attached to the center, opposite side as check against loading imbalances. The overall gage layout is given in Fig. 2.24. The specimens were tested in a universal tensile testing machine at a strain rate of 1.25 mm/min (0.05 in/min). All strain gages were connected to a data acquisition system and the strain data were collected through a laptop computer. A specimen with gages attached before connection of lead wires is shown in Fig. 2.25 and testing of a specimen is depicted in Fig. 2.26.

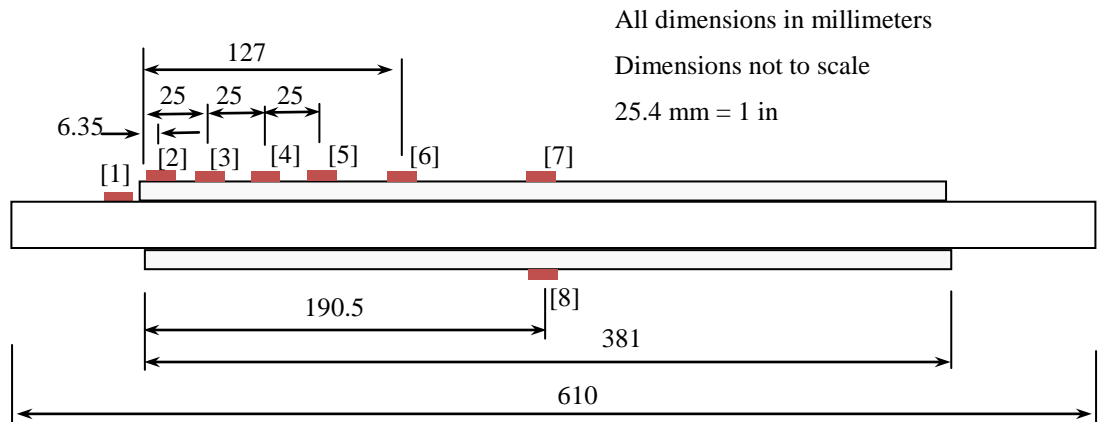


Fig. 2.24: Doubly Reinforced Steel Plate Specimen Gage Layout



Fig. 2.25: Doubly Reinforced Steel Plate with attached Strain Gages

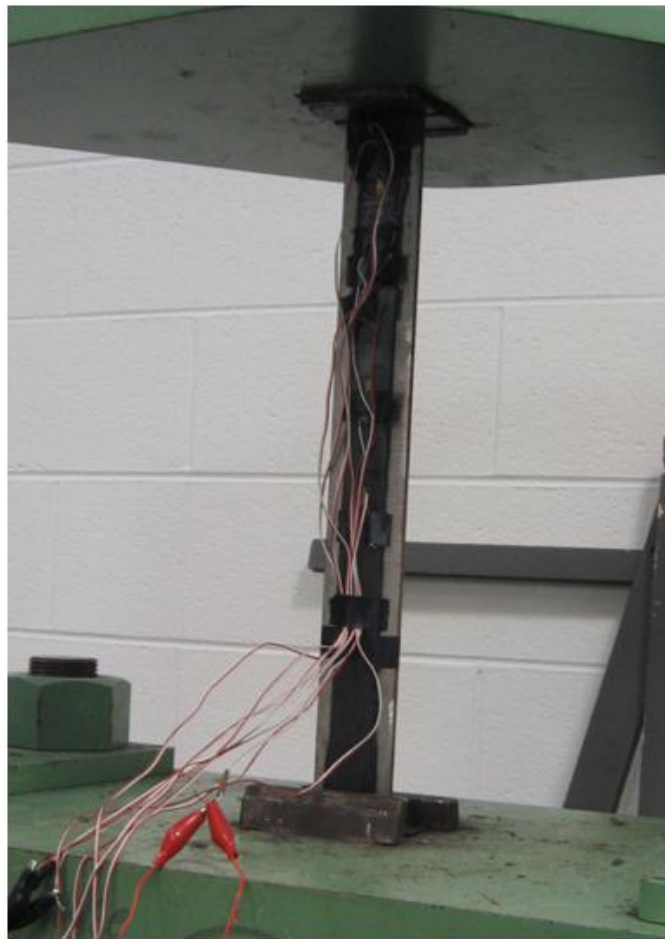


Fig. 2.26: Testing of Doubly Reinforced Steel Plate Specimen

2.3.4 Test Results

All six specimens failed in debonding between the steel-adhesive interfaces. Initial debonding occurred at the edges and proceeded to grow towards the center for both laminate types. Debonding close to the specimen center was observed, on one side of one of the ultra high modulus laminate specimens (UHM-1 in Fig. 2.29). In all cases, testing was halted upon as soon as debonding was observed. Fig. 2.27 shows the debonding locations and lengths observed for all three normal modulus laminate specimens and Fig. 2.28 shows the typical nature of the debonding observed in both types of laminate. Also, the debonding regions for the ultra high modulus laminates are shown in Fig. 2.29.

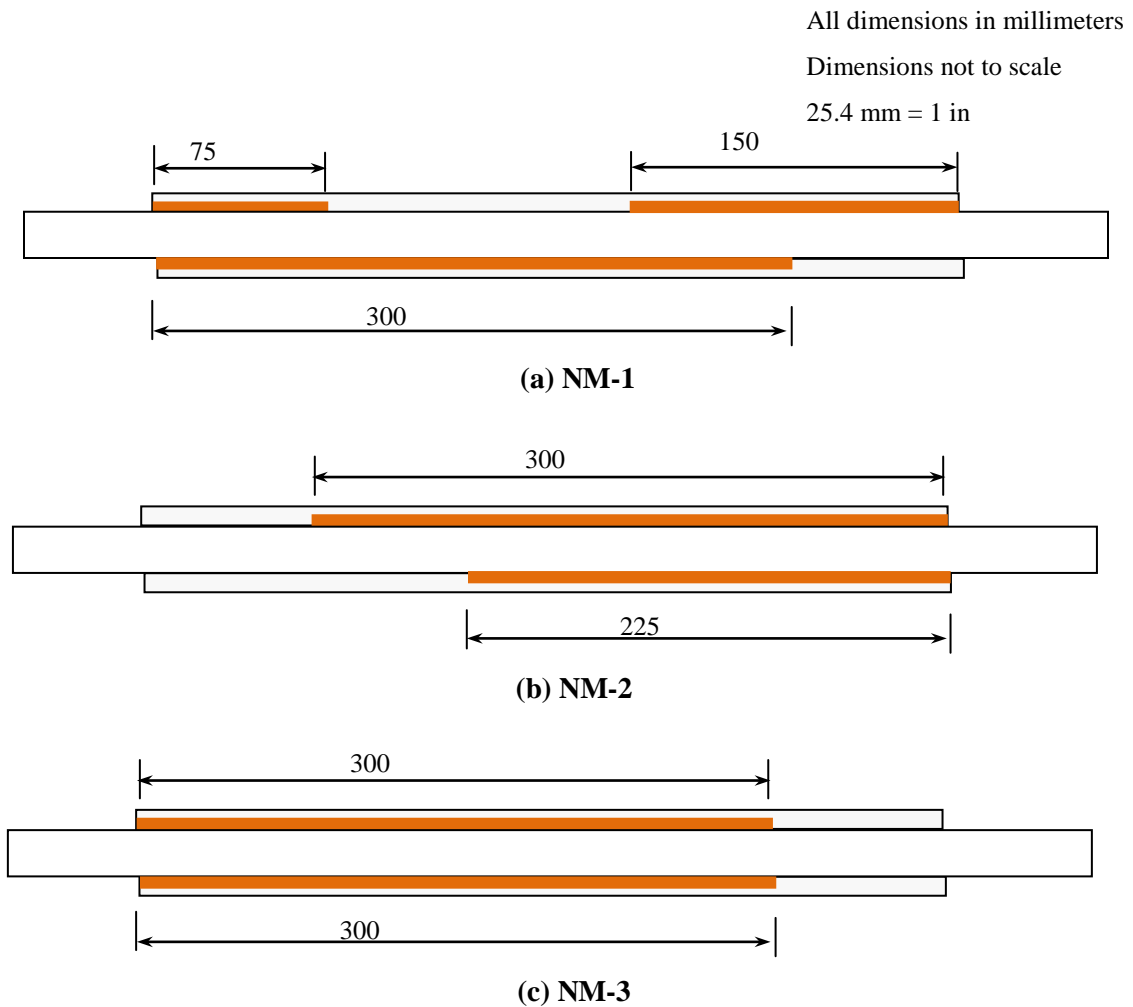


Fig. 2.27: Debonding locations on normal modulus CFRP specimens



Fig. 2.28: Debonding observed in doubly reinforced steel specimens

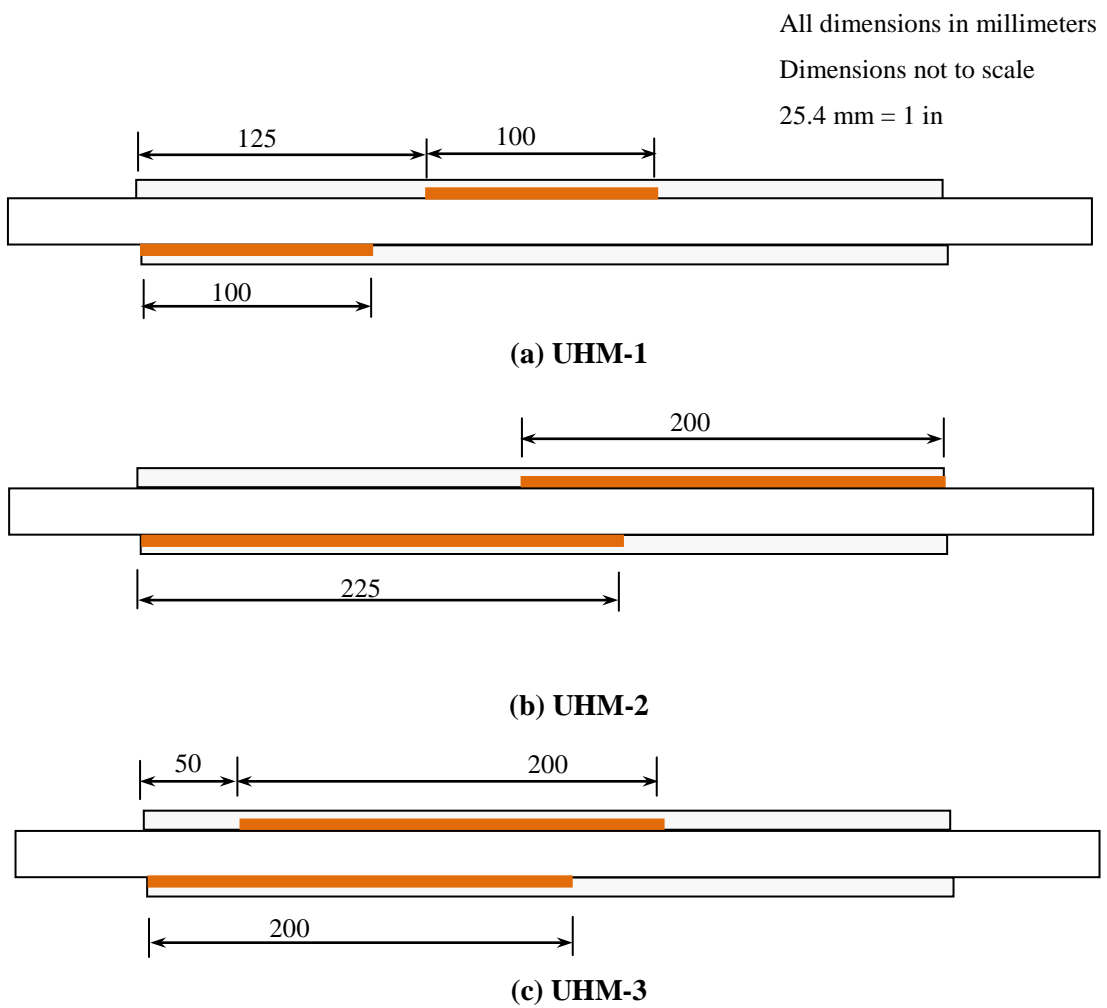


Fig. 2.29: Debonding locations on ultra high modulus CFRP specimens

Strain increases at the center of the laminates (for increasing load) are shown in Fig. 2.30 for all six specimens. The strains observed in the normal modulus CFRP laminates are seen to be larger than strains associated with the ultra high modulus laminates at the same load levels. While use of ultra high modulus laminates (as opposed to normal modulus laminates) leads to a reduction in average strain of more than 10%, the average ultimate load carrying capacity is seen to be 22% less.

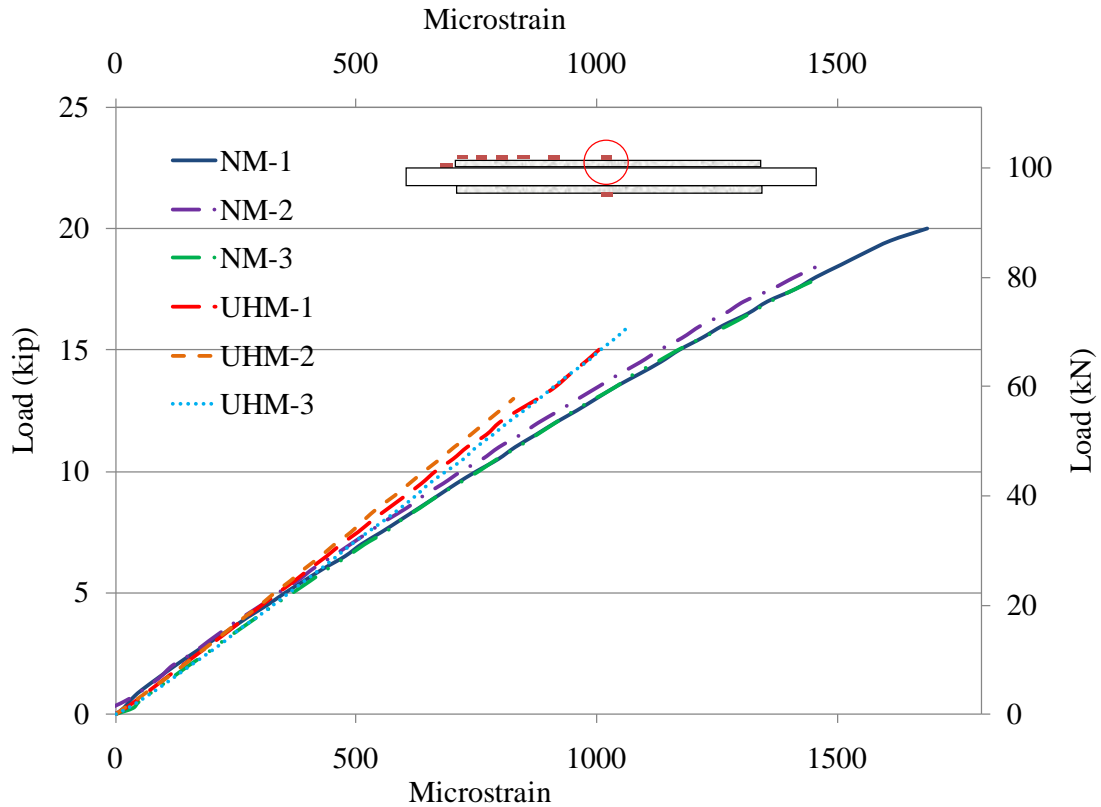


Fig. 2.30: Strain variation at center of the laminates

Strains measured along the centerline of the specimens at 44.4 kN (10 kip) are plotted in Fig. 2.31. The strains along the ultra high modulus laminate reinforced specimens are approximately 20% less than those of the normal modulus laminate reinforced specimens. Strain variation along specimen at different loads for all six specimens can be found in Appendix A. The development length for each laminate can be approximately evaluated from the strain profile observed in Fig. 2.31, where the normal modulus laminates have a development length of approximately 50 mm (2 in). In comparison, the ultra high modulus laminates have a longer development length approximately 75 mm (3 in). These

values seem to agree well with the development lengths found using the double strap joint specimens.

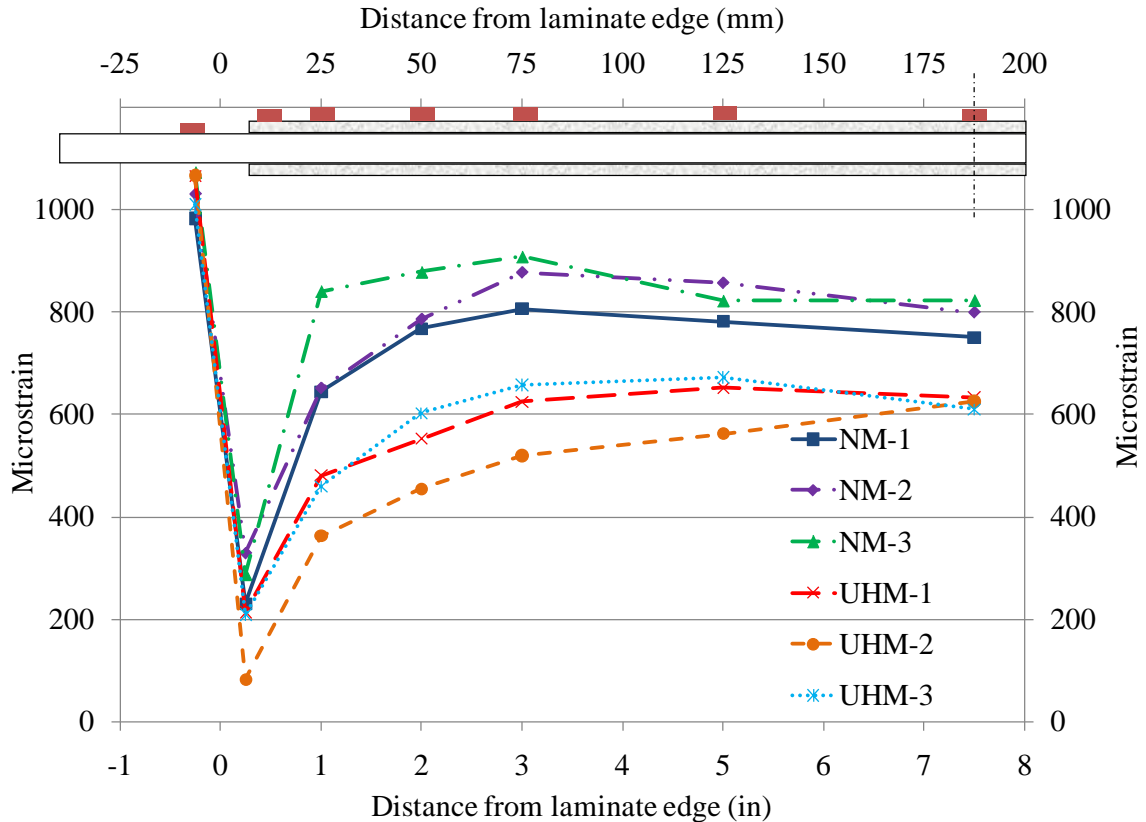


Fig. 2.31: Strain variation along specimen centerline at 44.4 kN (10 kip)

The yield strain, calculated from the yield stress, was evaluated from the material tests for the steel plate and found to be 0.00203 mm/mm. Strains developed in the steel plates are shown in Fig. 2.32, where these strains were measured using a strain gage attached to the steel plate (next to the laminate edge) in each doubly reinforced specimen. The results indicate that all three normal modulus CFRP laminate reinforced specimens fail in debonding, but only after the steel has yielded. In contrast the ultra high modulus laminate reinforced specimens fail before the steel has reached yield strain. As all specimens failed in debonding at the steel and epoxy adhesive interface, it is clear that the reason for failure was the strength limits of the bond, unlike in the double strap joint elements where other types of failure such as delamination and rupture were observed.

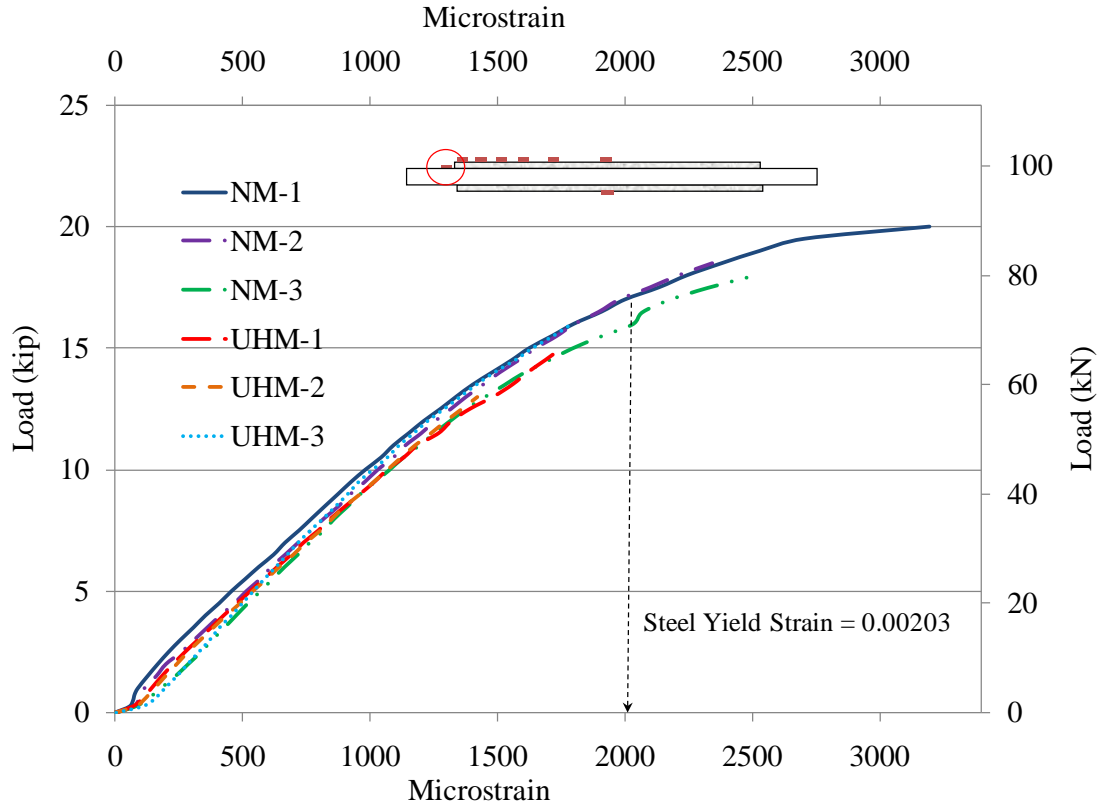


Fig. 2.32: Strain in steel plate

The adhesive shear stress (τ_a) along the bond length can be found considering the equilibrium of a laminate section bonded to a steel plate.

$$\tau_a(x) = \frac{d\sigma_L(x)}{dx} t_L \quad (2.1)$$

Where; σ_L = Laminate tensile stress
 t_L = Laminate thickness

The average adhesive shear stress between two known tensile strain locations on the laminate can therefore be found using the following equation;

$$\tau_a(x) = \frac{(\varepsilon_i - \varepsilon_{i-1})}{(x_i - x_{i-1})} E_L t_L \quad (2.2)$$

Where; ϵ_i = Measured laminate strain at location x_i
 E_L = Laminate tensile modulus

The calculated average shear stress between strain gage locations for all six doubly reinforced specimens, at a load of 4.44 kN (10 kip), is shown in Fig. 2.33. The ultra high modulus laminate specimens are seen to have a higher shear stress in the epoxy than the normal modulus laminate specimens. As a consequence, the ultra high modulus laminate doubly reinforced steel plate specimens are expected to reach peak shear at the edge first. The peak shear at the edge, though expected to be more than the previously calculated (see section 2.2.4) average bond shear strength of 27 MPa (3.9 ksi), is found to be less when failure in debonding occurs. While the average shear strength was calculated from the observed debonding in the normal modulus CFRP double strap specimens, the shear strength of the bond between the steel and the adhesive epoxy is not expected to vary due to differences between the laminate moduli.

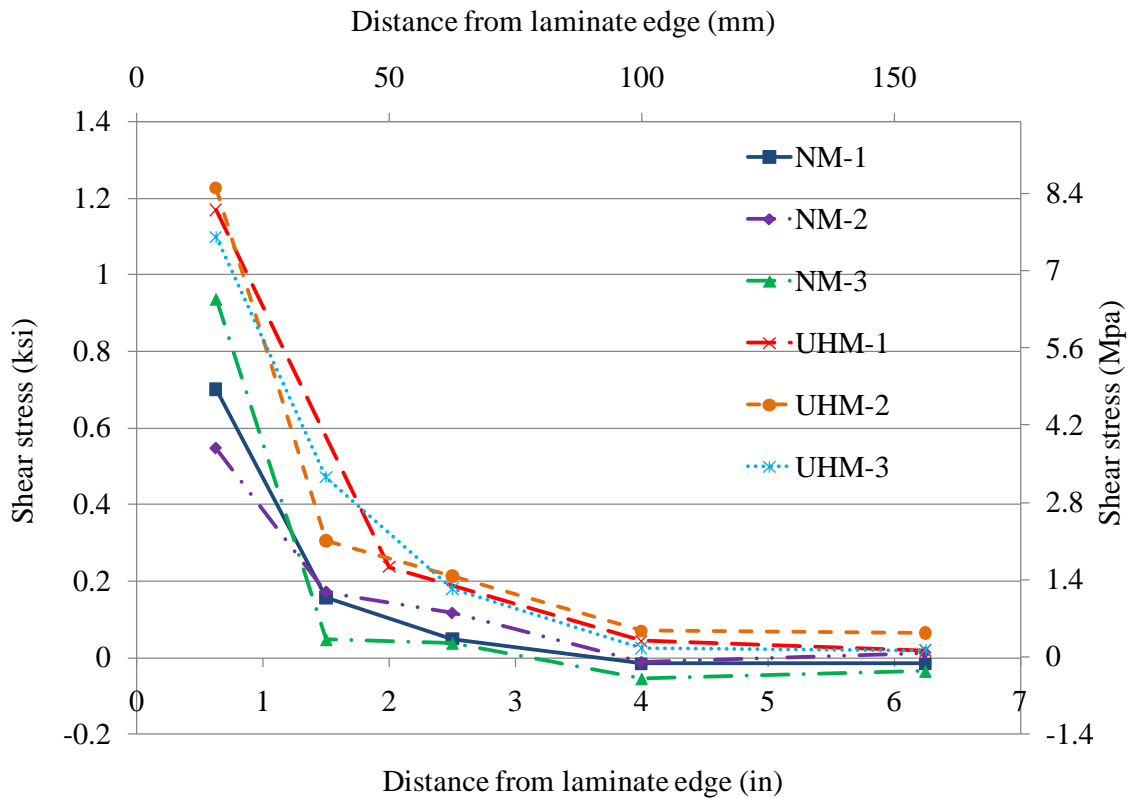


Fig. 2.33: Shear stress distribution at 44.4 kN (10 kip)

2.4 Steel Beam Tests

Four beam tests were carried out to evaluate the performance of ultra high modulus CFRP laminates under flexural loading. A typical strengthening is performed without laminate splicing and is compared with the novel strip panel type splice strengthened girders. Two different strip widths are tested and all strengthened beams are evaluated against a non-strengthened control beam.

2.4.1 Steel Beam Specimens

The steel beams used in the testing were W10×22 wide flange beams. In order to avoid compression failure at the top flange and to represent a composite concrete deck, a standard C7×9.8 channel section was welded to the top flange. The channel and wide flange beam composite section dimensions are shown in Fig. 2.34. The dimensions of the beam in elevation are provided in Fig. 2.35.

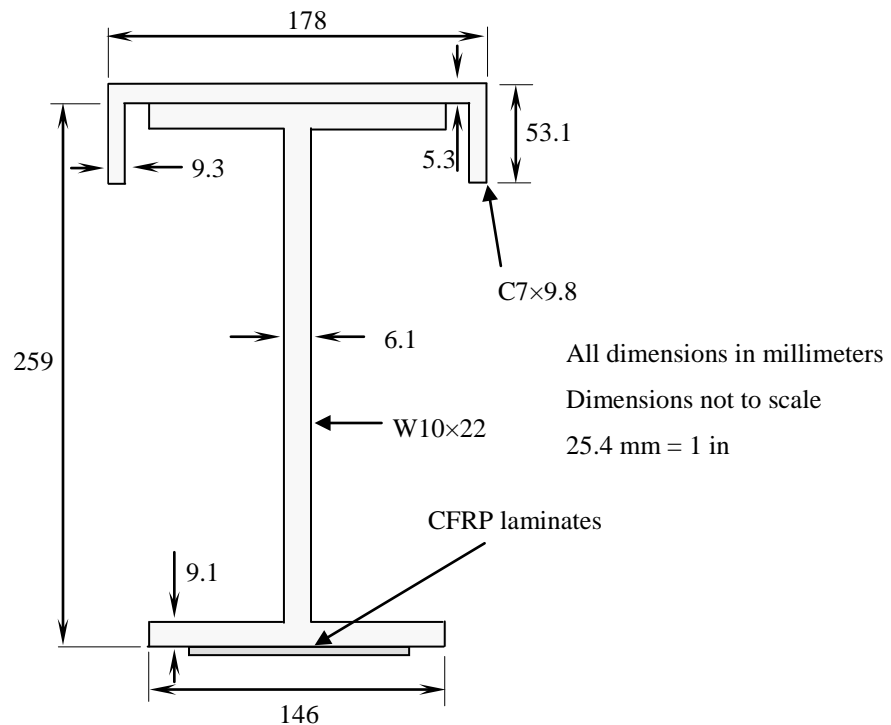


Fig. 2.34: Dimensions of W10×22 and C7×9.8 composite section

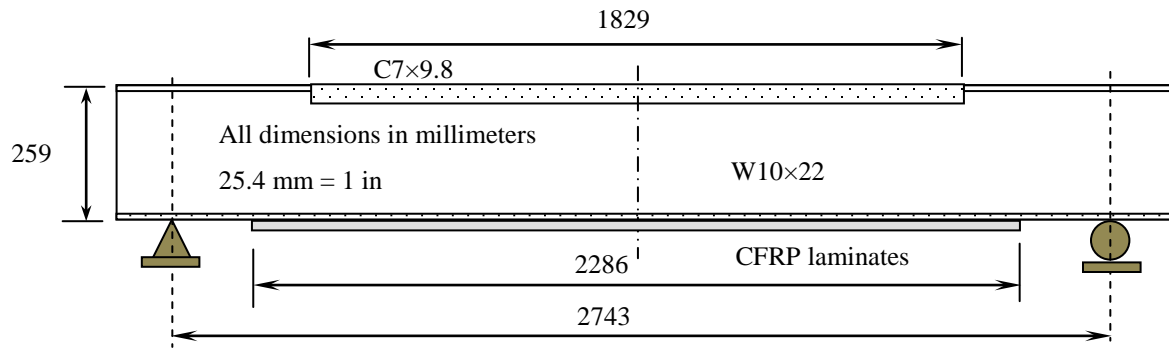


Fig. 2.35: Beam and laminate dimensions in elevation

The same type of 1.2 mm (0.047 in) thick, ultra high modulus CFRP laminates were used in the beam tests as those that were used in the double strap joint shear tests as well as the doubly reinforced steel plate tests. The control steel beam did not have any laminate strengthening. One beam was strengthened with a continuous laminate 2286 mm (90 in) long and 50 mm (2 in) wide. The splice panels applied on the two remaining beams were fabricated with laminate strips 10 mm (0.4 in), and 5 mm (0.2 in) wide. The total width of the splice strips was equal to 50 mm (2 in) and each panel was made to be 1219 mm (48 in) long. Two strip panels were brought together with a 150 mm (6 in) overlap ‘finger’ joint to create a strengthening system which had the same length and width as the continuous, unspliced CFRP laminate. It should be noted that each adjacent panel included an extra strip to maintain symmetrical load transfer. The orientations of two adjacent 10 mm (0.4 in) strip panels are shown in Fig. 2.36. The dimensions and layout of the 10 mm (0.4 in) strip panel and the ‘finger’ joint are shown in Fig. 2.37.

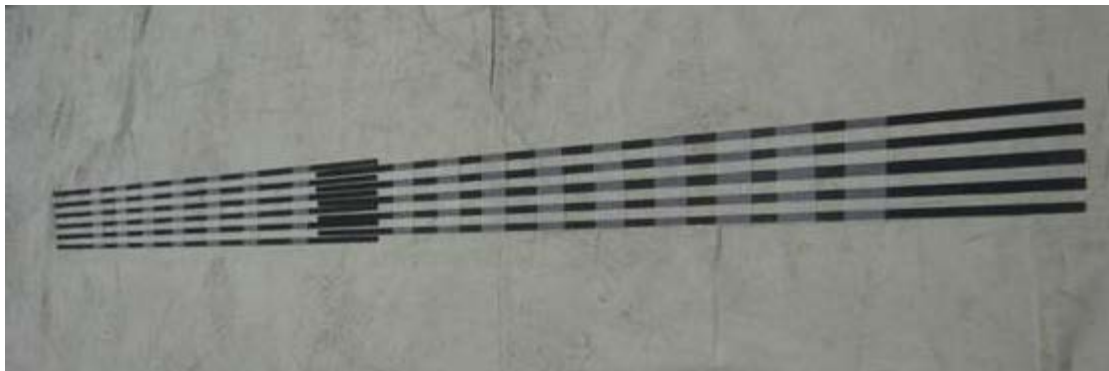
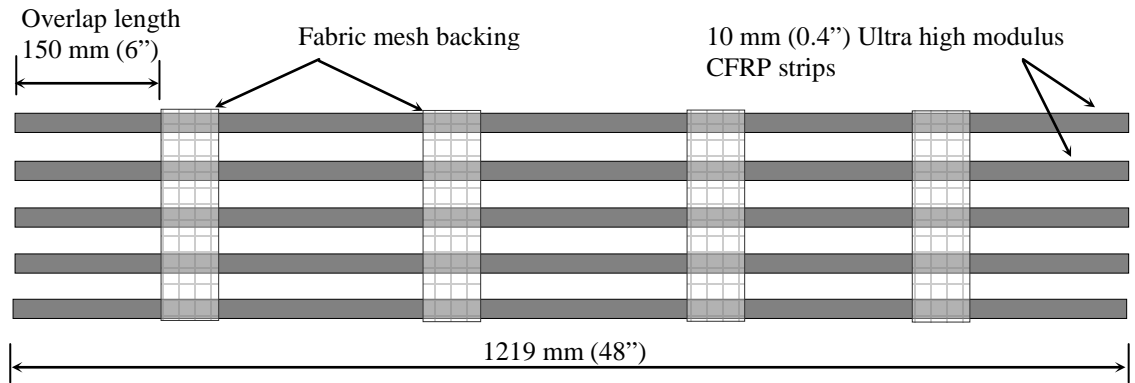
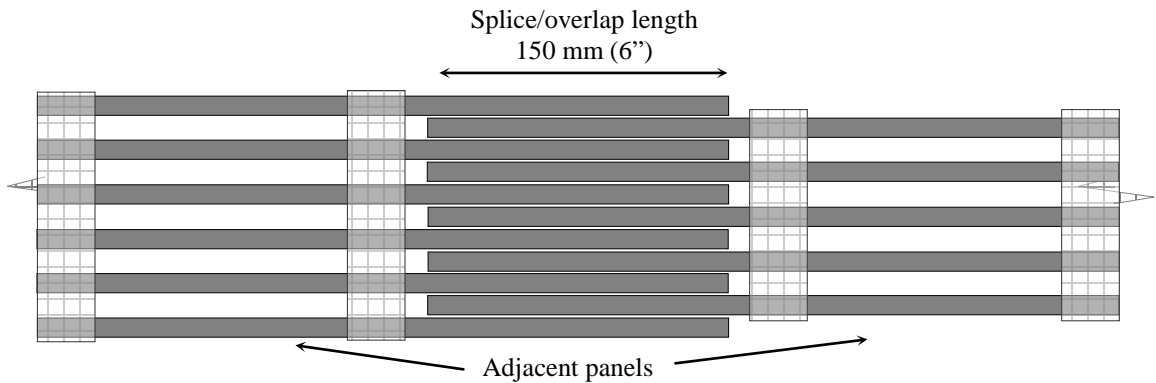


Fig. 2.36: Adjoining strip panels with ‘finger’ joint



(a) Ultra high modulus CFRP strip panel



(b) Finger joint between adjacent strip panels

Fig. 2.37: Dimensions and layout of strip panels

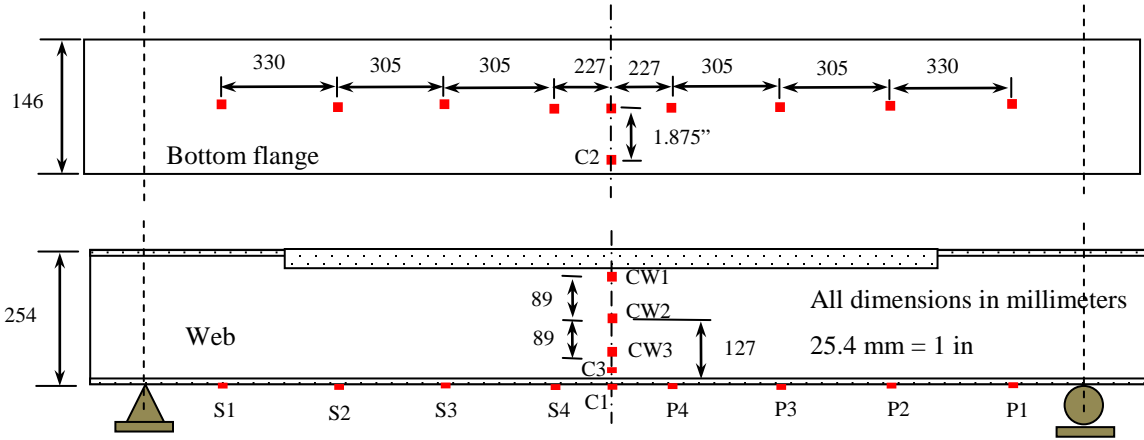
The channel sections were initially welded to the top flange of the wide flange beams, and then the beams were sand blasted to obtain a rough surface profile for laminate bonding. The laminate application surfaces of the steel beams were cleaned with Acetone before application of the epoxy. The same Spabond 345 two part epoxy used in the previous tests was used as the adhesive. The full width strip was bonded by applying the epoxy adhesive onto the laminate in a triangular profile and then flipping the laminate and placing it on the bottom flange of the beam. A 125 mm (5 in) wide and 2.5 mm (0.1 in) thick layer of epoxy was applied onto the bottom flange of the beams for attaching the strip panels. The panels were pressed into the epoxy adhesive until the epoxy, rising between the laminate strips, was flush with the top surface of the laminates.

2.4.2 Material Properties

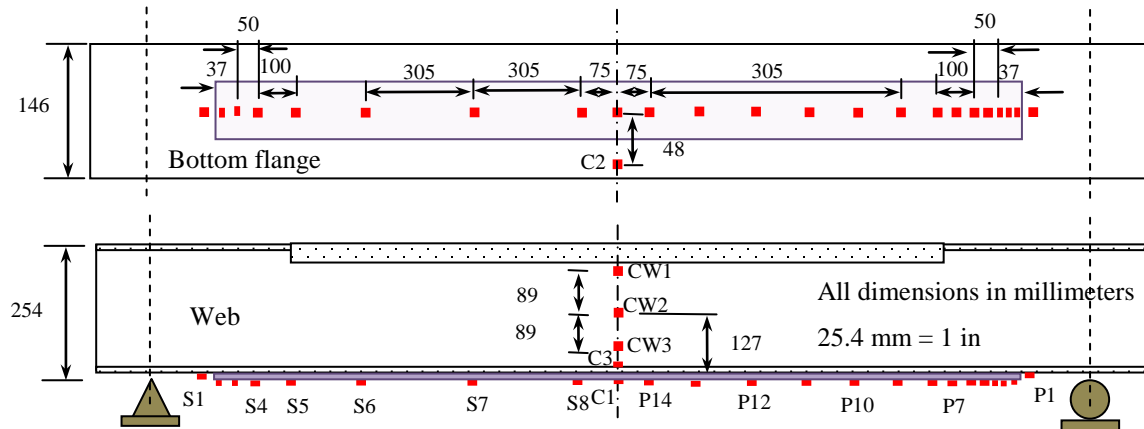
The same ultra high modulus laminates and epoxy used for the double strap joint tests and doubly reinforced steel plate tests were also used for the steel beam tests. Complete details of the experiments carried out to evaluate the mechanical material properties of the laminates and epoxy can be found in section 2.2.2. The steel properties of the beams were not evaluated through laboratory testing. The tensile and ultimate strengths were obtained from the material test report from the steel beam and channel manufacturer. The grade A36 C7×9.8 channel had a minimum yield strength of 414 MPa (60 ksi) and ultimate strength of 531 MPa (77 ksi). The grade A992 steel W10×22 wide flange beam had a reported yield strength of 407 MPa (59 ksi) and an ultimate strength of 510 MPa (74 ksi). The tensile modulus for both steel was taken as 200 GPa (29000 ksi).

2.4.3 Instrumentation and Testing

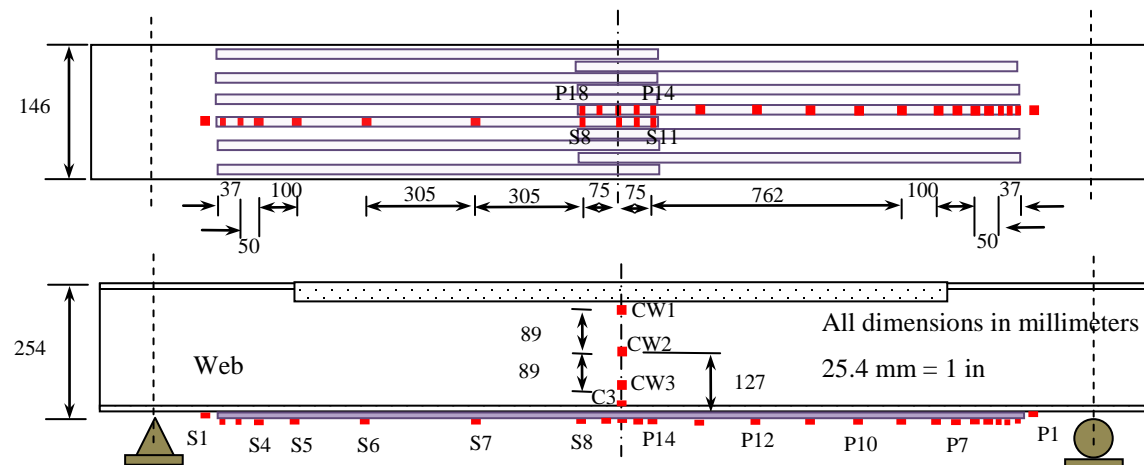
All steel beams were instrumented with foil type electrical resistance strain gages. The surface profiles on the ultra high modulus CFRP laminates were sanded down to obtain level yet rough surfaces for bonding with the gages. Gages were attached along the center line of the bottom flange as well as along the height of the web at mid span. The strip panel reinforced beams had gages along the center strip on the side with the odd number of strips. Only one of the two strips along the center, on the side with an even number of strips, was installed with strain gages. The panel with the low number of strips was called the primary (gages-prefix 'P'), and the other panel the secondary (gages-prefix 'S'). The gage layout is given in Fig. 2.38(a) for the unreinforced beam, Fig. 2.38(b) for the full width specimen and Fig. 2.38(c) for the 10 mm (0.4 in) strip panel reinforced specimen. The 5 mm (0.2 in) wide strip panel had the same gage layout as the 10 mm (0.4 in) strip panel. In addition to placing gages on the laminates adhered to the steel beam bottom flange, a strain gage was also attached to the steel beam at the edge of the laminate plate (P1, S1) and also on the top of the bottom flange (gage C3).



(a) Control steel beam



(b) Full width strengthened steel beam



(c) Strip panel strengthened steel beams

Fig. 2.38: Strain gage layout on steel beams

The beams were tested in four point bending with a 762 mm (30 in) constant moment region. The beam specimens were restricted from moving laterally with bracing attached to the ends as well as 457 mm (18 in) either side of mid span. The reaction frame and test setup are shown in Fig. 2.39. The loading was applied using an 890 kN (200 kip) ENERPAC hydraulic actuator. Loads were recorded using a load cell placed above the actuator cylinder head. Cable extension type displacement sensors were attached to the bottom flange on both sides of the specimen to evaluate the displacements at mid span. To prevent disruption of readings due to laminate rupture/debonding, the sensors were attached to magnetic bases fixed to the bottom flange. An additional displacement sensor was attached to the reaction frame to evaluate any displacements of the reaction frame due to the applied loading. All data, including the load cell readings, displacement sensor readings, as well as strain readings were obtained through a data acquisition system controlled using a laptop computer. The test setup is shown in Fig. 2.40.

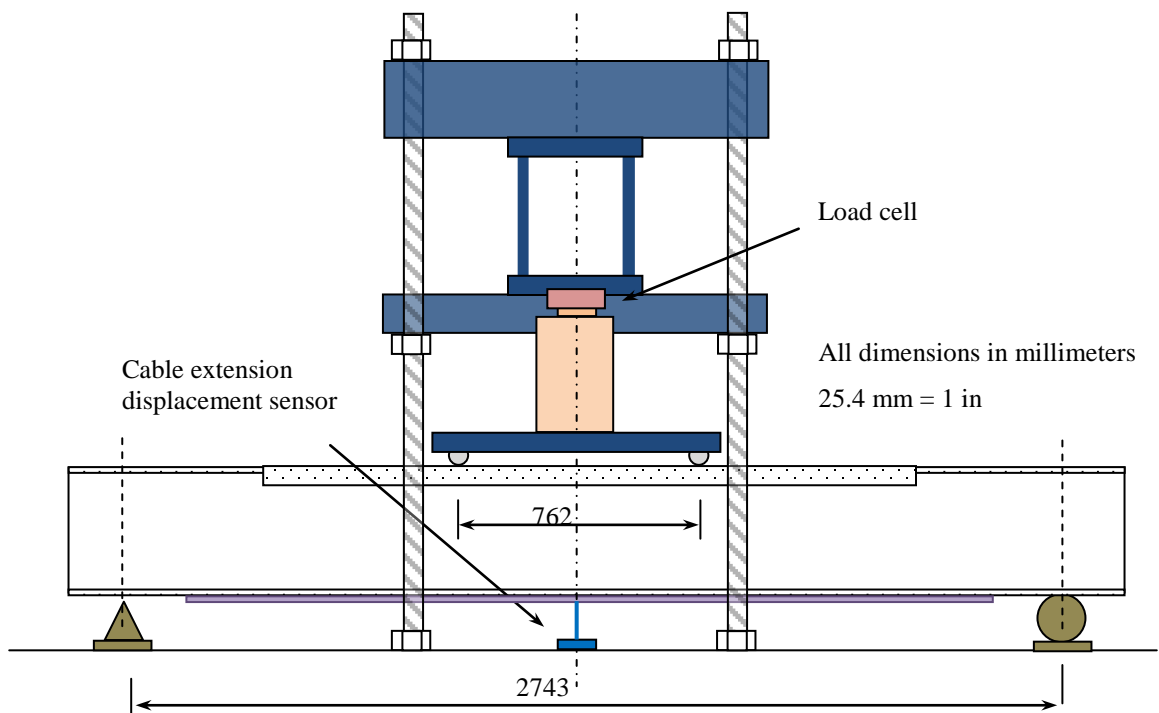


Fig. 2.39: Beam testing setup

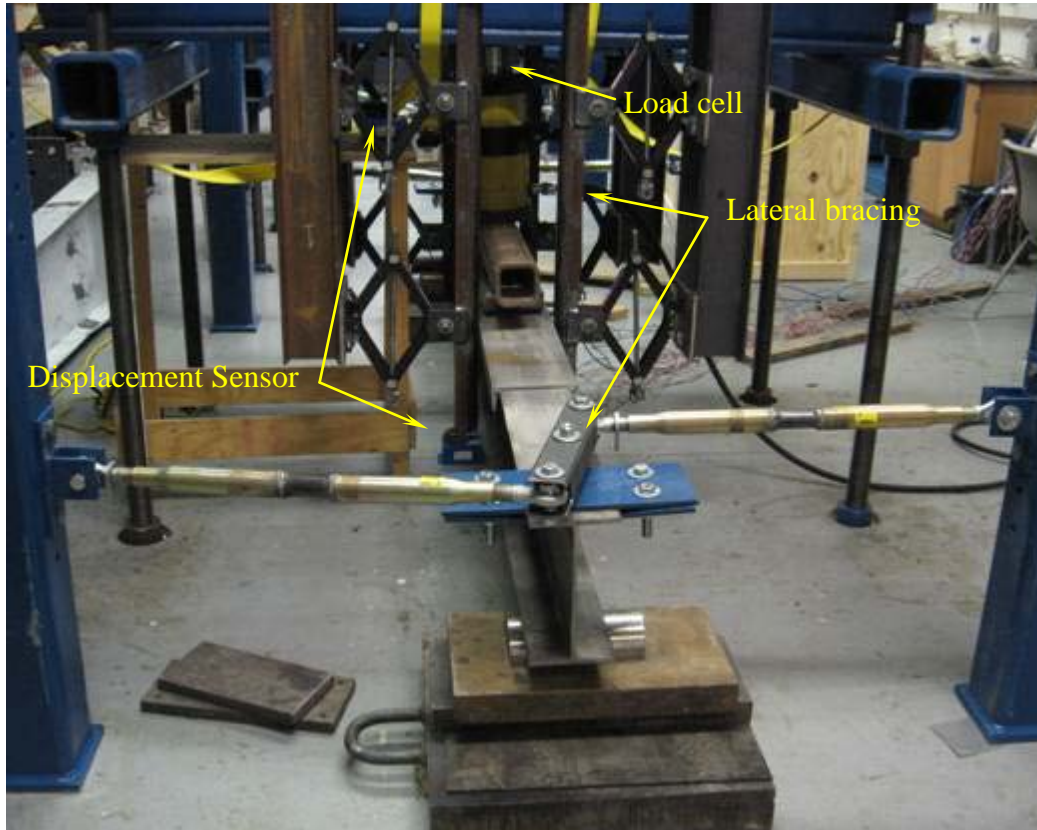


Fig. 2.40: Beam being tested

2.4.4 Test Results

The control (non-strengthened) steel beam was seen to yield at 290 kN (65 kip) and testing was halted at an ultimate load of 405 kN (91.2 kip). Measurements of mid-span load deflection for the tested beams are shown in Fig. 2.41. The increase in tension flange area due to the strengthening was approximately 11% of equivalent steel area. Due to the small increase in stiffness (as a result of laminate application), the initial load deflection curves are similar. The effect of laminate application becomes visible only beyond the expected yield point of the unstrengthened beam. The full width laminate strengthened specimen is seen to have a higher stiffness beyond steel yield and was seen to rupture at an ultimate load of 404 kN (90.8 kip). The strain in the steel is plotted at the common gage position C3 (refer to Fig. 2.38) on the top of the bottom flange in Fig. 2.42.

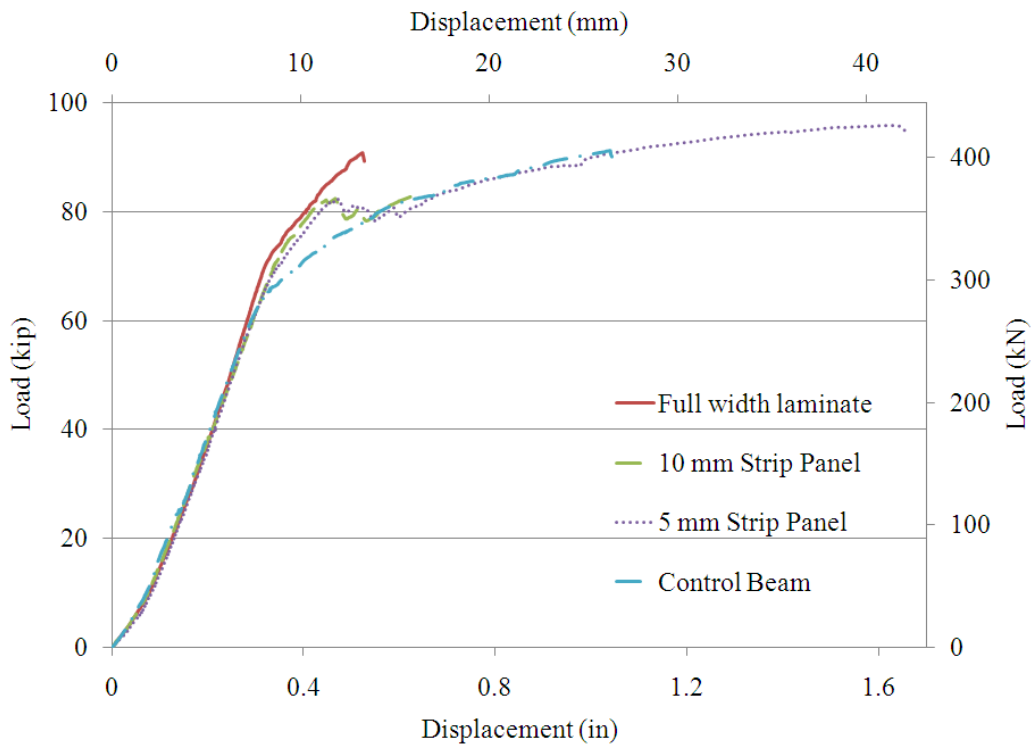


Fig. 2.41: Load vs. mid span displacement

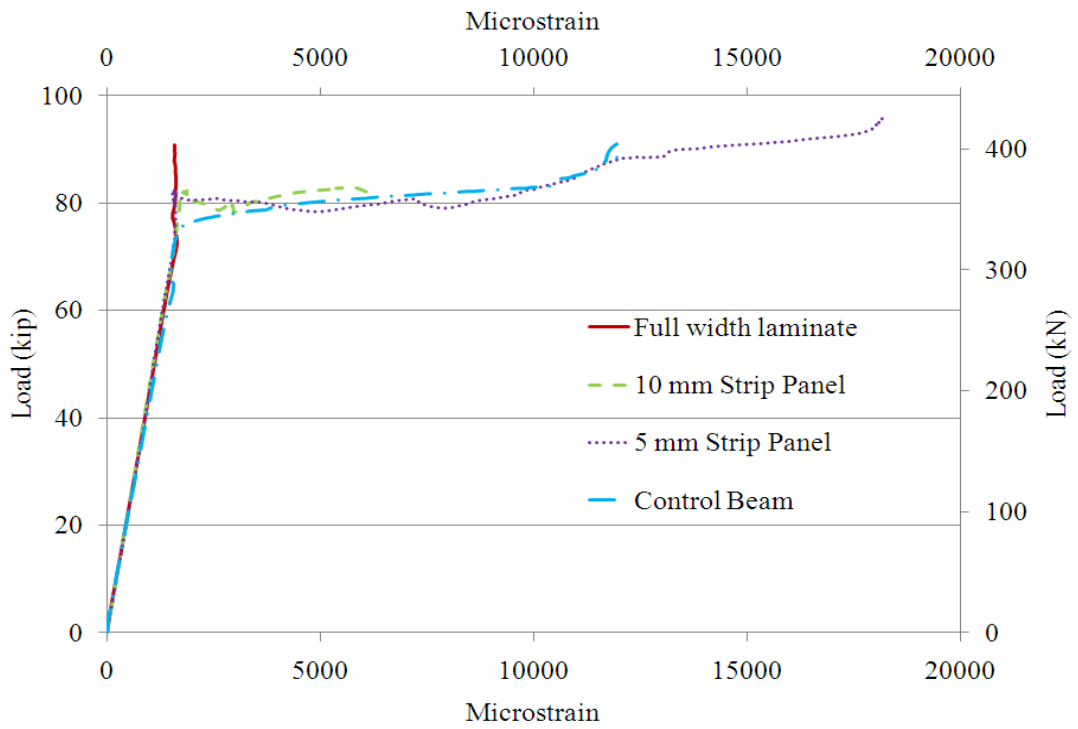


Fig. 2.42: Steel strain on top of bottom flange

All the tested beams have a curved load-displacement relationship at the beginning, even after preloading was carried out before testing (Fig. 2.41). This is attributed to the settlement of the reaction frame at the beginning of each test. The steel in the top edge of the bottom flange in the control beam is seen to start yielding at approximately 311 kN (70 kip). Initiation of yield was found to be 289 kN (65 kip) at the edge of the bottom flange through gage C2 (refer Fig. 2.38) located in the control steel beam. Yielding of steel is delayed by the application of strip panels, as seen in Fig. 2.42, where the onset of yielding occurs beyond loading of 356 kN (80 kip). In contrast, the steel on the top edge of the bottom flange had not yielded up to the point of rupture in the full width laminate strengthened beam.

The rupture observed in the full width laminate is shown in Fig. 2.43. The rupture of the laminate was primarily in the external fibers. Laminate rupture was accompanied by delamination of external fibers from the internal fibers, which remained attached to the epoxy. The maximum strain observed in the laminate outer fibers was 0.00432 at 404 kN (90.8 kip), which was more than 27% higher than the average maximum tensile strain observed in the material tests of 0.00332. Once the external fibers ruptured, the test was halted to prevent sudden failure of the steel beam. The strain and shear stress variation along the laminate length is shown in Fig.2.44. The strain on the steel, in the bottom flange (next to the laminate edge) is also included in the plot.



Fig. 2.43: Rupture of full width laminate

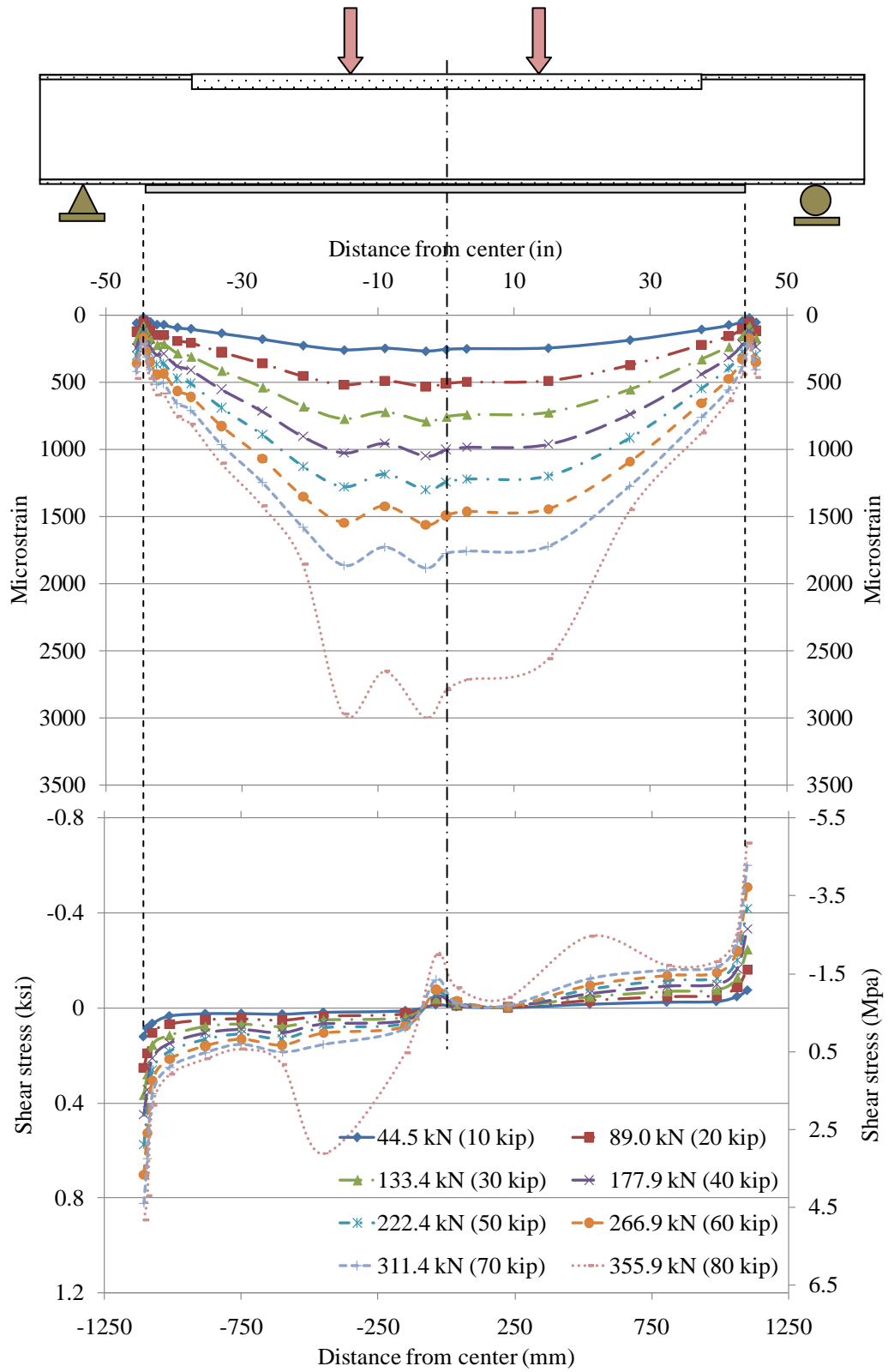


Fig. 2.44: Flexural strain and shear stress in full width laminate

From the strain distribution in Fig. 2.44, it is clear that once the steel underneath the laminate has yielded, at approximately 2070 microstrain, the strain within the laminate increases significantly. The strength increase in the full width laminate strengthened beam just before initial rupture was approximately 17% compared to the control beam at the same strain, while for the 10 mm (0.4 in) and the 5 mm (0.2 in) strip panel beams the increases in strength at the initiation of debonding were 13% and 12% respectively. The shear stress along the laminate calculated from the recorded strain data, determined in the same manner as described in section 2.3.4, shows that the maximum shear within the epoxy adhesive does not seem to reach even the average failure shear strength of 27 MPa (3.9 ksi) at the edges.

For the beams strengthened using the CFRP strip panels and tested in this study, the failure was initiated by debonding between the CFRP strip and the resin at the finger joint. The theoretical calculation of the nominal moment capacity of a steel beam strengthened using the strip panels is difficult as the failure is governed by the bond at the finger joint and not the strength of the materials. The load causing steel to yield in flexure in the unstrengthened control beam, P_y , is used herein as a datum to compare the effectiveness of the strengthening, for both the full width and strip panel CFRP laminate strengthened beams, by measuring the increase in load carrying capacity within the elastic region.

Both the 10 mm and 5 mm strip panel strengthened steel beams failed due to debonding between the steel bottom flange and epoxy adhesive at the ‘finger’ joint at the mid span of the beam. In both beams, debonding was not observed at the edges near the supports. The debonding observed in the 10 mm (0.4 in) strip panel strengthened beam is shown in Fig. 2.45, where the exposed steel surface is visible beneath the debonded laminate strips. A similar failure was observed in the 5 mm (0.2 in) strip panel strengthened beam. The strains and shear along the center strip on the primary side (5×10 mm (0.4 in) strips) of the 10 mm (0.4 in) strip panel strengthened beam is shown in Fig. 2.46. A similar plot for the secondary side (6×10 mm (0.4 in) strips) is in Fig. 2.47.

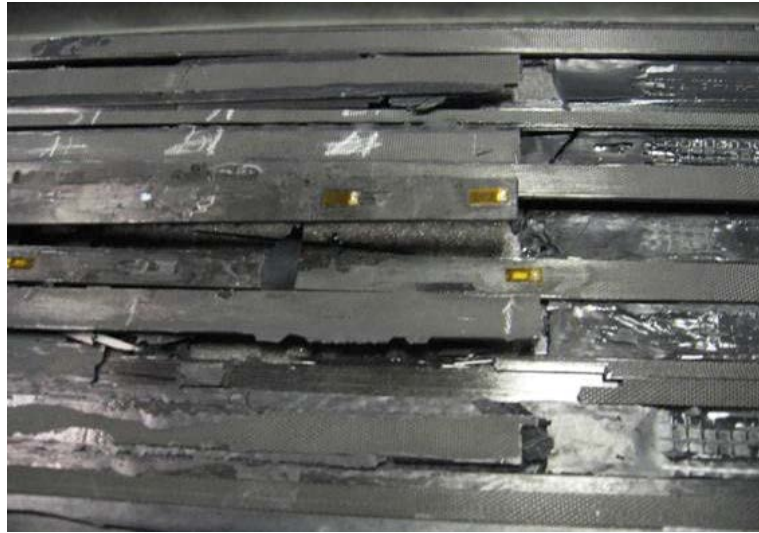


Fig. 2.45: Debonding at mid span ‘finger’ joint

The strains on the secondary side of the 10 mm (0.4 in) strip panel strengthened beam are seen to be 5%-10% less than the primary strip panel side. This is attributed to the additional strip of laminate on the secondary side. A similar strain distribution and shear stress variation is seen in the 5 mm (0.2 in) strip panel strengthened beam as well. The plots for the 5 mm (0.2 in) strip panel beam can be found in Appendix A.

Unlike in the full width laminate, the laminate strips are seen to debond before the strains within the laminate exceed the ultimate strains. This is understood by the sudden drop in strain observed in the strain gages close to mid-span at high loads. In contrast to the full width laminate, the strip panels are seen to have higher shear stress concentrations at the ‘finger’ joint at mid span. In both Fig. 2.46 and Fig. 2.47, it is clearly seen that the shear stress within the epoxy adhesive close to the panel edges at mid span at 311 kN (70 kip) is extremely close to the average shear strength of 27 MPa (3.9 ksi). From the observed results it is apparent that debonding at the ‘finger’ joint is the initial failure mechanism. A similar phenomenon is visible in the 5 mm (0.2 in) strip panel strengthened beam.

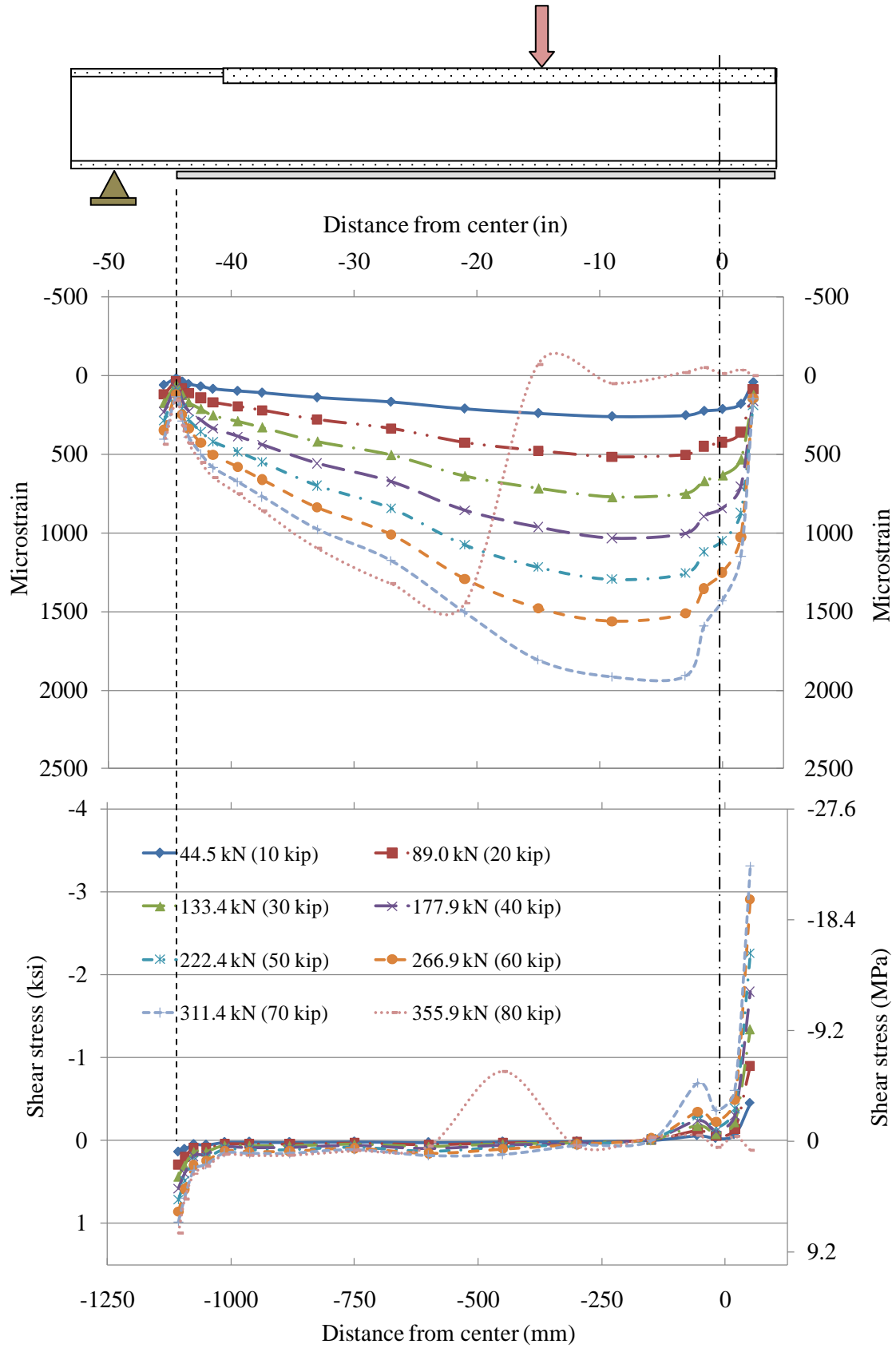


Fig. 2.46: Flexural strain and shear stress in primary 10 mm (0.4 in) strip panel

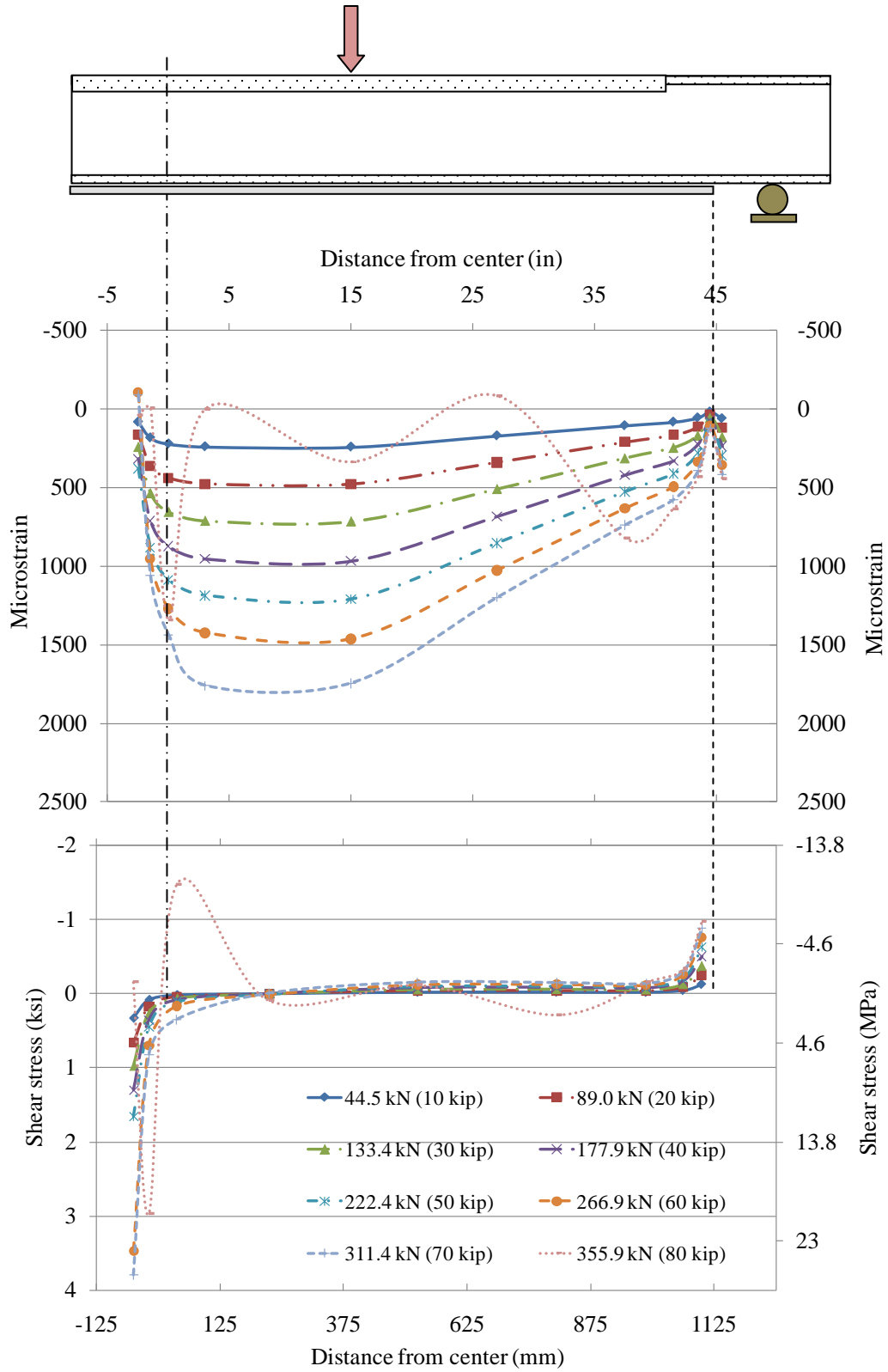


Fig. 2.47: Flexural strain and shear stress in secondary 10 mm (0.4 in) strip panel

It was noted that although the maximum strains seen in the full width and 10 mm strip panels were approximately the same at similar loads, the strains in the 5 mm strip panels were seen to be sometimes more than 20% greater for the same load. Since only a single strip of laminate was instrumented, on both the primary and secondary sides, it is not clear if the increase is due to possible premature debonding of other laminates or a difference in stress distribution between the edge strips and the middle. A single strip in the 5 mm (0.2 in) strip panel was seen to break off prematurely, well before the debonding observed at mid span, close to the primary side support. This is thought to be due to a possible kink induced onto the strip in the shear cutting process.

Evaluating the strain profile of the section along the height of the beam, the neutral axis of the composite section can be calculated. Averaging the values found at multiple loads, the neutral axis of the control beam was found to be 41 mm (1.60 in) higher than that of the wide flange beam section. Additionally, the full width laminate strengthened beam had a neutral axis 32 mm (1.26 in) above the neutral axis of the wide flange section. The respective distances to the neutral axes, for the 10 mm (0.4 in) and 5 mm (0.2 in) strip panel strengthened beams were 28 mm (1.10 in) and 30 mm (1.18 in). The two strip panel strengthened beams develop slightly greater shifts in the respective neutral axes (towards the bottom flange), as compared to the full width laminate, due to the additional 10 mm (0.4 in) and 5 mm (0.2 in) laminate strip in the secondary strip panel.

The effect of the laminate application is significant when considering the delay of yield in steel. The full width laminate strengthened beam did not observe yielding of steel up to rupture of the laminate, an increase of 39.7% load carrying capacity over the control steel beam. The steel was seen to yield only following the debonding of the laminate strips in the strip panel strengthened beams, with an increase in load carrying capacity of 26.4% and 25.8% for the 10 mm (0.4 in) and 5 mm (0.2 in) strip panels respectively. The strip panel method of splicing seems advantages compared to regular splice, which according to Dawood et al. (2009), were seen to debond at approximately 58% of the yield load of the control beam. Although the research also found that the tapering of the splice ends could nearly double the capacity of the splice.

CHAPTER 3

ANALYTICAL AND FINITE ELEMENT ANALYSIS OF BOND

3.1 Introduction

Understanding interfacial stresses and the corresponding delamination is necessary in order to design optimal strengthening systems. Numerous numerical and analytical solutions have been developed for tension member analysis as well as more specific flexural beam analysis, and are available in literature. Two approaches (stress distribution, fracture mechanics) have been used to predict the failure of adhesive joints. Both approaches have been used in predicting bond behavior in FRP strengthened steel as well as concrete beams.

The fracture mechanics based method examines the energy required for unstable crack propagation along the joint (Stratford and Cadei 2006). To predict crack propagation the energy release rate must be evaluated and compared to the critical fracture energy of the interface or of the constitutive materials. The interfacial fracture energy can be expressed in terms of the tensile strength of the adhesive and the ultimate slip. Therefore it is critical that an accurate bond-slip model for the required system be evaluated before an analysis can be carried out. Due to the heterogeneity of concrete, evaluating the bond-slip relation is complicated. However, this may not be the case for steel, which is isotropic. Lenwari and Thepchatri (2002), Wu et al. (2002) and Greco et al. (2007) developed fracture mechanics based failure criteria for bonded CFRP plates. Lenwari et al (2005) and Lenwari et al. (2006) evaluated the analytical method with experimental data. Bocciarelli et al. (2009) developed both a stress based and fracture mechanics based approach, and evaluated their performance against experimental data. While fracture mechanics based methods have been found to provide satisfactory results in predicting bond failure, most research has focused on developing stress based analytical solutions.

In the stress distribution based method, debonding failure takes place when interface stresses satisfy failure criteria dependent on material strength properties. An initial stress

based analysis of the interfacial stresses in bonded joints was developed by L.J. Hart-Smith for double-lap joints (1973(a)), single lap-joints (1973(b)), and scarf and stepped-lap joints (1973(c)). The work improved upon previous work on single-lap joints, performed by Goland and Reissner (1944), and double-lap joints, by Volkersen (1938), by considering an elastic-plastic behavior for the adhesive over simple elastic behavior (or a more complex non-linear representation). The Hart-Smith approach (1973(a)) provides an easy analytical approach to evaluate the bond development length and failure load of bonded double strap joints. It has been used to evaluate the bond development length between steel and normal modulus CFRP by Fawzia et al. (2006).

The Hart-Smith method for analyzing double-lap joints was modified by Albat and Romilly (1999) to analyze doubly reinforced plates, as well as tapered double-lap joints and tapered doubly reinforced plates. The analysis performed by Albat and Romilly also included corrections for shear-lag in the adherends. Both Miller et al. (2001) and Colombi and Poggi (2006), validates their experimental research of doubly reinforced steel plates using the method developed by Albat and Romilly. Pickett and Hollaway (1985), Tsai et al. (1998), and Diaz Diaz et al. (2009) have respectively developed new methods that incorporate non-linear adhesive stress distribution, adherend shear deformations, and interlaminar shear and normal stresses in the adhesive.

Stress distribution based analytical methods for beam analysis is based on equilibrium and deformation compatibility conditions in the FRP bonded beam system. While some methods were developed for the application of FRP to reinforced concrete, similar to the tension loaded analysis, several different models have been proposed. In order to obtain relatively simple closed form solutions, most methods assume shear and normal stresses to be constant across the thickness of the adhesive, while the adherend and adhesive materials are taken as linear elastic.

Vilnay (1998) proposed one of earliest methods of bond stress analysis, that was initially developed for bonded steel plates in reinforced concrete beams. The method does not include any axial deformation of the beam, bending deformation of the plate nor any

loading criteria other than a point load at mid-span of the beam. The governing equations are derived in terms of the vertical displacement of the bonded plate while utilizing the boundary condition of zero shear stress at point load location and also neglecting the effect of shear deformation. Täljsten (1997) incorporated axial deformations when analyzing the shear stresses, and also the bending deformation of the beam when analyzing the normal stresses. Täljsten (1997) also derived the governing equations in terms of the vertical displacement of the bonded plate and utilizes the boundary condition of zero shear stress at point load location while neglecting the effect of shear deformation. Colombi and Poggi (2006) verified their experimental data utilizing Täljsten's method, while Pellegrino et al. (2008) further developed the method to incorporate material non-linearities and various reinforcement configurations. The method proposed by Malek et al. (1998) derives its governing equations in terms of interfacial normal stresses. It is applicable to more general load cases as well, provided the originating moment can be expressed as a quadratic function. The axial deformations in the beam and the bending deformations in the plate are also partially considered when evaluating the shear stresses by analyzing the stresses based on the composite section. The method also uses the boundary condition of zero shear stress at point load location in developing the equations for shear stress, while also neglecting the effect of shear deformation.

Smith and Teng (2001) performed a review of available approximate closed-form solutions and proposed a highly accurate method, which has gained widespread use today. While linear elastic materials are assumed in this method along with invariant stresses across the adhesive layer, bending and axial deformation of both the beam and the plate are taken into consideration. The governing equations include shear deformation also, but are ignored when deriving the equations for shear and normal stress for simplicity. The Smith and Teng solution also provides continuity for shear stress and its first derivative at point load locations, unlike the previous methods. Deng et al. (2004) improved on the method proposed by Smith and Teng (2001) by incorporating both mechanical and thermal loads. While some high order analyses (Rabinovich and Frostig 2000; Shen et al. 2001) have been completed that satisfy the zero shear stress condition at

the end of the adhesive layer, such analyses are complex and do not provide explicit expressions for the interfacial stresses. Consequently, development of a design rule is not feasible. Advanced closed form solutions developed by Al-Emrani and Kliger (2006) and Benachour et al. (2008) provide methods of incorporating prestressed bonded laminates.

In the present study, the failure load and the bond development length observed experimentally are evaluated using the analytical method proposed by Hart-Smith (1973(a)). The doubly reinforced steel plate specimens are evaluated using the analytical method developed by Albat and Romilly (1999). The Smith and Teng (2001) method, identified as the most accurate simple closed-form solution available, is used to evaluate the strengthened steel beam specimen test data. All three tests are further studied using finite element analyses. The results are expected to provide insight into the viability of applying closed-form simple analytical methods for the evaluation of bond behavior between steel and ultra high modulus CFRP laminates. The finite element analyses are expected to validate the analytical and experimental results as well as to provide representative models for further evaluation of the performance of the steel-CFRP bond at different geometric, boundary and loading conditions.

3.2 Double Strap Joint

The analytical study of the double strap joint is carried out with the method developed by Hart-Smith (1973(a)). The failure loads as well as bond development lengths are calculated using the method and compared with experimental results. A finite element analysis of the double strap joint specimens is also carried out and a representative model is developed to perform parametric studies.

3.2.1 Analytical Study

The Hart-Smith (1973(a)) method derives the failure load for a double lap joint at both ends of the joint, the gap end and the laminate edge. The critical end of the joint would be governed by the adherend stiffness difference. Therefore the failure load, when neglecting thermal mismatch, is given by the lesser of the following:

$$P = 2\tau_{av}l = \sqrt{2k\tau_p t_a (\gamma_e + \gamma_p) 2E_i t_i \left[1 + \left(\frac{E_i t_i}{2E_o t_o} \right) \right]} \quad (3.1)$$

$$P = 2\tau_{av}l = \sqrt{2k\tau_p t_a (\gamma_e + \gamma_p) 4E_o t_o \left[1 + \left(\frac{2E_o t_o}{E_i t_i} \right) \right]} \quad (3.2)$$

$$\text{Where;} \quad k = \frac{\left(\frac{1}{2}\gamma_e + \gamma_p \right)}{(\gamma_e + \gamma_p)} \quad (3.3)$$

P	= Applied load on joint per unit width
τ_{av}	= Average adhesive shear stress
τ_p	= Plastic adhesive shear stress
l	= Bond/overlap length
γ_e	= Elastic adhesive shear strain
γ_p	= Plastic adhesive shear strain
t_a	= Thickness of adhesive layer
t_i	= Inside adherend thickness
t_o	= Outside adherend thickness
E_i	= Inside adherend longitudinal Young's modulus
E_o	= Outside adherend longitudinal Young's modulus

The required minimum bond length to achieve full shear strength capacity is given by:

$$l = \frac{P}{2\tau_p} + \frac{2}{\sqrt{\frac{\tau_p}{\eta\gamma_e} \left(\frac{1}{E_o t_o} + \frac{2}{E_i t_i} \right)}} \quad (3.4)$$

The thickness of the epoxy was conservatively taken as 0.6 mm (0.024 in), the minimum thickness measured for all specimens, for both types of laminate. The material properties evaluated in the previous chapter were used in the analytical study. The steel plate properties were entered as the inside adherend, and the CFRP laminate properties were used for the outside adherend. Since the minimum shear stress at the middle of the joint is almost as high as the ends for a short overlap (Hart-Smith 1994), the value of the plastic adhesive shear stress is taken as 27 MPa (3.9 ksi). The plastic adhesive shear stress was determined by averaging the shear stress for short bond length normal modulus CFRP specimens that failed in debonding at the steel adhesive interface.

Since the adhesive is taken to be isotropic in behavior, the elastic shear strain is calculated using the shear stress, 27 MPa (3.9 ksi), and the shear modulus, which in turn is calculated using the Young's modulus and Poisson's ratio evaluated through the material tests. The plastic shear strain is conservatively taken as twice the elastic shear strain to allow for some shear deformation at the joint. A value of 3 was adopted by Fawzia et al. (2005), but for a different adhesive when evaluating the failure load for normal modulus CFRP and steel. The plastic shear strain is found to be a key component in the Hart-Smith model. The experimental evaluation of the epoxy adhesive to obtain the shear stress-strain relation is important for use in the Hart-Smith analytical model.

Results obtained from the Hart-Smith model analysis are plotted against the test results for both the normal modulus (Fig. 3.1 and Fig. 3.2) and the ultra high modulus (Fig. 3.3 and Fig. 3.4) laminates (for both 5 mm (0.2 in) and 10 mm (0.4 in) wide strips). The experimental data are seen to be in good agreement with the model predictions.

The Hart-Smith model predicted a bond development length of 48 mm (1.9 in) for the normal modulus CFRP laminate double strap joint and a length of 72 mm (2.9 in) for the ultra high modulus CFRP laminate joint. The predicted failure load also increased with the increase in laminate modulus from 1.63 kN/mm (9.3 kip/in) for the normal modulus CFRP to 2.60 kN/mm (14.9 kip/in) for the ultra high modulus CFRP strap joint.

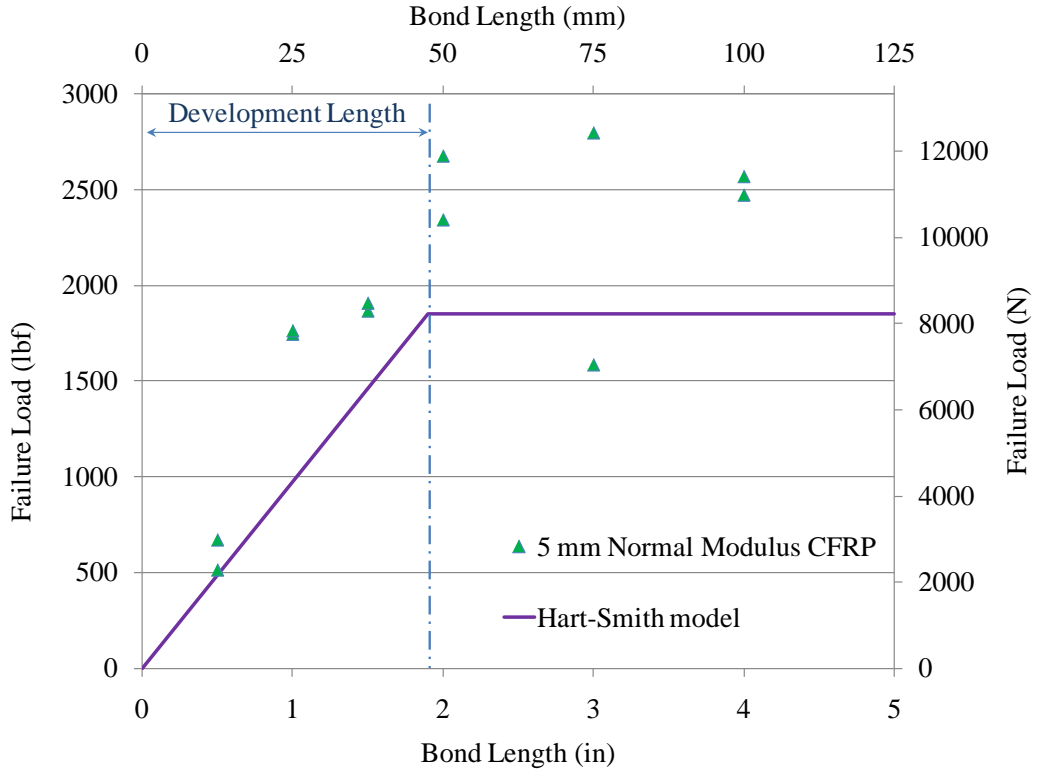


Fig. 3.1: Analytical and experimental results for NM 5 mm (0.2 in) specimens

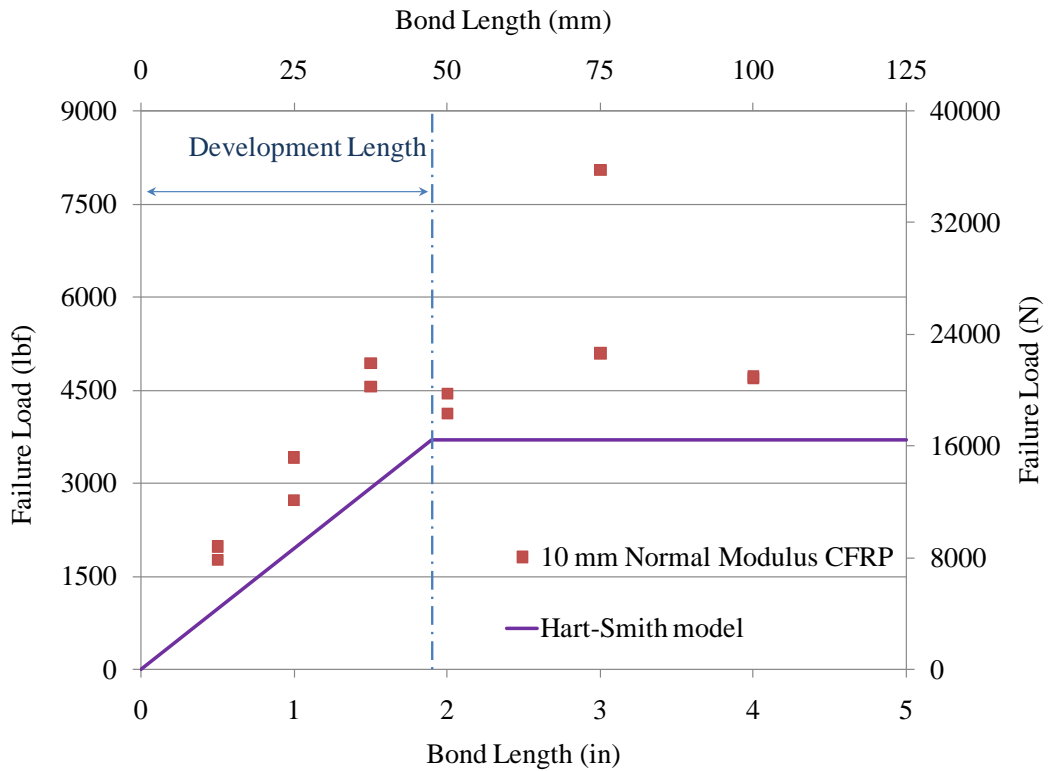


Fig. 3.2: Analytical and experimental results for NM 10 mm (0.4 in) specimens

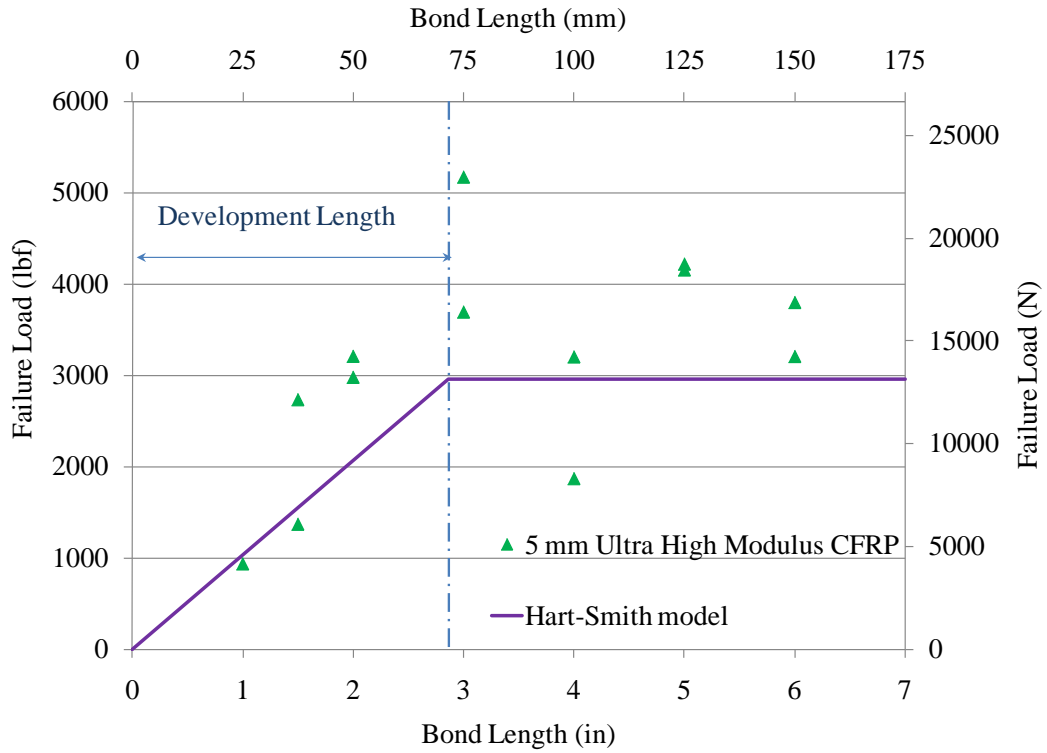


Fig. 3.3: Analytical and experimental results for UHM 5 mm (0.2 in) specimens

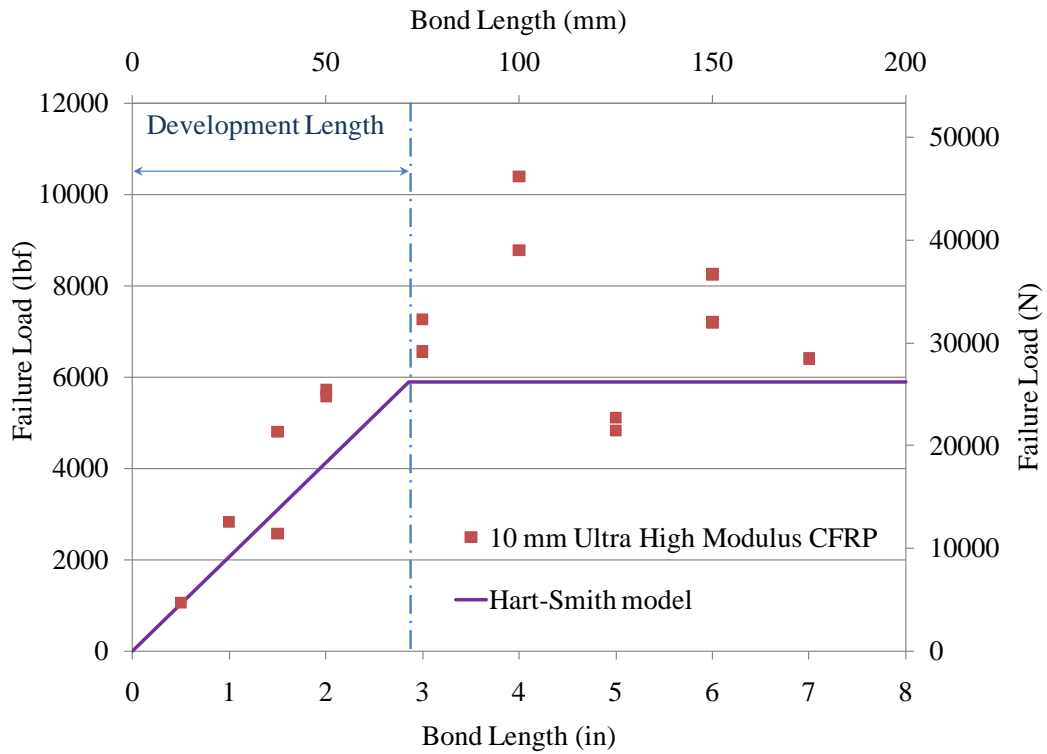


Fig. 3.4: Analytical and experimental results for UHM 10 mm (0.4 in) specimens

Fig. 3.5 shows the variation of the failure load and bond length due to change in laminate modulus when using the Hart-Smith model. The modulus of the laminate, or outside adherend, was taken as a factor of the modulus of the inside adherend steel (E_s). The increase in bond development length and load carrying capacity is evident in the figure, where the laminate or outer adherend modulus is increased from being half the inside adherend modulus to twice the inside adherend modulus.

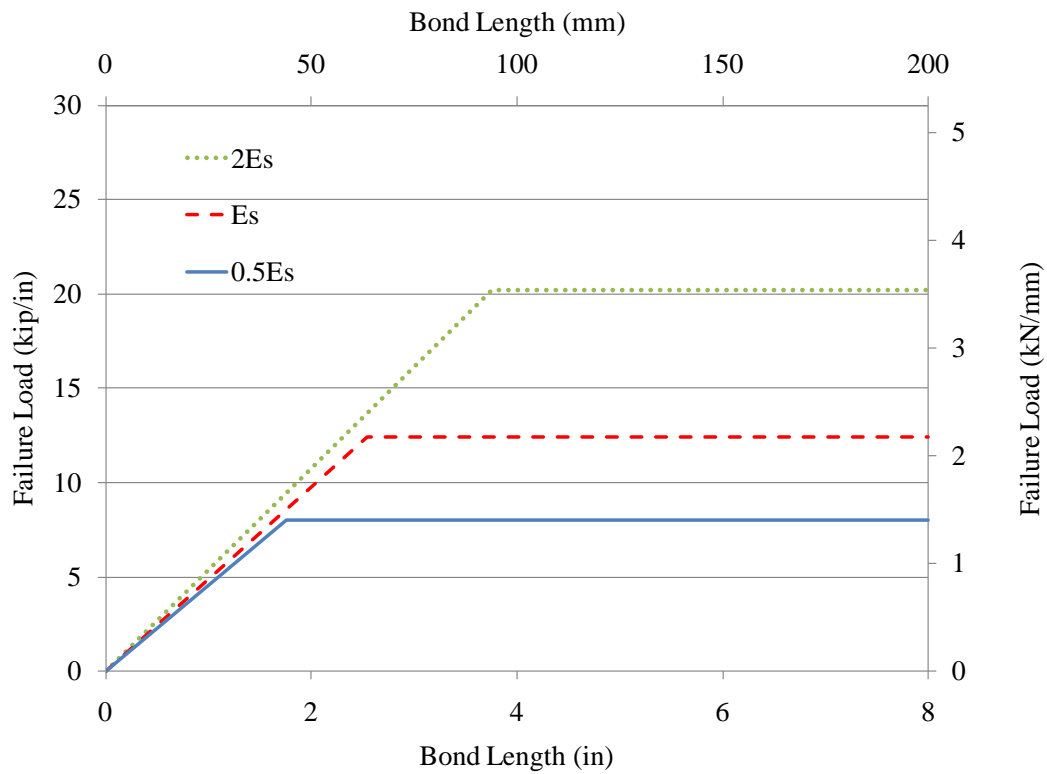


Fig. 3.5: Hart-Smith model for laminate joints of different Young's modulus

The effect of the epoxy thickness (t_a) on the bond length and failure load of a double strap joint was evaluated when using the analytical model, for an outside adherend of ultra high modulus CFRP laminate and inside adherend of steel, and is shown in Fig. 3.6. An increase in the required bond development length and failure load is seen with the increase in adhesive thickness, for an ultra high modulus CFRP laminate and steel double strap joint. Adhesive thicknesses of 0.6 mm (0.024 in), 1 mm (0.4 in) and 1.5 mm (0.06 in) thicknesses have been considered, where the 0.6 mm (0.024 in) thickness was representative of the test specimens.

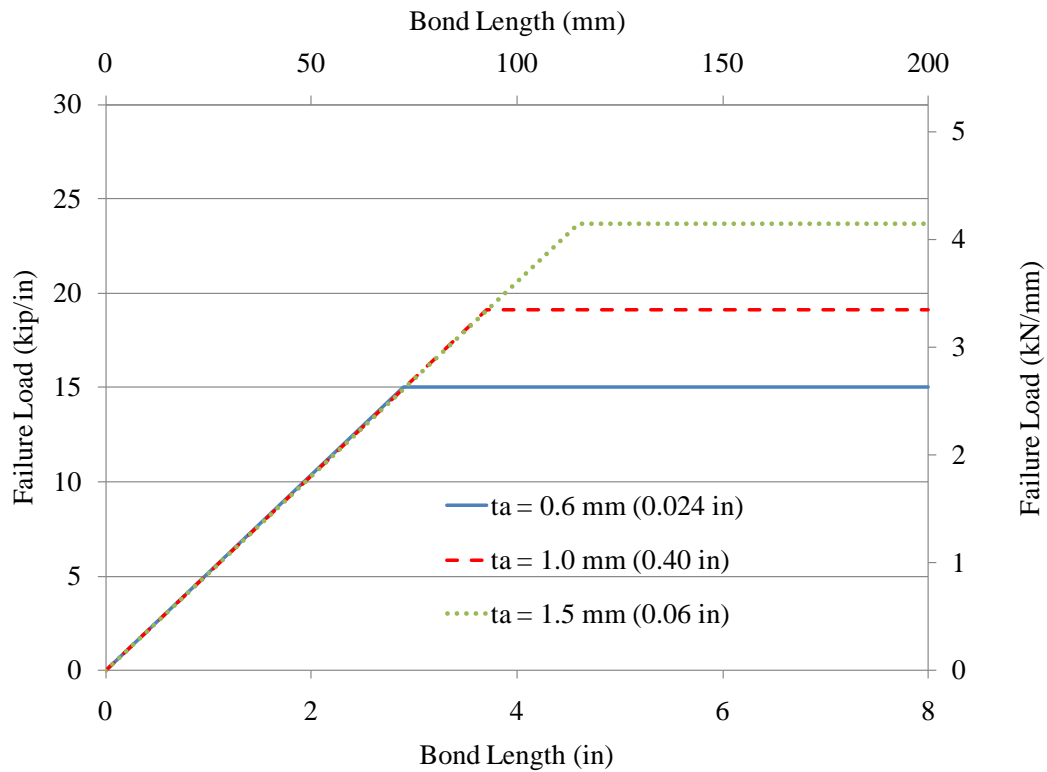


Fig. 3.6: Hart-Smith model for laminate joints with different adhesive thickness

3.2.2 Finite Element Analysis

In order to analyze the behavior of the double strap joint under different loads, various material and geometric variations, finite element models representing the different bond lengths were created. The models were built and analyzed using the finite element software ANSYS (ANSYS 2009) and are calibrated using the laboratory test strain data obtained from the mounted strain gages. As the double strap joint was symmetrical across two mutually perpendicular axes, and since the control side of the specimen was not required for the modeling, only an eighth of the specimen was modeled. Translational boundary conditions were implemented to accurately represent the symmetry of the specimen.

3.2.2.1 *Element Selection*

The double strap joint models were built up using 8-node SOLID45 elements available in the FEA software ANSYS. The element has three degrees of freedom at each node; three translations in the three mutually perpendicular x, y, and z axis. The SOLID45 element was selected as it had large deflection and strain capabilities, which were important to represent the adhesive epoxy deformation. The epoxy and CFRP layer thickness were modeled as a single layer of elements, while half the steel plate thickness modeled was represented by two element layers (Fig. 3.7).

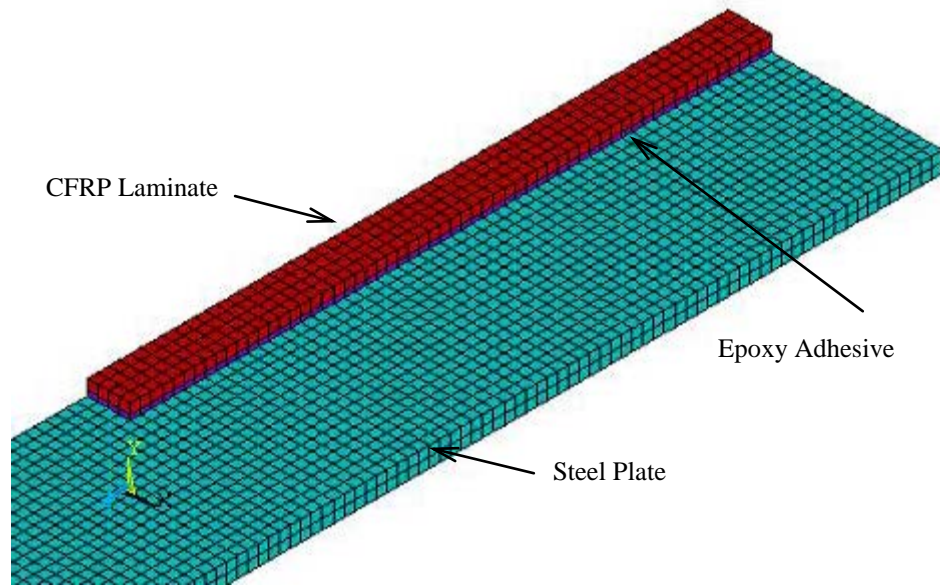


Fig. 3.7: 75 mm bond finite element model

3.2.2.2 *Material Models*

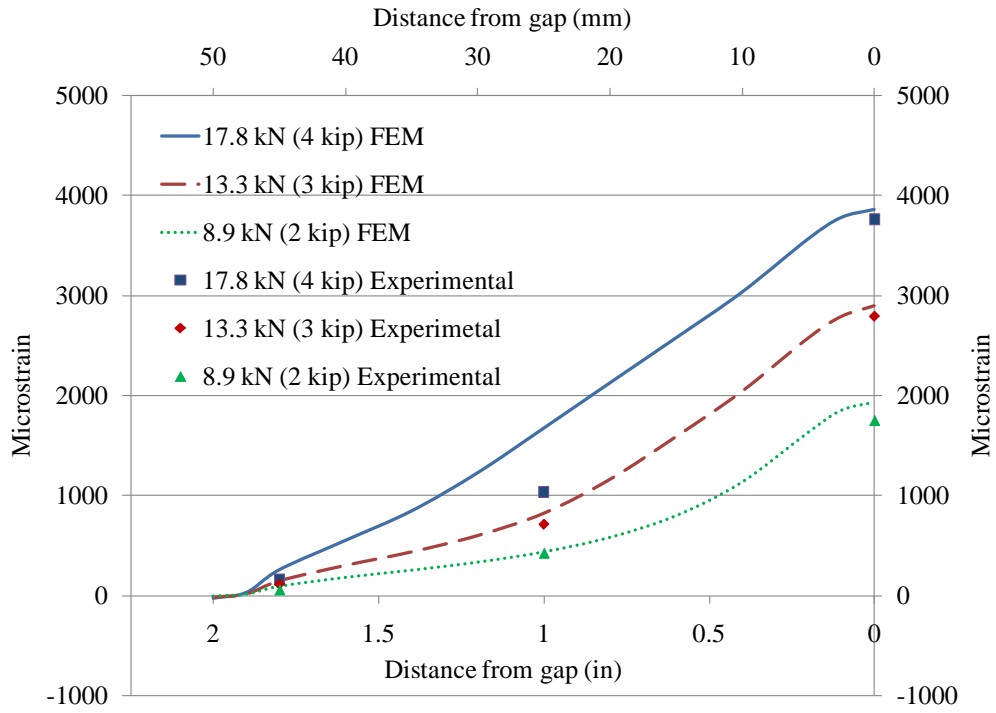
The steel plate was modeled as having bi-linear elastic-perfectly plastic steel material model with a yield strength of 409.7 MPa (59.4 ksi), as found in the material testing. A linear stress-strain relationship was taken for the both CFRP material with an ultimate strength of 2979 MPa (432 ksi) for the normal modulus CFRP and 1923 MPa (279 ksi) for the ultra high modulus CFRP. The tensile modulus for the laminates were also set at the experimentally measured values of 187 GPa (27017 ksi) for the normal modulus and 514 GPa (74586 ksi) for the ultra high modulus CFRP. The epoxy adhesive was modeled as having a linear stress-strain distribution up to tensile strength of 34.5 MPa (5.0 ksi), with a tensile modulus of 3007 GPa (436 ksi). Beyond the ultimate tensile strength, a small plastic region was modeled to facilitate the identification of the failure location. The Von Mises failure criterion, available for the material model, was used to predict the failure of the epoxy adhesive.

3.2.2.3 *Analysis and Results*

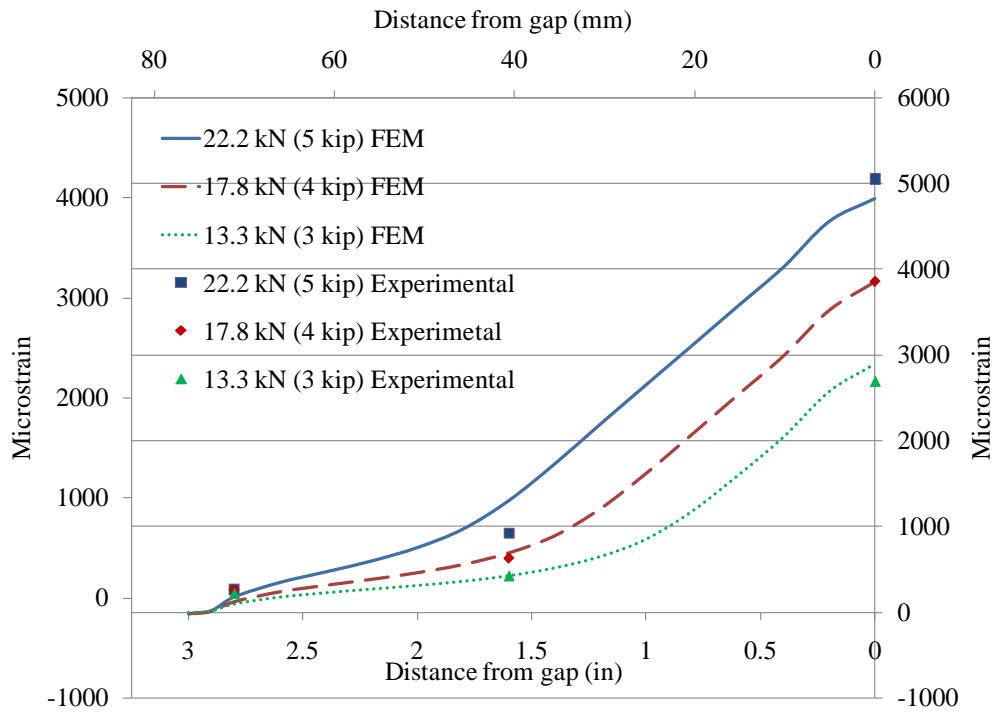
The Newton-Raphson procedure was used to solve the nonlinear equations with the Arc-Length method employed to improve convergence. Load increments were automated and handled by the ANSYS solution algorithm.

The strain data were obtained along the bond line and compared with measurements taken in the laboratory tests (Fig. 3.8 and 3.9). The strains along the bond center line for the 10 mm (0.4 in) wide, 50 mm (2 in) and 75 mm (3 in) bond length normal modulus CFRP double strap joint specimen is given in Fig. 3.8, and the same laminate width and bond length specimens of ultra high modulus CFRP is shown in Fig. 3.9.

Only three gages were placed along the bond length for specimens with a bond length less than 100 mm (4 in). One gage was placed close to the center of the bond, another gage close to the laminate edge, and one across the gap (refer to Fig. 2.8 in Chapter 2). The strain closer to the center at high loads in the normal modulus CFRP laminates (Fig. 3.8) showed a lesser strain than predicted by the finite element model. The experimental strains suggest a more exponential strain increase closer to the gap relative to that shown by the finite element solution. The validity of this phenomenon requires further testing with more gages along the bond length. This would have facilitated a more accurate evaluation of the finite element model. While the strains observed at the gap are found not to collaborate the finite element analysis strains perfectly, the experimental and finite element strains observed for the ultra high modulus laminate double strap joints are seen to be in good agreement at most locations at different loads (Fig. 3.9).

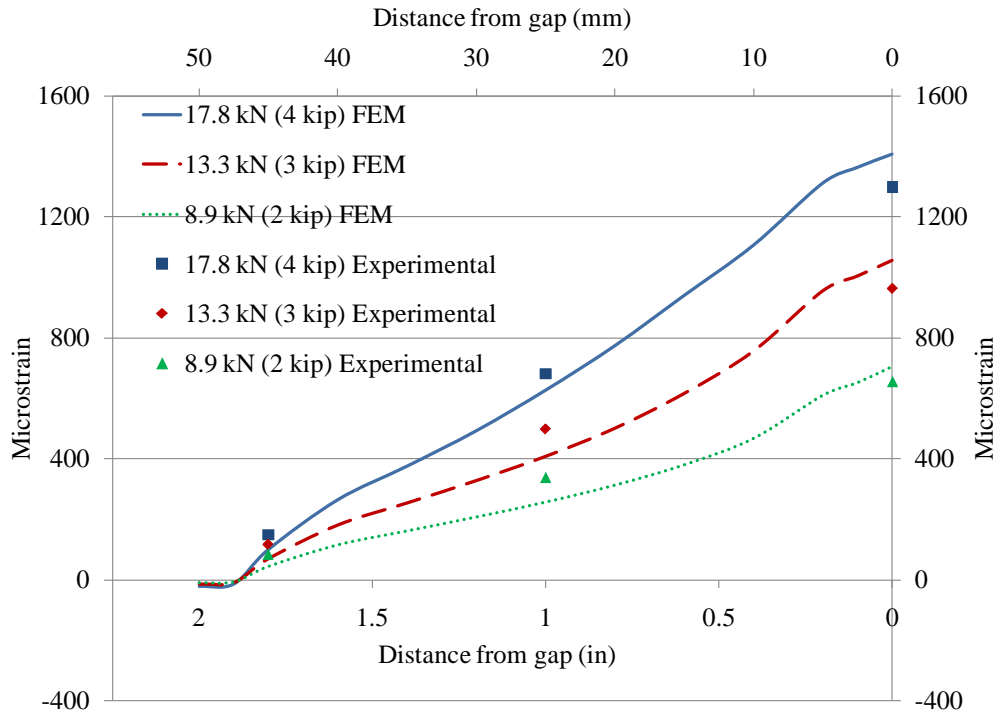


(a) 50 mm (2 in) bond length

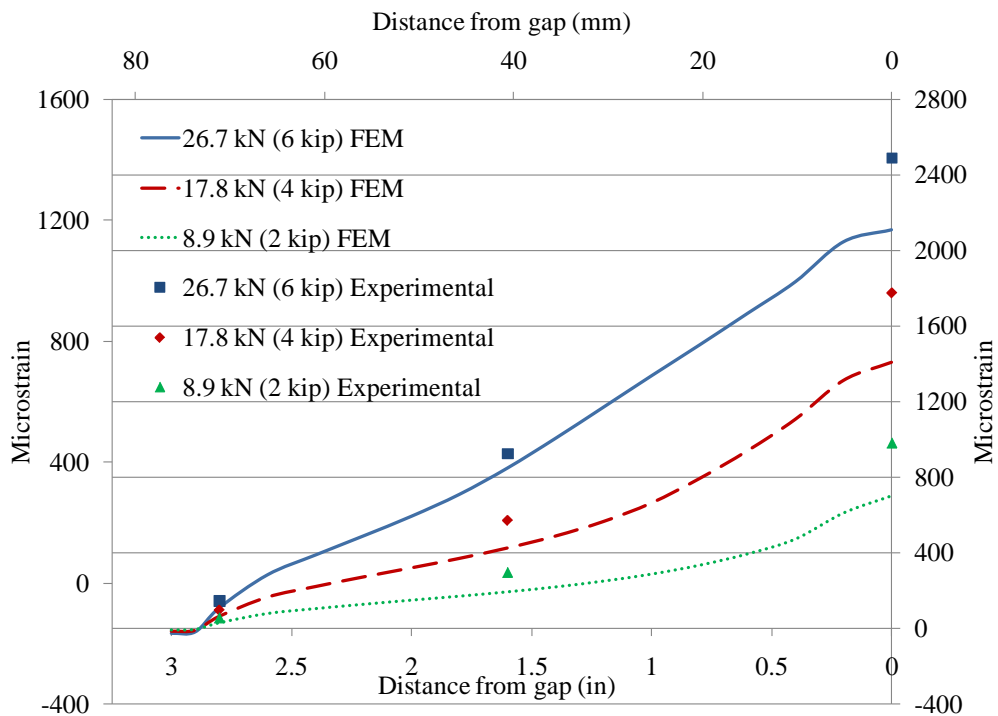


(b) 75 mm (3 in) bond length

Fig. 3.8: Tensile strains along bond for 10 mm (0.4 in) wide normal modulus specimens



(a) 50 mm (2 in) bond length

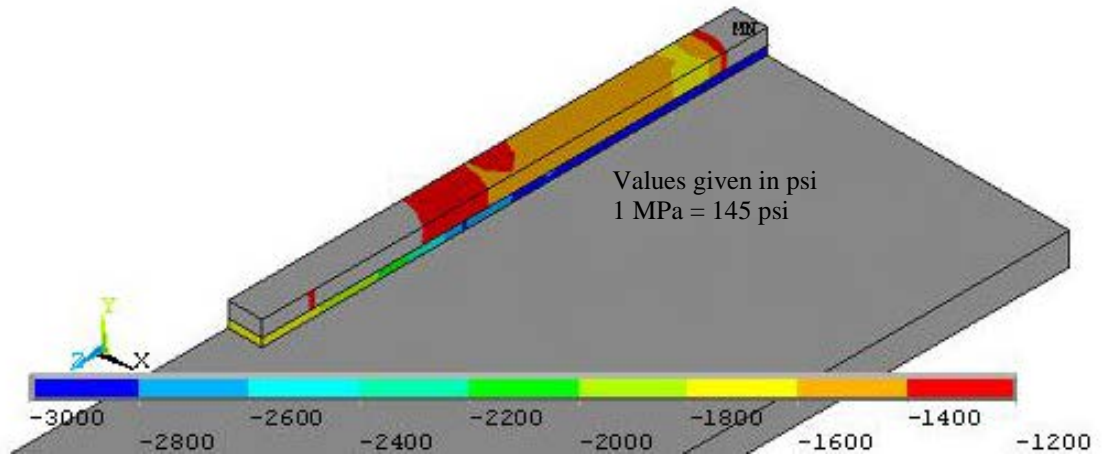


(b) 75 mm (3 in) bond length

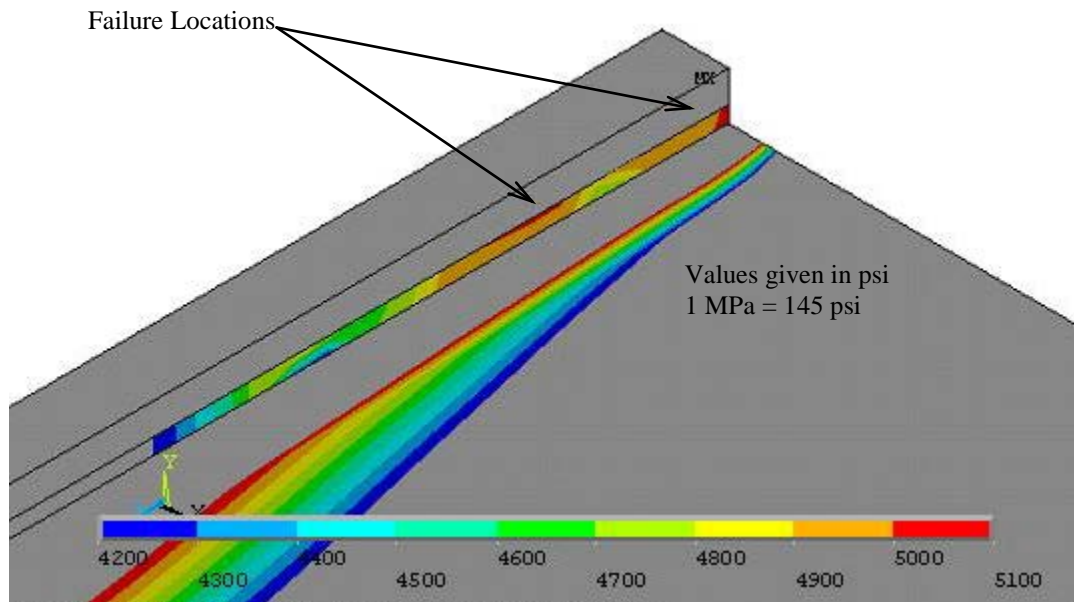
Fig. 3.9: Tensile strains along bond for 10 mm (0.4 in) wide ultra high modulus specimens

The ultimate load for each bond length was taken as the load at which the Von Mises failure criterion was achieved within the epoxy adhesive. While some plastic shear deformation would occur beyond meeting the failure criterion (providing more strength to the bond), the Von Mises or similar failure criterion is found to be a more conservative approach in predicting the failure of the bond, when the plastic shear deformation capacity of the epoxy adhesive is unknown. A similar approach was adopted by Fawzia et al. (2006) for evaluating normal modulus CFRP double strap joints. Fig. 3.10(a) depicts the shear stress distribution and Fig. 3.10(b) depicts the Von Mises stress distribution at failure of the 5 mm (0.2 in), 37.5 mm (1.5 in) bond length normal modulus CFRP double strap joint model. While the shear stresses (Fig. 3.10(a)) are yet to exceed the average shear strength of the bond of 27 MPa (3.9 ksi), the Von Mises stresses (Fig. 3.10(b)) are seen to exceed the ultimate strength of 34.5 MPa (5 ksi) at certain locations of the bond. The red locations within the epoxy layer indicate locations where the Von Mises stress has exceeded the maximum stress of 34.5 MPa (5 ksi).

Short specimens up to approximately 50 mm (2 in) bond lengths showed failure initiating at the gap and then propagating inwards as seen in Fig. 3.10(b). Although debonding between the steel and adhesive interface was observed for the shorter bond lengths of normal modulus CFRP double strap joints, the initiation of failure by exceeding the Von Mises failure stress was always close to the CFRP laminate and adhesive interface. In longer bond lengths the initiation of adhesive failure was seen to occur some distance away from the gap as seen in the normal modulus 10 mm (0.4 in), 100 mm (4 in) bond length specimen shown in Fig. 3.11. The ultimate failure of a typical specimen where the adhesive yields in shear is depicted in Fig. 3.12.



(a) Shear stress at failure in adhesive



(b) Von Mises stress at failure in adhesive

Fig. 3.10: Shear and Von Mises stress at initiation of failure in adhesive

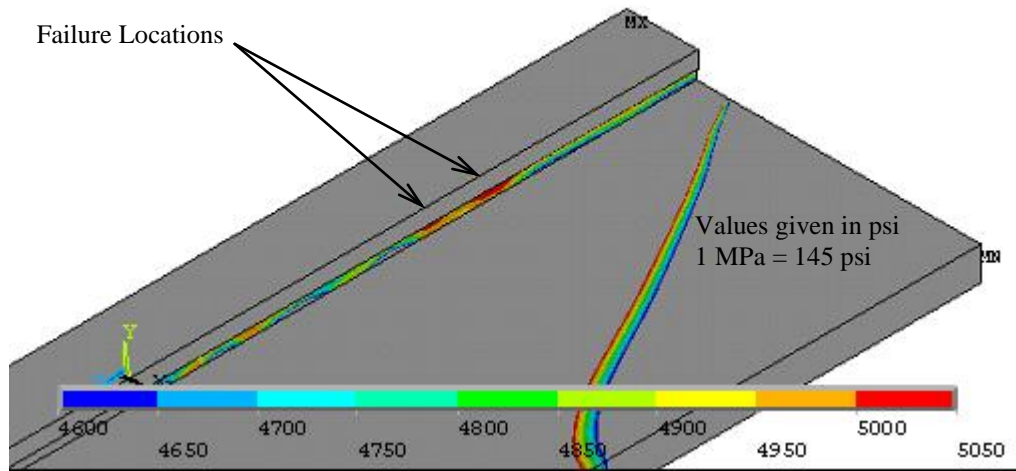


Fig. 3.11: Typical failure in adhesive seen in longer bond lengths

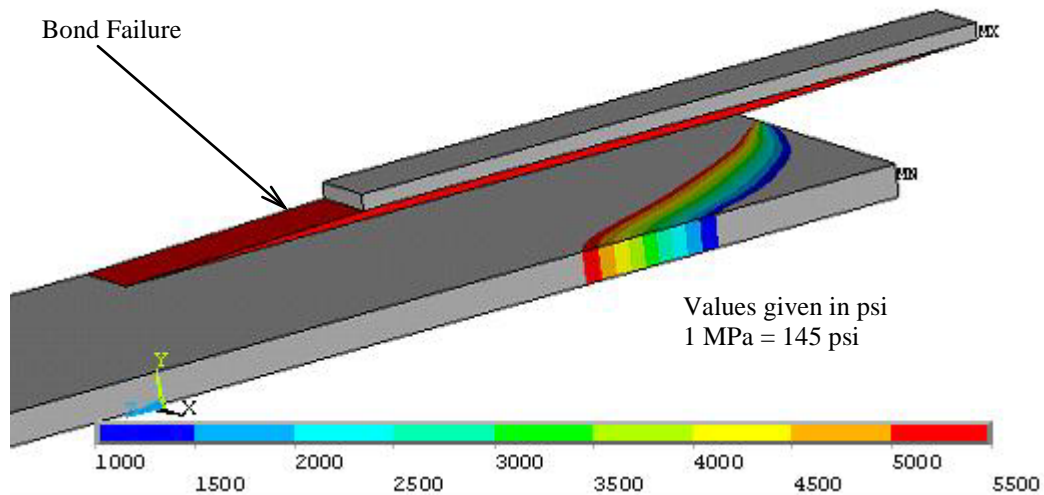


Fig. 3.12: Ultimate failure of bond

The failure loads observed at each bond length for both types of CFRP laminates are shown in Fig. 3.13 and Fig. 3.14 for the 5 mm (0.2 in) and 10 mm (0.4 in) wide laminate strips of the normal modulus CFRP laminate double strap joints. Analogous results for the ultra high modulus CFRP laminates are shown in Fig. 3.15 and 3.16.

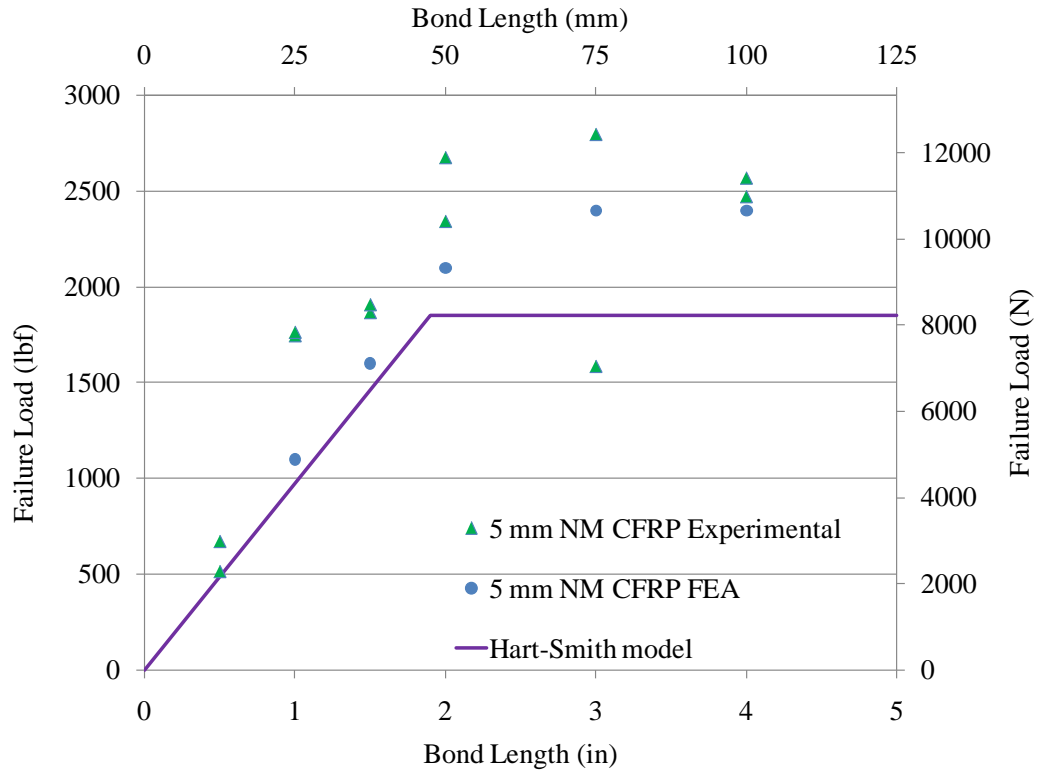


Fig. 3.13: Finite element and experimental results for NM 5 mm (0.2 in) specimens

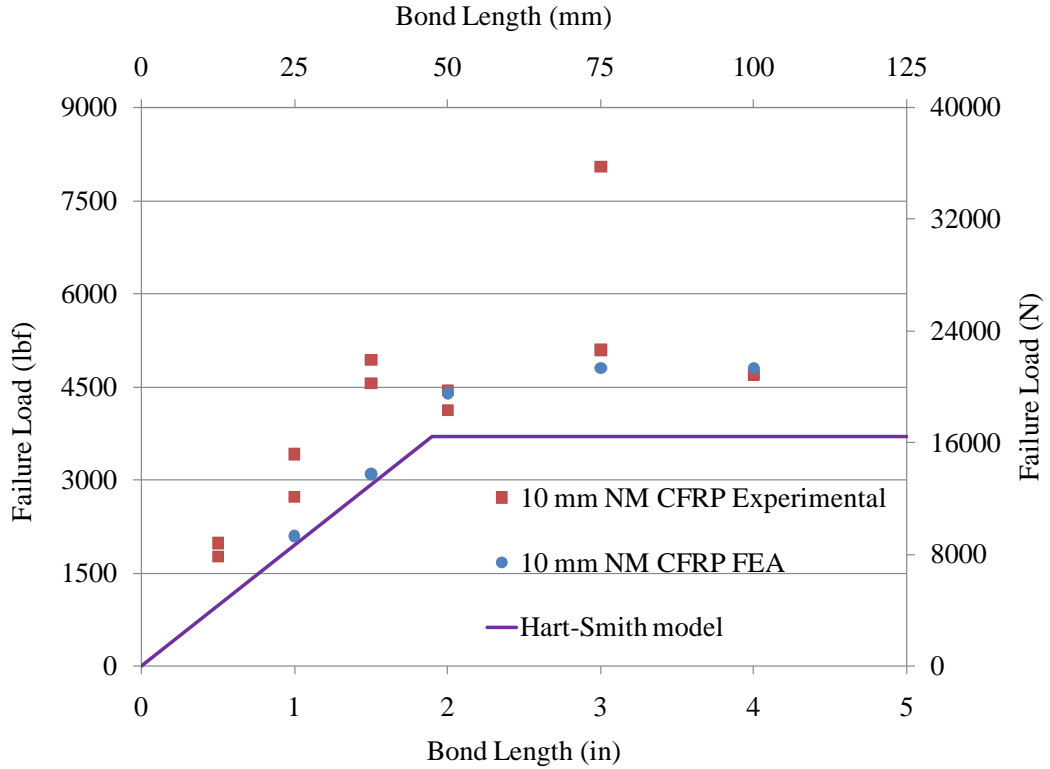


Fig. 3.14: Finite element and experimental results for NM 10 mm (0.4 in) specimens

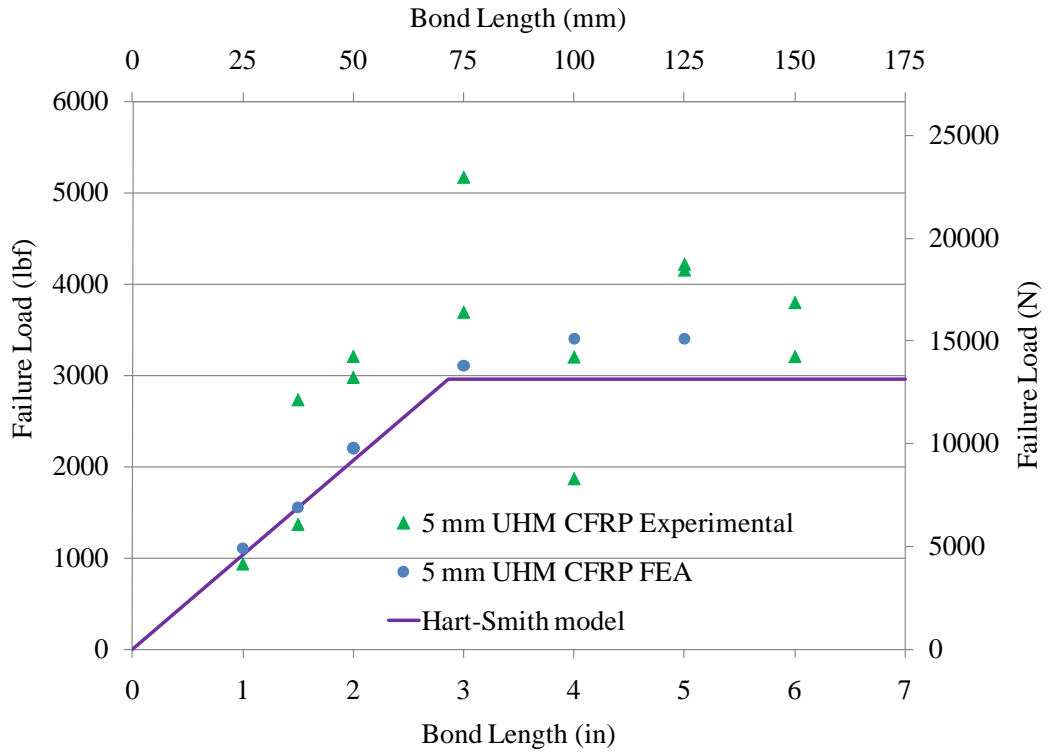


Fig. 3.15: Finite element and experimental results for UHM 5 mm (0.2 in) specimens

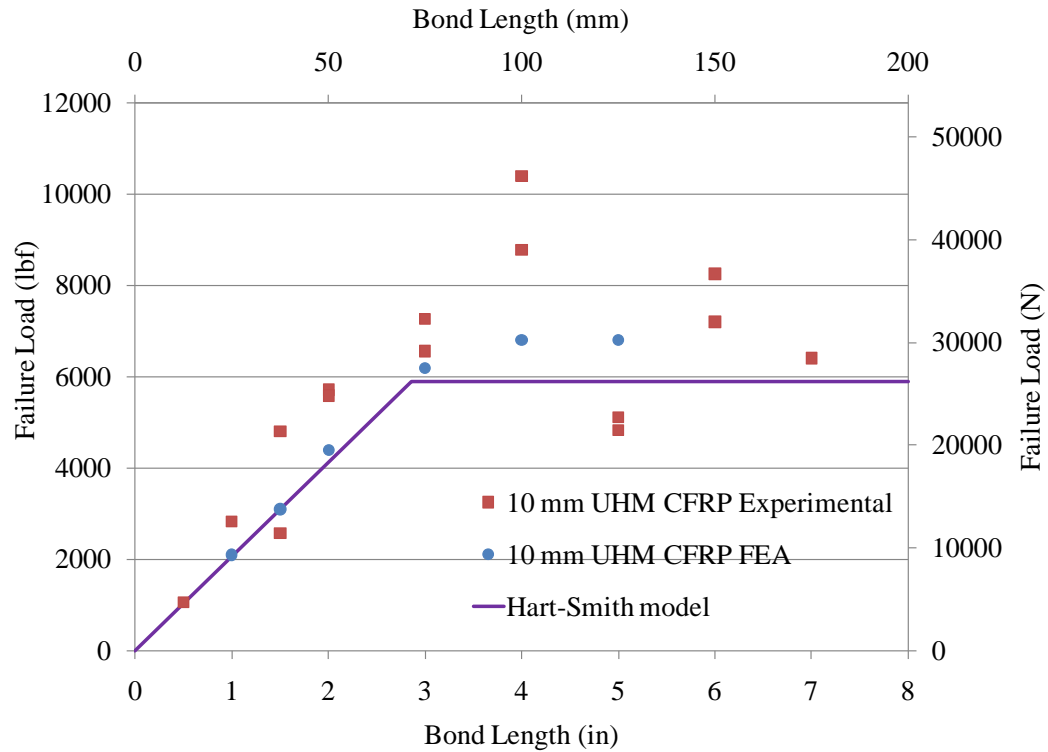


Fig. 3.16: Finite element and experimental results for UHM 10 mm (0.4 in) specimens

Failure loads obtained from the finite element analysis are seen to be in good agreement with the experimental results. The analytical Hart-Smith model, plotted in each figure, is seen to provide a conservative failure load when compared with the experimental and finite element results. The numerically predicted failure loads are seen to be more than 25% greater than the Hart-smith predictions for the normal modulus CFRP double strap joints and more than 15% greater for the ultra high modulus CFRP joints. The predicted bond development length is seen to be greater for the finite element model results when compared with the Hart-Smith model. The width of the CFRP laminate does not seem to affect the failure load or the bond development length.

3.3 Doubly Reinforced Steel Plate

The analytical study of the doubly reinforced steel plate is carried out with the derivations given in Albat and Romilly (1998). The shear stress within the adhesive as well as the tensile stresses in the laminate are calculated and compared with experimental results. A finite element analysis of the doubly reinforced specimens is also carried out and a representative model is developed to perform parametric studies.

3.3.1 Analytical Study

Albat and Romilly (1998) expanded the Hart-Smith (1973(a)) method to analyze tapered double strap joints as well as tapered doubly reinforced plates. The Hart-Smith approach, extended by Albat and Romilly, provides linear elastic solutions for the adhesive shear stress as well as the adherend stress distribution for doubly reinforced plates. The derived stress distribution, ignoring thermal effects, is given by the following equations:

$$\tau_a(x) = P \left(\frac{E_o t_o}{E_i t_i + 2E_o t_o} \right) \lambda \frac{\sinh(\lambda x)}{\cosh(\lambda l)} \quad (3.5)$$

$$\sigma_o(x) = \frac{P}{t_p} \left(\frac{E_o t_o}{E_i t_i + 2E_o t_o} \right) \left(1 - \frac{\cosh(\lambda x)}{\cosh(\lambda l)} \right) \quad (3.6)$$

Where; $\lambda = \frac{G_a}{t_a} \left(\frac{1}{E_o t_o} + \frac{2}{E_i t_i} \right)$ (3.7)

$$-l \leq x \leq l \quad (3.8)$$

- P = Applied load on joint per unit width
- τ_a = Adhesive shear stress
- G_a = Adhesive shear modulus
- σ_o = Outer adherend tensile stress
- l = Bond length from center

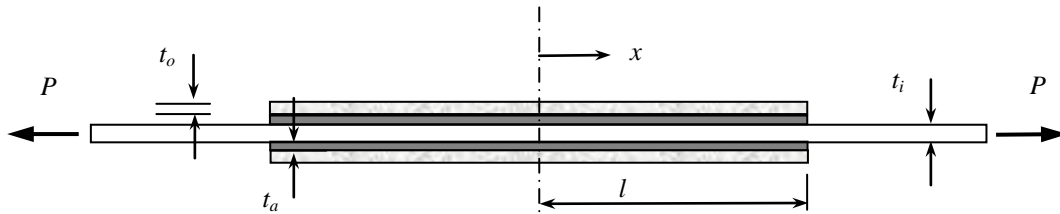


Fig. 3.17: Doubly reinforced plate

The thickness of the epoxy adhesive layer was taken as 1.25 mm (0.05 in), the average thickness measured for all specimens, for both types of laminate. The material properties presented in the Chapter 2 were used in the analytical study. The steel plate properties were entered as the inside adherend, and the CFRP laminate properties were used for the outside adherend. The adhesive shear modulus was calculated from the adhesive Young's modulus and Poisson's ratio, assuming isotropic material properties, to be 1.09 GPa (158 ksi).

The doubly reinforced steel plates were tested to represent actual field applicability of CFRP laminate strengthening. In order to replicate an actual field implementation, where sometimes the full width of the steel section will not be covered by the laminate, only half the plate area was strengthened on either side. The derivations provided by Albat and Romilly (1998) are directly applicable only if the plate is strengthened throughout the entire width. In order to employ the above equations, the portion of the applied force directly resisted by the strengthened section needed to be calculated. This was achieved by transforming the CFRP laminate section to an equivalent steel section, and evaluating the total strengthened area, over the total area of the section. The normal modulus CFRP

laminated strengthened plate had a strengthened area equivalent to 59.7% of the total section area, while the ultra high modulus CFRP laminated strengthened steel plate had a 69.8% equivalent strengthened area. Only this percentage of the applied load was used with the analytical method to validate the experimental data.

The results obtained for the tensile and shear stress distribution from the analytical method are plotted against the test results for both the normal modulus (Fig. 3.18 and Fig. 3.19) and the ultra high modulus (Fig. 3.20 and Fig. 3.21) laminated strengthened steel plates at a load of 44.5 kN (10 kip). The tensile stress data were obtained by multiplying physically measured strains with the corresponding laminate Young's modulus. The shear stresses were calculated using the recorded tensile strain data using the method described in Chapter 2 (section 2.3.4). The experimental data are seen to be in good agreement with the analytical predictions. The experimental tensile stress beyond the development length is seen to be slightly higher than the analytical prediction for both types of laminates.

The effect of the outer adherend, CFRP laminate, modulus on the tensile stress distribution along the adherend is evaluated using the analytical formulation by Albat and Romilly, and the results are plotted in Fig. 3.22. Physically measured specimen dimensions and material properties were used in the parametric study, except for the outer adherend Young's modulus, which was taken as a factor of the inside adherend steel modulus (E_s), and varied from half the modulus to twice the modulus of steel. It is clear from the plot that the greater modulus laminate would carry more stress along the bond length. This is evident from the experimental results shown in Fig. 3.18 and Fig. 3.20, respectively, for the normal and ultra high modulus laminates.

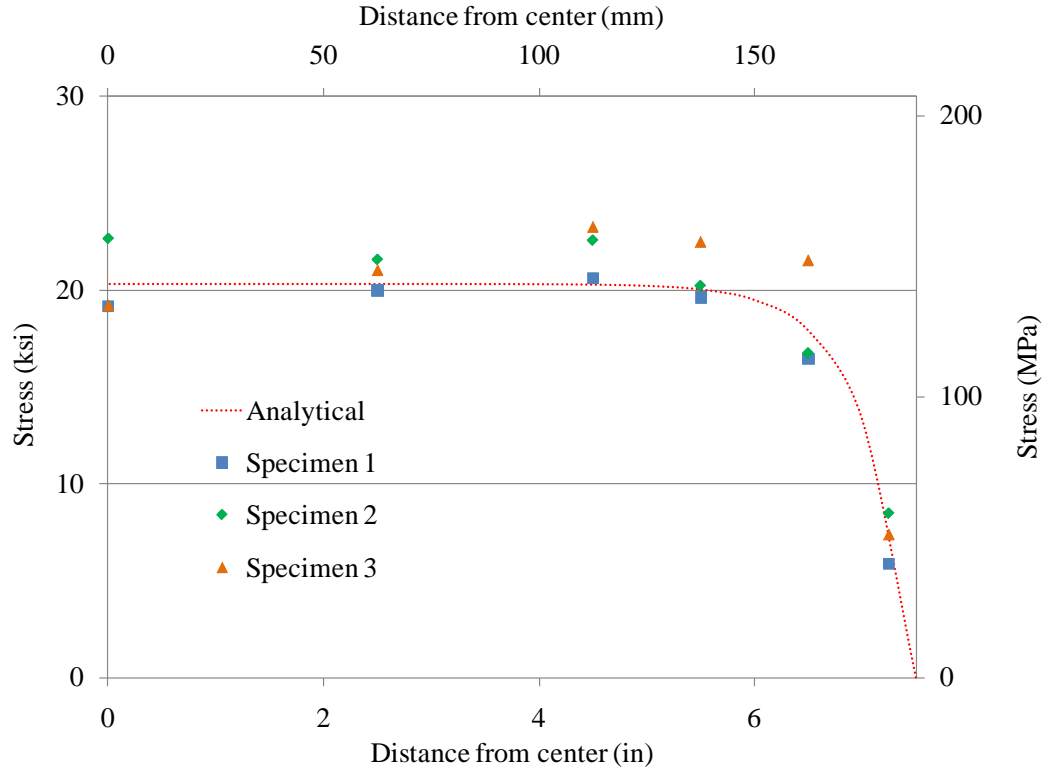


Fig. 3.18: Tensile stress distribution – NM specimens at 44.5 kN (10 kip)

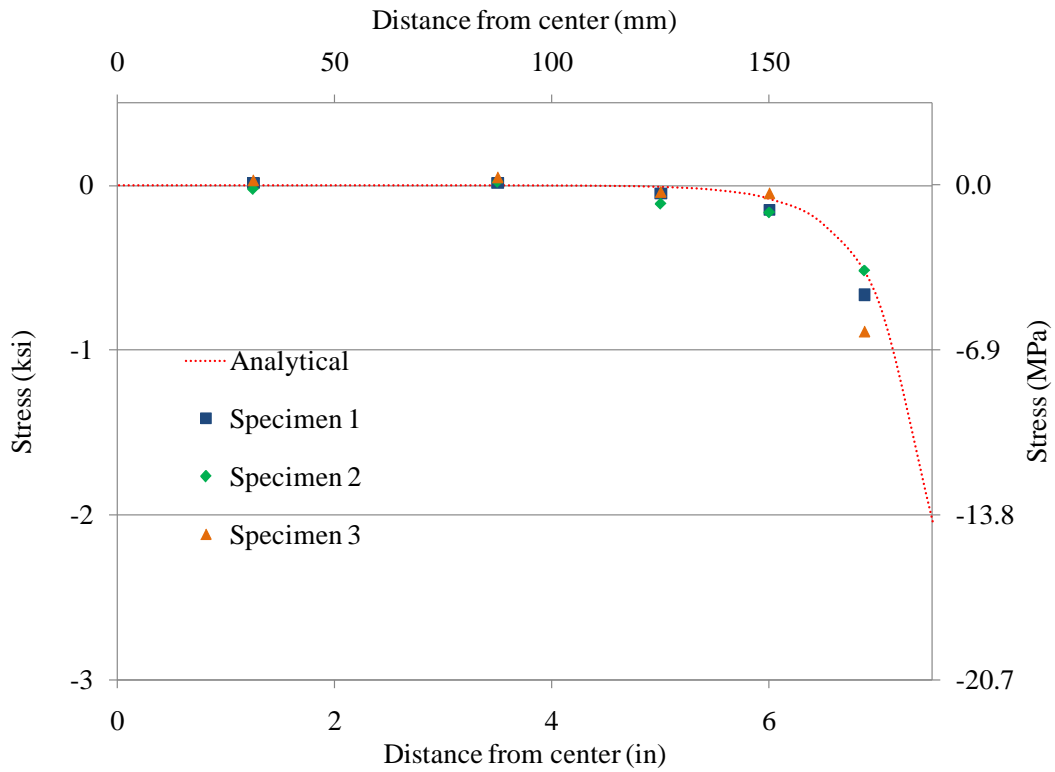


Fig. 3.19: Shear stress distribution - NM specimens at 44.5 kN (10 kip)

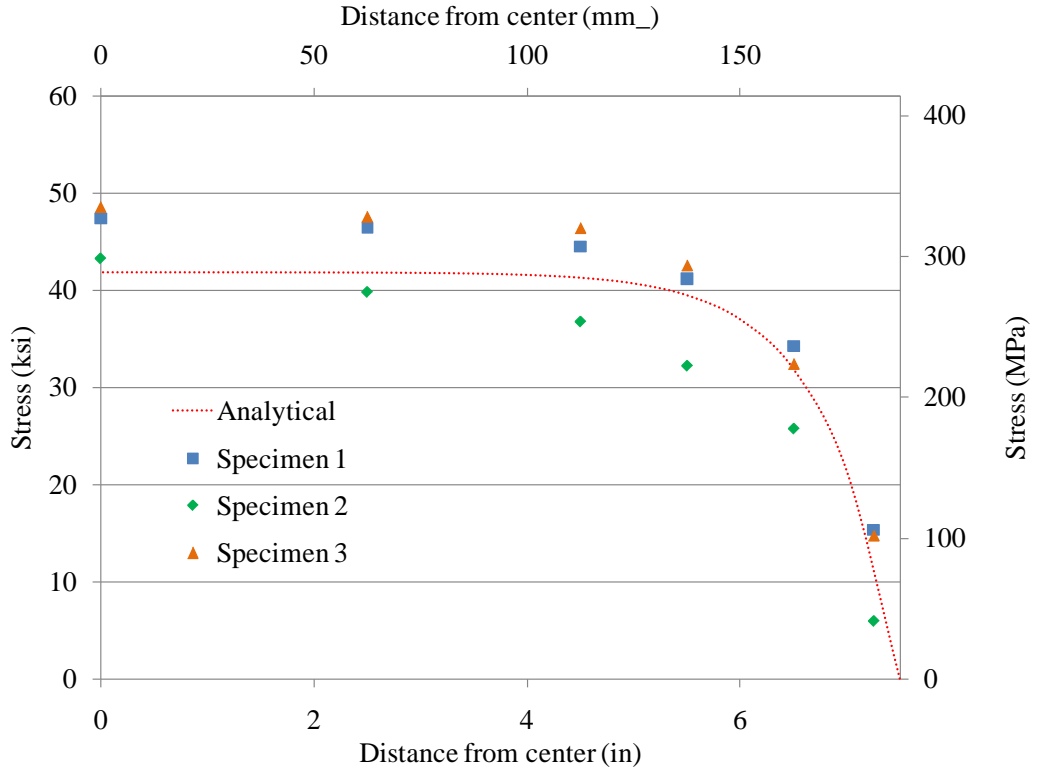


Fig. 3.20: Tensile stress distribution – UHM specimens at 44.5 kN (10 kip)

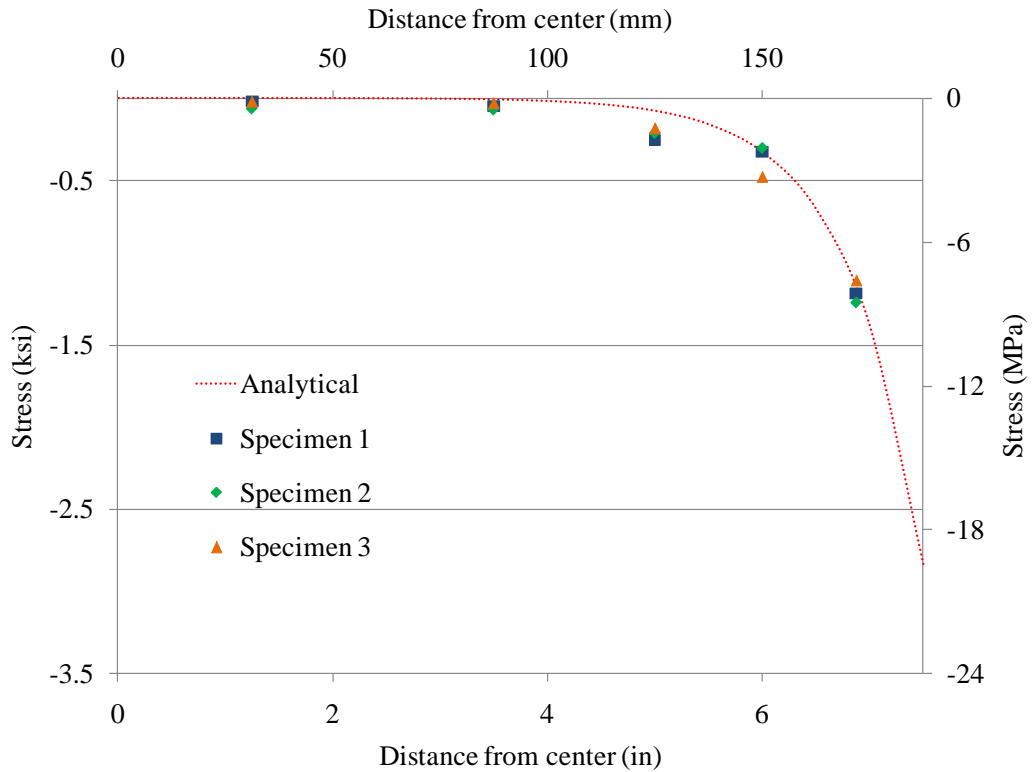


Fig. 3.21: Shear stress distribution - UHM specimens at 44.5 kN (10 kip)

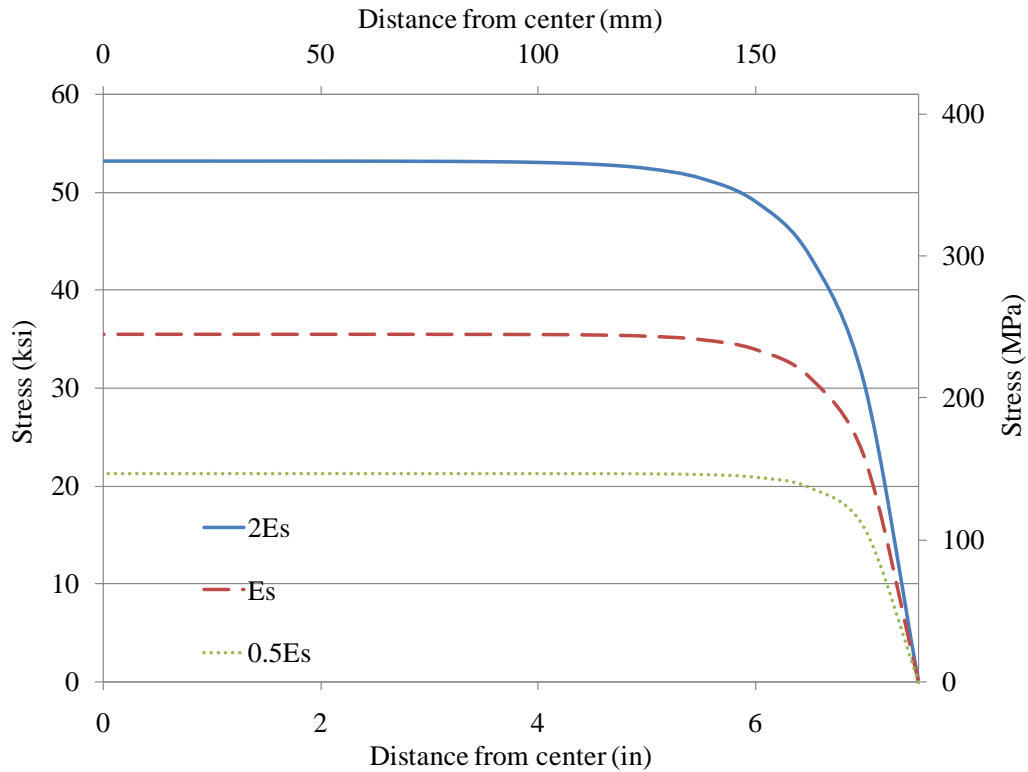


Fig. 3.22: Tensile stress distribution variation due to outer adherend modulus

The effect of the outer adherend modulus on the shear stress distribution is shown in Fig. 3.23. Similar to the tensile stress distribution, the shear stress at the laminate edge is seen to be greater for the higher modulus laminates. The shear stresses are also seen to be higher for a longer distance away from the laminate edge, a fact found earlier where the development length for ultra high modulus laminates were found to be longer than the normal modulus laminates. The effect of the adhesive epoxy thickness was also evaluated, but within the region of adhesive thickness typically recommended for use with CFRP in civil engineering strengthening applications, which is less than 2 mm (0.08 in) (Schnerch et al. 2007). The effect was found not to be significant for a given laminate modulus.

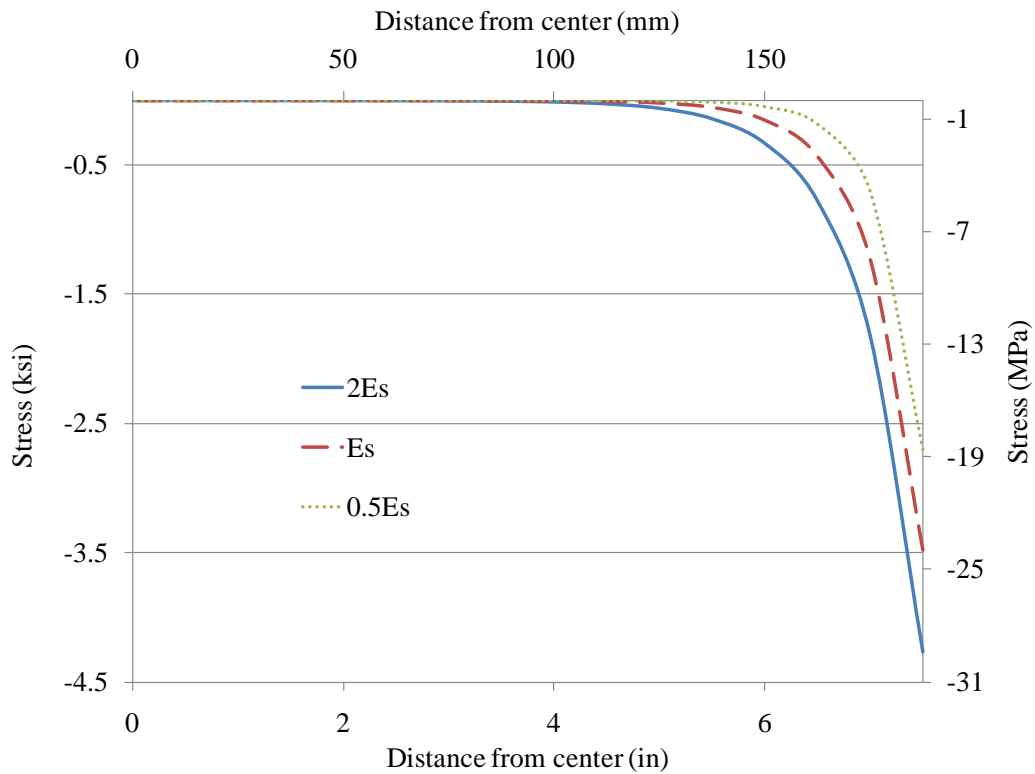


Fig. 3.23: Shear stress distribution variation due to outer adherend modulus

3.3.2 Finite Element Analysis

Similar to the double strap joint, a finite element model representing the doubly reinforced steel plate specimens were developed to analyze the specimen under different loads, various materials, and geometries. The model was built and analyzed using the finite element software ANSYS (ANSYS 2009) and was calibrated using the laboratory test strain data obtained from the mounted strain gages. As the doubly reinforced steel plate specimens were symmetric across three mutually perpendicular axes, only an eighth of the specimen was modeled similar to the double strap joint.

3.3.2.1 *Element Selection*

The double strap joint model developed earlier using 8-node SOLID45 elements was modified to represent the doubly reinforced steel plate specimen. The epoxy adhesive layer thickness was increased to represent the average thickness of the doubly reinforced steel plate specimen adhesive thickness, and CFRP layer width was increased to represent half the width of the laminates in the actual specimens (12.5 mm/ 0.5 in). The boundary conditions were adjusted to remove the ‘gap’ in the double strap joint and to represent a continuous steel plate.

3.3.2.2 *Material Models*

The material properties were the same as for the double strap joint model. The steel plate was modeled as having bi-linear elastic-perfectly plastic steel material model with yield strength of 409.7 MPa (59.4 ksi). A linear stress-strain relationship was taken for both of the CFRP materials with an ultimate strength of 2979 MPa (432 ksi) for the normal modulus CFRP and 1923 MPa (279 ksi) for the ultra high modulus CFRP. The tensile modulus for the laminates were also set at 187 GPa (27017 ksi) for the normal modulus and 514 GPa (74586 ksi) for the ultra high modulus CFRP. The epoxy adhesive was modeled as having a linear stress-strain distribution until it reaches the tensile strength of 34.5 MPa (5.0 ksi) with a tensile modulus of 3007 GPa (436 ksi). Similar to the double strap joint analysis, the Von Mises failure criterion, available for the material model, was used to predict the failure of the epoxy.

3.3.2.3 *Analysis and Results*

The Newton-Raphson procedure was used to solve the nonlinear equations with the Arc-Length method employed to improve convergence. Load increments were automated and handled by the ANSYS solution algorithm. The tensile stress data were obtained along the bond line and compared with calculated stresses, which were determined from physical testing. The stress along the bond center line for normal modulus CFRP doubly reinforced steel plate is given in Fig. 3.24 and Fig. 3.25 for loads of 22.2 kN (5 kip) and 44.5 kN (10 kip). Analogous results are shown for the ultra high modulus CFRP specimens in Fig. 3.26 and Fig. 3.27. The finite element analysis results are seen to be in good agreement with the analytical and experimental data for the normal modulus CFRP strengthened steel plates. The finite element analysis predicted tensile stress for the ultra high modulus CFRP laminate, similar to the analytical results, is seen to be less than the calculated stresses from the experimental strain readings. Further specimen testing will be required to evaluate if this phenomenon is to be seen in all ultra high modulus laminates. Small compressive stresses were also observed on the top surface at the extreme edge of both types of laminate in the finite element analysis, possibly due to the occurrence of peel stresses at the edges.

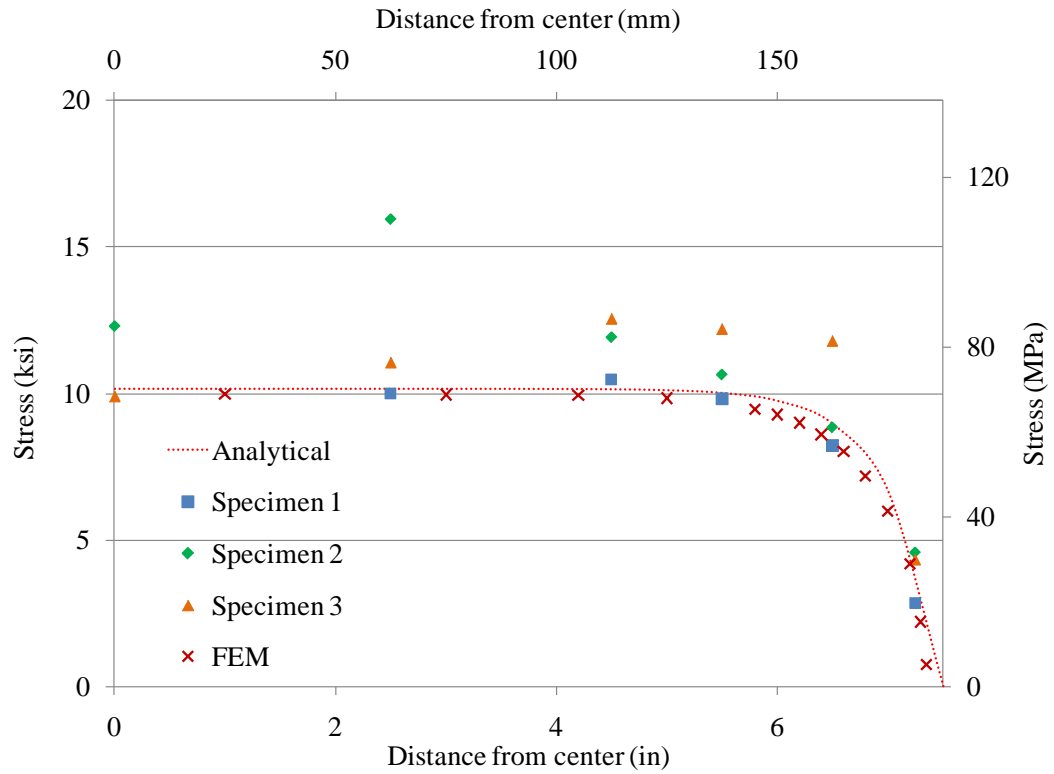


Fig. 3.24: FEA and experimental results for NM laminate tensile stress – 22.2 kN (5 kip)

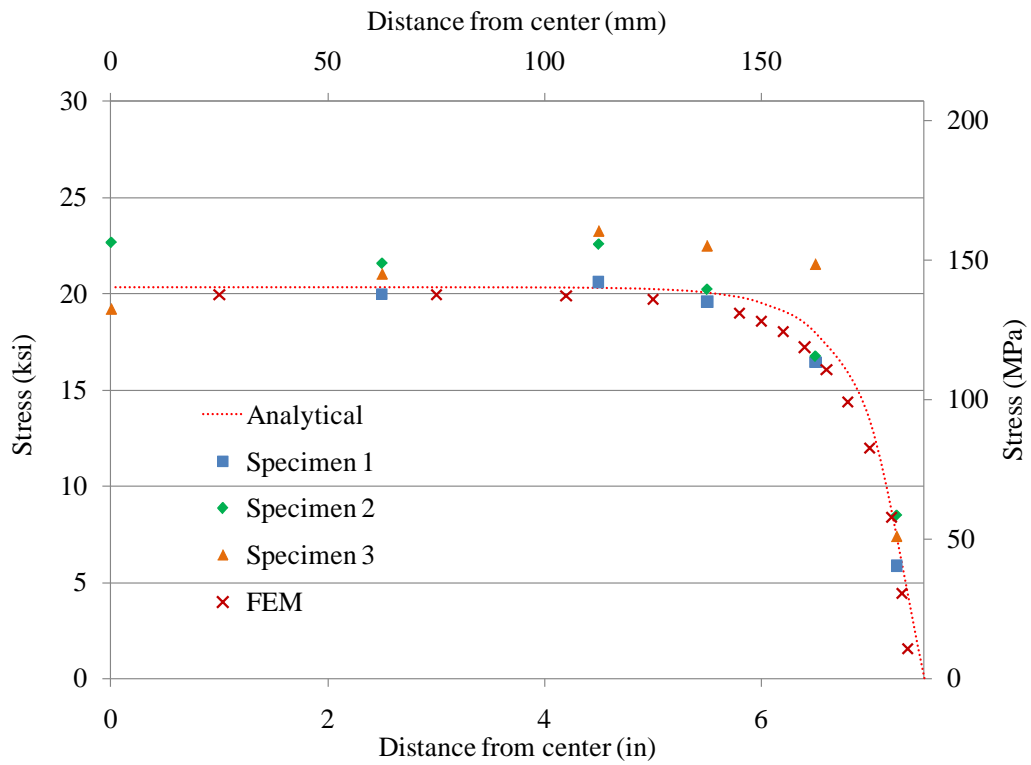


Fig. 3.25: FEA and experimental results for NM laminate tensile stress – 44.5 kN (10 kip)

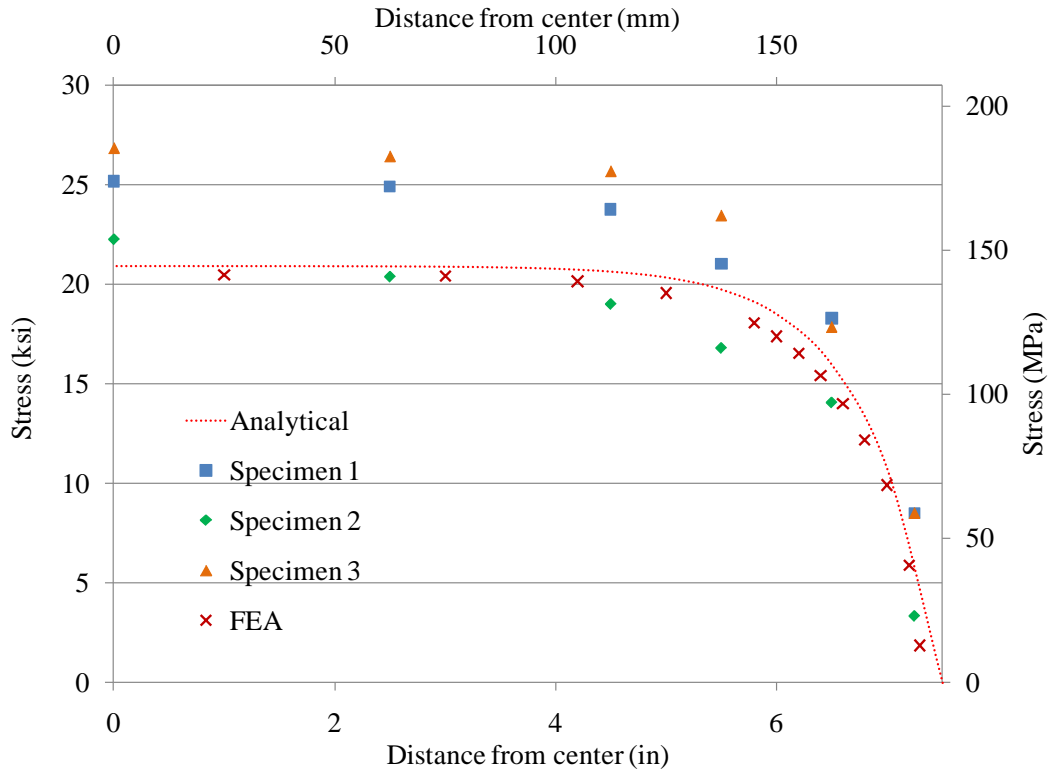


Fig. 3.26: FEA and experimental results for UHM laminate tensile stress – 22.2 kN (5 kip)

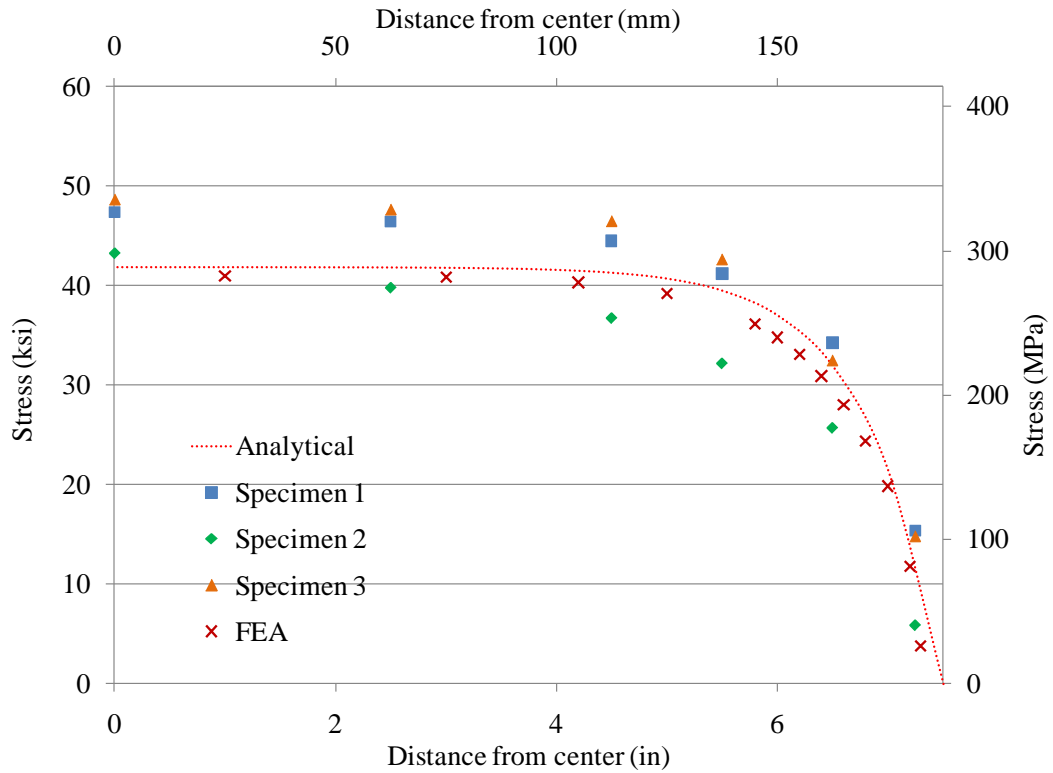


Fig. 3.27: FEA and experimental results for UHM laminate tensile stress – 44.5 kN (10 kip)

The shear stress distribution for the normal modulus CFRP doubly reinforced steel plate is shown in Fig. 3.28, the analogous plot for ultra high modulus CFRP is given in Fig. 3.29. The shear stress at both the center and the edge of the specimen for the adhesive-laminate interface are also shown. The reason for the increasing shear stress at the laminate edge in the analytical model is due to the assumptions made in derivation, where the interfacial shear stress is assumed to be constant across the adhesive thickness. In the finite element analysis, a sudden decrease in shear stress is observed in both types of laminates near the location of the stress singularity; a phenomenon which has been observed in previous analyses performed by Teng and Zhang (2005) and also by Al-Emrani and Kligler (2006).

While the shear stress along the longitudinal edge of the laminate is seen to be slightly higher than the stress along the center, both stress distributions are seen to be low compared to the experimental and analytical solutions. A more refined finite element model is thought to be able to more accurately capture the end shear stresses. The analytical as well as the calculated experimental shear strains are derived assuming plane stress conditions, as the stress is seen to vary along the width of the laminate, it is possible that the method of evaluating shear stresses requires further investigation when the bonded laminate width is smaller than the steel plate.

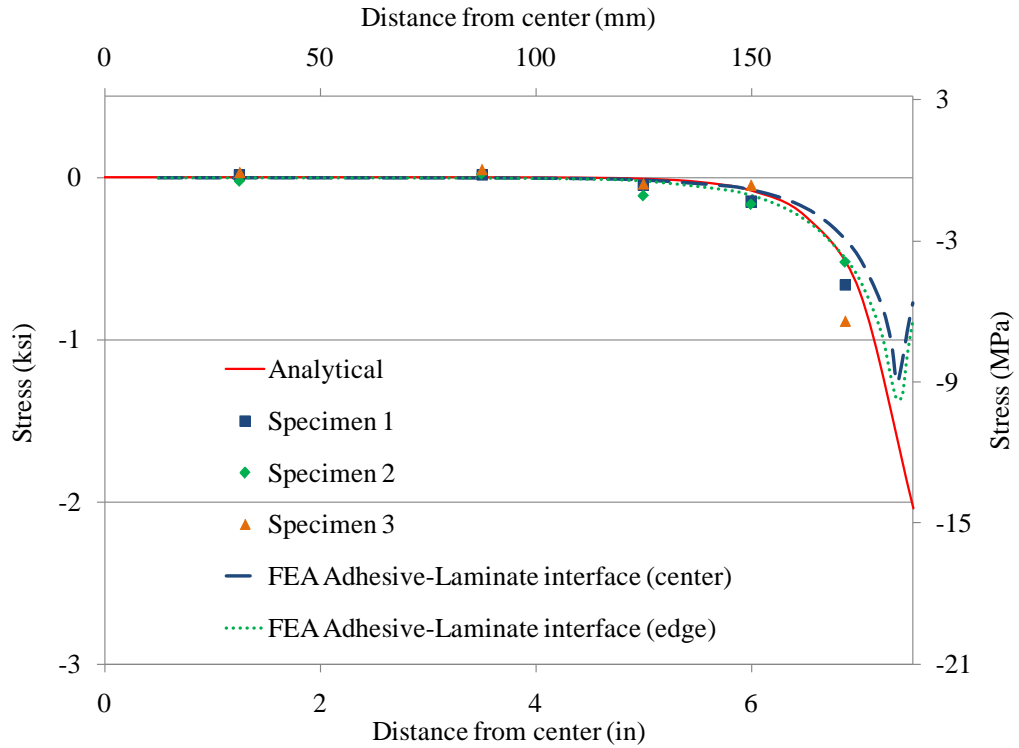


Fig. 3.28: FEA and experimental results for NM laminate shear stress – 44.5 kN (10 kip)

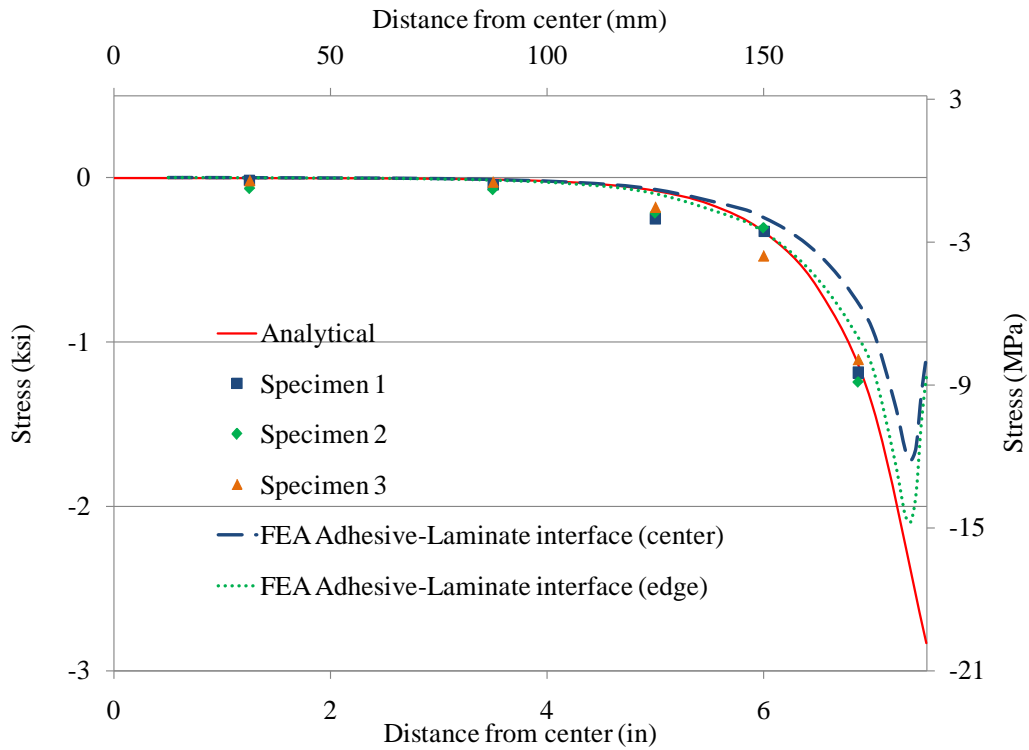


Fig. 3.29: FEA and experimental results for UHM laminate shear stress – 44.5 kN (10 kip)

The shear stress distribution just before failure in the normal modulus doubly reinforced finite element model is shown in Fig. 3.30. Although the doubly reinforced steel plate specimens failed in debonding between the steel and adhesive interface, the shear stresses were not seen to reach the average experimental shear strength of 27 MPa (3.9 ksi). The failure of the specimens was predicted using the Von Mises failure criteria in the finite element analysis, similar to the double strap joints.

The initial Von Mises failure stress seen in the normal modulus CFRP laminate doubly reinforced steel plate specimen is shown in Fig. 3.31. The failure is seen to occur at the outside edge close to the laminate and adhesive interface. The predicted failure loads were 57.8 kN (13.0 kip), for the ultra high modulus CFRP laminates and 75.6 kN (17.0 kip) for the normal modulus CFRP laminates. Considering the failure criterion does not consider any plastic deformation of the adhesive epoxy, these compare well with the average experimental failure loads of 65.4 kN (14.7 kip) and 84.5 kN (19.0 kip) recorded for the test specimens for each laminate type, respectively.

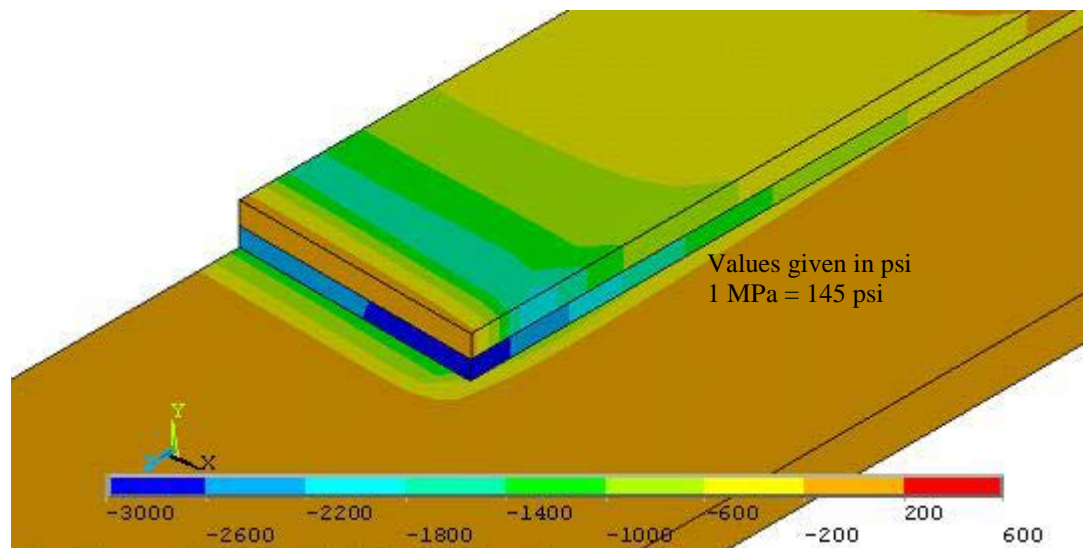


Fig. 3.30: Shear distribution in NM CFRP doubly reinforced steel plate

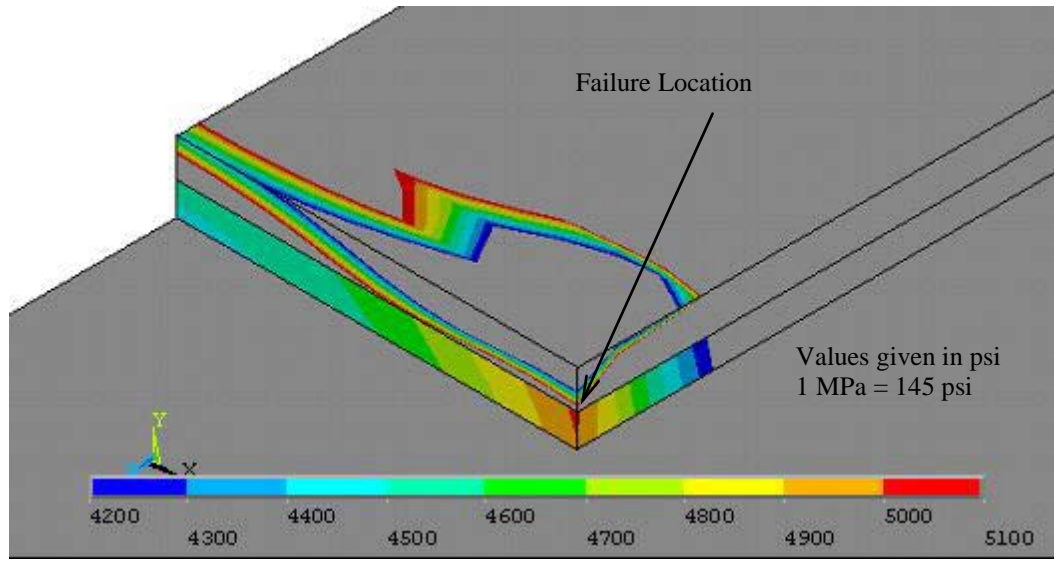


Fig. 3.31: Failure of adhesive layer in NM CFRP doubly reinforced steel plate

3.4 Steel Beams

The analytical study of the steel beams is carried out with derivations found in Smith and Teng (2001). The shear stress within the adhesive are calculated and compared with experimental results. A finite element analysis of the steel beams strengthened with the full width ultra high modulus laminate as well as the 10 mm (0.4 in) wide strip panels is also carried out and a representative model is developed to perform parametric studies.

3.4.1 Analytical Study

Smith and Teng (2001) performed a review of existing closed-form solutions, available for the evaluation of interfacial stresses, for plates bonded to the soffits of beams. They developed a closed-form solution for interfacial stresses which addressed many of the short comings of previous researches. The method proposed by Smith and Teng (2001) is applicable to general load cases, while the expressions for an arbitrarily placed point load, uniformly distributed load and two symmetrically positioned point loads have been specifically provided. The derived shear stress distribution, for four point bending as depicted in Fig. 3.32, is given by the following equation:

$$\tau(x) = \frac{m_2}{\lambda} PL_0 e^{-\lambda x} + m_1 P - m_1 P \cosh(\lambda x) e^{-k} \quad 0 \leq x \leq (b - L_0) \quad (3.9)$$

$$\tau(x) = \frac{m_2}{\lambda} PL_0 e^{-\lambda x} + m_1 P \sinh(k) e^{-\lambda x} \quad (b - L_0) \leq x \leq \left(\frac{L_L}{2}\right) \quad (3.10)$$

Where;

$$\lambda^2 = \frac{G_a b_L}{t_a} \left(\frac{\left(y_b + \frac{t_L}{2}\right) \left(y_b + \frac{t_L}{2} + t_a\right)}{E_B I_B + E_L I_L} + \frac{1}{E_B A_B} + \frac{1}{E_L A_L} \right) \quad (3.11)$$

$$m_1 = \frac{G_a}{t_a \lambda^2} \left(\frac{y_b + \frac{t_L}{2}}{E_B I_B + E_L I_L} \right) \quad (3.12)$$

$$m_2 = \frac{G_a y_b}{t_a E_B I_B} \quad (3.13)$$

$$k = \lambda(b - L_0) \quad (3.14)$$

- τ_a = Adhesive shear stress
- G_a = Adhesive shear modulus
- t_a = Adhesive thickness
- E_L = Laminate Young's modulus
- I_L = Laminate section second moment of area
- t_L = Laminate thickness
- b_L = Laminate width
- E_B = Beam material Young's modulus
- t_B = Beam section second moment of area
- y_b = Distance from centroid to bottom of beam

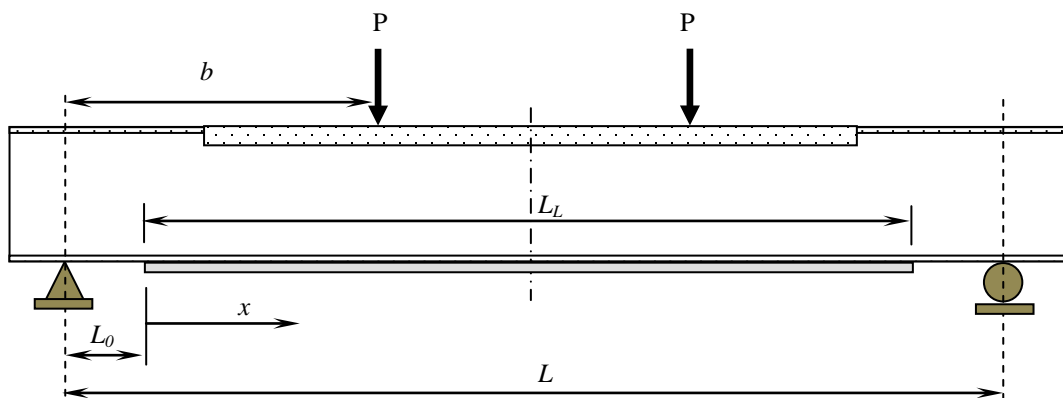


Fig. 3.32: Bonded laminate on beam soffit

The thickness of the epoxy adhesive layer was taken as 1.25 mm (0.05 in). The material properties presented in the previous chapter were used in the analytical study. The second moment of area as well as the location of the centroid for the composite beam and channel section were evaluated from section transformation and used with the Smith and Teng (2001) derivations. The shear stress variation along the bond length obtained from the analytical method is compared with the shear stress values obtained experimentally in Fig. 3.33. The experimental results for three different load levels are seen to agree well with the analytical predictions. The analytical model predicts a shear stress of 15.8 MPa (2.3 ksi) at the edge, upon reaching the laminate ruptured load of 405 kN (91.2 kip). The stress is lower than the experimentally evaluated average shear strength of 27 MPa (3.9 ksi), and no debonding was observed during the experiment. Similar to the doubly reinforced steel plate specimens, the analytical solution over predicts the end shear due to the assumptions made in the derivation. It should also be noted that both the analytical and experimental shear stress derivations assume the beam and laminate have the same width.

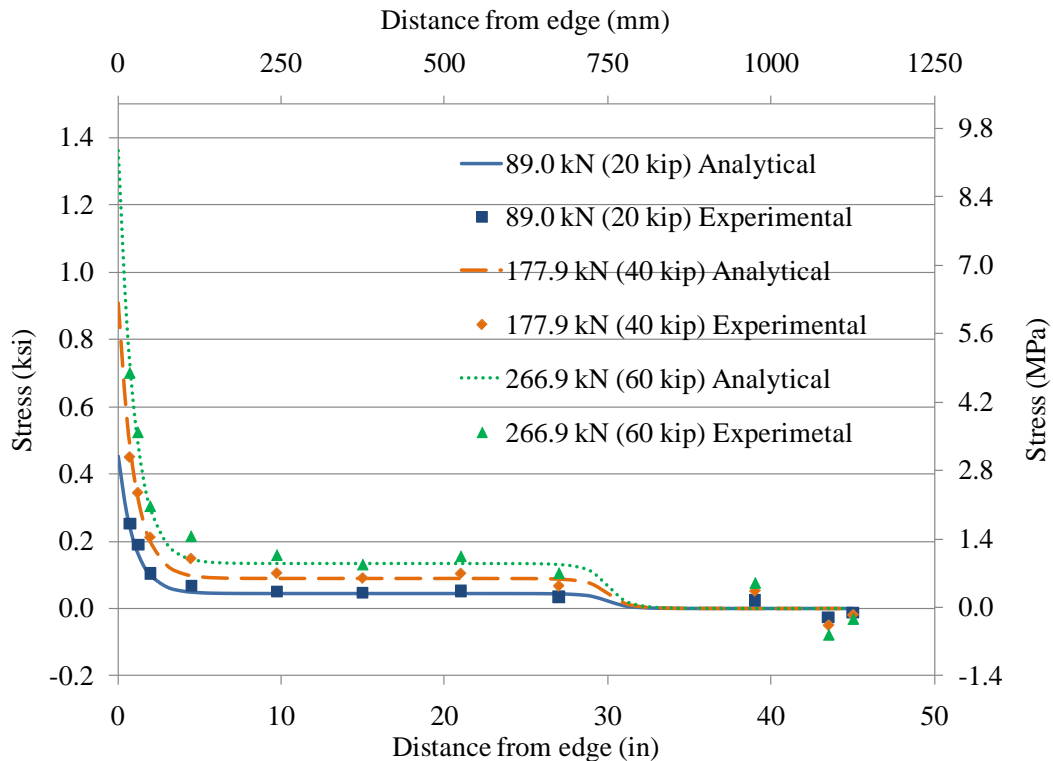


Fig. 3.33: Analytical and experimental shear stress distribution

A parametric study on the effect of laminate modulus on the shear stress distribution was carried out using the Smith and Teng (2001) method. The dimensions of the steel beam were held constant and the modulus of the CFRP laminate was varied from half the modulus of steel ($0.5 E_s$) to three times the modulus of steel ($3E_s$). The results for an applied load of 266.7 kN (60 kip) are shown in Fig. 3.34. It is seen that the shear stress at the laminate edge becomes critical in designing strengthening applications with ultra high modulus CFRP laminates due to the increase in shear stress, with the increase in tensile modulus.

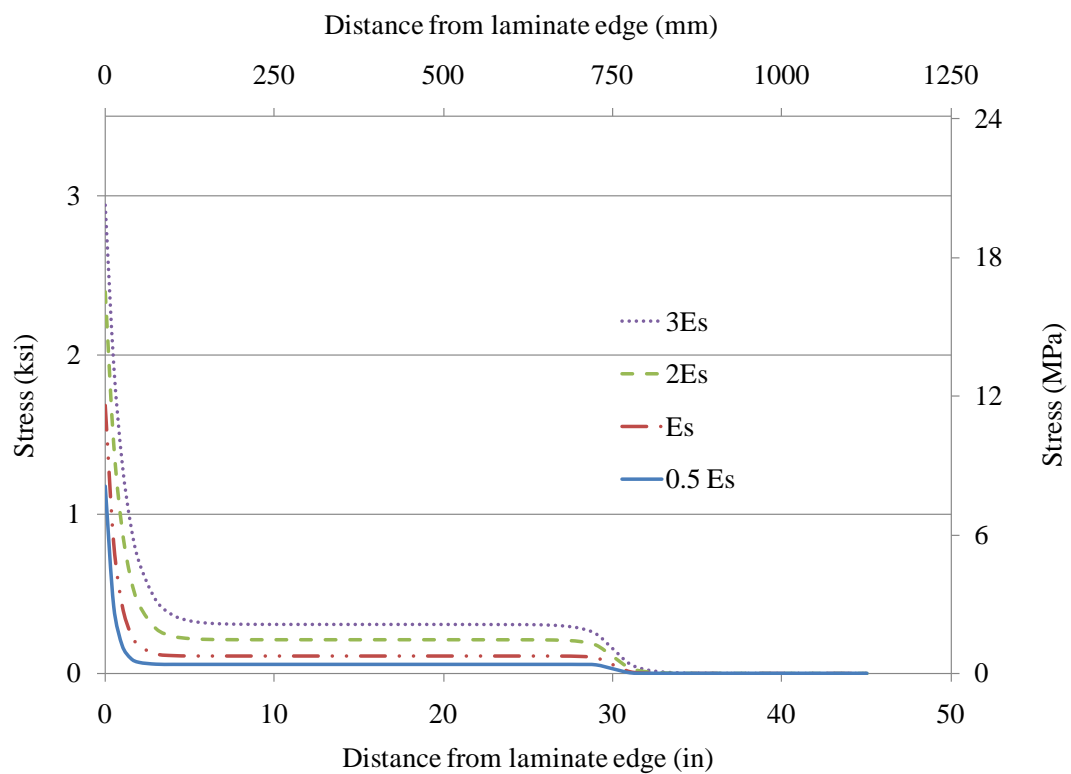


Fig. 3.34: Shear stress variation with tensile modulus of laminate

3.4.2 Finite Element Analysis

Finite element models representing the strengthened steel beams were developed to analyze the specimens under different loads, material properties and geometries. The models were built and analyzed using the finite element software ANSYS (ANSYS 2009) and were calibrated using the strain and deflection data obtained during the laboratory testing.

3.4.2.1 *Element Selection*

Bonds in the double strap joint as well as the doubly reinforced steel plate were modeled using 8-node SOLID45 elements. However, since the number of elements required to model the beam would present enormous computational costs, shell elements were used in modeling the beam models. The beam and channel section were built up using 4-node SHELL181 elements. The element has six degrees of freedom at each node; three translations and three rotations in the three mutually perpendicular x, y, and z axis. The element has the capability to be modified to depict the applied ultra high modulus CFRP laminates by changing the element characteristics to represent layered construction. Each layer can be assigned a thickness, material properties, and a number of integration points through the thickness separately. Although the control beam and the beam strengthened with the full width laminate were symmetric in construction, the whole beam was modeled since the strip panel strengthened beams were not symmetric. Only the 10 mm (0.4 in) strip panel strengthened beam was modeled; the 5 mm (0.2 in) smaller strip panel required smaller element sizes, requiring a prohibitively large numbers of nodes and elements. The results are also expected to be similar to the 10 mm (0.4 in) strip panel.

Several simplifying assumptions have been made in the SHELL181 element construction. The through thickness stress is always zero (ANSYS, 2009). The calculation of interlaminar shear in the SHELL181 element is based on unidirectional, uncoupled bending in each direction (ANSYS, 2009). Due to the simplified assumptions in the calculation of interlaminar shear stresses, the shear stresses at the laminate edges were

not expected to be accurate in the built up beam model. While debonding was not an issue with the full width strengthened beam, to overcome the limitations of the shell element model, a separate finite element model was created with SOLID45 elements to replicate the behavior at the finger joint in the strip panel strengthened beam model.

3.4.2.2 *Material Models*

The steel beam was modeled with a bi-linear steel material model with yield strength of 407 MPa (59 ksi). The channel section steel also had a similar material model with a yield strength of 414 MPa (60 ksi). The tensile modulus for both beam and channel steel was taken as 200 GPa (29000 ksi). A tangent modulus of 4.8 GPa (700 ksi) was used between yield and ultimate stresses for both steel models. A linear stress-strain relationship was taken for the CFRP material with an ultimate strength of 1923 MPa (279 ksi) and a tensile modulus of 514 GPa (74500 ksi) for the ultra high modulus CFRP. The epoxy adhesive was modeled as having a linear stress-strain distribution, with a tensile strength of 34.5 MPa (5.0 ksi) and tensile modulus of 3007 GPa (436 ksi).

3.4.2.3 *Analysis and Results*

Similar to the previous finite element analyses, the Newton-Raphson procedure was used to solve the nonlinear equations with the Arc-Length method employed to improve convergence. Load increments were automated and handled by the ANSYS solution algorithm. The displacement at mid-span as well as strain reading along the length of the beam were evaluated through the finite element analysis and compared with the experimental data. The beam model developed for the analysis is shown in Fig. 3.35.

A fine element mesh was used close to the laminate edges as well as at mid-span for the evaluation of the stresses in the finger joint of the strip panel models. The bottom flange of the beam was also created with a fine mesh to assist in the modeling of the CFRP strip

panels. The loading was applied along a line on the top flange, while simple support boundary conditions were set for the nodes at the support locations.

The load displacement relationship obtained from the analysis is plotted against the experimental readings for the control beam in Fig. 3.36. The experimental load-deflection relation for all tested beams exhibits small amounts of curvature at small strains, which as discussed in Chapter 2, is attributed to settlement of the reaction frame. The load-deflection data for the full width strip strengthened beam as well as the 10 mm (0.4 in) strip panel strengthened beam are given in Fig. 3.37 and Fig. 3.38. The finite element model predicted control beam load-deflection relation is also plotted for comparison.

The finite element analysis load-deflection data are seen to agree well with the experimental data, considering the non-linear nature of the test data. The analysis curves for both the full width laminate as well as the 10 mm (0.4 in) strip panel strengthened beams are found to be very similar with the strip panel having a slightly higher stiffness. The full width strengthened beam failed by reaching the maximum tensile stress in the laminate at 440 kN (99 kip), whereas the laboratory test failed with initial fiber rupture at 404 kN (91 kip). The strip panel finite element model did not predict the failure of the beam, in tensile or shear failure of the bond, or tensile failure of the laminate, even up to an applied load of 400 kN (90 kip). This is attributed to the simplified assumptions in the calculation of interlaminar shear stresses in the SHELL181.

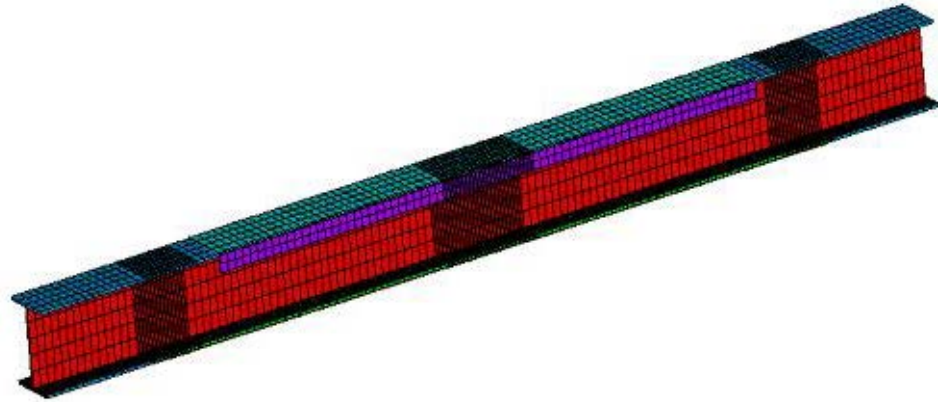


Fig. 3.35: Finite element beam model

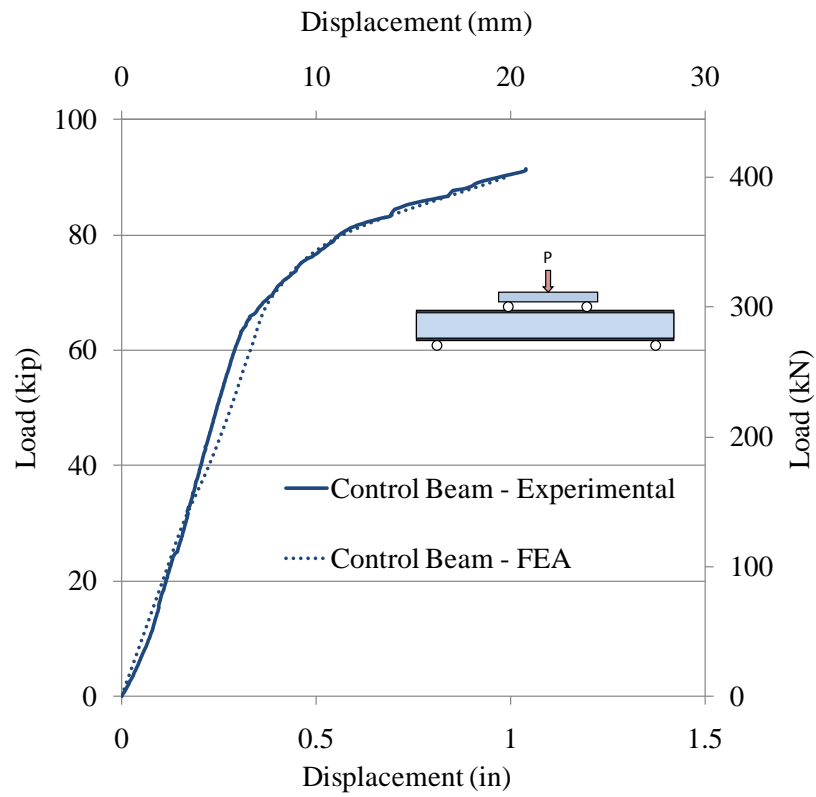


Fig. 3.36: Load deflection relation for control beam

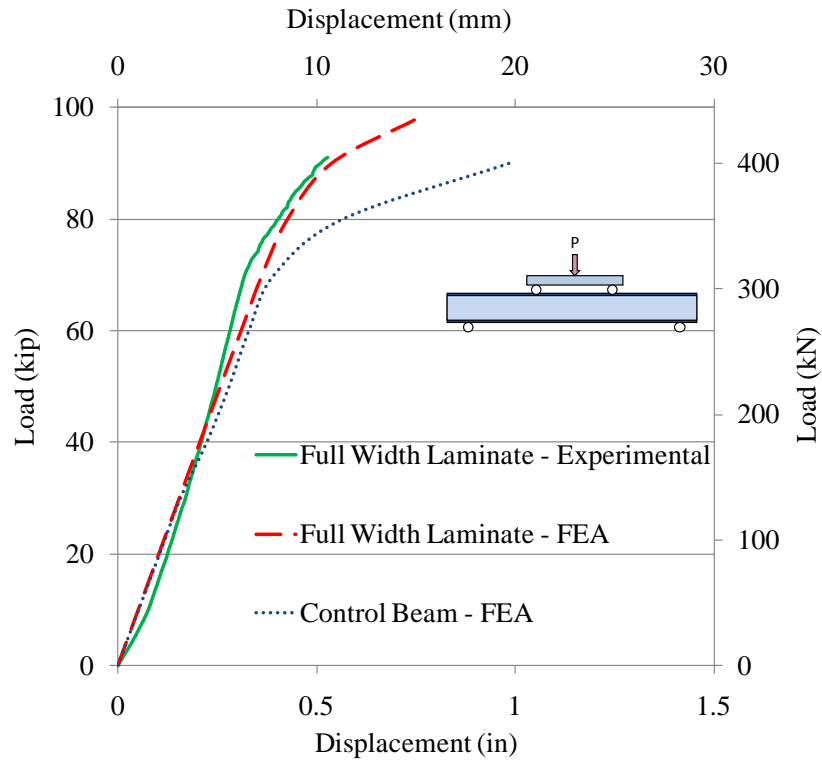


Fig. 3.37: Load deflection relation for full width laminate strengthened beam

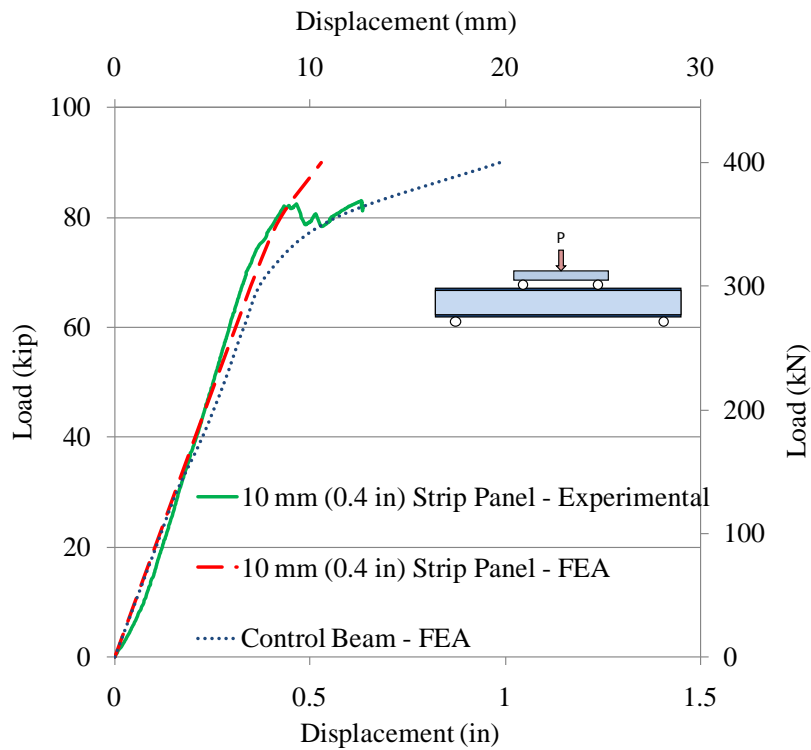


Fig. 3.38: Load deflection relation for 10 mm (0.4 in) strip panel strengthened beam

The recorded strain readings for each beam are compared with the finite element analysis predicted readings for the control beam in Fig. 3.39, the full width laminate strengthened beam in Fig. 3.40, and the 10 mm (0.4 in) strip panel strengthened beam in Fig. 3.41. The strains at 177.9 kN (40 kip) and 311.4 kN (70 kip) load are presented, depicting loads before and after the yielding of the steel beam.

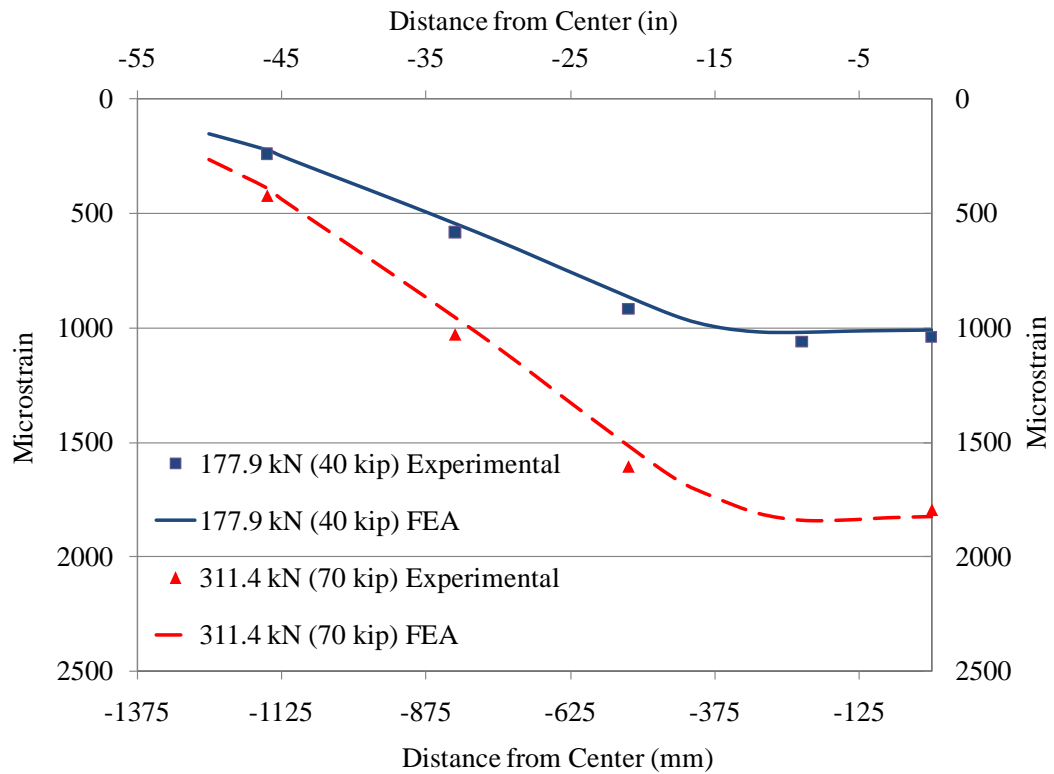


Fig. 3.39: Strain distribution in control beam

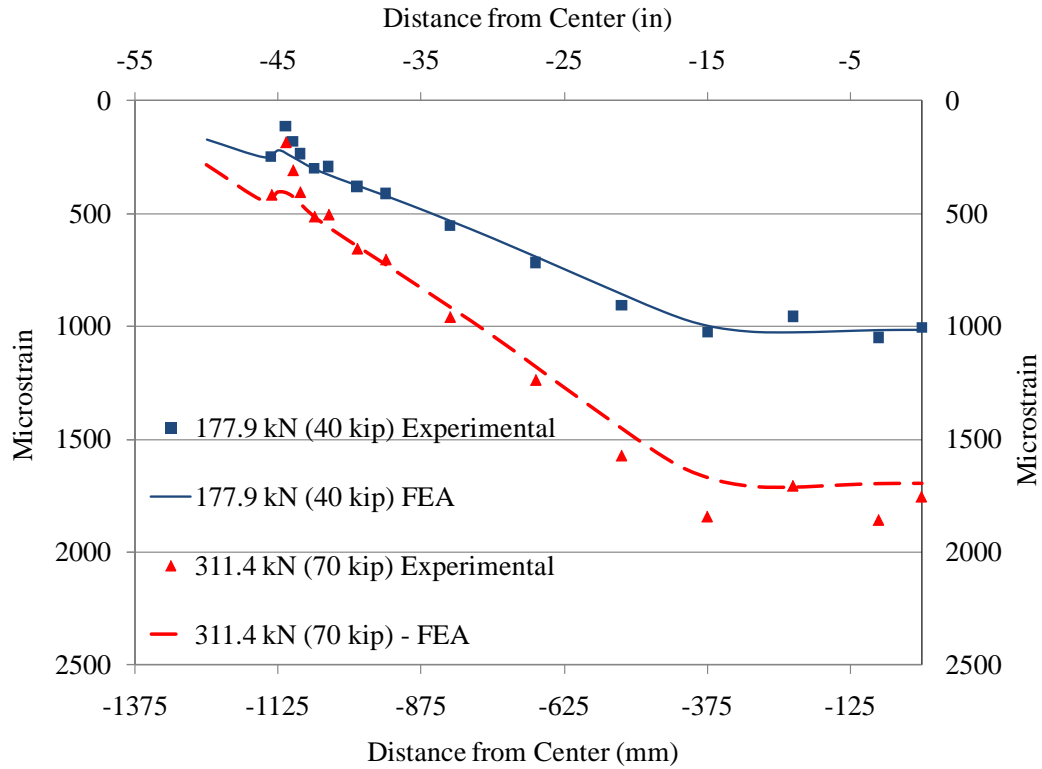


Fig. 3.40: Strain distribution in full width laminate strengthened beam

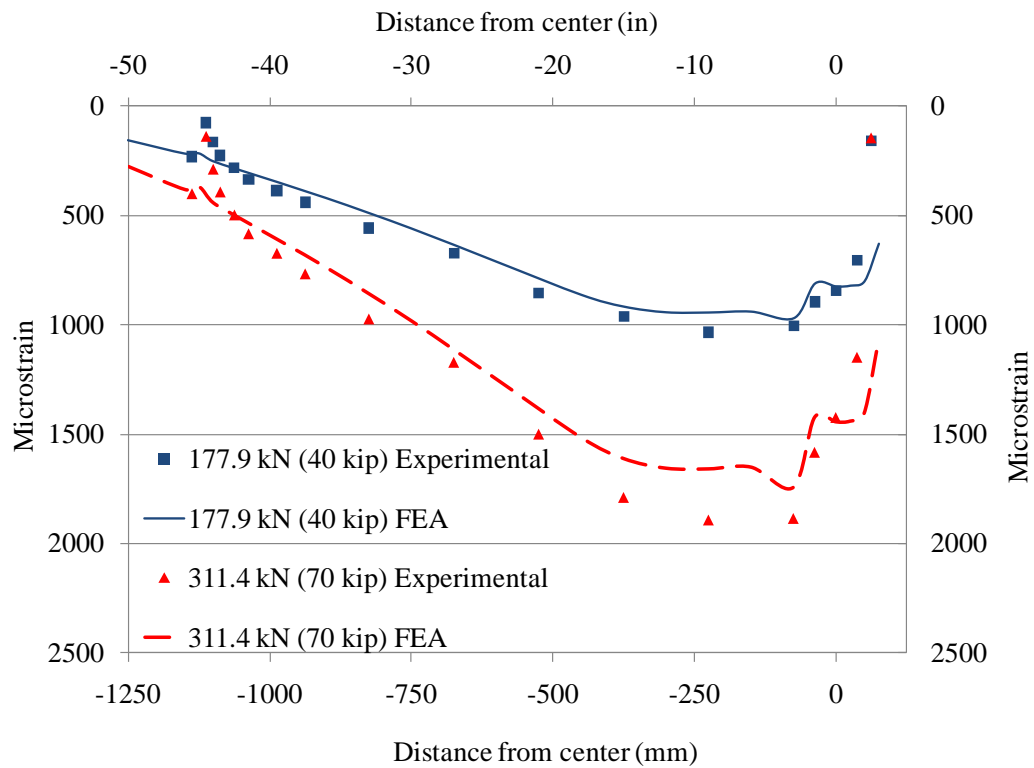


Fig. 3.41: Strain distribution in 10 mm (0.4 in) strip panel strengthened beam

The finite element model predicted strains along the beam are seen to provide reasonably accurate values when compared with the experimental strain readings. The experimental strains are consistently seen to be slightly higher than the finite element strains in all the beams. While the overall predictions are found to agree well with the experimental results, the strains close to the laminate edges are seen to be quite different. This again is due to the simplifying assumptions in the shell element formulation.

While the full width laminate strengthened beam failed in rupture and not in debonding, from inspection of the stresses on the laminate, it is seen that the failure could have easily occurred through edge debonding. The stress at the laminate edge just before failure in rupture as shown in Fig.3.42, is seen to exceed 331 MPa (48 ksi) approximately 50 mm (2 in) from the laminate edge, and within the development length of the laminate. This was identified as the stress at failure of the bond, where the Von Mises stress would exceed the yield strength of the adhesive. However, as it was found in the doubly reinforced steel plate specimens, the actual failure is seen to be higher than conservatively predicted by the Von Mises failure criterion.

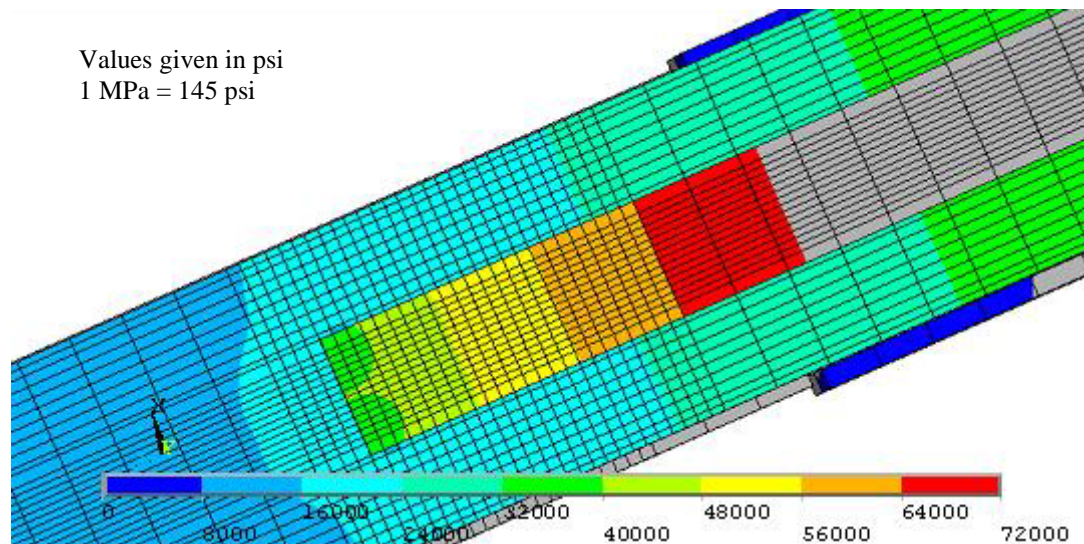


Fig. 3.42: Tensile stress distribution in laminate edge at failure

As the strip panel strengthened beams were observed to physically undergo debonding of the laminates at mid-span, it was important for the finite element model to be able to predict the same debonding failure. The interlaminar shear stresses between the adhesive and the laminate at an applied load of 311.4 kN (70 kip) are shown in Fig. 3.43. The maximum shear stresses are seen to be much smaller than the experimentally evaluated maximum stress of 22.8 MPa (3.3 ksi). While this was understood to be due to the simplified assumptions in the laminated shell element formulation, to obtain a better representation of the joint in the strip panel, a model of the joint was built up using SOLID45 elements. The strip panel joint model was 300 mm (12 in) in length, and was developed, considering symmetry, to represent half of the beam.

As the beam is under four-point bending, it is taken that the tensile stress within the constant moment region is uniform. Although a slight drop in stress is observed between the locations just underneath the load points up to mid-span of the beam, the stresses are found to be fairly even along the length of the laminate between the two load points, from both experimental and analytical data. The observed tensile stress in the constant moment region was applied as loading to the strip panel joint model. The tensile stresses at 311.4 kN (70 kip) load in the layered shell element built up beam are shown in Fig. 3.44. The same stresses observed in the strip panel finger joint model are shown in Fig. 3.45.

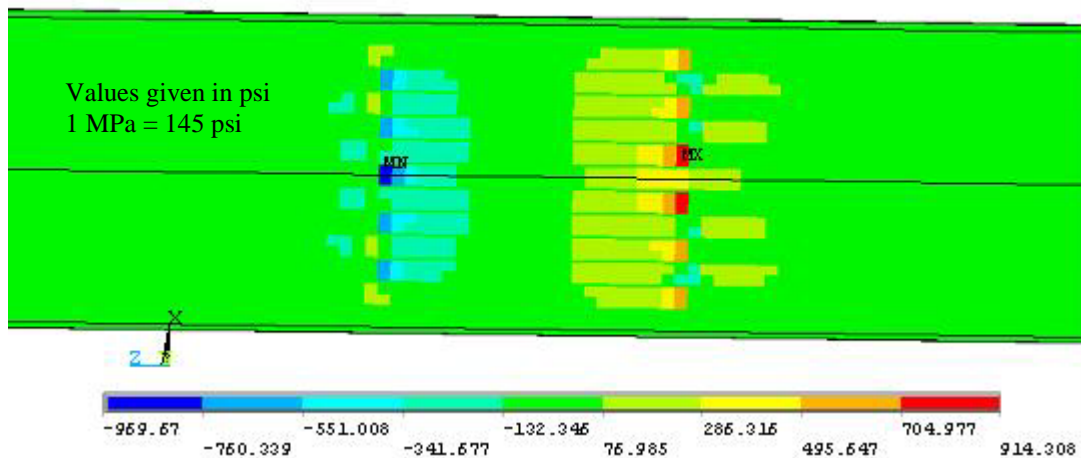


Fig. 3.43: Shear stresses at the strip panel joint with layered shell elements

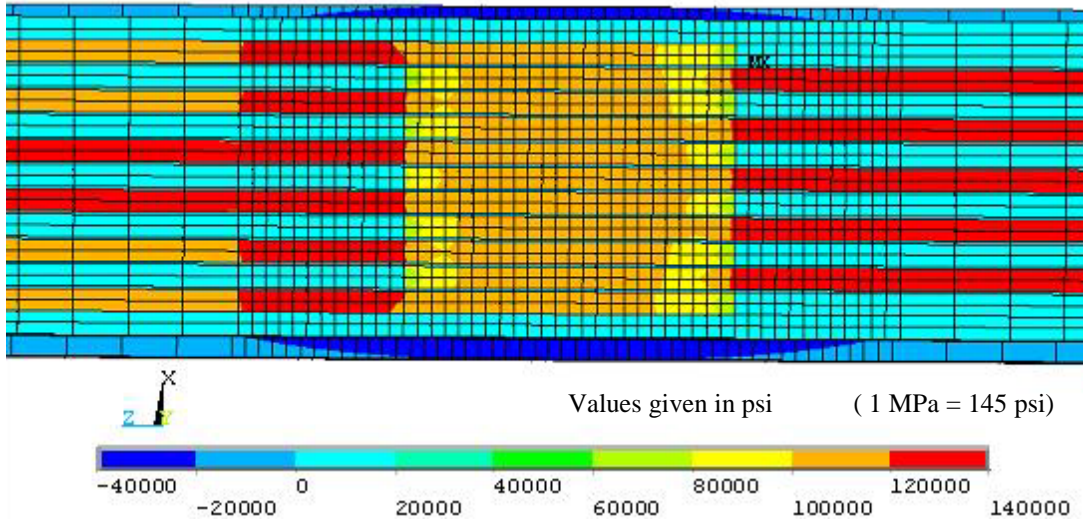


Fig. 3.44: Tensile stresses at the strip panel joint at 311.4 kN (70 kip)

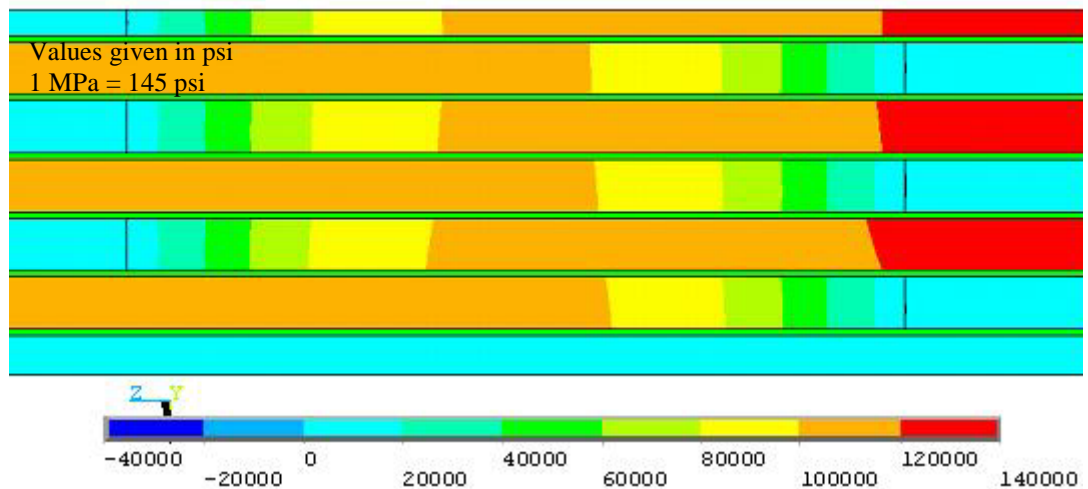


Fig. 3.45: Tensile stresses in the strip panel finger joint model to match beam stresses

Unlike the layered shell element model, the development of stresses in each 10 mm (0.4 in) strip of CRFP is visible in the solid element ‘sub’ model. The shear stresses evaluated from the experimental strain reading are compared with the predicted values from the finite element models in Fig. 3.46. The stresses obtained from the strip panel finger joint model are added to the existing layered shell element beam model predicted stresses to obtain a better representation of the actual conditions.

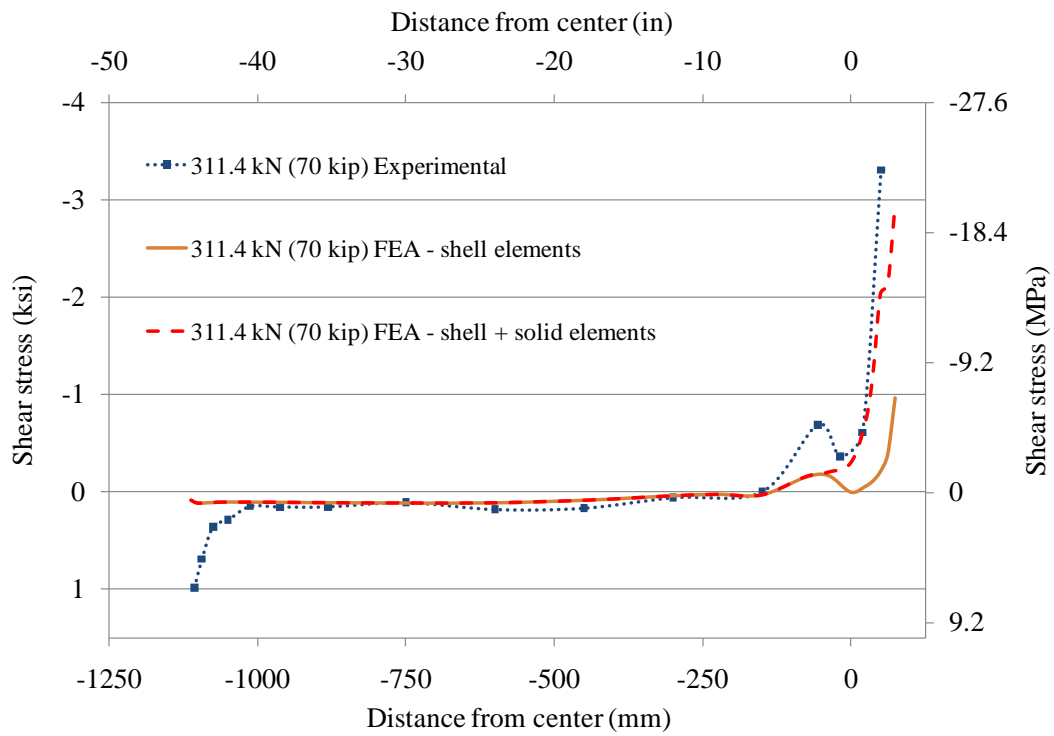


Fig. 3.46: Shear stress distribution in the 10 mm (0.4 in) strip panel

CHAPTER 4

PRELIMINARY ANALYSIS AND LOAD RATING OF KY 32 BRIDGE

4.1 Introduction

In order to investigate the effectiveness of strengthening steel-concrete composite bridges with ultra high modulus CFRP laminates, it was deemed beneficial that field testing be performed on an active bridge before and after retrofit. The candidate bridge, provided by the Kentucky Transportation Cabinet, was the KY 32 Bridge over Lytles creek in Scott County, Kentucky. Details of the bridge are presented, followed by a simple beam analysis as well as a finite element beam analysis performed to evaluate the most efficient method of retrofit. A load rating of the bridge is also carried out and summarized here with additional details provided in Appendix B.

4.2 KY 32 Bridge

The bridge over Lytles Creek, on state route 32, located in Scott County KY (referred to as the KY 32 Bridge) is a single span steel girder bridge (Fig. 4.1). The bridge is 6.96 m (22.8 ft) wide, and has a deck length of 6.71 m (22 ft). The reinforced concrete bridge deck is supported on five W14x30 steel girders and was cast non-composite with the girders. While theoretically the bridge is considered simply supported, the steel girders were embedded in concrete diaphragms at the abutments (Fig. 4.1(c)), which were cast integral with the deck. The concrete deck had also been cast such that the top flanges of the steel girders were embedded. The dimensions of the bridge in plan and section as well as the dimensions of the W14x30 steel section are shown in Fig. 4.2. The application of ultra high modulus CFRP laminates was expected to increase the load carrying capacity and eliminate the need for the 124.6 kN (14 ton) load posting on the KY 32 Bridge.



(a) Side view

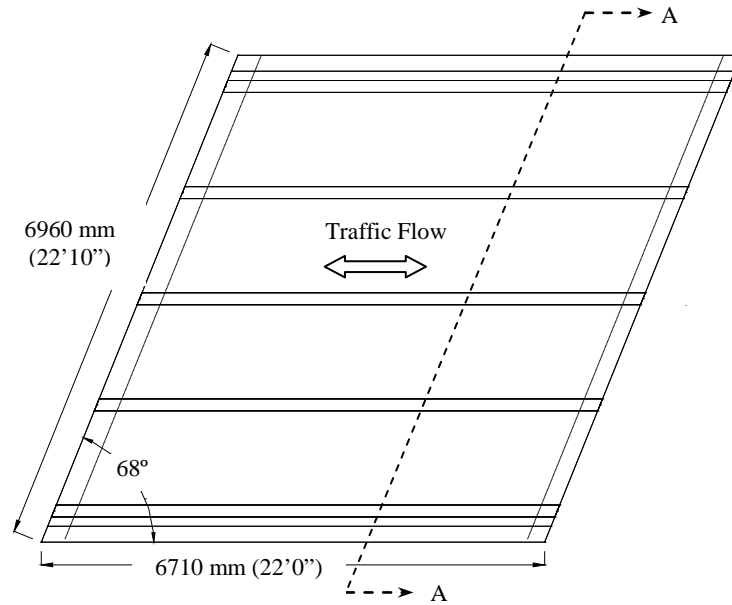


(b) View from roadway

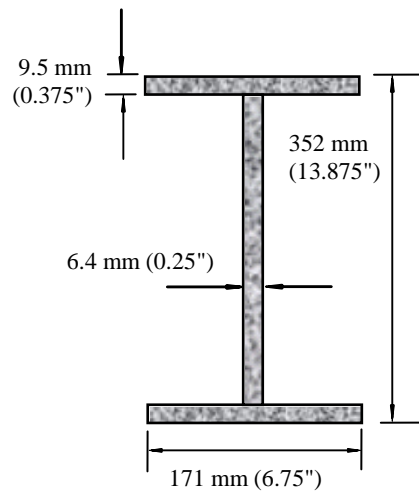


(c) Underneath the deck

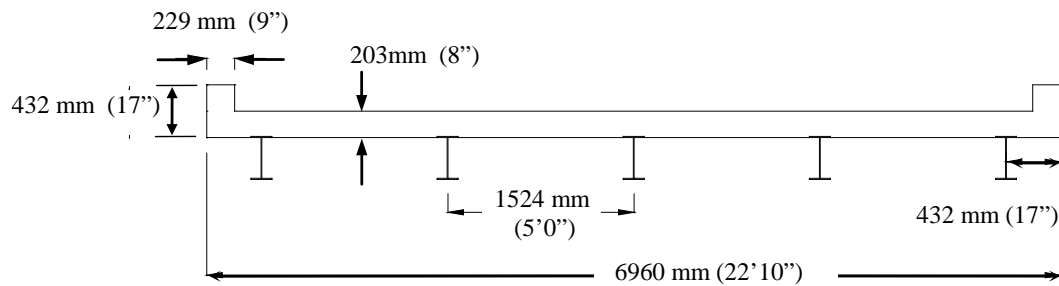
Fig. 4.1: KY 32 over Lytles Creek Bridge in Scott County, KY



Plan view of bridge



W14x30^c Steel section



Section A-A of bridge

Fig. 4.2: Layout of KY32 Bridge

4.3 Simple Beam Analysis

A simple beam analysis was carried out on a simply supported non-composite girder, with similar cross section and material properties to the beams in the KY 32 bridge. The beam was loaded at mid span to represent half the rear axle load of a truck. The analysis revealed that the live load deflection would govern the retrofit design. Furthermore, applying up to 4 mm (0.16 in) thick laminates to the tension flange, 50 mm (4 in) wide, would not increase the load carrying capacity to the expected 89 kN (20 kip) or half of the AASHTO HS-25 truck rear axle weight of 178 kN (40 kip). Although an increase in load carrying capacity of over 20% could be achieved with the 4 mm (0.16 in) thick laminates, due to the low section modulus of the non-composite beam, the increase was insufficient to reduce deflections and did not utilize the laminates effectively due to the low strains along the bottom flange. Complete details of the analysis can be found in Appendix B.

In order to maximize the laminates tensile capacity it was found that some degree of composite action between the girder and the concrete deck had to be established. A moment-curvature analysis was carried out assuming the concrete deck to be fully composite with the steel girders. Whitney's stress block (Whitney 1942) was assumed for the concrete compressive stress distribution and the tensile strength of concrete was not considered. While the controlling parameter was still the live load deflection, the analysis revealed that a fully composite single girder could carry 89 kN (20 kip) or half the AASHTO HS-25 rear axle load even without laminate strengthening. The application of laminates was seen to further increase the load carrying capacity by 15% for the 4mm (0.16 in) thick laminates. Further details of the composite beam analysis can be found in Appendix B. In order to achieve more efficient use of the laminate, post installation of shear studs was considered as a means to obtain some degree of composite action between the concrete deck and steel girders.

4.4 Post Installed Shear Studs

Post installation of shear studs was considered as a means of achieving the required degree of composite action. Recent research carried out at the University of Texas at Austin in collaboration with the Texas Department of Transportation has examined the possibility of achieving composite action through post-installed shear studs to connect the existing deck to the steel girders (Kwon et al. 2007, Kwon 2008). Several methods of installing shear studs were studied by Kwon (2008) and three methods were selected for experimental and analytical evaluation: double-nut bolt, high tension friction grip bolt, and adhesive anchor. The research concluded that using a partial composite design deploying 30 to 50% of the studs typically required for a full composite design, a 40 to 50% increase in load carrying capacity could be achieved. Due to the better fatigue performance of post-installed shear connectors as compared to the American Association of State Highway and Transportation Officials (AASHTO) curve for conventional welded shear studs (Kwon et al. 2010), fatigue is not thought to control the stud requirement as in the case of welded studs. Kwon et al. (2009) field tested each of the three selected post-installed shear stud systems on each span of a 3-span bridge in the San Antonio District of Texas and were successful in developing a significant amount of composite action in the girders.

In order to minimize traffic disruption and construction costs, it was determined that the post installed shear studs for the KY 32 Bridge should be inserted through the top flange of the steel girder into holes filled with adhesive epoxy (referred to as Adhesive Anchor Shear Studs) in the concrete deck in a manner similar to the adhesive anchor method used by Kwon et al. (2009). An AASHTO shear stud requirement calculation as per the AASHTO *Standard Specifications for Highway Bridges* (AASHTO 2002) revealed the shear stud requirement of 21 studs per half span for a fully composite design when neglecting the reduction factor (refer to Appendix B). A finite element analysis (FEA) was performed using the commercial FEA software ANSYS (2009) to evaluate several different shear stud distributions, in order to obtain a satisfactory shear stud spacing requirement to achieve a minimum load rating of HS25 from the retrofit process.

4.5 Finite Element Beam Analysis of Shear Stud Distribution

4.5.1 Element Selection

A simply supported girder was modeled and subjected to a patch load at mid-span. The same wide flange section used in the KY 32 bridge was taken as the beam section for the analysis and was built up using 4-node SHELL181 elements available in the FEA software ANSYS (2009). The element has six degrees of freedom at each node; three translations and three rotations in the three mutually perpendicular x, y, and z axis.

The concrete deck was modeled using the 8-node SOLID185 element. Each element has three translational degrees of freedom in the nodal x, y, and z directions. The element type also has large deflection and large strain capabilities. The 203 mm (8 in) deck was modeled using 3 layers of SOLID185 elements, with the layer boundaries corresponding to the reinforcing bar mat location. The effective deck width modeled in the analysis was 1524 mm (60 in).

The two node LINK8 truss element was used to model the reinforcing steel bars. The LINK8 element is a uniaxial tension-compression element with three translational degrees of freedom at each node. The LINK8 elements were modeled to represent ASTM #4 bars, 12.7 mm (0.5 in.) in diameter, in both the longitudinal and transverse directions. The reinforcing bars on the top and bottom mats spaced 305 mm (12 in.) in both directions.

The shear studs were modeled using the two node BEAM4 element which is a uniaxial element with tension, compression and flexural capabilities. Each element has six degrees of freedom at each node, three translational and three rotational degrees of freedom in the x, y, and z axis. Some researchers have used connector/spring type elements to model shear stud with specified load-slip relations (Kwon 2008) to represent the slip at the steel-concrete interface when under flexure. In this preliminary analysis load-slip is not considered since the beam type elements are expected to provide sufficiently accurate

results. ASTM A193 B7 threaded rods of 19 mm (0.75 in) diameter were assumed as the post installed shear studs, which were modeled using the BEAM4 elements.

4.5.2 Material Models

The girder steel was taken as having a yield strength of 345 MPa (50 ksi). The reinforcing bar steel was assumed to have a yield strength of 414 MPa (60 ksi) while the shear studs were modeled to have a yield strength of 724 MPa (105 ksi) to represent ASTM A193 B7 steel. All steel was modeled to have a bi-linear stress-strain relation with an elastic modulus of 200 GPa (29000 ksi). A small tangent modulus beyond yielding was employed to ensure stability of the analysis.

The deck concrete strength was taken as having an ultimate compressive strength (f'_c) of 24.1 MPa (3.5 ksi). A multi-linear stress-strain material model was used for the concrete to represent a modified Hognestad (1951) stress-strain relationship. The tensile strength was taken as $0.1\sqrt{f'_c}$.

4.5.3 Analysis and Results

Several shear stud layouts were analyzed using the developed finite element models. In the case of the non-composite girder, only the steel girder was modeled and the concrete deck was not modeled. Instead, the weight of the concrete was distributed along the length. For the partially composite girder analysis, as seen in Fig. 4.3, the concrete deck was modeled and the elements for the shear studs were inserted in accordance with the stud layout. The stud requirement for the AASHTO fully composite girder included a total of 42 shear studs per girder (without considering the reduction factor) at 21 locations (2 studs per location) at 305 mm (12 in./ 1 ft.) pitch equally spaced along the girder (referred as AASHTO-1ft).

A shear connector ratio (the ratio of shear connectors installed to the number of shear connectors required for fully composite design) of 33%, or a total of 14 studs per girder at 7 locations, was also evaluated, with most of the studs being concentrated near the abutments. The stud spacing was 305 mm (12 in. /1ft.) for the first two studs and 610 mm (24 in. /2 ft.) for the next and then 2134 mm (84 in. /7ft.) to the stud at mid-span (referred as Composite 1-1-2-7ft). A significant increase in stiffness resulted with an increased ultimate load carrying capacity of approximately 85% at yielding of the bottom flange, over the non-composite girder.

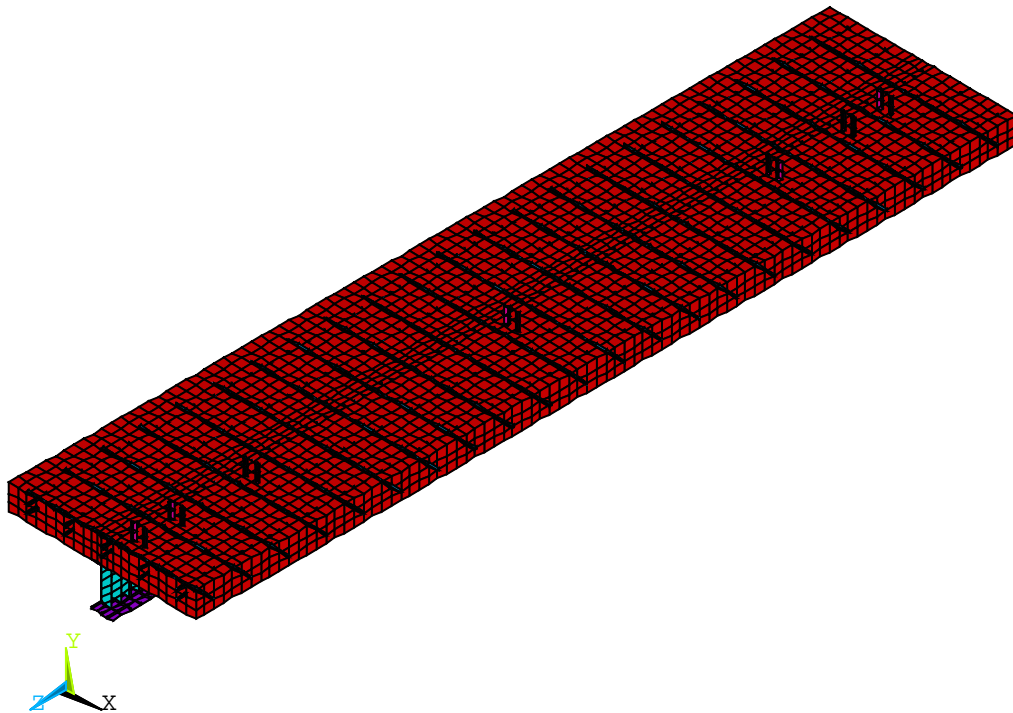


Fig. 4.3: FEA model for Composite 1-1-2-7ft stud spacing girder

The previous research by Kwon et al. (2009) also recommended increasing the number of studs than what would be required from a theoretical strength standpoint for adhesive anchor shear studs due to their low fatigue performance when compared with the other two methods of post installing shear studs. Considering the fatigue performance and also the shear force distribution along the length of the bridge especially at ultimate loads a

more conservative number of studs was considered and the distribution varied with more studs concentrated close to the abutments (referred as Composite 0.5-1-1-1.5-2-2-1.5-1.5ft). This was the selected stud distribution for the field testing, which included a total of 30 studs per girder providing a shear connector ratio of 71% of the AASHTO fully composite girder. The load deflection plots for the selected distribution, the AASHTO fully composite distribution, the composite 1-1-2-7 ft distribution, and the non composite girder are shown in Fig. 4.4.

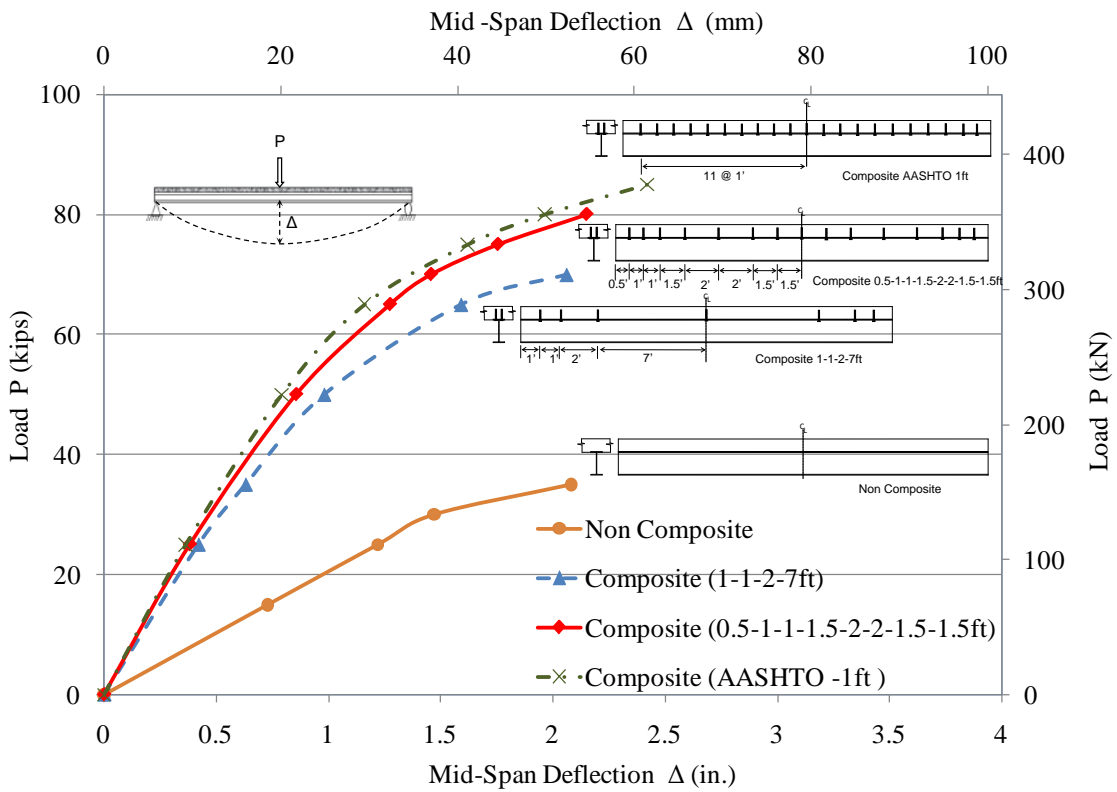


Fig. 4.4: Load-deflection curves for different shear stud layouts

It was clear from the analysis that even with only 33% of the AASHTO fully composite shear stud requirement (Composite 1-1-2-7ft shear stud layout) the load carrying capacity could be nearly doubled, while the selected shear stud layout for field application provide more than a 120% increase in load carrying capacity. All three shear stud layouts also achieved a load carrying capacity of 89 kN (20 kips) or half of the AASHTO HS25 truck

rear axle load at the AASHTO serviceability requirement of $L/800$, or 8.4 mm (0.33 in.) in maximum deflection.

4.6 Load Rating of KY 32 Bridge

In order to evaluate the capacity of the KY 32 Bridge, before and after shear stud installation, a load rating was performed according to the load factor method in the *AASHTO Manual for Condition Evaluation of Bridges* (AASHTO 2003) for different truck types. The truck types were selected as typical trucks traversing the bridge with different axle combinations and positions. The selected truck types with their respective axle weight, wheel spacing and axle spacing are shown in Table 4.1. Due to the short span of the bridge, the rear axle placed at mid-span of a typical beam was seen to create the largest displacements. Further details on the axle placement on the KY 32 Bridge deck are given in Appendix B.

The rating factor (RF) is found using the equation given below:

$$RF = \frac{C - A_1 D}{A_2 L (1 + I)} \quad (4.1)$$

where;

RF = Rating Factor for the live-load carrying capacity.

C = Capacity of member

D = Dead load effect on member

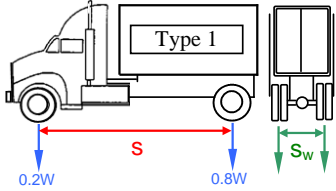
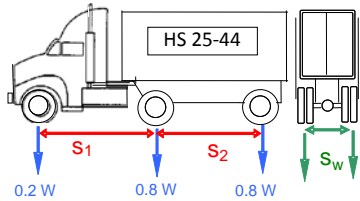
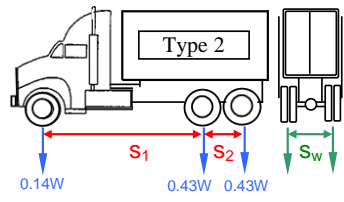
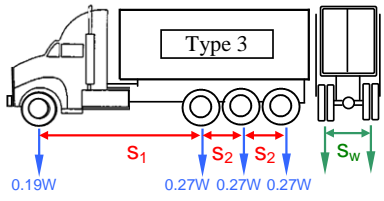
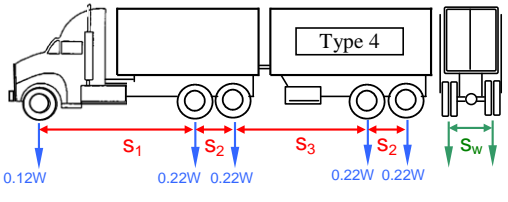
L = Live load effect on member

I = Impact factor to be used with the live load effect

A_1 = Factor for dead loads

A_2 = Factor for live loads

Table 4.1: Different Truck Types for Load Rating

Truck Type	Truck Information		
	Gross Vehicle Weight W	Axle Spacing S	Wheel Spacing S_w
	178 kN (40,000 lbs)	$s = 4.27 \text{ m}$ ($s = 14\text{'-}0\text{'}$)	1.83 m (6'-0")
	400 kN (90,000 lbs)	$s_1 = 4.27 \text{ m}$ ($s_1 = 14\text{'-}0\text{'}$) $s_2 = 4.27\text{-}9.14 \text{ m}$ ($s_2 = 14\text{'-}0\text{'-}30\text{'-}0\text{'}$)	1.83 m (6'-0")
	252 kN (56,700 lbs)	$s_1 = 3.66 \text{ m}$ ($s_1 = 12\text{'-}0\text{'}$) $s_2 = 1.22 \text{ m}$ ($s_2 = 4\text{'-}0\text{'}$)	1.83 m (6'-0")
	327 kN (73,500 lbs)	$s_1 = 3.66 \text{ m}$ ($s_1 = 12\text{'-}0\text{'}$) $s_2 = 1.22 \text{ m}$ ($s_2 = 4\text{'-}0\text{'}$)	1.83 m (6'-0")
	356 kN (80,000 lbs)	$s_1 = 3.66 \text{ m}$ ($s_1 = 12\text{'-}0\text{'}$) $s_2 = 1.22 \text{ m}$ ($s_2 = 4\text{'-}0\text{'}$) $s_3 = 4.27 \text{ m}$ ($s_3 = 14\text{'-}0\text{'}$)	1.83 m (6'-0")

The rating factor should be found for both strength criterion and serviceability criterion. AASHTO Design Specifications 10.57.1 stipulate that the maximum stress under overloaded conditions should be limited to $0.8F_y$ for non-composite sections and $0.95F_y$ for composite sections. Since the girders are only expected to be partially composite, the steel stress is conservatively limited to $f_s \leq 0.8F_y$.

For AASHTO H and HS loadings, the overload is defined as the un-factored dead load (D) + $5(1+I)/3$ times the live load (L).

The rating factor is then multiplied by the rating vehicle in kN/tons to give the rating of the structure.

$$RT = (RF) W \quad (4.2)$$

Where;

RT = bridge member rating in tons

W = weight (kN/tons) of nominal truck used in determining the live load effect

The load rating for the KY 32 Bridge before retrofit assigned an Inventory level rating for serviceability of 11.4 tons for a Type 1 Truck. Details of the load rating analysis for different truck types with various axle orientations are given in Appendix B.

While AASHTO specifications do not include provisions for partially composite girder design, AISC LRFD specifications (AISC 2005) use plastic sectional analysis to evaluate the moment capacity of partially composite girders. The total horizontal shear force at the concrete – steel interface between the point of maximum positive moment and the point of zero moment will be the lesser of;

$$C = A_s F_y \quad (4.3)$$

$$C = 0.85 f'_c A_c \quad (4.4)$$

$$C = \sum Q_n \quad (4.5)$$

Where;

- A_s = Area of steel section
- A_c = Area of concrete slab within effective width
- F_y = Yield strength of steel
- f'_c = Compressive strength of concrete
- $\sum Q_n$ = Sum of nominal strength of shear connectors between maximum positive moment and zero moment points

The strength of the deck concrete was evaluated through non-destructive rebound hammer tests and was found to be 34.5 MPa (5 ksi).

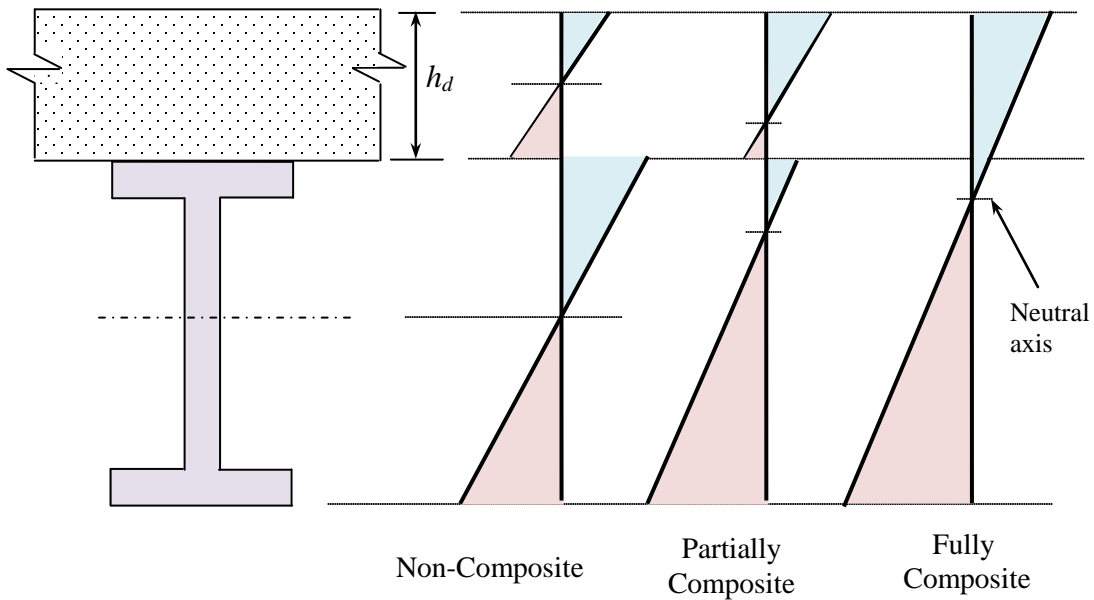
The depth of the concrete compression block a is obtained from;

$$a = C / 0.85f'_c b_e \quad (4.6)$$

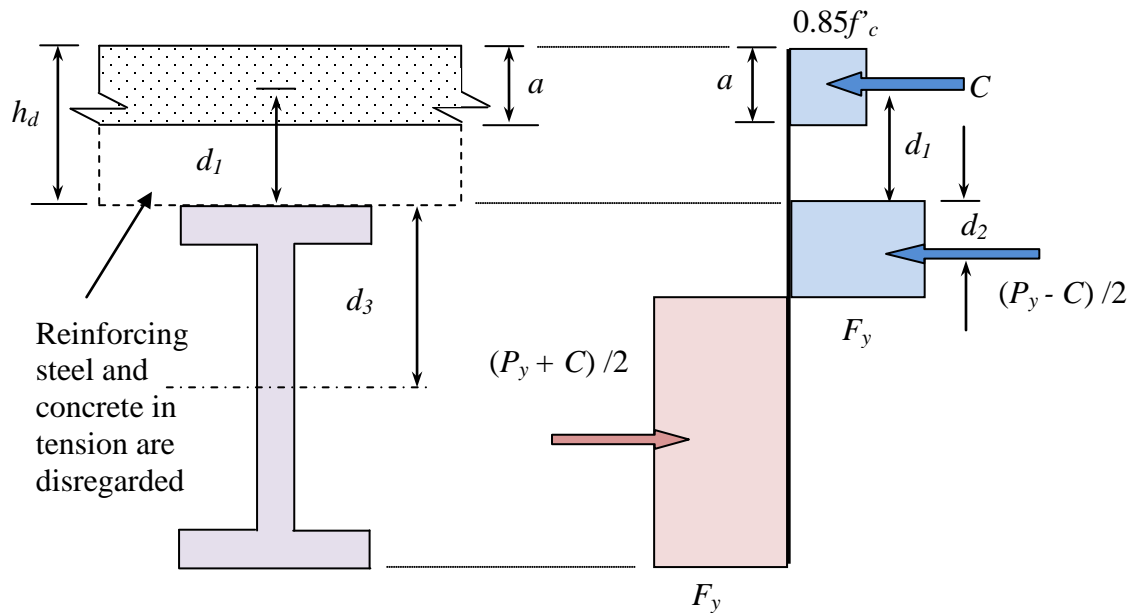
The depth of the concrete compression stress block ' a ' is equal or less than the slab thickness.

Typical strain diagrams are presented in Fig. 4.5(a) for non-composite, partially composite, and fully composite sections. For partially and fully composite sections, the neutral axis is drawn for the case when it is located in the web. The location of the neutral axis for both the partially and fully composite sections will vary depending on the section and material properties, girder geometry (length and end conditions), and loading conditions. The strain profile for the partially composite section is also influenced by the degree of composite action (or number and type of shear studs).

The AISC (2005) plastic stress distribution for a partially or fully composite section in positive bending is presented in Fig. 4.5(b). In the AISC LRFD specifications (AISC 2005), the tensile strength of the concrete and the contribution of the longitudinal reinforcement to the flexural strength of the cross section are neglected.



(a) Strain profiles for Non-Composite, Partially Composite, and Fully Composite sections
 (Note: For partially and Fully Composite sections, the neutral axis is drawn for the case when it is located in the web)



(b) AISC Plastic stress distribution for positive bending in composite sections (AISC 2005)

Fig. 4.5: Strain profiles and plastic stress distribution for positive bending

It should be noted that the AISC specifications do not include a factor to modify the depth of the concrete compression stress block depending on the strength of the concrete. The derivations also assume a rectangular Whitney's stress block for the concrete stress distribution even when the plastic neutral axis falls below the concrete deck, and hence the strain profile within the concrete is no longer triangular.

The nominal plastic moment capacity M_n is then obtained from;

$$M_n = C (d_1 + d_2) + P_y (d_3 - d_2) \quad (4.7)$$

Where;

- P_y = Tensile strength of steel section $A_s F_y$
- d_1 = Distance from centroid of compression force C to top of steel section
- d_2 = Distance from centroid of compression force in steel to top of steel section, for no compression in steel $d_2 = 0$
- d_3 = Distance from centroid of steel section to the top of Non-Composite steel section

The nominal strength of a shear connector Q_n according to AISC LRFD specifications is given by;

$$Q_n = 0.5 A_{sc} (f'_c E_c)^{0.5} \leq A_{sc} F_u \quad (4.8)$$

- Where; A_{sc} = Cross sectional area of shear stud
- E_c = Modulus of elasticity of concrete (taken as $33 w_c^{1.5} \sqrt{f'_c}$)
- F_u = Specified minimum tensile strength of shear connector

While 19 mm (0.75 in) diameter ASTM B7 threaded rods were used as the shear connectors in the initial beam analysis, 22 mm (0.875 in) diameter rods were installed in the KY 32 Bridge to be conservative.

The effective section modulus (S_{eff}) is calculated according to commentary in the AISC specifications (AISC 2005) to evaluate the stresses in the beam for serviceability.

$$S_{eff} = S_s + \frac{\sqrt{(\sum Q_n / C_f)}(S_{tr} - S_s)}{\sqrt{\quad}} \quad (4.9)$$

where;

- S_{eff} = Effective section modulus
- S_s = Section modulus for the structural steel section
- S_{tr} = Section modulus for the fully composite uncracked transformed section
- C_f = Compression force in concrete slab for fully composite beam; smaller of $A_s F_y$ and $0.85 f'_c A_c$
- $\sum Q_n$ = Strength of shear connectors between point of maximum positive moment and point of zero moment

The load rating for the KY 32 Bridge after post installation of shear studs, corresponded to an Inventory level rating for serviceability of 26.8 tons for a Type 1 truck. Both before and after shear stud installation, a Type 1 truck was found to carry the critical load. Also, the rating after the installation of shear studs increased the load carrying capacity of the bridge slightly above that required for passage of an HS25 truck load. A summary of the load rating obtained for each truck type is provided in Table 4.2 for the non-composite bridge prior to retrofit; and, Table 4.3 for the partially composite bridge (following the post installation of shear studs). Details of the load rating analysis for different truck types with various axle orientations for both before and after retrofit are given in Appendix B.

Table 4.2a: Truck Weight Analysis according to AASHTO guidelines (Non-Composite bridge – prior to retrofit) – Metric Units

Truck Type	Rear Axle Weight (kN)	Non-Composite Bridge			
		Dead Load Moment (kN-m)	Live Load Moment (kN-m)	“Inventory Level” Truck Weight (kN)	“Operational Level” Truck Weight (kN)
Type 1	142.3	42.1	119.3	101.4	169.0
HS25	177.9	42.1	149.1	184.2	304.3
Type 2	108.4	42.1	148.7	116.0	191.7
Type 3	88.3	42.1	167.8	134.1	222.3
Type 4	78.3	42.1	107.4	224.2	373.6

Table 4.2b: Truck Weight Analysis according to AASHTO guidelines (Non-Composite bridge – prior to retrofit) – Customary US Units

Truck Type	Rear Axle Weight (kips)	Non-Composite Bridge			
		Dead Load Moment (kip-ft)	Live Load Moment (kip-ft)	“Inventory Level” Truck Weight (tons)	“Operational Level” Truck Weight (tons)
Type 1	32.0	31.06	88.0	11.4	19.0
HS25	40.0	31.06	110.0	20.7	34.2
Type 2	24.38	31.06	109.7	13.0	21.5
Type 3	19.84	31.06	123.7	15.1	25.0
Type 4	17.6	31.06	79.2	25.2	42.0

Table 4.3a: Truck Weight Analysis according to AASHTO guidelines (Partially Composite bridge – after retrofit) – Metric Units

Truck Type	Rear Axle Weight (kN)	Composite Bridge			
		Dead Load Moment (kN-m)	Live Load Moment (kN-m)	“Inventory Level” Truck Weight (kN)	“Operational Level” Truck Weight (kN)
Type 1	142.3	42.1	119.3	238.4	396.8
HS25	177.9	42.1	149.1	427.9	716.2
Type 2	108.4	42.1	148.7	269.8	448.9
Type 3	88.3	42.1	167.8	310.6	516.5
Type 4	78.3	42.1	107.4	530.2	882.5

Table 4.3b: Truck Weight Analysis according to AASHTO guidelines (Partially Composite bridge – after retrofit) – Customary US Units

Truck Type	Rear Axle Weight (kips)	Composite Bridge			
		Dead Load Moment (kip-ft)	Live Load Moment (kip-ft)	“Inventory Level” Truck Weight (tons)	“Operational Level” Truck Weight (tons)
Type 1	32.0	31.06	88.0	26.8	44.6
HS25	40.0	31.06	110.0	48.1	80.5
Type 2	24.38	31.06	109.7	30.3	50.5
Type 3	19.84	31.06	123.7	34.9	58.1
Type 4	17.6	31.06	79.2	59.6	99.2

CHAPTER 5

EXPRIMENTAL BRIDGE GIRDER STRENGTHENING WITH UHM CFRP

5.1 Introduction

The load rating of the KY 32 Bridge before retrofit corresponded to an Inventory level rating for serviceability of 101.4 kN (11.4 tons). At the same time, since section analysis showed that application of laminates on the non-composite girders would not increase the stiffness of the girders to the expected load carrying capacity required for the passage of a HS25 truck, post installed shear studs were identified as a means of obtaining some degree of composite action between the steel girders and concrete deck. Furthermore the retrofit would act to increase the stiffness of the bridge, and also utilize the CFRP laminates more effectively. A post installed shear stud layout was identified for field implementation from a finite element beam analysis (as discussed in Chapter 4) with a shear connector ratio of 71% of the AASHTO fully composite girder.

The load rating of the bridge with the post installed shear studs corresponded to an Inventory level rating for serviceability of 238.4 kN (26.8 tons). While this rating is higher than the required load carrying capacity associated with HS25 loading, it was decided to apply ultra high modulus CFRP laminates on to the steel girders to experimentally evaluate the performance of the CFRP laminates in field conditions. The KY 32 Bridge strengthening would be the first field application of ultra high modulus CFRP laminates in the United States and was expected to provide valuable insight on the field application of ultra high modulus CFRP laminates. As increasing the load carrying capacity was not of primary concern following the post installation of shear studs, 1.2 mm (0.047 in) thick laminates were chosen for the strengthening process rather than the thicker 2 mm (0.079 in) or 4 mm (0.157 in) thick CFRP laminates.

As the KY 32 Bridge was to be strengthened using both post installed shear studs as well as ultra high modulus CFRP laminates, performance evaluation of the bridge before and after the different phases of strengthening needed to be carried out. The entire repair and

testing process was divided into several key stages as depicted in the flowchart in Figure 5.1. While strengthening and testing were the primary objectives, several key processes were involved in facilitating the whole retrofit process. The strengthening required the locating of rebars, drilling holes for shear studs, installing shear studs, grit blasting to remove paint and rust, the application of the ultra high modulus CFRP laminates, and finally painting of the bridge.

Load tests were performed before strengthening (or “as is”); then following the drilling of holes for the installation of shear studs; after the installation of shear studs; and, after the application of ultra high modulus CFRP laminates. The load test following the drilling of holes was performed to ensure that no significant decrease in stiffness occurred due to the reduction in steel from both the top and bottom flanges. Two load tests were performed following the application of the ultra high modulus CFRP; the first to evaluate the performance of the bridge, and the second to evaluate the strain variation in the laminates.

Traffic control during the strengthening and testing process was provided by the Kentucky Transportation Cabinet. Only a single instance of bridge closure took place during the strengthening process, where closure was necessary for the installation of shear studs. Specifically, traffic was rerouted during the installation process, and speed limits were applied following the installation until the end of the curing period of the epoxy. During the laminate application and the load tests traffic control with speed limits were employed.

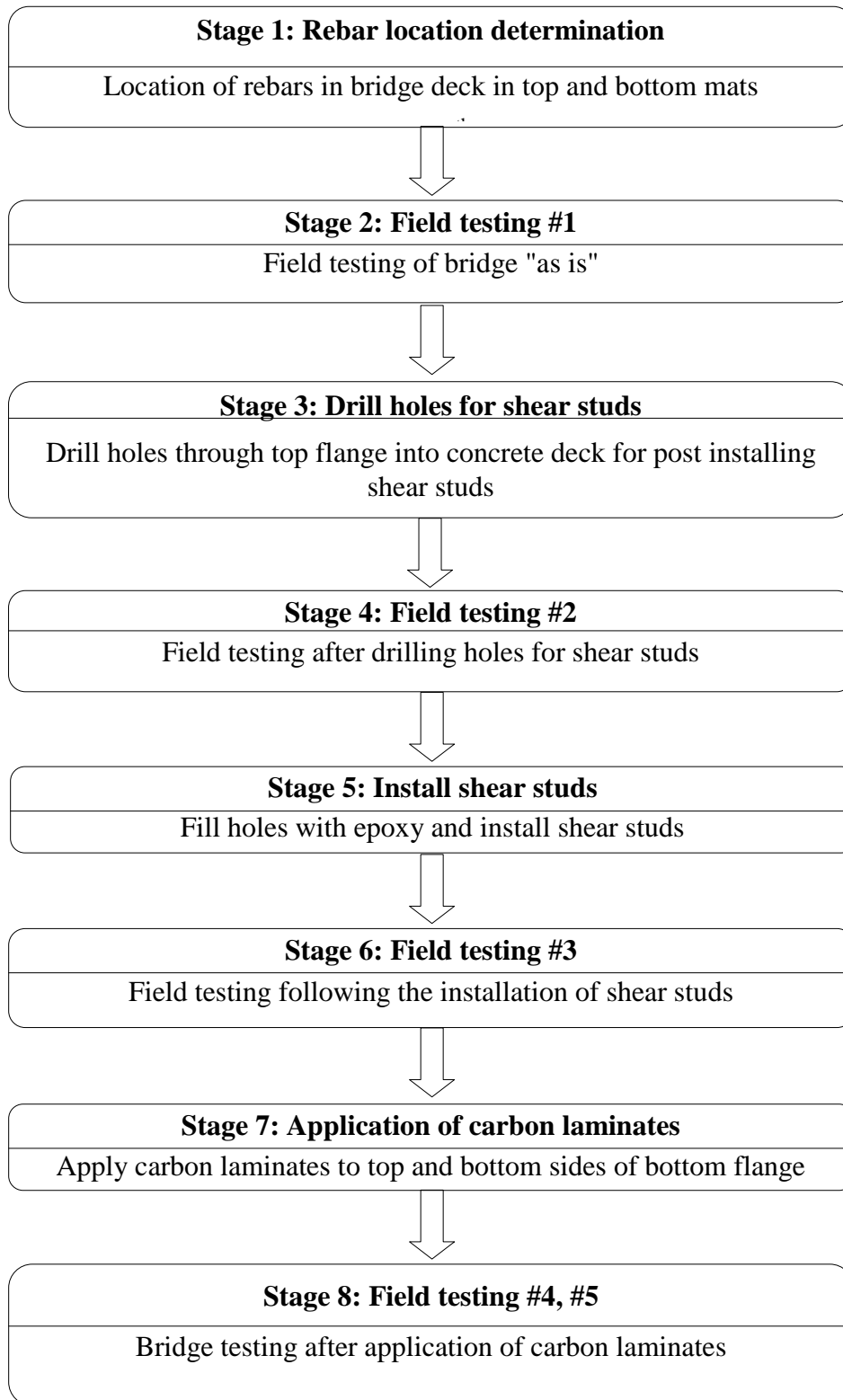


Fig. 5.1: Stages in the repair and testing of KY 32 Bridge

5.2 Rebar Location

As the KY 32 Bridge did not have any bridge plans or drawings, the rebar locations needed to be marked out before any drilling could be carried out for the shear studs. Therefore, as depicted in Fig. 5.2, ground penetrating radar equipment (GSSI SIR-3000) was employed to determine the placement of the top and bottom rebar mats in order to prevent damaging the rebars when drilling holes for the shear studs. The layout of the rebar mat is shown in Fig. 5.3.



(a) Locating rebar positions on the top surface



(b) Locating rebar positions on the bottom surface

Fig. 5.2: Locating rebars on the top and bottom of the KY32 Bridge

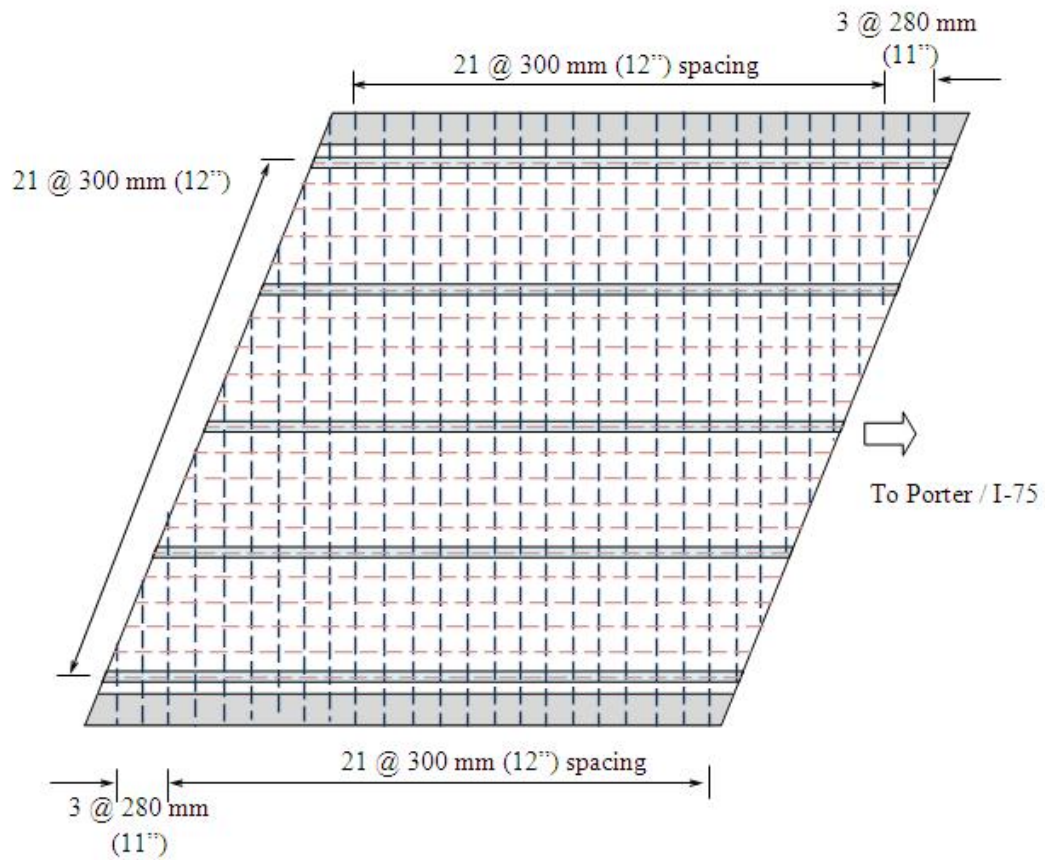


Fig. 5.3: Layout of top and bottom rebar mat

The locations were marked on the bottom surface of the concrete deck and stud hole locations were shifted when required to avoid damaging the rebars. Both top and bottom rebar mats were found to be identical with #5 bars, 15.9 mm (0.625 in) in diameter, in both longitudinal and transverse directions. Ground penetrating radar was also used to find the location and spacing of the rebar within the curb wall and also to approximately evaluate the concrete cover over the top and bottom rebar mats.

5.3 Drilling and Installing Shear Studs

From the initial load tests, it was determined that the bridge (which was initially modeled as non-composite and simply supported) had a degree of compositeness due to the friction between the embedded top flange and concrete deck. Also the degree of fixity over the abutments was not consistent with that of simply supported construction, with the girder ends being enclosed by concrete diaphragms, which were integral with the deck. The deck was to be made partially composite with the girders with the aid of post installed shear studs, even though the deflections observed were within AASHTO serviceability limitations. Importantly, the composite action due to friction could not be relied upon to increase the load capacity of the bridge.

Following the results of the preliminary analysis, ASTM A193 B7 threaded rods, with a minimum manufacturer specified yield strength of 724 MPa (105 ksi), an ultimate strength of 827 MPa (120ksi) and having a diameter of 22 mm (0.875 in) were selected as shear connectors for the retrofit of the KY32 Bridge (Fig. .5.4). A total of 30 shear connectors per girder, decided after the initial finite element beam analysis (discussed in Chapter 4), were to be spaced along each girder as shown in Fig. 5.5.

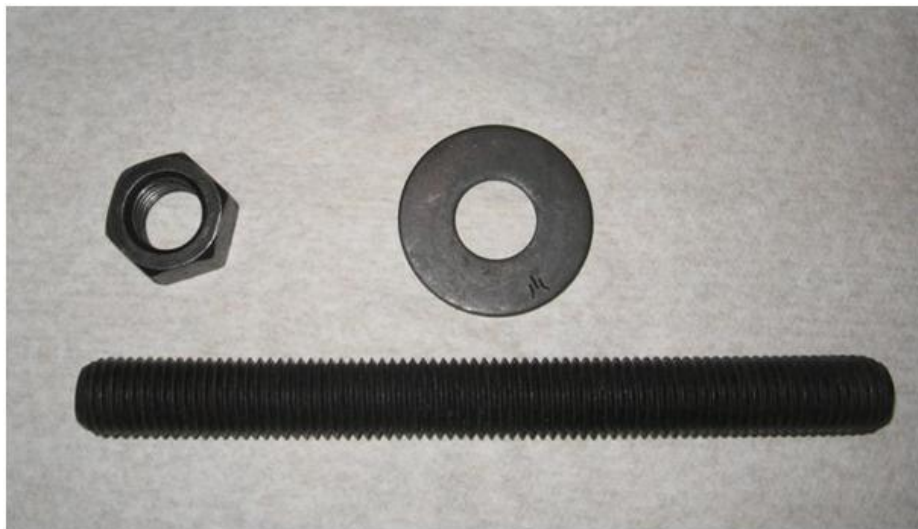


Fig. 5.4: ASTM 193 B7 threaded rod and nut

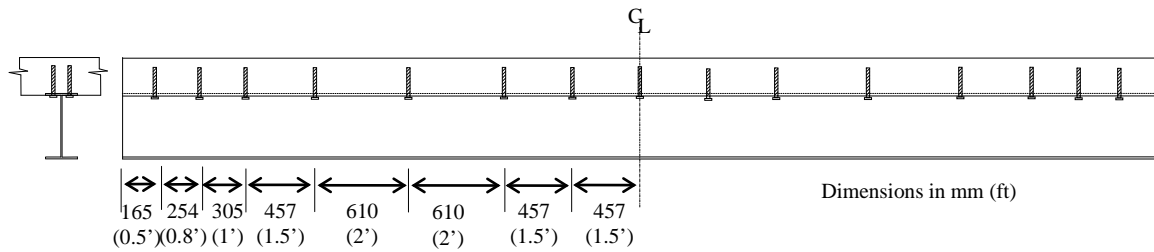


Fig. 5.5: Shear connector location on girders

The threaded rods having a length of 216 mm (8.5 in) were to be inserted 152 mm (6 in) into the concrete as shown in Fig. 5.6. The clear distance between the top and bottom flanges of approximately 330 mm (13 in) was limited by the reach of the available drilling equipment. It was deemed necessary to drill 27 mm (1.0625 in) diameter holes through the bottom flange up to the top flange and then through to the bottom of the deck.

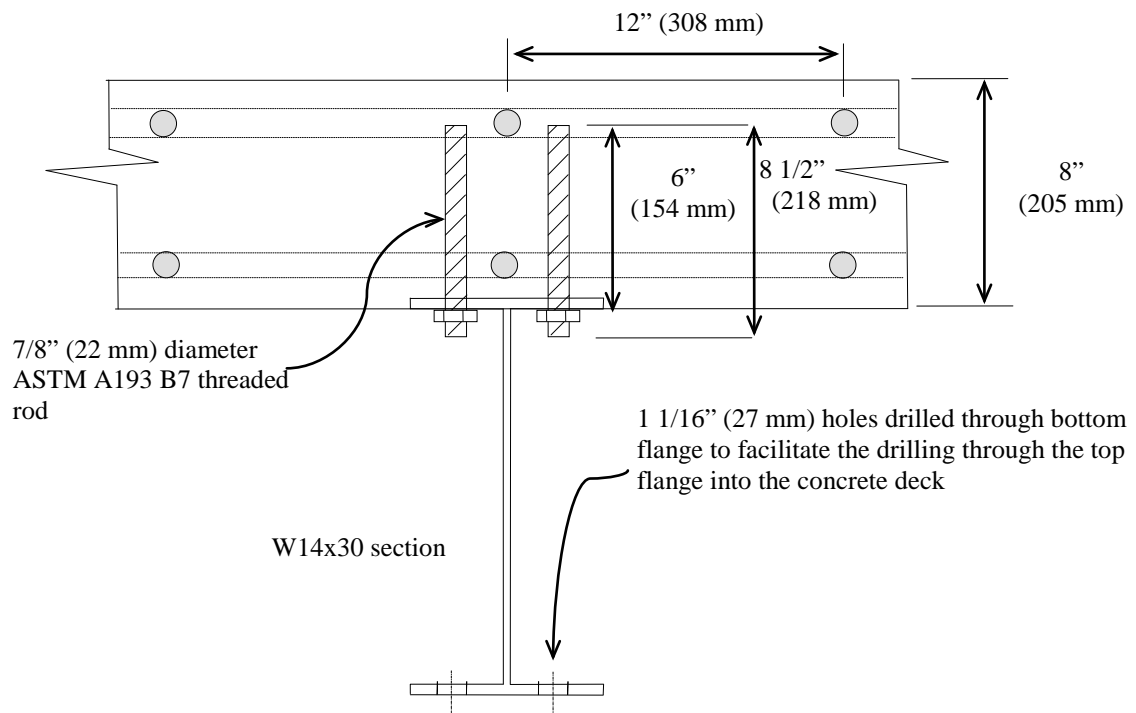


Fig. 5.6: Shear connector placement

Initially, a smaller diameter hole was hand drilled through the bottom flange at the corresponding position for the specified stud locations on the top flange. A drill rig attached to the bottom flange was used to drill all the way 152 mm (6 in) in to the concrete deck. The rig was fixed on to the bottom flange and could traverse the length of each girder (Fig. 5.7) while drilling on either side of the web. Fig. 5.8 depicts a hole being drilled through both the bottom and top flange into the concrete deck using the drill rig.



Fig. 5.7: Drilling rig fixed to the bottom flange



Fig. 5.8: Drilling through the bottom flange into the concrete deck

Once all the holes were drilled, they were cleaned by blowing compressed air to remove any residual particles and dust. A two-part acrylic adhesive (RED HEAD® A7) was inserted through a hand dispenser gun filling up to 2/3 of the hole's volume (Fig. 5.9).



Fig. 5.9: Inserting of adhesive into drilled hole



Fig. 5.10: Inserting threaded rod with twisting motion

The threaded rods were then inserted with a twisting motion and held in place for the specified curing time of the adhesive (Fig. 5.11). After the specified curing time, a washer and nut were inserted into each threaded rod, and tightened up to 237 Nm (175 ft-lbs) using a torque wrench as seen in Fig. 5.12.



Fig. 5.11: Threaded rods held in place during curing



Fig. 5.12: Tightening of nut to specified torque

5.4 Application of ultra high modulus CFRP

Although the expected load carrying capacity was achieved through post installation of shear studs, in order to quantify the performance of UHM CFRP laminates and to evaluate the feasibility of applying them in the field, it was decided that the laminates would be used to strengthen the girders.

Before the application of laminates on to the KY 32 Bridge girders all paint and rust had to be removed from the steel surface. Grit blasting has been recommended (Schnerch et al. 2007) as the best method of cleaning and obtaining a rough profile on the steel surface. While only the bottom flange was to be strengthened with CFRP laminates, the entire exposed girder was grit blasted in order to facilitate painting immediately following the application of laminates. Fig. 5.13 depicts the enclosure built to collect the removed paint and used grit and the temporary platform built over the creek to carry out the grit blasting as well as the laminate application. Once the paint was removed from the beams exposing the metal underneath, the beams were vacuumed to remove any dust or residue left on the steel surface. The enclosure was removed after collecting all the paint and used grit.



Fig. 5.13: Temporary platform and enclosing for grit blasting

The UHM CFRP laminates used for the strengthening were distributed by Mitsubishi Plastics Composites America, Inc. The chosen laminates had a manufacturer specified modulus of 450 GPa (65,000 ksi) and a tensile strength of 1,200 MPa (174 ksi). From the different laminate thicknesses available, the 1.2 mm (0.047 in) thick laminate was selected for application with two 50 mm (2 in) strips on the underside of the bottom flange and two more on the top of the bottom flange, as shown in Fig. 5.14. In addition to the strengthening, this configuration was also expected to cover up the drill holes made in the bottom flange of the girders when drilling for the shear studs. Spabond 345 produced by SP[®] systems was the selected epoxy adhesive to be used with the UHM CFRP laminates. The 400 ml (0.105 gal) Spabond 345 twin cartridge with separate epoxy and hardener compartments was selected for its convenience in application. From the different hardener types available from the manufacturer, the fast hardener with a pot life of 20 minutes at 15°C (59°F) was selected to obtain the specified 36.6 MPa (5.3 ksi) shear strength on steel when cured at 21°C (69.8°F) for 28 days.

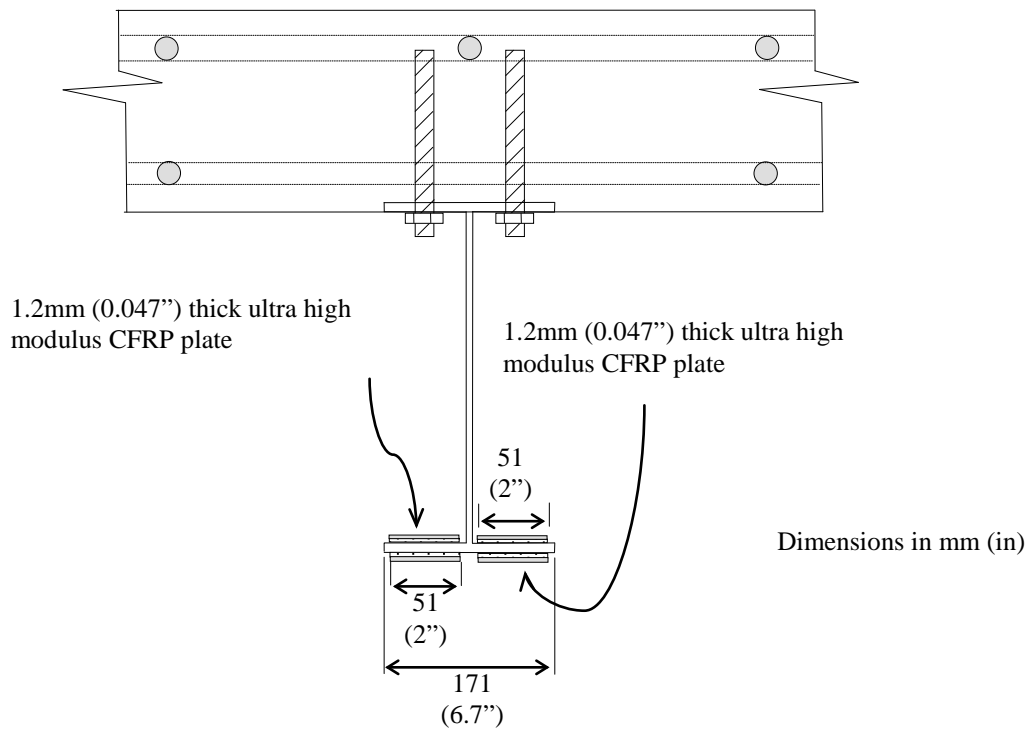


Fig. 5.14: UHM CFRP laminate placement on bottom flange

The installation of the UHM CFRP strips was carried out according to the guidelines provided by Schnerch et al. (2007). As preparing and applying long laminates without splicing is one of the problems in laminate application, CFRP laminate strips 6.1 m (20 ft) long were selected to evaluate the feasibility of field application. While longer laminates also minimize peel and shear stresses at the ends, the finite element model developed concurrently (discussed in Chapter 6) showed that the ends of the girders of the KY 32 Bridge were in compression due to partial fixity at the abutments. While the bond strength between the laminate and steel is not thought to differ in tension and compression, the compressive strengths of unidirectional CFRP laminates have been found to be less than 60% of the corresponding tensile strengths (Budiansky and Fleck 1993). The compressive stresses at the ends of the laminates from the finite element analysis were found to be significantly small so as not to be of concern with compressive failure. The ends of each laminate strip were reverse tapered, as shown in Fig. 5.15, to limit stress concentrations (Schnerch et al. 2007). The recommended taper by Schnerch et al. (2007) is 10°-20°, but due to the small thickness of 1.2 mm (0.047 in), only a 45° taper could be applied on the laminates on the KY32 Bridge.

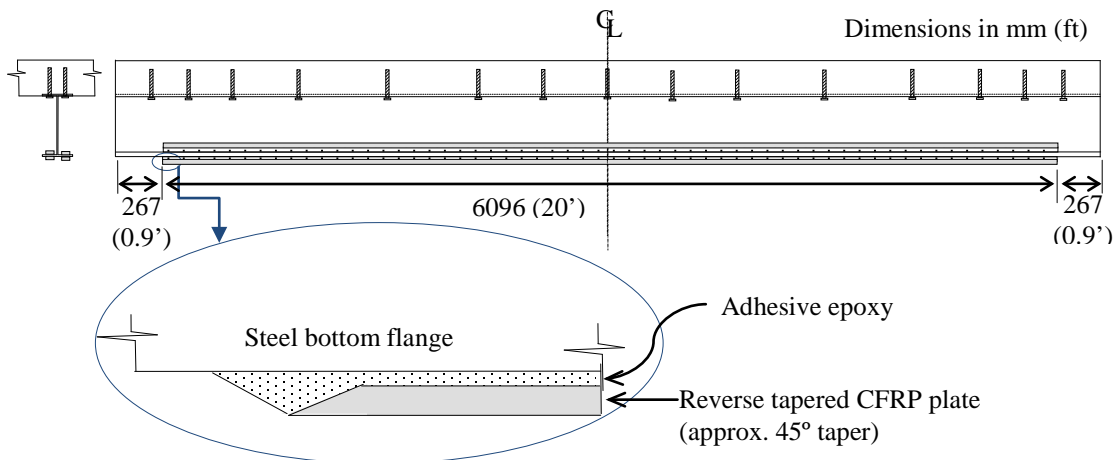


Fig. 5.15: Layout of UHM CFRP laminates on each girder



Fig. 5.16: Sanding laminate edges to obtain reverse taper

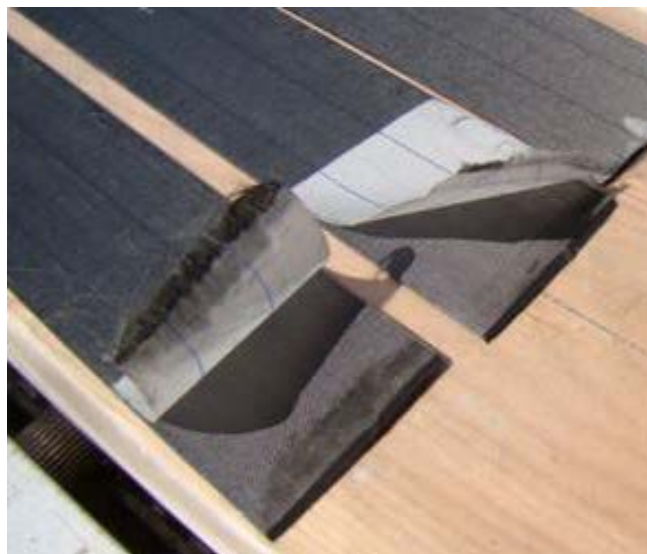


Fig. 5.17: Tapered laminate edges

The ultra high modulus CFRP laminates were applied one day after the grit blasting was completed. While thicker laminates come in shorter lengths, the 1.2 mm (0.047 in) thick

laminates, which come in reels of 15.2 m (50ft), were cut to 6.1 m (20 ft) in the field using a hand saw and then tapered to approximately 45° using a sander (Fig. 5.16). The peel ply on both sides of the laminate was peeled back at the edges to facilitate sanding but was not entirely removed at this time. The tapered laminate edges with the peeled back peel ply are depicted in Fig. 5.17.

The laminate placement was performed in two consecutive days. On the first day, laminates were placed on the bottom surface of the bottom flange, and on the next day the remaining laminates were applied to the top surface of the bottom flange. All the steel surfaces were vacuumed and the bottom flanges of the steel beams were then wiped down using a solvent (Acetone). The peel ply protecting the surface of the laminate from contamination on the top of the laminates was removed and epoxy was applied from the two-part (epoxy and hardener) cartridges using the manufacturer recommended dispenser guns (Fig. 5.18). Two dispenser guns were employed simultaneously on two strips in order to have the epoxy distributed and the two laminates on the steel surface within the recommended 'pot life' of the epoxy. As the epoxy was applied, it was spread using a 5 mm (0.02 in) v-notch trowel in order to obtain a triangular epoxy profile on the laminate (Schnerch et al.2007) as seen in Fig.5.19.



Fig. 5.18: Application of epoxy on to the top surface of the laminate



Fig. 5.19: Spreading of epoxy with V-notch trowel

Following the spreading of epoxy, 1mm (0.04 in) diameter glass spacer beads were placed along the bond length at approximately 154 mm (6 in) intervals to obtain even bond thickness. The laminates to be adhered to the bottom surface were then placed between tabs pasted on wooden boards, approximately the same width as the bottom flange, that were wrapped in wax paper for easy removal. The boards were pressed against the steel surface and then clamped using mechanical grip clamps.

Laminates were then installed on the top surface of the bottom flange via a similar process 24 hours later. Small wooden tabs were pasted on the top surface as guides to set the laminates. The epoxy was spread on the laminates to be adhered to the top steel surface of the bottom flange in a manner similar to that employed in the previous application. However, unlike the bottom laminates, the top laminates were flipped (Fig. 5.20) and set between guide tabs on the top surface of the flange. Unlike the bottom laminates, the top surface laminates were installed one at a time. The clamps on one side of the bottom flange holding the bottom laminates in place were temporarily removed to install the top laminates. Once the top laminates were placed, a wooden board was placed on top of the assembly and clamped to the bottom board as shown in Fig. 5.21.



Fig. 5.20: Placing laminate on the top flange



Fig. 5.21: Clamping both top and bottom laminates

All clamps and boards were removed 24 hours after installation of the top laminates. The laminates were allowed to cure for five additional days before the remaining peel ply on the outside was also removed. Subsequently paint was applied to the entire steel girder, including the laminates. Fig. 5.22 depicts the underside of the bottom flange after the clamps and boards were removed (Fig. 5.22(a)) and the application of paint (Fig. 5.22(b)).



(a) Before painting



(b) After painting

Fig. 5.22: Laminates on bottom flange before and after painting

5.5 Bridge Instrumentation and Load Tests

Load tests were performed before and after installing the shear studs (referred to as Test #1 and test #3, respectively). An additional test was performed (referred to as Test #2) soon after drilling holes for the shear studs to evaluate the effect of the loss of steel girder section, on the stiffness of the bridge. Two load tests were also carried out after the installation of ultra high modulus CFRP laminates. Specifically, Test #4 was performed approximately one month after laminate application to evaluate the performance of the bridge. The final test, Test #5, was carried out specifically to obtain strain readings from the laminates, which were not evaluated during the previous test.

The instrumentation on the bridge consisted of reusable strain gages attached to the girders and linear variable differential transformers (LVDT). The placement of the reusable strain gages (Bridge Diagnostic Inc. Strain Transducers) and the LVDTs (Macro Sensors GHSD/GHSDR 750 series) are depicted in Fig.5.23. Instrumentation was placed on girders G1, G3 and G5 at mid span (locations L1, L2 and L3) and at quarter span on girder G3 (L4). At each instrumentation point, three strain gages were placed at the top, center, and bottom of the web and one strain gage on the bottom flange parallel to the direction of traffic. The reusable strain gage locations on the girders were first cleaned using a grinder to remove any paint, and the steel tabs for mounting the strain gages were attached as seen in Fig. 5.24. The same reusable strain gage positions were used in all five field tests. All four LVDTs, measuring the vertical displacement of the bridge, were placed adjacent to the reusable strain gage on the bottom flange. Wire mounted weights were positioned below the reusable strain gage on the bottom flange at each instrumentation location, as shown in Fig. 5.25. As depicted in figure 5.26, the stands with mounted LVDTs were placed on the creek bed underneath the hanging weights. All data from the reusable strain gages were collected via two signal conditioners (Sensotec SA-10D) and along with the LVDT data were recorded using a laptop computer (Fig. 5.27).

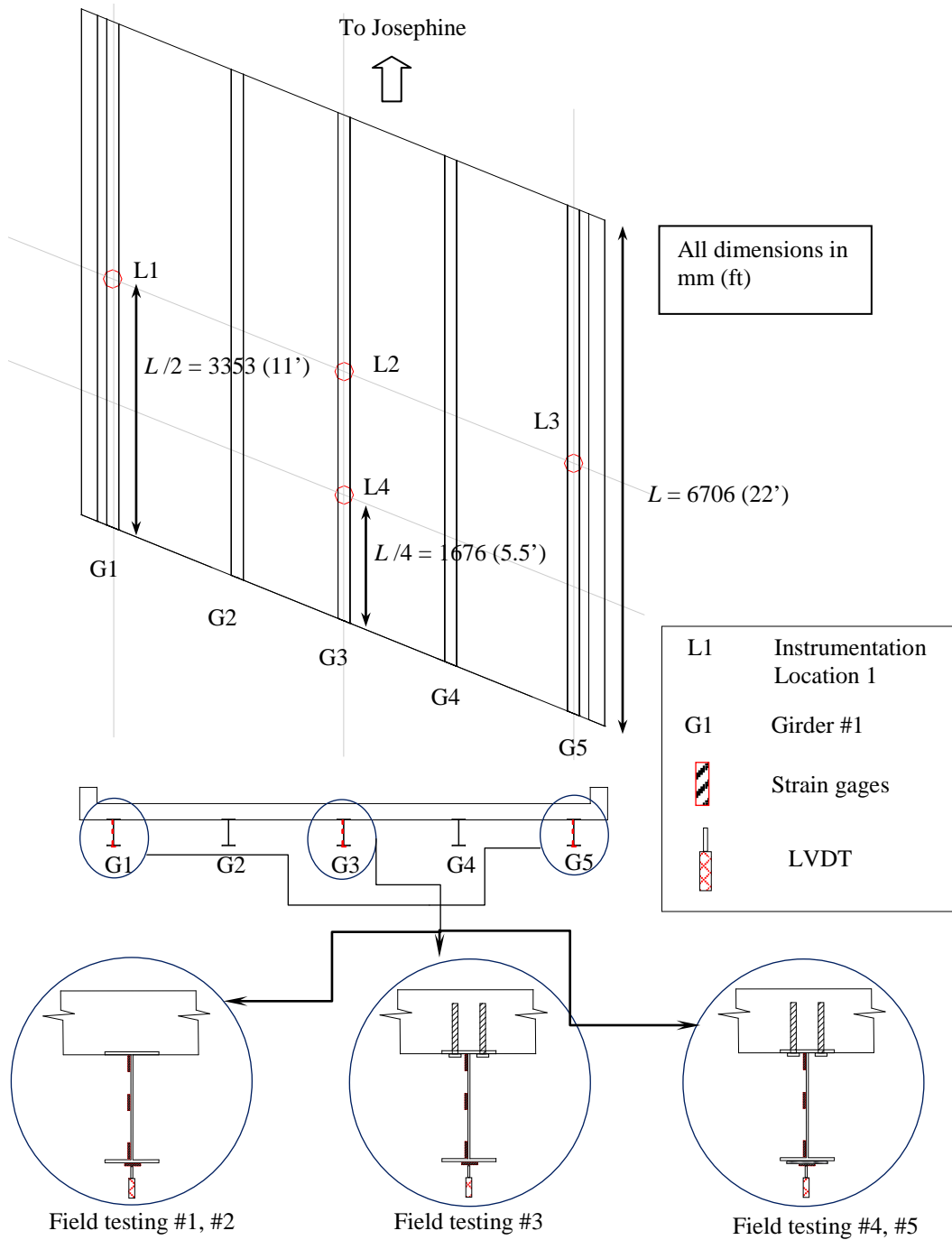


Fig. 5.23: Reusable strain gage and LVDT positions on KY32 Bridge



(a) Attaching tabs for gages



(b) Attached reusable strain gages

Fig. 5.24: Attaching reusable strain gages



Fig. 5.25: Wire mounted weights hung above LVDT locations on girder G3

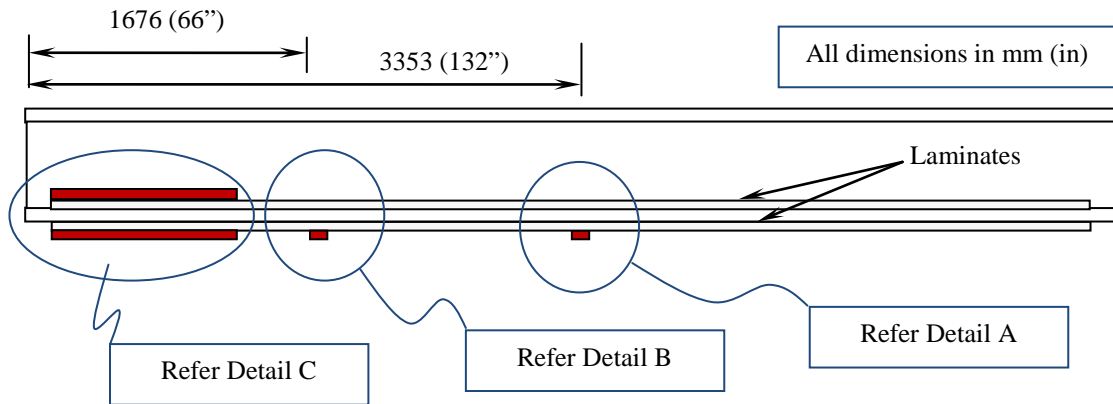


Fig. 5.26: Instrumentation under the bridge at all four locations



Fig. 5.27: Data acquisition to laptop computer via two signal conditioners

In addition to the gage arrangement in Fig. 5.23, foil type strain gages were installed on the laminates prior to Test #5. These gages were attached to both the bottom laminates and one top laminate on Girder G3 and one bottom laminate in girder G5. The layout of the foil type strain gages is shown in Fig. 5.28. Several gages were also attached to the steel girders. The laminate surfaces were sanded to remove paint and to make a rough profile, and subsequently cleaned with Acetone before the strain gages were attached.



Side view of typical girder with foil type strain gages

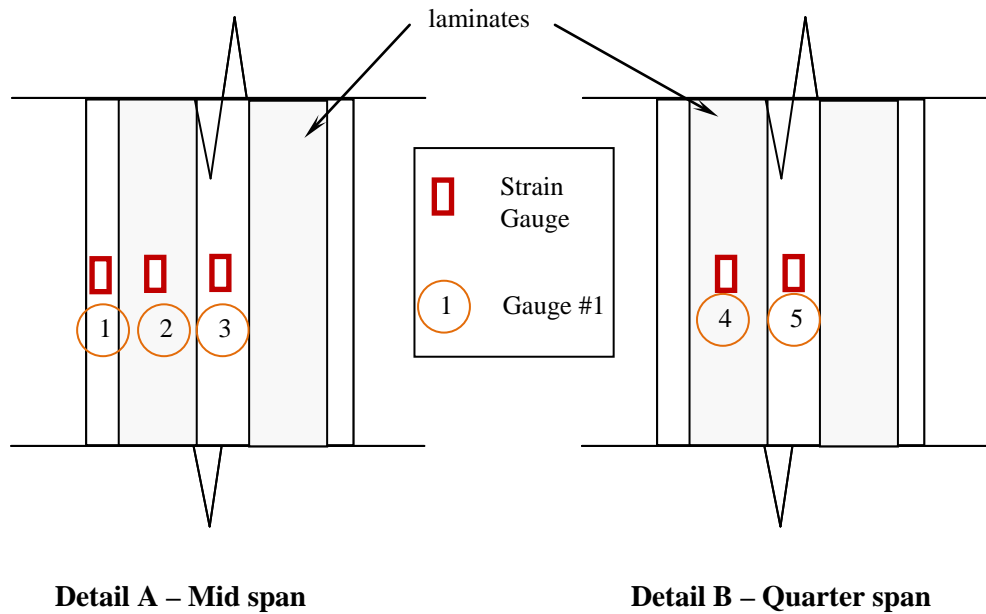
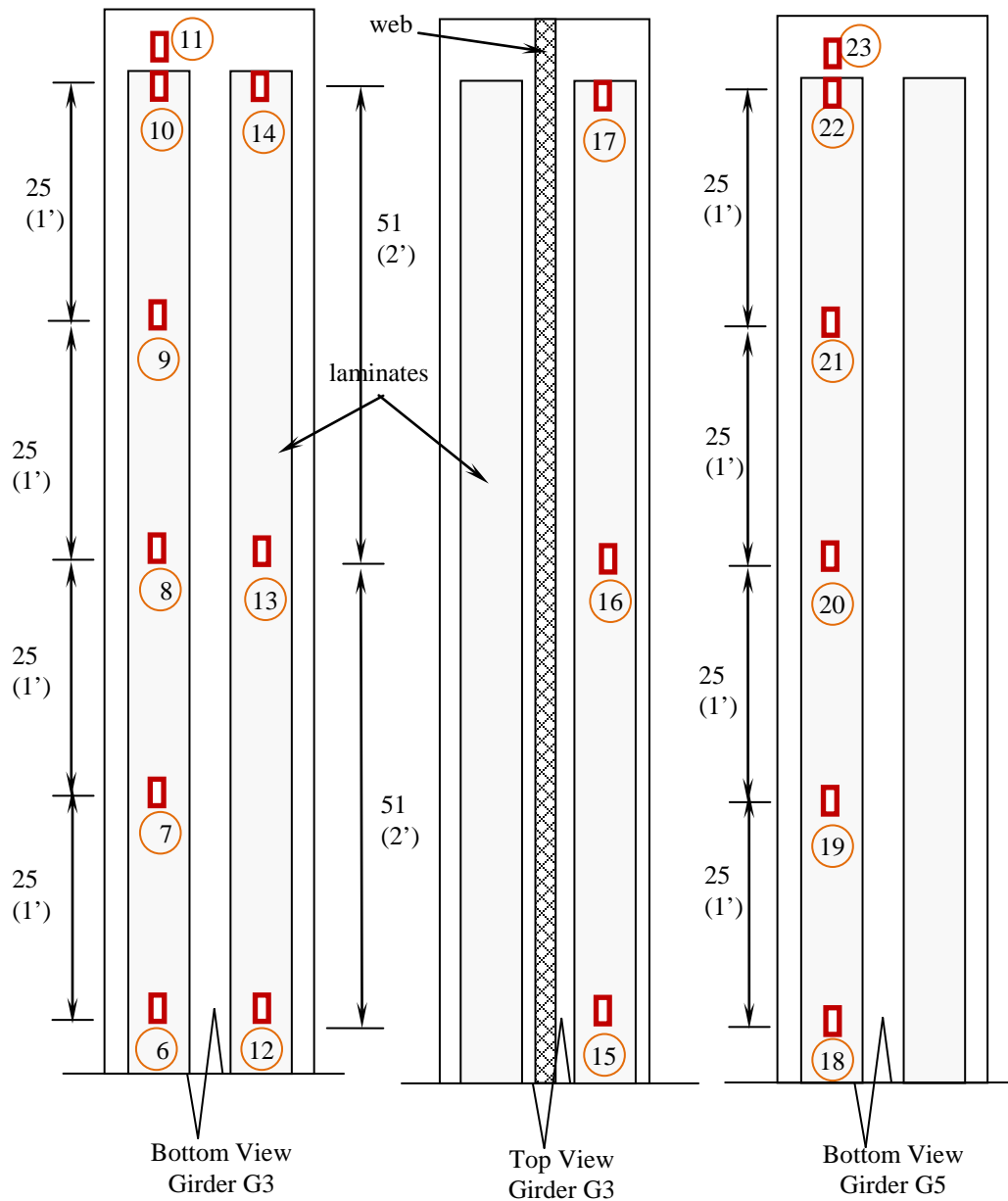


Fig. 5.28: Location of strain gages on laminates



Detail C – Edge of laminate

Fig. 5.28: Location of strain gages on laminates (Contd.)

Several foil type strain gages located at the edge of the bottom laminates on the center girder (G3), are shown in Fig. 5.29 (note that the gages were subsequently connected to lead wires). A separate data acquisition system (Vishay System 7000) was used to collect the strain data from the gages on the laminates (Fig. 5.30).



Fig. 5.29: Attached strain gages on the two bottom laminates on girder G3



Fig. 5.30: Separate data acquisition system and laptop for laminate strain data

The dimensions of the dump truck provided by the Kentucky Transportation Cabinet (KyTC) and used to load the bridge for all the load tests are shown in Fig. 5.31. Due to the short span length of the bridge only the rear truck axle was used to load the bridge. A total of 9 load positions were used to obtain data for the behavior of the bridge.

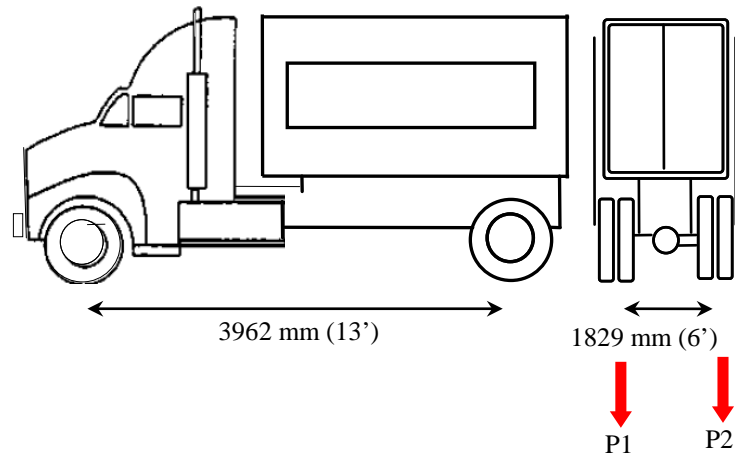


Fig. 5.31: Load test truck dimensions

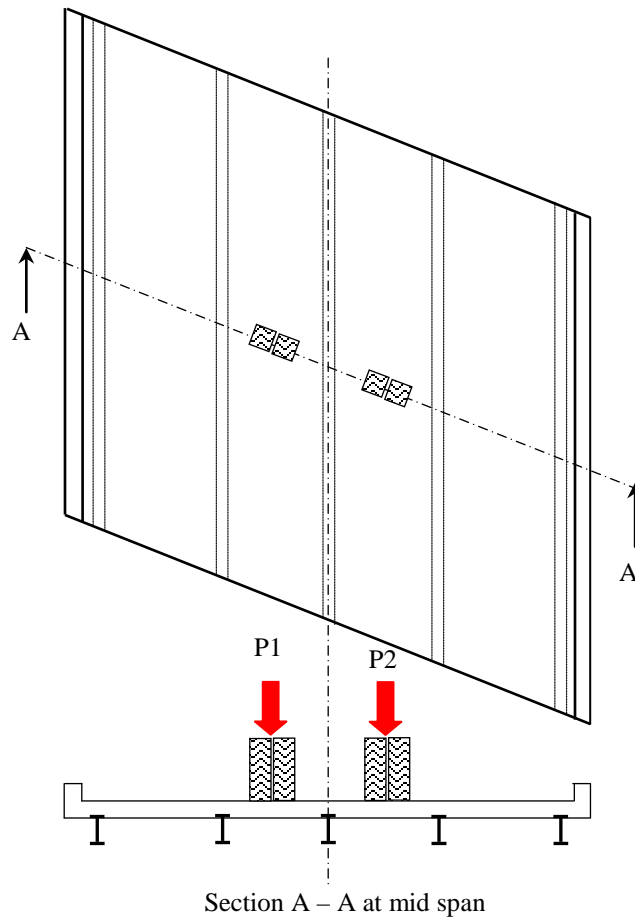


Fig. 5.32: Load position on deck at mid span

The load rating analysis (Appendix B) showed that the most critical axle combination for the KY32 Bridge was a Type 1 truck or an AASHTO HS20 type truck. The most critical load case for the short span bridge KY 32 Bridge was identified as the case where the rear axle is over the mid-span of the bridge. Therefore from the total of 9 load positions that were evaluated, only those data measured for the load case associated with the maximum displacements and strains, when the rear axle is placed symmetrically at mid-span as in Fig. 5.32, are presented here.

The dump truck used for the load testing was preloaded and weighed at a weigh station before each test and the load under each axle was noted. Although the same dump truck was used for all 5 load tests, the axle weight was different each time since the riprap amount used to fill the truck varied. The time interval between the first and last load test was approximately 14 months, and Table 5.1 below provides weight measurements taken for the dual tires on the rear axle (P1, P2) of the truck for all tests (Test #1 - #5).

Table 5.1: Truck tire loads

Load Test	Dual Tire Weight P1 kN (kips)	Dual Tire Weight P2 kN (kips)	Total Rear Axle Weight kN (kips)
Test #1 - Before retrofit	52.3 (11.75)	56.0 (12.60)	108.3 (24.35)
Test #2 – After drilling holes	56.3 (12.65)	60.7 (13.65)	117.0 (26.30)
Test #3 – Post installed shear studs	53.8 (12.10)	66.5 (14.95)	120.3 (27.05)
Test #4 – UHM CFRP laminates (1)	65.2 (14.65)	70.5 (15.85)	135.7 (30..50)
Test #5 – UHM CFRP laminates (2)	53.9 (12.12)	59.9 (13.46)	113.8 (25.58)

5.6 Load Test Results

Data gathered from the load tests included strains in the steel girders and deflections at the four instrumentation locations. The data were analyzed to understand the behavior of the KY32 Bridge after each of the stages of retrofit. The reusable strain gage data (Fig. 5.23) from the three gages mounted along the height of the web and also the one on the bottom flange at each instrumentation location were initially used to understand the degree of composite action between the girders and the concrete deck. Specifically, composite action was estimated by successfully determining the location of the neutral axis. Strain data from the following tests were compared to evaluate the change in neutral axis location and hence the degree of composite action achieved by post installing shear studs, as well as the shift in neutral axis due to the application of ultra high modulus CFRP laminates. The deflection data were similarly compared, and since the tests data indicated that the bridge members remained within the elastic limits, the deflection data obtained from the LVDTs were correlated to the elastic stiffness of the bridge.

5.6.1 Load Test #1, #2 – Before Retrofit

Both load Tests #1 and #2 were carried out prior to the installation of shear studs. While load Test #1 was performed before any action pertaining to the retrofit was performed on the KY 32 Bridge, load Test #2 was carried out to evaluate if any significant loss of stiffness occurred due to the removal of material from the bottom flange of the steel girders that took place during drilling of the shear stud holes. Fig. 5.33 depicts the deflections observed perpendicular to traffic along the mid span of the bridge. The deflections are seen to be very similar with a slight increase in deflection for Test #2, although it should be noted that the rear axle weight was slightly larger for Test #2. The maximum deflections observed at mid-span were less than 2 mm (0.079 in.) for both tests.



Fig. 5.33: Displacement perpendicular to direction of traffic at mid-span – before retrofit

The strain profile at mid span on the center girder (G3) is shown in Fig. 5.34. Both strain profiles appear close to each other, with a difference of less than 20 micro strains at each gage location. The neutral axis for a non composite girder would be at mid-height of the W14x30 steel beam section. The theoretical elastic neutral axis for the fully composite girder evaluated from section transformation was calculated to be 245 mm (9.64 in.) above the theoretical non composite neutral axis. Thus the strain readings confirmed that the bridge does not behave in a strictly non-composite fashion. The strain measurements also reveal that the bridge remained within the elastic limits during the load tests. The maximum tensile strain in the bottom flange was less than 127 microstrains for both Test #1 and #2. The neutral axis of the center girder (G3) for the non-composite bridge obtained from the measured data is above the theoretical neutral axis for a non-composite beam, but below the theoretical neutral axis for fully composite action, where the latter case, the neutral axis would reside within the concrete deck.

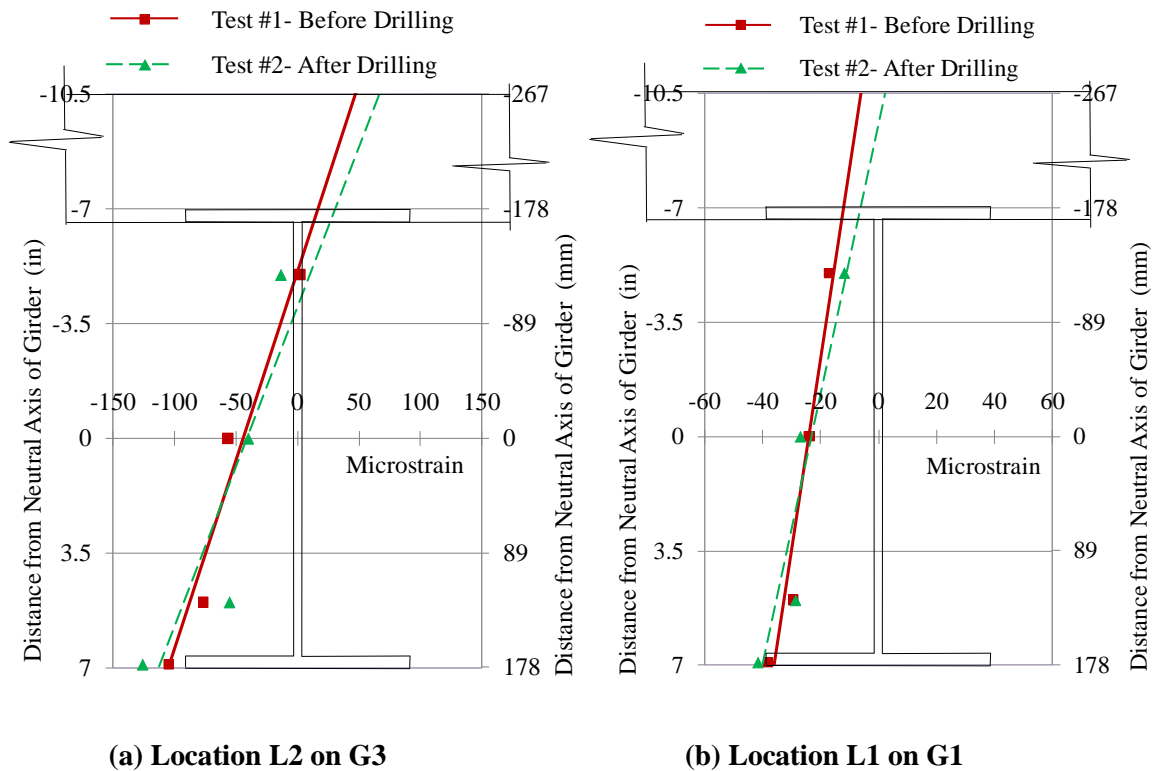


Fig. 5.34: Strain profile on center girder (G3) and edge girder (G1) at mid-span – before retrofit

Some composite action is thought to occur through friction due to the embedment of the top flange of the steel beams in the deck concrete. Additionally, the effect of the barrier/curb wall cast integral with the deck is considered to shift the neutral axis above the theoretical value. This is clearly visible in Fig. 5.34 (b) from the strain profile at mid-span instrumentation locations L1 at of edge girder (G1), where L1 lies approximately 203 mm (8 in.) away from the inside edge of the barrier. The neutral axis at this location is found in both of the initial tests to lie within the concrete deck.

The deflection results indicate that, under an AASHTO HS25 truck load, bridge response remains within the allowable serviceability criteria of $L/800$, or 8.4mm (0.33 in), even without any strengthening. From the measured strain and displacement data, it was understood that no significant loss of stiffness had occurred due to the drilling and

therefore post installation of shear studs could be carried out while permitting traffic to cross the bridge. From the two tests, only the data from Test #1 are used for comparison with the retrofitted bridge at each stage of strengthening.

5.6.2 Load Test #3 – After Post Installing Shear Studs

Due to the different truck weights used in the field tests, strain and deflection data was measured from individual tests were normalized to an AASHTO HS20 truck load, rear axle weight 142 kN (32,000 lbs), to facilitate comparisons. While such normalizations introduce small errors in the dataset (due to the differences in the two dual tire loads on either side of the truck), the effect of this on the results from the center girder (G3) for the load case described in Fig. 5.32, is thought to be minimal. This is especially true when the proximity of the loads on either side of the girder are taken into account.

Normalized deflection results along the mid-span in the direction perpendicular to traffic for the two load cases, before strengthening (Test #1) and after post installing shear studs (Test #3), are shown in Fig. 5.35. The deflections along the direction of traffic up to mid-span along the center girder (G3) are shown in Fig. 5.36. From the normalized deflection results in both figures, a decrease in deflection is seen at every instrumentation location, with a reduction of 27.2% being observed at mid-span due to the post installation of shear studs.

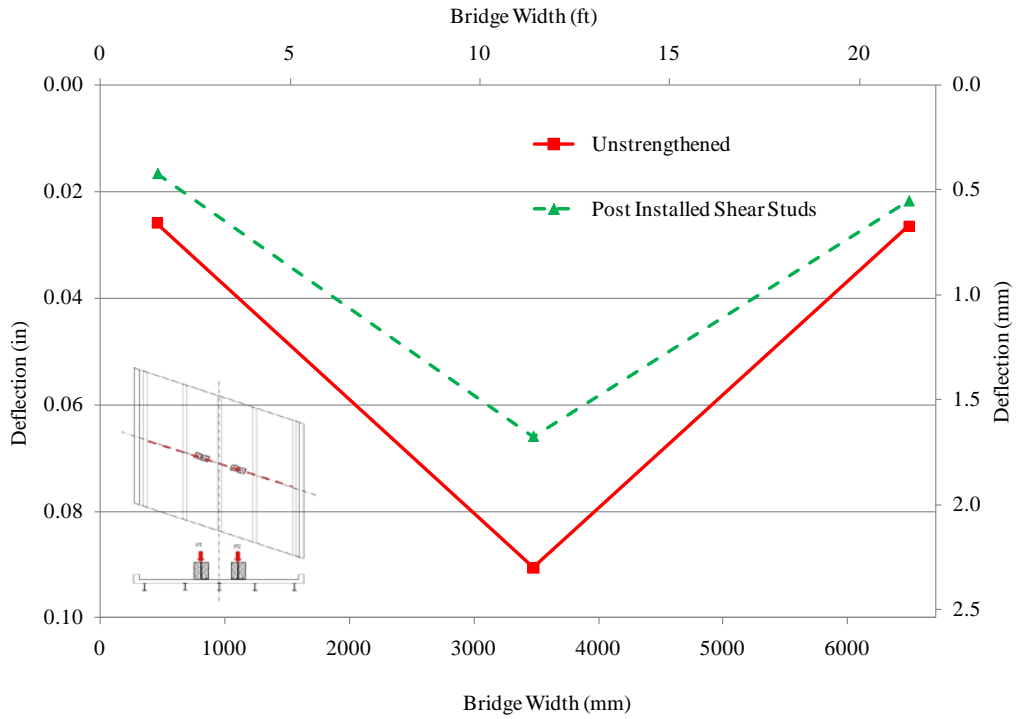


Fig. 5.35: Displacement perpendicular to direction of traffic at mid-span under HS20 truck load – before and after installing shear studs

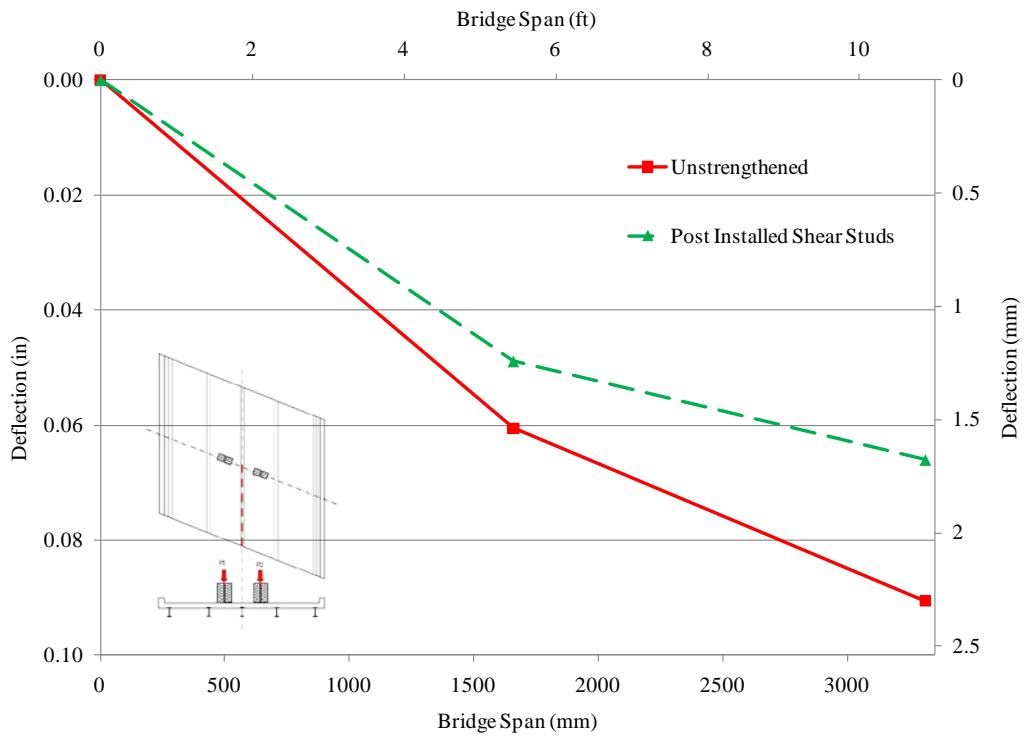


Fig. 5.36: Displacement along direction of traffic under HS20 truck load – before and after installing shear studs

The normalized strain results for the steel girder section at mid-span for the two load cases, before strengthening (Test #1) and after post installing shear studs (Test #3) are shown in Fig. 5.37. The strain profile at mid span of the center girder (L2 on G3) is seen to have shifted; a larger tensile strain is observed at all four strain gage locations on the beam compared to the beam before retrofit under the same normalized HS20 rear axle weight. The experimental neutral axis for the section after post installing shear studs, being only partially composite, is seen to be below the theoretical fully composite neutral axis and close to the top of the steel section. While the shift in the neutral axis position between the two field tests is attributed to post installation of shear studs, friction between the steel beams and concrete deck is considered to be the reason for the shift of neutral axis above the theoretical neutral axis.

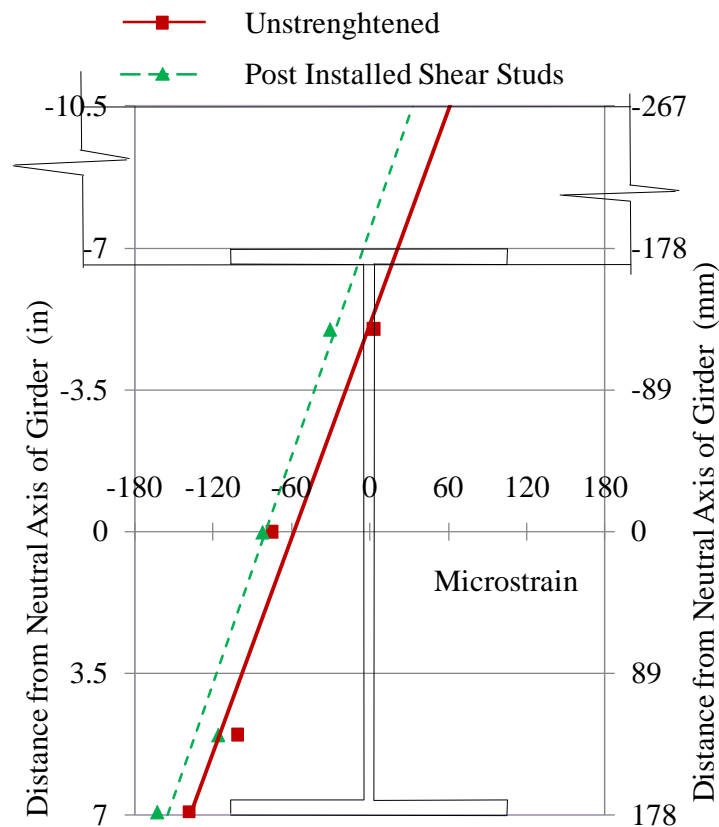


Fig. 5.37: Strain profile on center girder (G3) at mid-span under HS20 truck load – before and after installing shear studs

5.6.3 Load Test #4, #5 – After Applying UHM CFRP Laminates

Although the expected deflection criteria for the bridge was achieved through the post installation of shear studs, in order to evaluate the performance of UHM CFRP laminates in an actual field application each girder of the KY32 bridge was strengthened using 4 ultra high modulus CFRP laminates that were 1.2 mm (0.047 in.) thick and 6.096 m (20 ft.) long. The laminate sections represent an area approximately 14.5% of the area of the bottom flange. Test #4 performed approximately 4 weeks after application of laminates, and included use of the same instrumentation as the previous tests. In Test #5 foil type strain gages were attached to the laminates as described earlier, in addition to the typical instrumentation setup as all the other tests. The deflection and strain readings from Test #5 were also used to supplement the data obtained from Test #4. The performance of the bridge due to the application of ultra high modulus CFRP laminates is assessed as before using the normalized deflection and strain results obtained from Test #4 and compared with the results from Test #3 and Test #1.

Fig. 5.38 and Fig. 5.39 depict the normalized deflections perpendicular to traffic at mid-span and along the direction of traffic respectively. A general reduction in deflection is seen at all instrumentation locations except location L1, which is possibly be due to the difference in wheel loads on either side of the truck. A 5.3% reduction in deflection at mid-span of the center girder (G3) is observed over the post installed shear stud strengthened bridge. This corresponds to a total reduction of 31% in deflection over the initially unstrengthened bridge.

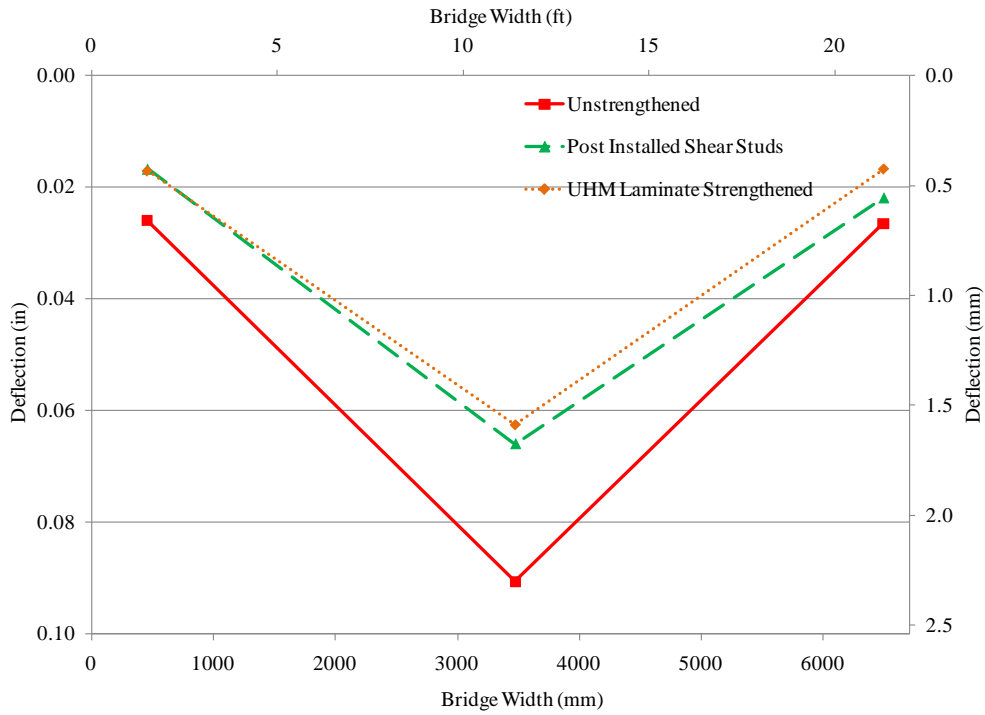


Fig. 5.38: Displacement perpendicular to direction of traffic at mid-span under HS20 truck load – before and after application of UHM CFRP laminates

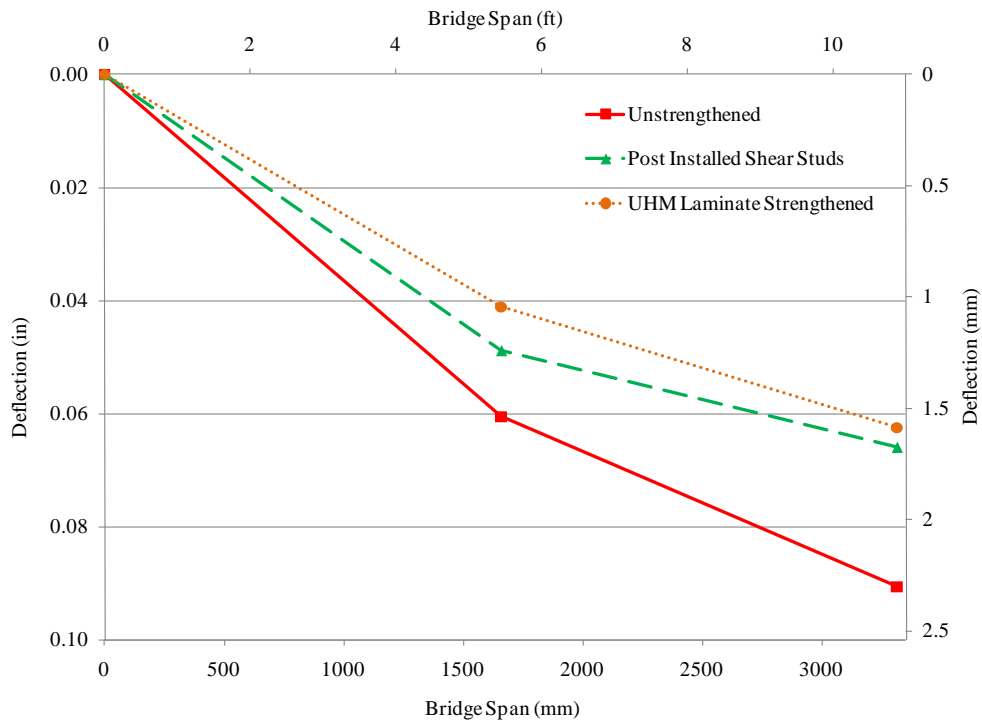


Fig. 5.39: Displacement along direction of traffic under HS20 truck load – before and after application of UHM CFRP laminates

The strain profile on the ultra high modulus CFRP strengthened steel section at mid-span of the center girder (G3) is shown in Fig. 5.40. As expected, strain in the steel has been reduced due to the application of laminates but the neutral axis has shifted slightly above the neutral axis observed after post installing shear studs.

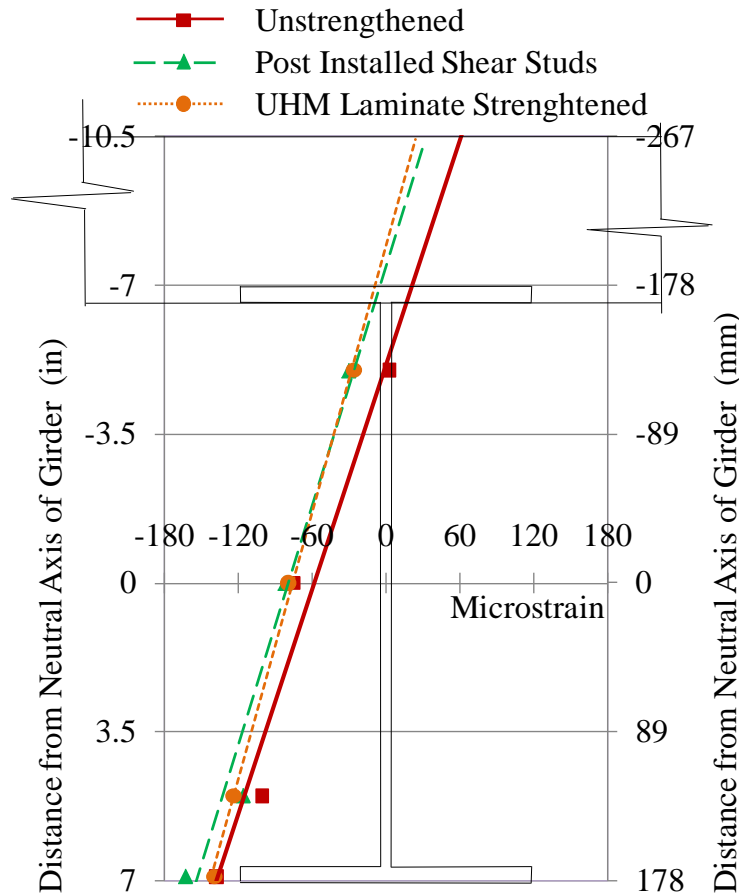


Fig. 5.40: Strain profile on center girder (G3) at mid-span under HS20 truck load – before and after application of UHM CFRP laminates

Strain profiles along the laminates were obtained from the normalized strain data, which were measured during Test #5. Data along the top and bottom laminates on the bottom flange of the center girder (G3) is shown in Fig. 5.41. The strain profile of the bottom left laminate has been plotted up to the center of the girder while the corresponding readings obtained from the strain gages on the top and right laminate for corroboration have been

added to the plot. As seen in the figure, beyond approximately 2290 mm (90 in) from mid-span, strains in the laminates become compressive. This was expected due to the support conditions of the bridge not behaving completely as a simply supported bridge. The maximum recorded strain at mid-span was 171 microstrains, which is less than 5% of the minimum rupture strain observed experimentally (Chapter 2). Due to the low strains within the compressive region of the bottom flange, the propensity for compressive failure and debonding of the laminate is small.

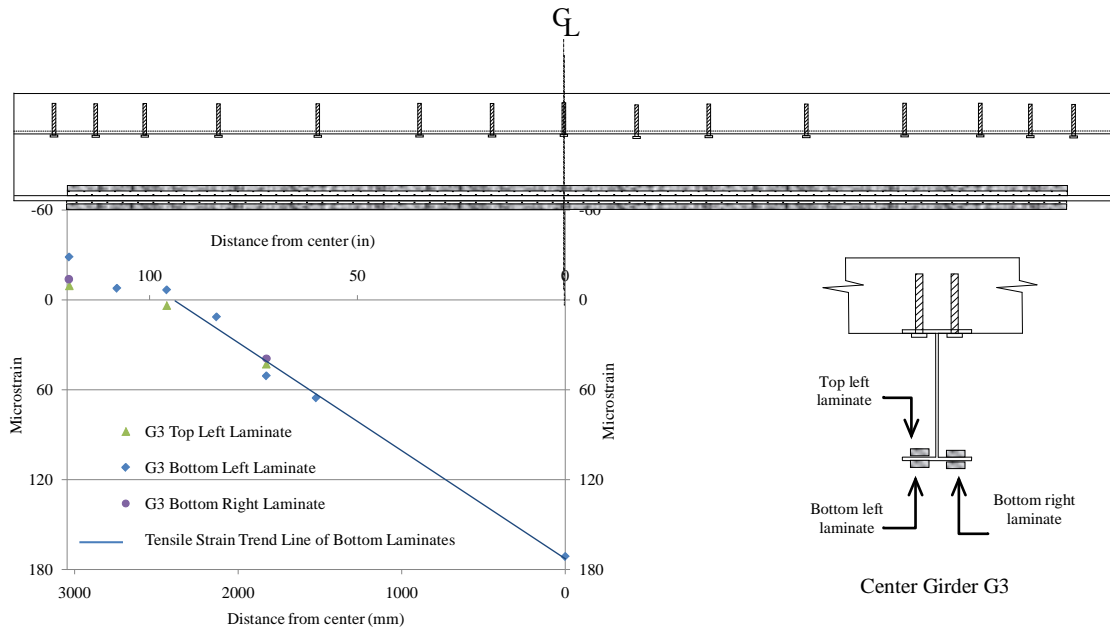


Fig. 5.41: Strain profile in the UHM CFRP laminates on the center girder (G3) under an HS20 truck load

CHAPTER 6

FINITE ELEMENT ANALYSIS AND PARAMETRIC STUDY OF BRIDGE

6.1 Introduction

The analytical study of the KY32 Bridge comprised of two main sections of finite element analysis (FEA). The first part of the finite element analysis composed of developing a representative finite element model to depict the behavior of the field tested bridge. The initial load test results from different load cases were used to model the behavior of the bridge in the “unstrengthened” state. The model was changed at each stage of strengthening to represent the strengthening processes by adding or changing the elements to represent the effect of shear studs and laminates. Once the different stages of strengthening were completed and the data from the field tests were evaluated, the model predicted results were compared with the field test data. The model was able to simulate the reaction of the bridge to the applied loads satisfactorily at each stage of strengthening.

The second part of the analysis focused on the application of the calibrated bridge model. The three different models representing the unstrengthened, strengthened using post-installed shear studs and further strengthened by the application of ultra high modulus CFRP laminates were used to predict the behavior of the bridge under different truck type loads. Furthermore, the models were used to assess the load rating of the bridge. The load rating obtained using the stresses obtained through the finite element models are thought to better represent the performance of the bridge than the load rating of the bridge performed assuming theoretical conditions (detailed in Chapter 4). The bridge model was further used to perform a parametric study of the bridge to evaluate the performance of the bridge under different laminate thicknesses and support conditions.

6.2 KY 32 Bridge Finite Element Analysis

In order to understand the behavior of the bridge, before and after each stage of strengthening, as well as to predict bridge behavior under various loads, a representative finite element model of the KY 32 Bridge was developed. The model was built and analyzed using finite element software ANSYS (ANSYS 2009). The model is calibrated using field test data in the form of deflections and strains obtained at the four instrumentation locations discussed in Chapter 5. As the bridge plans and technical notes were unavailable for the KY 32 Bridge, material properties had to be estimated. Additionally, while the support conditions were assumed to be simply supported for theoretical calculations, the physical conditions were closer to being fixed since concrete diaphragms were cast over the steel girders at the abutments.

6.2.1 Element Selection

The wide flange steel girders in the KY 32 bridge model were built up using 4-node SHELL181 elements available in the FEA software ANSYS. The element has six degrees of freedom at each node; three translations and three rotations in the three mutually perpendicular x, y, and z axis. The SHELL181 element was selected as it has the capacity to be modified later to depict the applied ultra high modulus CFRP laminates, specifically, by changing the element characteristics to represent layered construction. The original steel shell section can be modified to represent a section where the steel section is sandwiched between an epoxy and CFRP layer and the thickness, material properties and the number of integration points through the thickness can be input separately for each layer.

The concrete deck was modeled in ANSYS using SOLID185 elements. Each element has 8-nodes and three translational degrees of freedom at each node in the nodal x, y, and z directions. The element type also has large deflection and large strain capabilities. Three layers of elements were utilized in creating the 203 mm (8 in) deck with the layer

boundaries corresponding to the reinforcing bar mat location. The reinforcement within the deck was modeled using 2-node LINK8 spar elements, which are uniaxial tension-compression element with three translational degrees of freedom at each node. The LINK8 elements were modeled to represent ASTM #5 bars in both the longitudinal and transverse directions, where each bar is 15.9 mm (0.625 in) in diameter. The reinforcing bars on the top and bottom mats spaced 305 mm (12 in) in both directions.

From the field measurements it was clear that some degree of composite action existed between the steel beam and the concrete deck. This was thought to be due to friction between the top flange of the steel section and the concrete deck. The model was developed with overlapping nodes at the steel girder and concrete deck interface. Since the deck was cast covering the top flange of the steel girders, the displacement perpendicular to the direction of traffic was restricted in the structure. Therefore overlapping nodes in the steel girder top flange and concrete deck were coupled in the corresponding degrees of freedom. Since separation of the concrete deck from the steel beams was also not observed, the vertical degrees of freedom were also coupled between overlapping nodes. The element COMBIN40 was used to represent friction between the concrete deck and the steel beams. The element has a spring-slider mechanism and a damper in parallel coupled to a gap in series with only one degree of freedom at each node. In the model, this degree of freedom was defined as translation along the direction of traffic on the bridge. The damper capabilities were removed from the analysis.

While in the preliminary beam analysis (refer to Chapter 4) 'beam' type elements were used to model the shear connectors, in order to incorporate the slip at the steel concrete interface, shear connectors were later modeled using COMBIN39 elements. A similar approach was used by Kwon (2008). The element can be set as a uniaxial tension-compression element with three degrees of translational freedom at each node. The advantage of the element in utilizing it to represent shear connector slip is its nonlinear force-deflection capability. The load-slip relationship was modeled using the equation proposed by Ollgaard et al. (1971).

$$Q = Q_u (1 - e^{-18\Delta})^{2/5} \quad (6.1)$$

Where; Q_u = Ultimate strength of shear connector
 Δ = Slip of shear connector

The ultimate strength of a shear connector Q_u according to Ollgaard et al. (1971) and adopted by the AISC LRFD specifications (2005) is given by;

$$Q_u = 0.5A_{sc}(f'_c E_c)^{0.5} \leq A_{sc}F_u \quad (6.2)$$

Where; A_{sc} = Cross sectional area of shear stud
 E_c = Modulus of elasticity of concrete (taken as $33w_c^{1.5}\sqrt{f'_c}$)
 F_u = Specified minimum tensile strength of shear connector

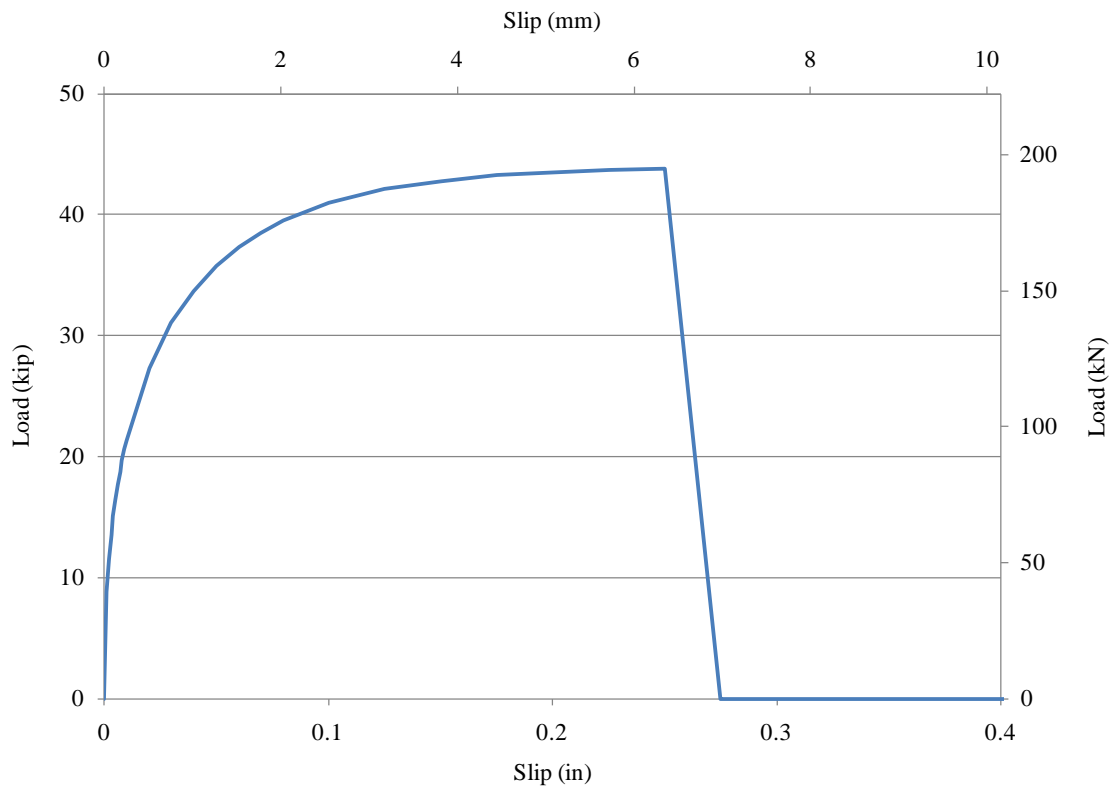


Fig. 6.1: Load-slip relation for shear connectors

Selection of the 2 node unidirectional element, which has the capability to incorporate a non-linear force-deflection relationship, enabled the modeling of load-slip for the shear studs. The load-slip relation for the 22 mm (0.875 in) diameter shear studs with a manufacturer specified yield strength of 724 MPa (105 ksi) is shown in Fig. 6.1. While the use of this type of element can accurately predict the behavior of the shear connectors, it is thought that the analysis might be affected when the section neutral axis is within the concrete, causing the concrete to fail in tension. While the elements performed well for this study, their application following concrete failure in tension should be evaluated for sections with the neutral axis within the concrete deck. Laboratory beam tests carried out by Kwon (2008) found the maximum slip at the ends to be 6.86 mm (0.27 in) for the adhesive anchor type shear connectors. A similar maximum slip was adopted for the load-slip relation as seen in the Fig. 6.1.

The 'spring' like element COMBIN14 was used to model the partial fixity at the girder ends. The girder ends were restricted in movement in the vertical direction and also in a direction perpendicular to traffic due to the concrete diaphragm. As a result the nodal degrees of freedom at the girder ends were restricted in these directions. The 2 node longitudinal COMBIN14 element was modeled to resist only uniaxial tension-compression in the direction of traffic and the spring stiffness was adjusted to match the observed field measurements.

6.2.2 Material Models

The size and location of the rebars were found from ground penetrating radar (GPR) as described in Chapter 5. Both the transverse and longitudinal rebars were found to be ASTM #5 bars with a diameter of 15.9 mm (0.625 in). The rebars were modeled as having bi-linear elastic-perfectly plastic steel material model with a yield strength of 414 MPa (60 ksi).

The steel girders of the KY 32 Bridge, from the measured dimensions, were found to be W14 × 30 standard wide flange sections. Therefore the steel was identified as ASTM A992 with minimum yield strength of 345 MPa (50 ksi). Both the rebar and girder steel were modeled to have bi-linear elastic-perfectly plastic stress-strain relations with an elastic modulus of 200 GPa (29000 ksi). Strain hardening was not considered, but a small tangent modulus beyond yielding was employed for the stability of the analysis. The yield stress of the girder steel was not adjusted to account for the dead load of the bridge as the field tests showed that the steel would remain in the elastic range.

The deck concrete strength was measured through non-destructive rebound hammer tests. Average compressive strength of the concrete was evaluated as 34.5 MPa (5 ksi). A multi-linear stress-strain material model was used for the concrete to represent a modified Hognestad (1951) stress-strain relationship. The tensile strength was taken as $0.1\sqrt{f'_c}$. The material model used for concrete in the analysis is shown in Fig. 6.2.

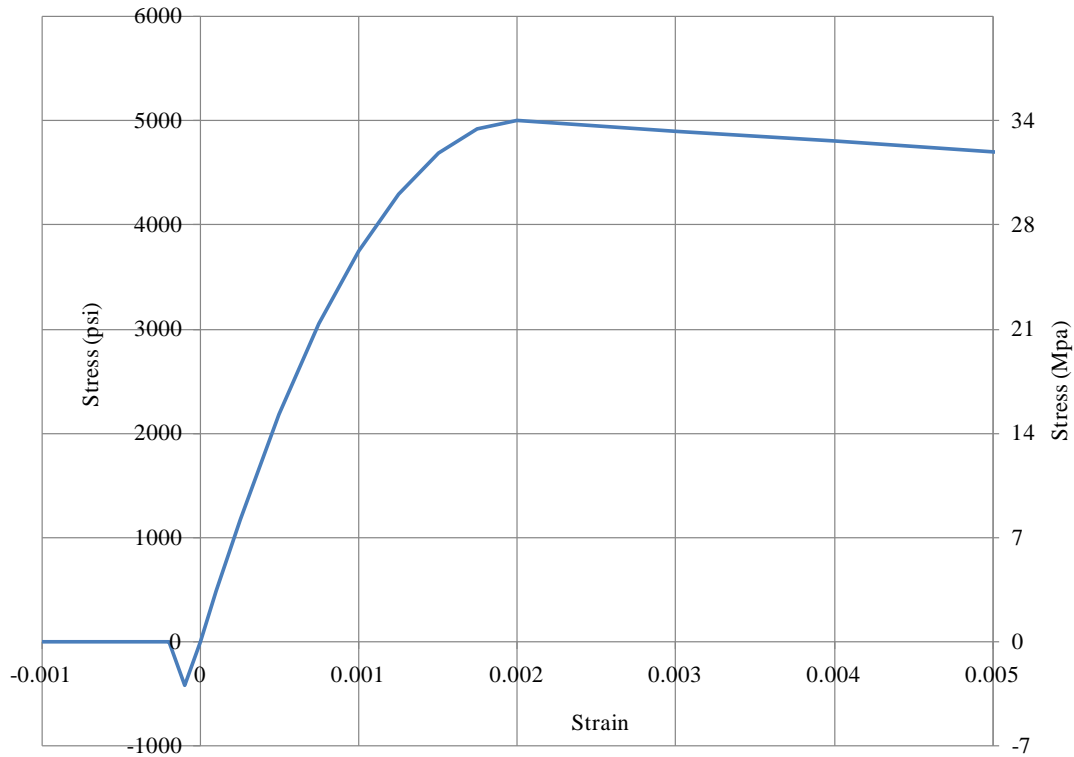


Fig. 6.2: Concrete Stress-Strain curve

The modulus of the ultra high modulus CFRP was taken as 483 GPa (70,000 ksi) as found in the material testing. While the laboratory testing showed a higher tensile strength than the manufacturer specified strength, since the laminates were not expected to reach their ultimate strengths, the maximum tensile strength was set to the manufacturer specified strength of 1200 MPa (174 ksi). The epoxy was modeled with an elastic modulus of 3.0 GPa (436 ksi) and a tensile strength of 37.1 MPa (5 ksi). The values were obtained from the extensive research carried out by Shnerch (2005) and Dawood (2005) on the same epoxy, and also supported by the laboratory testing (see Chapter 2). A linear stress-strain relation was specified up to failure for both the CFRP and epoxy.

6.2.3 Analysis and Results

Patch loads representing the dual axle tire positions of the load truck used in the field tests were applied in the bridge deck model. The static finite element analysis considered both the material nonlinearities as well as geometric nonlinearities. The Newton-Raphson procedure was used to solve the nonlinear equations with the Arc-Length method employed to improve convergence. Load increments were automated and handled by the ANSYS solution algorithm. The final bridge model is depicted in Fig. 6.3.

The deflection and strain data were obtained for the corresponding locations from where measurements were obtained in the field tests and plotted for comparison. The deflections obtained using the finite element model along the direction of traffic and perpendicular to traffic are compared to the experimental values in Fig. 6.4 and Fig. 6.5. While the deflections at mid-span of the edge girders are seen to be slightly greater than the measured values, and at mid-span of the center girder the model predicted deflections are slightly lower than the field test data, overall the analytical deflection results match the experimental results well.

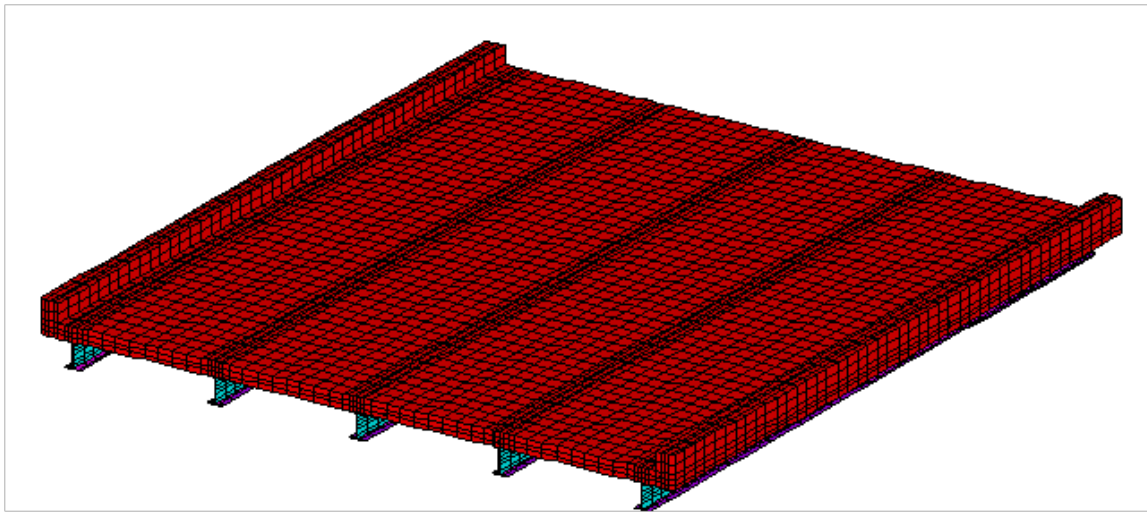


Fig. 6.3: 3-D Bridge model

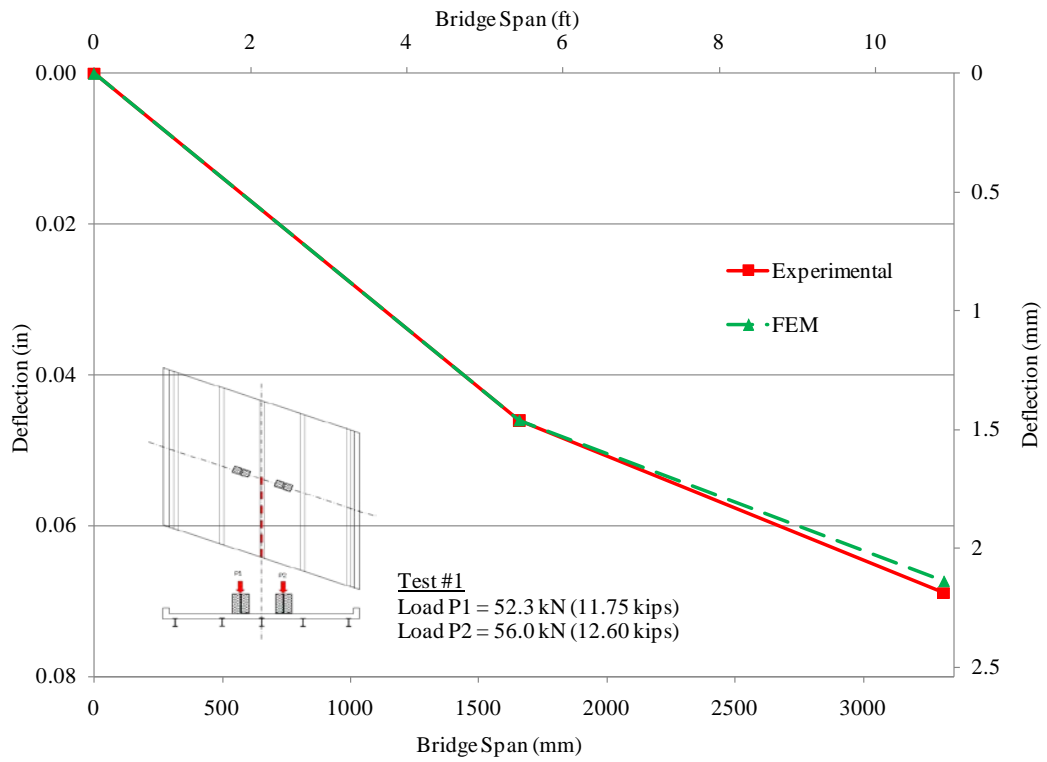


Fig. 6.4: Displacement along the direction of traffic – before retrofit

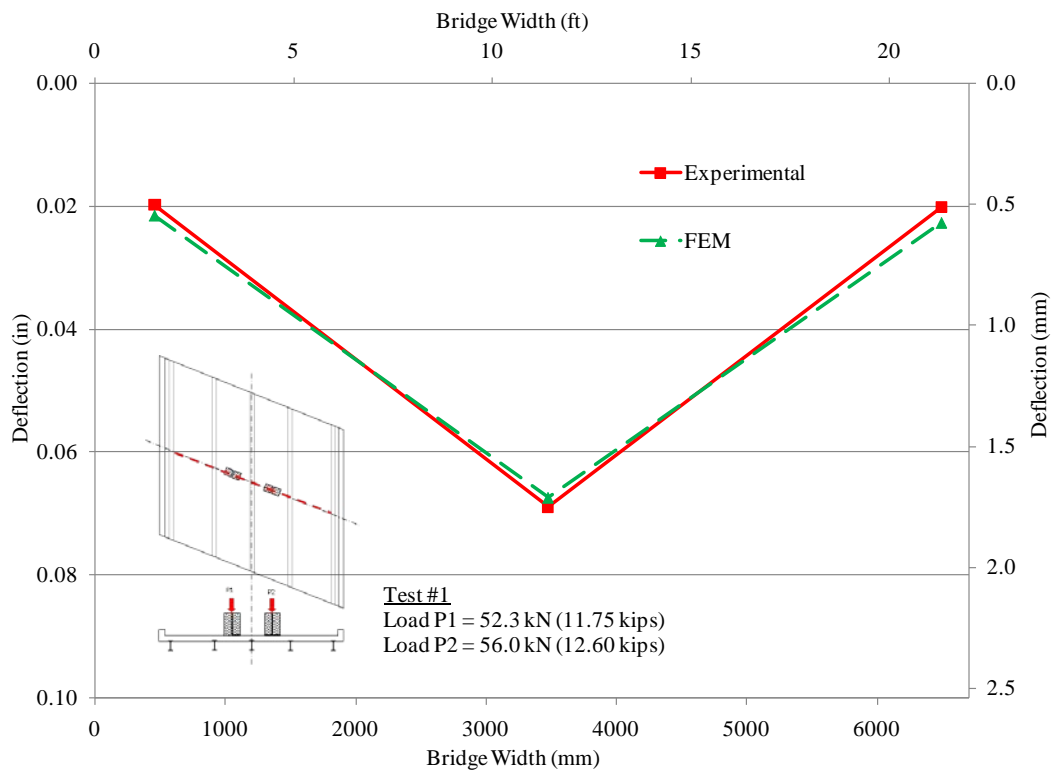


Fig. 6.5: Displacement perpendicular to direction of traffic at mid-span – before retrofit

The strain profiles obtained from the finite element analysis at mid-span of the center girder (G3) and edge girder (G1) are compared with the experimental readings obtained through strain gages in Fig. 6.6. The experimental results show a slightly higher degree of composite action than the finite element results at both locations, considering the unknown geometric and material properties of the bridge, the results are thought to be acceptable in validating the finite element model.

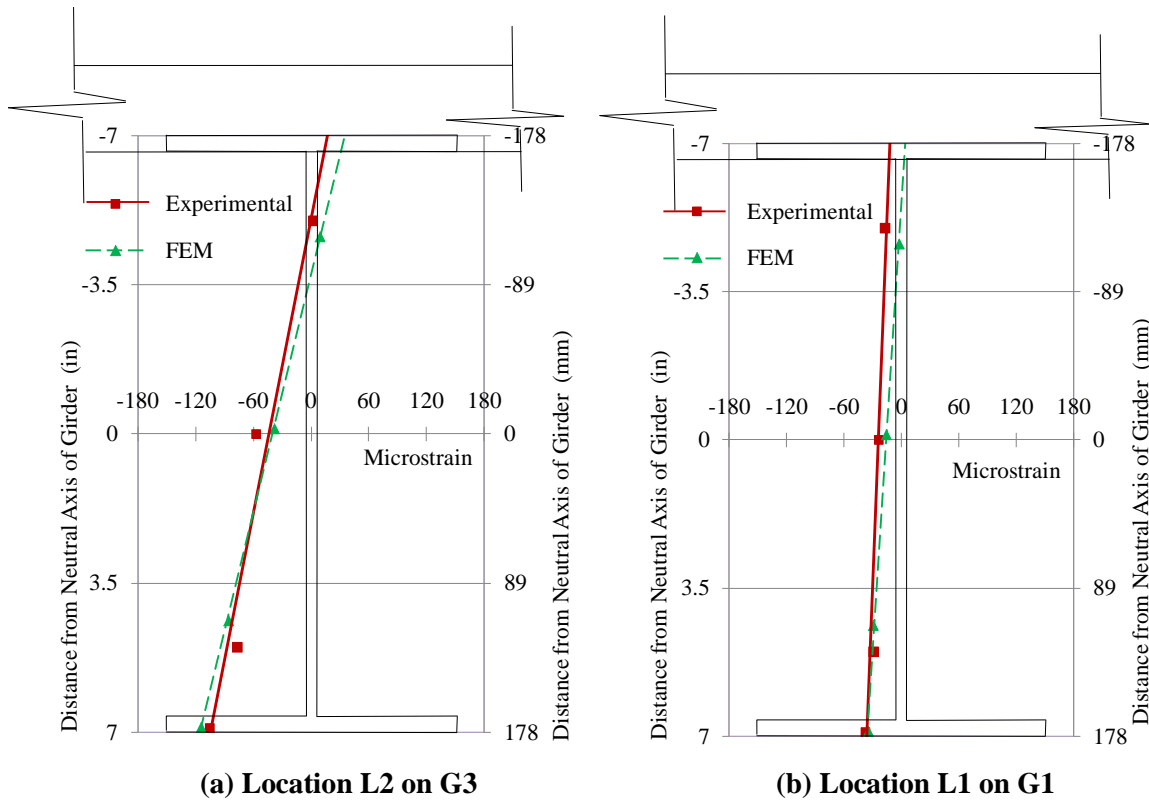


Fig. 6.6: Strain profile on center girder (G3) and edge girder (G1) at mid-span – before retrofit

When analyzing the bridge with the shear studs installed the model was modified by including the COMBIN39 elements representing the shear studs at the corresponding locations (refer to Fig. 5.5 for shear stud locations on each beam). It should be noted that the field application points were not always consistent with Fig. 5.5, since holes for the studs were drilled while avoiding rebar locations. Moreover some of the stud locations on the finite element model were shifted slightly from actual field application points to correspond with node locations in the model. The applied load was also modified in the analysis to match the field load test truck weight, which differed slightly from the truck weight used prior the retrofit. Deflections along the direction of traffic and perpendicular to traffic at mid-span are compared between the field test data and finite element analysis data in Fig. 6.7 and Fig. 6.8.

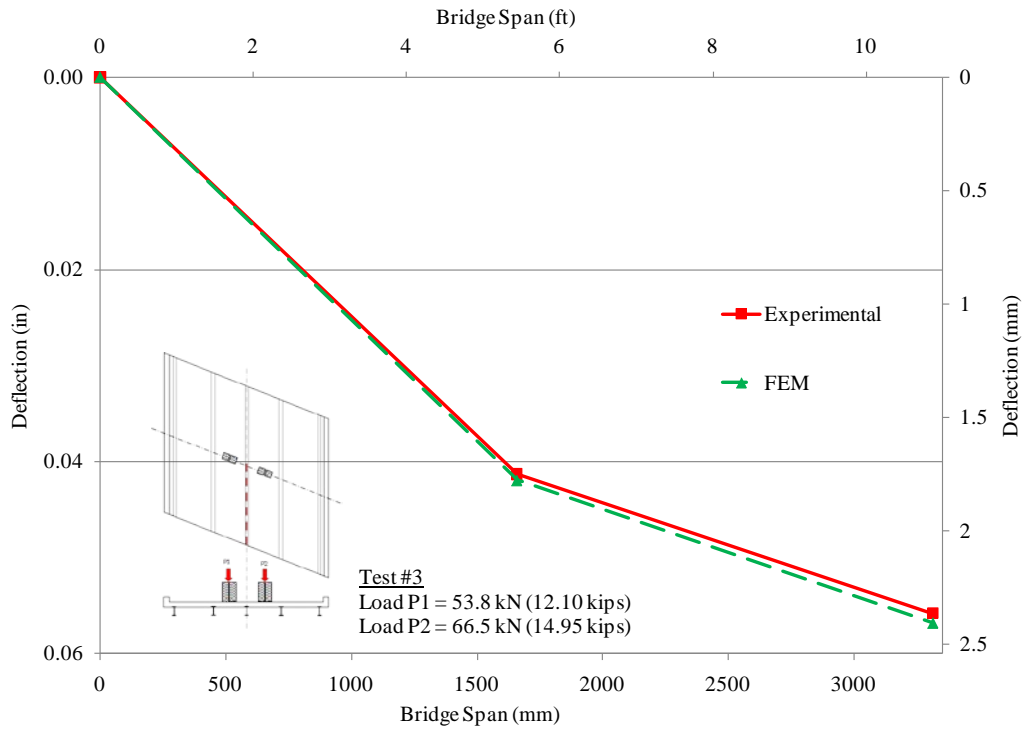


Fig. 6.7: Displacement along the direction of traffic – after post installing shear studs

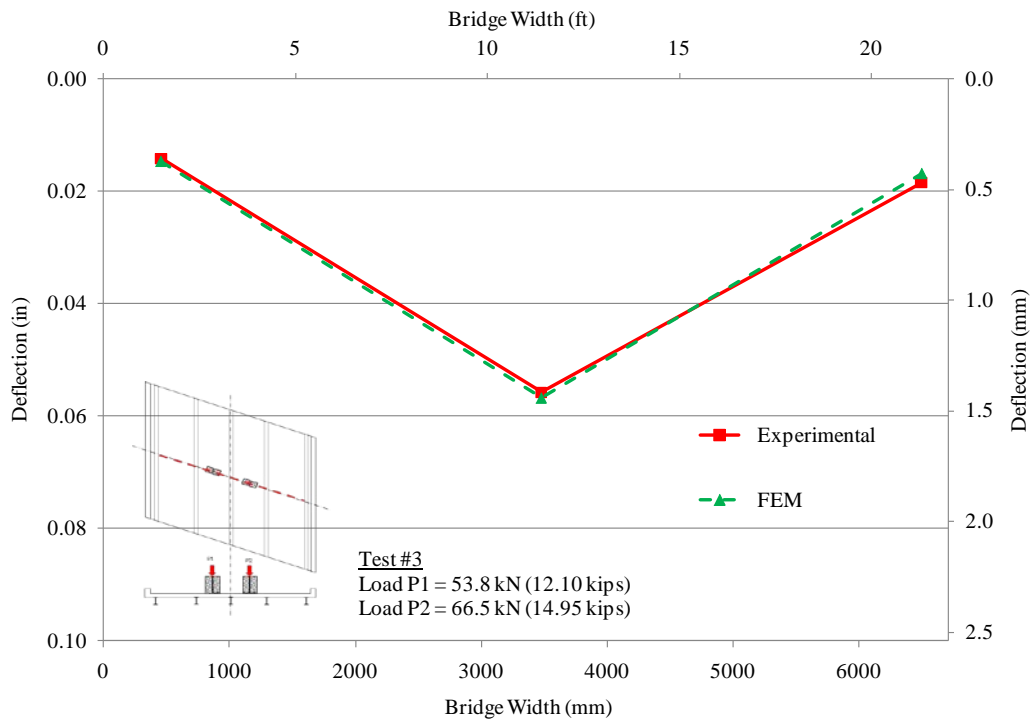


Fig. 6.8: Displacement perpendicular to direction of traffic at mid-span – after post installing shear studs

The deflections were seen to match the field measurements in both directions quite well. The strain measurements taken at mid-span of the center girder (G3), instrumentation location L2, and edge girder (G1), instrumentation location L1, are compared with the finite element model predictions in Fig. 6.9. The strain values are also seen to match the field measured values well. The experimental and finite element model predicted neutral axis is seen to be approximately at the steel-concrete interface. Both the experimental and analytical neutral axis is found to be below the theoretical fully composite neutral axis, which is 245 mm (9.64 in) above the theoretical non-composite neutral axis, or approximately 66 mm (2.6 in) above the top of the steel beam.

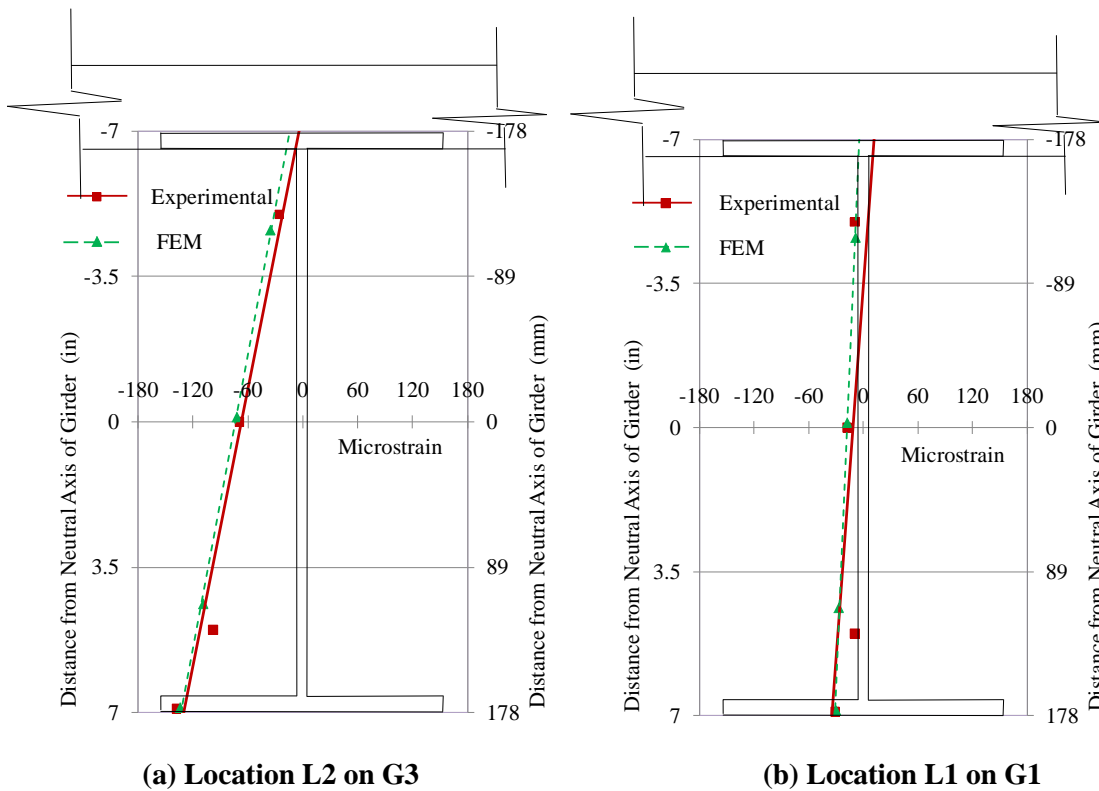


Fig. 6.9: Strain profile on center girder (G3) and edge girder (G1) at mid-span – after post installing shear studs

The SHELL181 element used to model the bottom flange of the steel section was modified to a layered shell section to model the applied CFRP laminates. A layer of ultra high modulus CFRP laminate and epoxy was added to the top and bottom of the existing steel in two elements of the four element wide bottom flange to represent the total width of the applied laminates. Each layer was given the corresponding material properties and thickness. While in the actual application of laminates a 25.4 mm (1 in) gap was left between the two laminate strips, the strips were modeled adjoining each other for simplicity. Fig. 6.10 shows the applied laminate at the edge of one of the steel beams.

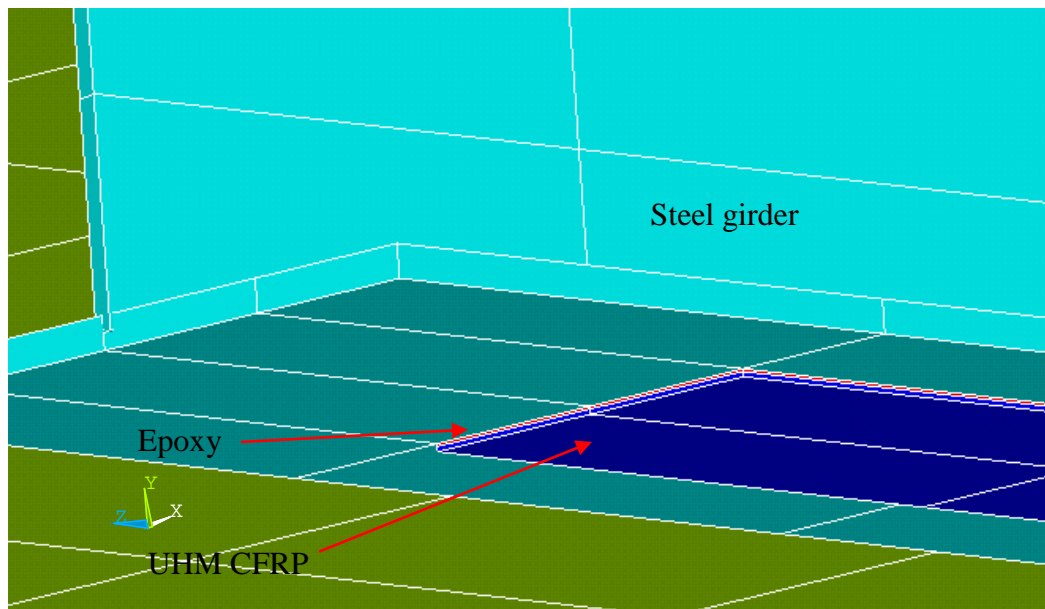


Fig. 6.10: Steel girder model with epoxy and CFRP layer

The deflections along the direction of traffic as well as perpendicular to traffic at mid-span are compared from the field test data and the analytical finite element data in Fig. 6.11 and Fig. 6.12 for the applied load of 135.7 kN (30.5 kip). The deflection results obtained from the finite element model are seen to be in good agreement with the field data obtained via LVDTs at the instrumentation locations.

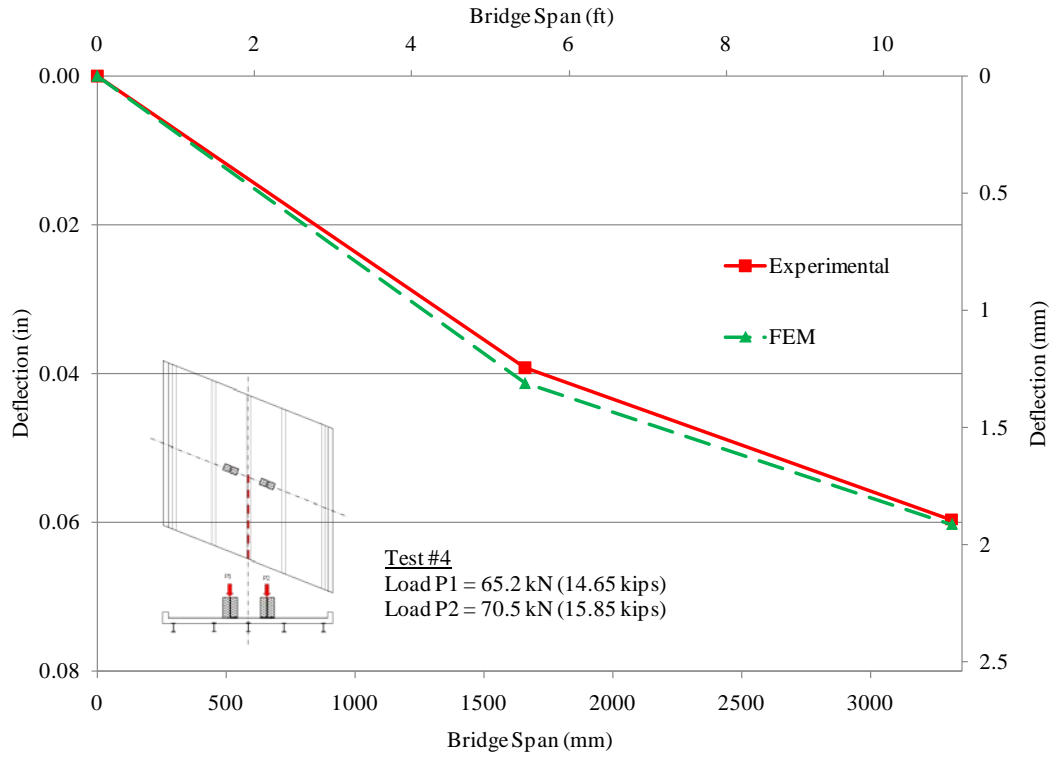


Fig. 6.11: Displacement along the direction of traffic – after laminate application

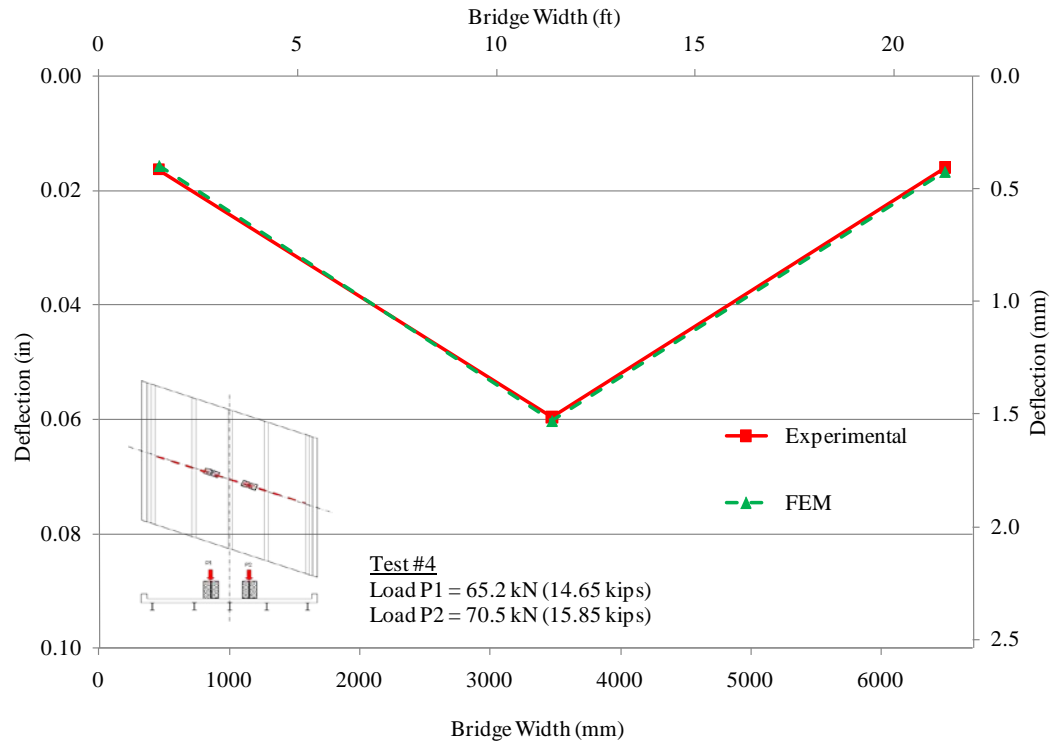


Fig. 6.12: Displacement perpendicular to direction of traffic at mid-span – after laminate application

The strains recorded in the field using strain gages are compared with the strains obtained from the bridge model in Fig. 6.13. The finite element model strains are seen to be in good agreement with the values observed in the field test. Both the experimental and finite element model predicted neutral axis lie slightly above the steel concrete interface.

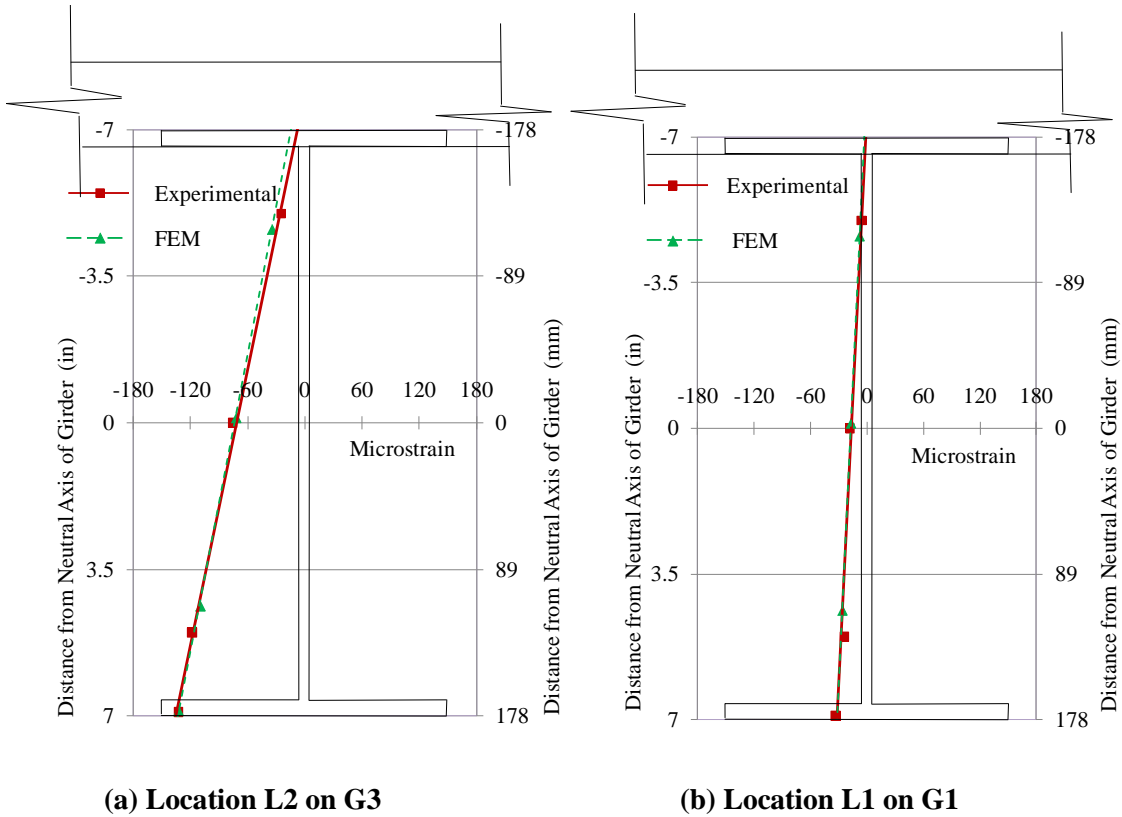


Fig. 6.13: Strain profile on center girder (G3) and edge girder (G1) at mid-span – after laminate application

The results of the strengthening process, as seen by utilizing the calibrated finite element model, are shown in Fig. 6.14 and Fig. 6.15. Specifically, deflections in the direction of traffic (Fig. 6.14) and perpendicular to traffic (Fig. 6.15) at mid-span are shown before strengthening and following each stage of strengthening under an HS20 truck load with a rear axle weight of 142 kN (32,000 lbs). The reduction in deflections due to post installation of shear studs is approximately 24.2% at mid span. The reduction due to application of laminates over the post-installed shear studs at mid-span is approximately 5.9%, while the overall reduction in deflection due to both types of strengthening is 28.7%.

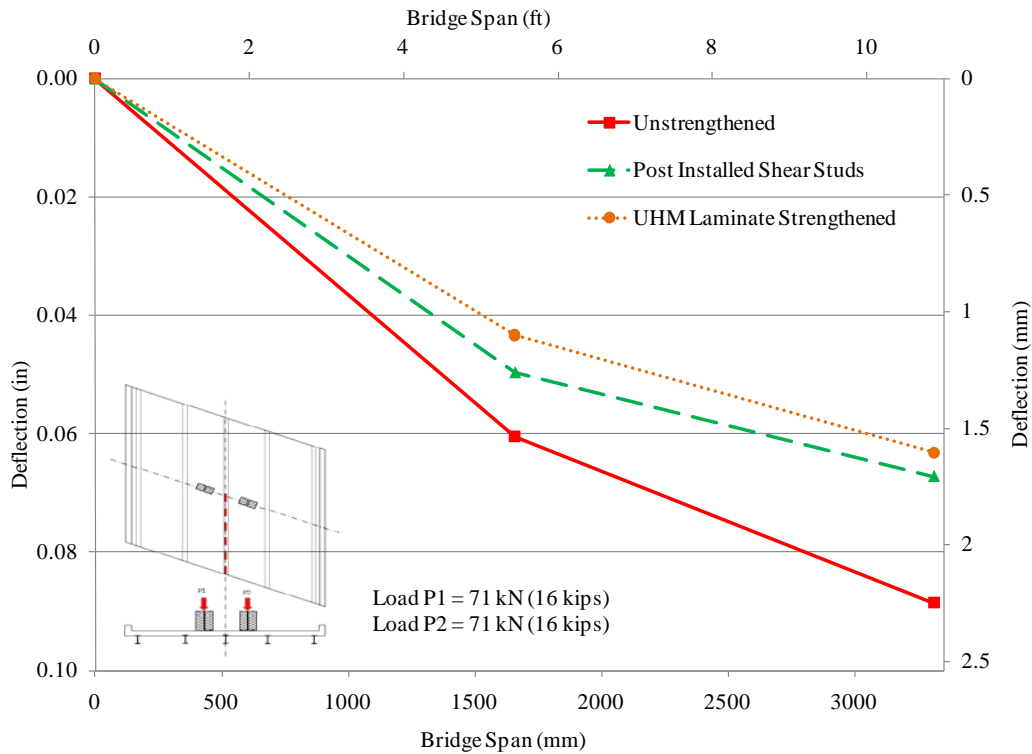


Fig. 6.14: Displacement along the direction of traffic under HS20 truck load

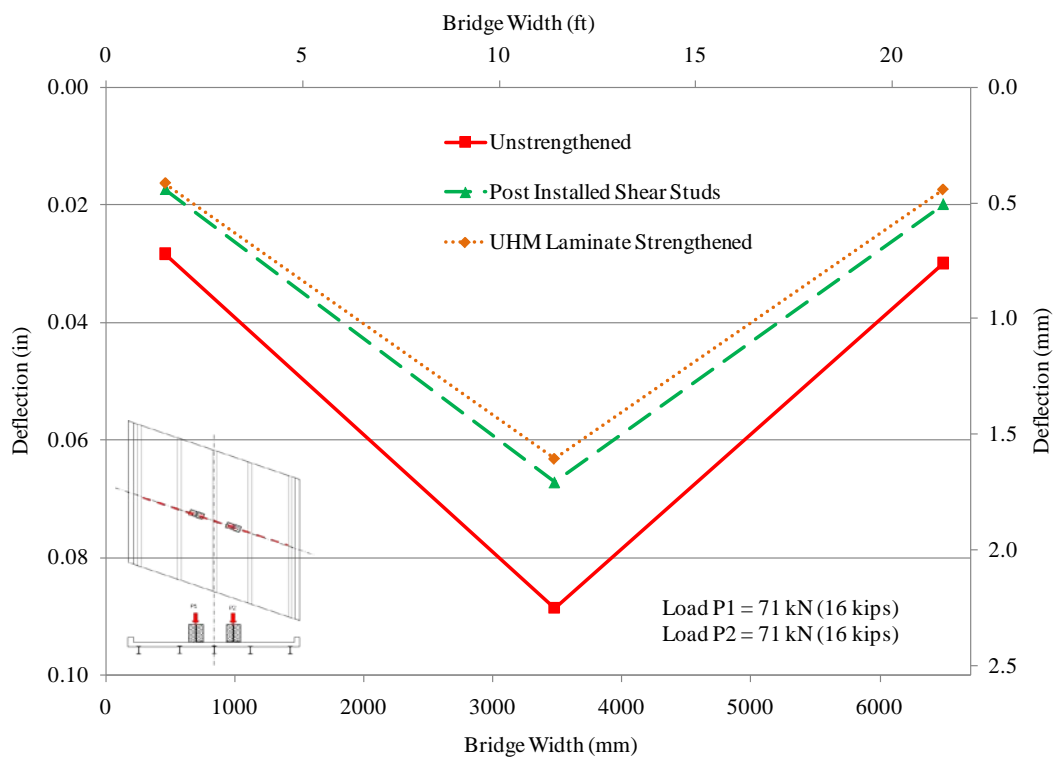


Fig. 6.15: Displacement perpendicular to direction of traffic at mid-span under HS20 truck load

The strain profiles obtained using the models at mid span of the center girder (G3) and edge girder (G1) are given in Fig. 6.16. The distance to the neutral axis from the center of the steel section is seen to increase after post installing shear studs, and then decrease slightly due to the added stiffness of the ultra high modulus CFRP laminates at the bottom flange. The strains in the steel section are also seen to be reduced due to application of the CFRP laminates.

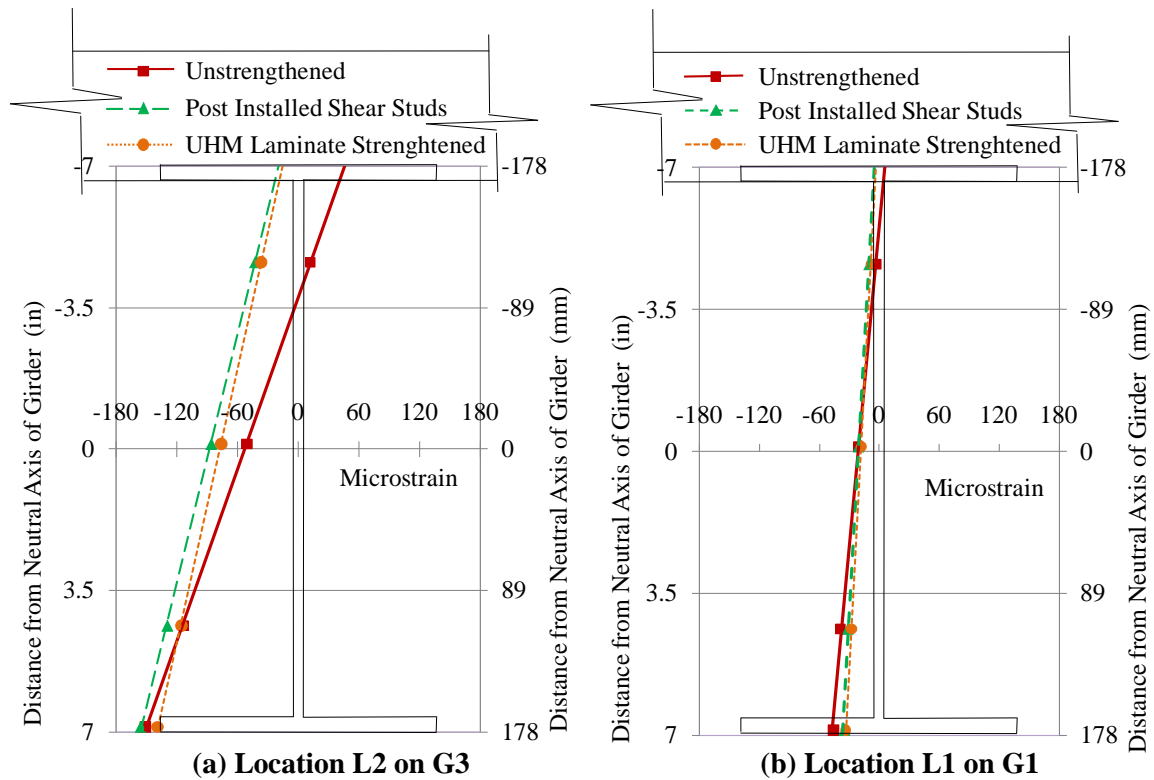


Fig. 6.16: Strain profile on center girder (G3) and edge girder (G1) at mid-span – after laminate application

6.3 Load Rating Using Finite Element Results

The calibrated finite element model was used to perform a load rating analysis on the KY32 Bridge under different truck types with different rear axle configurations and weights to supplement the rating obtained theoretically. Maximum stresses were recorded at mid-span of the center girder at location L2, recall Fig. 5.23, for the different truck types detailed in Chapter 4. Only the non-composite model and the model with post installed shear studs are considered for the load rating in order to compare with the theoretical load rating. Since the degree of composite action due to friction between the steel top flange and concrete deck is difficult to measure, the section modulus of the fully composite girder is used conservatively to obtain both Dead and Live load moments. Complete details of the analysis are given in Appendix B. A summary of the load rating results before and after post installing shear studs is given in Table 6.1 and Table 6.2.

**Table 6.1a: Truck Weight Analysis using data from calibrated finite element model
(Non-Composite bridge – prior to retrofit) – Metric Units**

Truck Type	Rear Axle Weight (kN)	Non-Composite Bridge			
		Dead Load Moment (MPa)	Live Load Moment (MPa)	“Inventory Level” Truck Weight (kN)	“Operational Level” Truck Weight (kN)
Type 1	142.3	19.3	30.3	322.1	537.3
HS25	177.9	19.3	37.9	580.0	968.8
Type 2	108.4	19.3	43.4	317.6	532.0
Type 3	88.3	19.3	47.6	376.3	630.8
Type 4	78.3	19.3	31.7	615.6	1028.4

**Table 6.1b: Truck Weight Analysis using data from calibrated finite element model
(Non-Composite bridge – prior to retrofit) – Customary US Units**

Truck Type	Rear Axle Weight (kips)	Non-Composite Bridge			
		Dead Load Stress (ksi)	Live Load Stress (ksi)	“Inventory Level” Truck Weight (tons)	“Operational Level” Truck Weight (tons)
Type 1	32.0	2.8	4.4	36.2	60.4
HS25	40.0	2.8	5.5	65.2	108.9
Type 2	24.38	2.8	6.3	35.7	59.8
Type 3	19.84	2.8	6.9	42.3	70.9
Type 4	17.6	2.8	4.6	69.2	115.6

**Table 6.2a: Truck Weight Analysis using data from calibrated finite element model
(Composite bridge – after retrofit) – Metric Units**

Truck Type	Rear Axle Weight (kN)	Composite Bridge			
		Dead Load Moment (MPa)	Live Load Moment (MPa)	“Inventory Level” Truck Weight (kN)	“Operational Level” Truck Weight (kN)
Type 1	142.3	19.3	31.7	663.7	1106.7
HS25	177.9	19.3	40.0	1185.0	1973.2
Type 2	108.4	19.3	44.8	665.5	1109.4
Type 3	88.3	19.3	49.0	790.9	1317.6
Type 4	78.3	19.3	32.4	1298.9	2167.24

**Table 6.2b: Truck Weight Analysis using data from calibrated finite element model
(Composite bridge – after retrofit) – Customary US Units**

Truck Type	Rear Axle Weight (kips)	Composite Bridge			
		Dead Load Stress (ksi)	Live Load Stress (ksi)	“Inventory Level” Truck Weight (tons)	“Operational Level” Truck Weight (tons)
Type 1	32.0	2.8	4.6	74.6	124.4
HS25	40.0	2.8	5.8	133.2	221.8
Type 2	24.38	2.8	6.5	74.8	124.7
Type 3	19.84	2.8	7.1	88.9	148.1
Type 4	17.6	2.8	4.7	146.0	243.6

6.4 Parametric Study of KY 32 Bridge

The calibrated finite element model can be used to predict the behavior of the bridge under different load conditions as well as different boundary conditions. The model was further used in a parametric study to evaluate the effectiveness of the application of thicker UHM CFRP laminates on the KY32 Bridge. Fig. 6.17 depicts the displacement perpendicular to traffic at mid-span of the bridge under an HS20 truck load at each stage of strengthening while the predicted displacements with commercially available 4 mm (0.157 in.) thick laminates has been also included. As layering of laminates is common to obtain thicker laminate sections, the effect of applying an additional 4 mm laminate over the bottom layer of laminates on the bottom flange was also evaluated and shown in Fig. 6.17.

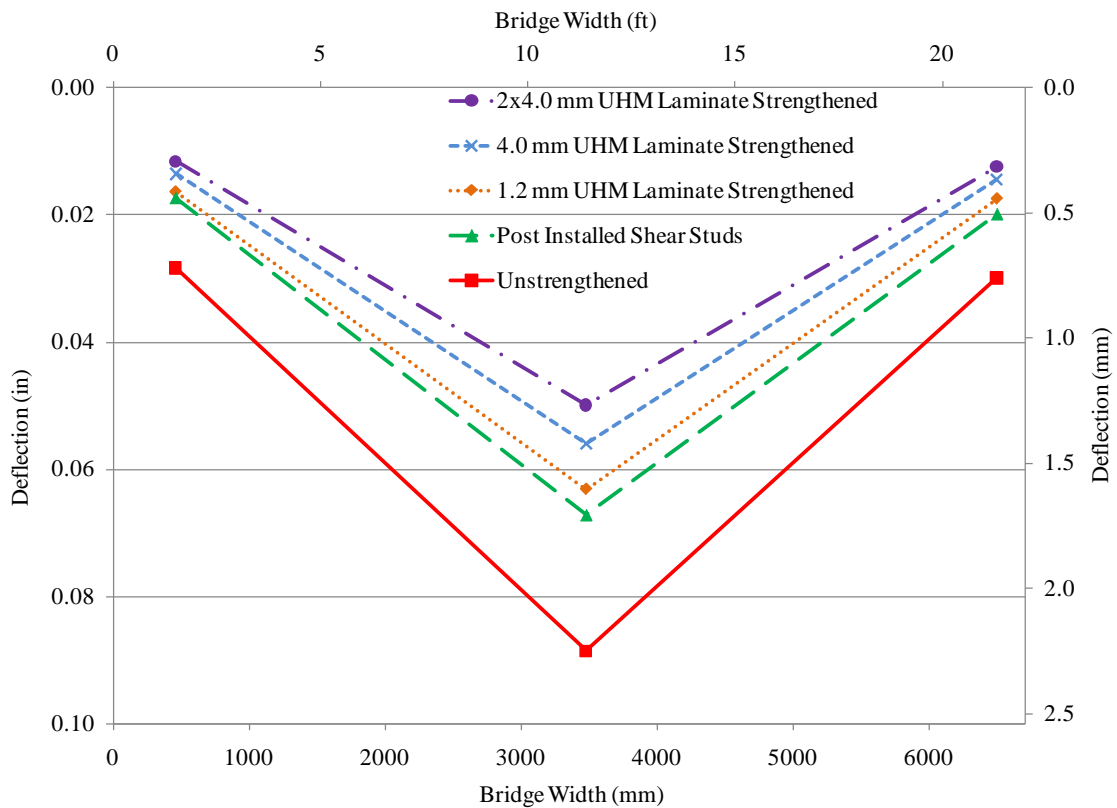


Fig. 6.17: Displacement perpendicular to direction of traffic at mid-span – at each stage of strengthening with different laminate thicknesses

The displacement is seen to be reduced by more than 16.5% at mid-span above the reduction achieved by the post installed shear studs when using the 4mm (0.157 in) thick laminates. While only a 5.9% reduction was achieved using 1.2mm (0.047 in) laminates. The overall reduction compared to the unstrengthened bridge has also increased up to 36.7% when replacing the 1.2mm (0.047 in) with 4mm (0.157 in) laminates. By adding another layer of 1mm (0.039 in) thick epoxy and 4mm (0.157 in) thick UHM CFRP laminate to the bottom of the bottom flange the deflections are seen to be reduced by more than 25.6% over the shear stud installed bridge for an overall reduction of more than 43.6%.

As the KY32 Bridge was not considered a ‘typical’ simply supported non-composite bridge due to the support conditions as well as the cast in place barrier wall, a parametric study was carried out to evaluate the CFRP laminates under simple support conditions without the barrier wall and also neglecting friction between the steel girders and concrete deck. A simply supported non-composite bridge model was developed by modifying the existing model to include simple support boundary conditions and exclude the barrier wall and friction forces between the girders and deck. As the tension of concrete under the truck axle loads governed the ultimate loading of the ‘theoretical’ simply supported non-composite finite element model, an HS5 truck with a rear axle load of only 35.6 kN (8 kips), 25% of the HS20, was considered in the analysis. Separation of steel girders and concrete deck was prevented by constraining the vertical degrees of freedom. Fig. 6.18 shows the effect on the deflection at mid span of the bridge, as initially, the barrier wall is removed from the existing KY32 bridge model. Subsequently, the support conditions are set to be simply supported and finally the friction forces between the steel beams and concrete deck are reduced. The deflection observed in the KY32 Bridge before retrofit is seen to be approximately 30% less than the theoretical simply supported non-composite bridge.

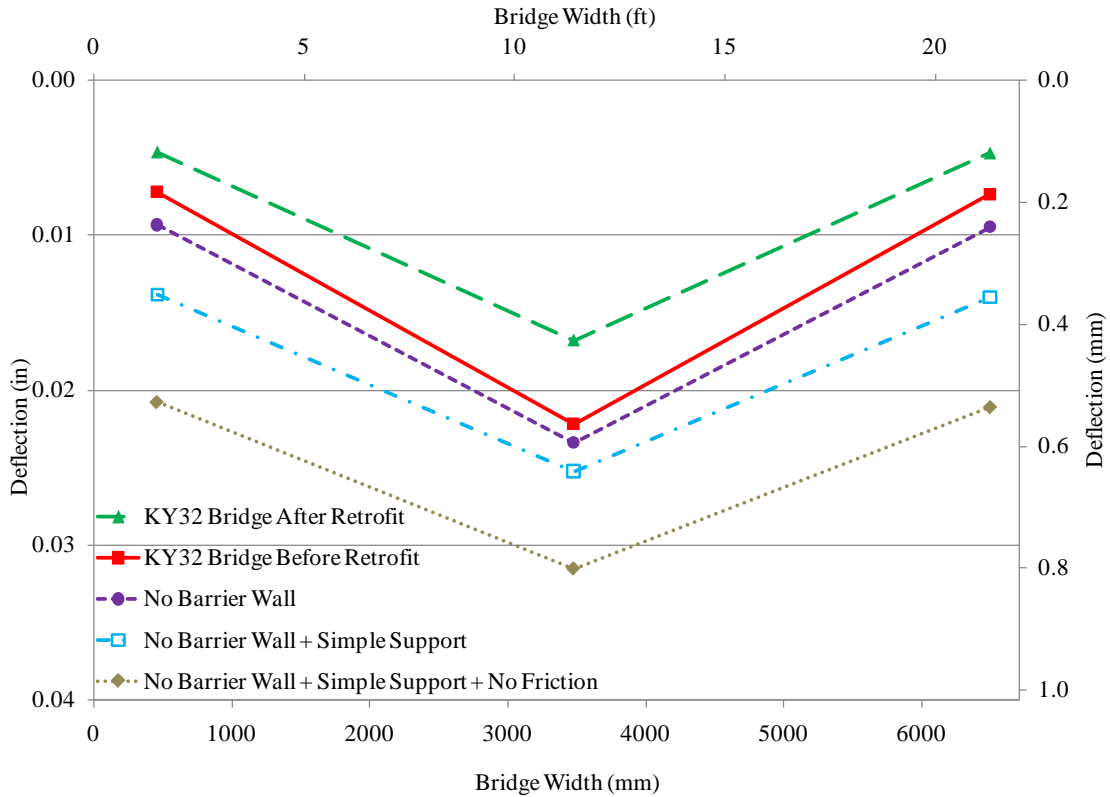


Fig. 6.18: Displacement perpendicular to direction of traffic at mid-span – theoretical simple support without barrier wall and friction forces

The same shear stud layout is applied to the simply supported non-composite bridge model, after which both the 1.2 mm (0.047 in) as well as the 4 mm (0.157 in) ultra high modulus CFRP laminates were applied. The deflections at mid-span perpendicular to the direction of traffic for each case are depicted in Fig. 6.19. The reduction in deflection due to post installation of shear studs (41.1%) as well as the overall reduction in deflection (45.2% for 1.2 mm laminate and 51.9% for 4 mm laminate) is comparatively more for the simply supported non-composite bridge when compared with the actual KY32 Bridge. The effect of the laminates themselves are seen to be more pronounced, where a 7.1% reduction is seen over the shear stud strengthened bridge for the 1.2 mm (0.047 in) thick laminate and a 18.4 % reduction for the 4 mm (0.157 in) thick laminate.

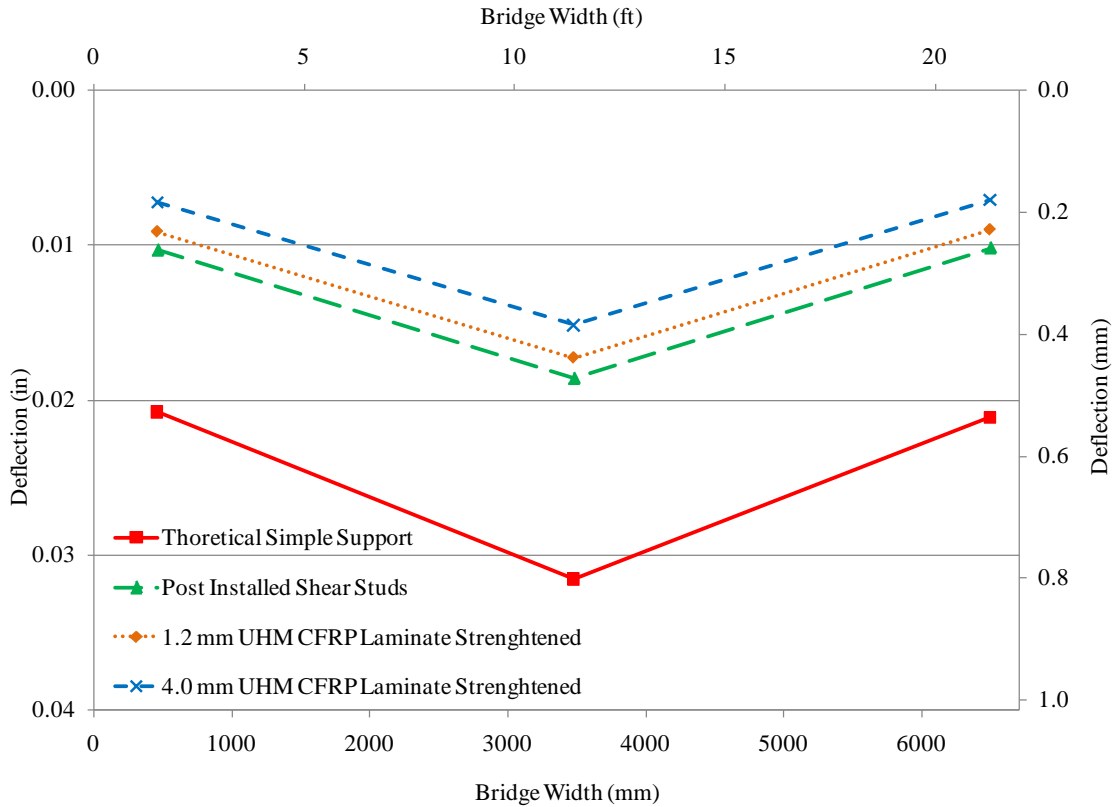


Fig. 6.19: Displacement perpendicular to direction of traffic at mid-span – theoretical simple support non-composite bridge strengthening

From the parametric study it is apparent that the partial fixity of the supports, the barrier wall, and the friction forces between the steel beams and the concrete deck of the KY32 Bridge, while increasing the stiffness of the bridge, have also reduced the effectiveness of the strengthening process. The use of thicker laminates as well as the application of additional layers of UHM CFRP laminates is seen to increase the stiffness of the bridge significantly.

CHAPTER 7

CONCLUSIONS AND RECOMENDATIONS

7.1 Summary and Conclusions

The research investigated both analytically and experimentally the bond characteristics between ultra high modulus CFRP strengthened steel members and the flexural behavior of these members. The first documented field application of ultra high modulus CFRP laminates in strengthening steel bridge girders was carried out, and the performance evaluated.

7.1.1 Summary of laboratory testing and analysis

The first part of the study focused on evaluating the bond characteristics and behavior of ultra high modulus CFRP strengthened steel members. Three different types of experimental testing were performed in the form of double strap joints, doubly reinforced steel plates and steel beams. The double strap and doubly reinforced plate tests were carried out for both normal and ultra high modulus CFRP laminates and the failure modes were compared. Commonly used closed form analytical solutions were reviewed for their applicability with different strengthening methods and finite element analysis were undertaken to model the experimental test specimens and validate some of the findings. The findings of the first part of the research are summarized below.

- Material tests of the ultra high modulus CFRP laminates underwent a different form of rupture in tension, as compared to the normal modulus CFRP laminates. The ultra high modulus laminate was seen to split into smaller pieces, whereas the normal modulus laminates exhibited an ‘explosive’ type of failure. The tensile modulus of the ultra high modulus CFRP laminates was found to be more than 14% higher than the manufacturer specifications, while the ultimate strength was found to be more than 60% higher.

- In the normal modulus CFRP double strap joint tests, debonding between the steel and epoxy adhesive was observed for most of the tests involving shorter bond lengths, while delamination within the CFRP laminate was observed for tests involving longer bond lengths. Complete debonding between the steel and epoxy adhesive on both sides was not observed in any of the ultra high modulus CFRP laminate double strap specimens. Shorter bond lengths were found to correlate with mixed debonding and delamination, while longer bond lengths failed mostly in rupture.
- The experimental development length for the normal modulus CFRP was found to be 41 mm (1.6 in), while for the ultra high modulus CFRP, the development length was 64 mm (2.5 in). The bond strength for the normal modulus laminates was found to be 2.1 kN/mm (12 kip/in), and for the ultra high modulus laminates the bond strength was 3.0 kN/mm (17 kip/in).
- The shear strength of the epoxy adhesive and the steel was evaluated using the normal modulus CFRP double strap joints that showed complete debonding between the steel and epoxy adhesive. The average shear strength was found to be 27 MPa (3.9 ksi).
- The Hart-Smith (1973(a)) proposed method was evaluated for applicability with the experimental data. The Hart-Smith model predicted a bond development length of 48 mm (1.9 in) for the normal modulus CFRP laminate double strap joint and a length of 72 mm (2.9 in) for the ultra high modulus CFRP laminate joint. The Hart-Smith model predicted failure load also increased with the increase in laminate modulus, with 1.63 kN/mm (9.3 kip/in) for the normal modulus CFRP increasing to 2.60 kN/mm (14.9 kip/in) for the ultra high modulus CFRP double strap joint.
- The Von Mises failure criterion was used to predict the failure of the epoxy in the finite element analysis. The finite element results provided accurate failure loads that compared well with the experimental data. Validation of the Hart-Smith

method more accurately requires evaluation of the epoxy adhesive shear stress-strain relationship, including both elastic and plastic shear strains.

- Both normal modulus and ultra high modulus doubly reinforced steel plates failed in debonding, between the steel and epoxy adhesive, at the laminate edges. The debonding was seen to progress towards the center following the initial debonding at the edge. Due to the higher modulus, the strains in the ultra high modulus laminates were seen to be lower at the same applied loads. However, the ultra high modulus laminates debonded before the normal modulus laminates. Consequently, the normal modulus laminates had an average load carrying capacity 22% higher than the ultra high modulus CFRP laminates.
- The ultra high modulus laminates were seen to debond before the steel plate yielded, whereas the normal modulus laminates debonded only after the steel plate yielded. This would be important to consider when strengthening tensile uncracked members with ultra high modulus CFRP laminates.
- Development lengths derived from the double strap joint tests were confirmed by the observed strain profile along the bond line of the two different laminates. While the experimentally calculated shear stresses were higher for the ultra high modulus CFRP laminates than for the normal modulus CFRP laminates, the stresses were not seen to reach the calculated average shear strength of the bond at failure.
- The shear stresses within the epoxy as well as the normal stresses within the CFRP laminates, for both ultra high modulus and normal modulus laminates, were confirmed by the Albat and Romilly (1998) proposed closed form solutions. Since only half the width of the steel plate was strengthened, the Albat and Romilly (1998) method was applied by evaluating the percentage of load carried by the strengthened area of the steel plate using section transformation.

- The finite element study confirmed that the bond failure was not due to high shear stresses, but due to high tensile stresses within the epoxy. The failure in debonding was again predicted by using the Von Mises failure criterion.
- Due to the small area of applied ultra high modulus CFRP material, the increase in flexural stiffness was seen to be very small for the full width strengthened and also the novel strip panel strengthened steel beam specimens. Rupture was the ultimate failure observed in the full width strengthened beam, where a 39.7% increase in strength at yield was attained. Both ultra high modulus CFRP strip panel strengthened beams failed in debonding at the strip panel finger joint at mid span. The increase in strength at steel yield was 26.4% and 25.8% for the 10 mm (0.4 in) and 5 mm (0.2 in) wide strip panel strengthened beams respectively.
- The Smith and Teng (2001) derivation for the shear stress distribution along the laminate was seen to match the experimentally calculated shear stresses at different load levels.
- The tensile strain readings, along the bond of the full width laminate strengthened beam and the 10 mm (0.4 in) strip panel strengthened beam, were predicted fairly accurately by the finite element analysis to match the experimental findings. The analytically predicted failure mode for the full width laminate strengthened beam was rupture. Failure was predicted to occur at a slightly higher load than that measured experimentally.
- The experimentally calculated shear stresses, close to the finger joint at mid span, were seen to be higher than the stresses at the laminate edges closer to the support. However, even just before failure in debonding, the shear stresses were seen to be lower than the experimentally calculated average shear strength of the bond.
- The shell element beam model was unable to predict the debonding of the strip panel strengthened steel beam. A substructure model of the finger joint area was built with solid elements, and the same tensile stresses observed in the main beam model were applied to evaluate bond stresses in the joint. The substructure model

was able to predict the shear stress variation at the joint with good accuracy, while predicting the debonding through the Von Mises failure criterion.

7.1.2 Conclusions of laboratory testing and analysis

Conclusions drawn from the observed test results and analysis data are presented below.

- Ultra high modulus CFRP laminates have higher bond strength and a longer development length than normal modulus CFRP laminates in double strap shear.
- The stress-strain relationship of the epoxy adhesive in shear is required to accurately evaluate the applicability of the Hart-Smith model. Albat and Romilly (1998) and Smith and Teng (2001) derivations for stress distribution provide good approximations.
- The maximum tensile stress of the epoxy adhesive was identified to govern the failure of the bond, but not the shear stresses at the interface.
- Ultra high modulus laminate doubly reinforced steel specimens have a higher load carrying capacity, but a lower ultimate load in tension as compared to plates strengthened with normal modulus laminates. Ultra high modulus laminates would not be suitable for tensile strengthening where the steel beneath the laminate edge would have a large strain increment.
- The load carrying capacity up to the yielding of steel in beams can be significantly increased through use of ultra high modulus CFRP laminates.
- Splice panels are found to be a better alternative than regular splice joints when considering the ultimate load carrying capacity of the joint.

7.1.3 Summary of field application of ultra high modulus CFRP laminates

The first field application of ultra high modulus CFRP laminates in strengthening a steel-concrete composite bridge in the United States was undertaken as the second phase of the research. In order to validate the effectiveness of the retrofit, full scale field testing was performed on the bridge before and after retrofit. The candidate bridge, provided by the Kentucky Transportation Cabinet, was the KY 32 Bridge over Lytles creek in Scott County, Kentucky.

- A simple beam analysis showed that the application of ultra high modulus CFRP laminates on a non-composite steel girder, while increasing the load carrying capacity, would not achieve the required load rating of the bridge. In order to achieve more efficient use of the laminate, post installation of shear studs was considered as a means to obtain some degree of composite action between the concrete deck and steel girders. A finite element beam analysis was performed to evaluate the post installed shear stud layout. From the several layouts analyzed, the selected layout was a shear stud ratio of 71% of the AASHTO fully composite girder. The layout was conservative, and had a higher concentration of studs close to the abutments, while providing the required ultimate and serviceability requirements.
- An AASHTO load rating was performed to evaluate the bridge rating before and after the post installation of shear studs. Five different truck types with different axle combinations and weights were considered and the Inventory level and Operational level truck weights were found for each truck type.
- The retrofit of the bridge was carried out in several stages. Rebar location using ground penetrating radar, drilling holes for shear studs, installation of the shear studs and later the ultra high modulus laminates were the four main stages in the retrofit process. The bridge was instrumented and field testing was carried out between the different stages to evaluate the performance of the bridge. A field test was performed before and after drilling the holes for the shear studs to assess if the

loss of material from the steel beam flanges would affect the bridge behavior. Another test after installing the shear studs assisted in estimating the effectiveness of post installed shear studs. Two tests carried out after installing the laminates were used to estimate the performance of the ultra high modulus CFRP laminates.

- Adhesive anchor type post installed shear studs, where threaded rods are inserted onto the concrete deck through holes in the top flange of the steel beam, was chosen for implementation to minimize traffic disruption and construction costs. Four strips of ultra high modulus laminates were installed along the bottom flange of each beam. Two strips were placed on the top surface, on either side of the web, and two on the bottom surface of the flange. The laminate application was performed over two days, with all steps in the application process carried out at the bridge site.
- Initial load tests on the bridge revealed that the bridge, although theoretically considered to be non-composite, possessed a degree of composite action between the steel beams and concrete deck through friction due to the deck being cast over the top flange of the beams. The supports were also found not to be simply supported, due to the concrete diaphragms at the abutments.
- Normalized field deflection data showed that the post installed shear studs reduced the deflections by 27.2%, while the strain data indicated shifting of the neutral axis toward the concrete deck. Application of the ultra high modulus CFRP laminates reduced the deflections by 5.3% at mid span, and also reduced the strain in the steel bottom flange. The tensile strains on the laminates were less than 5% of the experimentally measured ultimate strains.
- A finite element model of the bridge was shown to be capable of responding in a manner that was consistent with the experimental findings at the various stages of retrofit. A load rating of the bridge was also performed using the finite element model as the bridge was identified as neither fully non-composite nor simply supported.

7.1.4 Conclusions of field application of ultra high modulus CFRP laminates

Conclusions drawn from the load test results and analysis data are presented below.

- Post installed shear studs are capable of significantly increasing the load carrying capacity of non-composite bridges.
- Adhesive anchor type shear stud installation is cost effective when compared with other types of post installed shear studs and has minimal impact on traffic.
- Thick ultra high modulus laminates can be used to strengthen and increase the load carrying capacity of steel composite bridges.
- Field application of ultra high modulus CFRP laminates is labor intensive, but can be cost effective considering application time and cost of alternative procedures.
- The laminate application process should be planned to minimize time between grit blasting of the steel beams to curing of the epoxy adhesive. The work time of the epoxy, time for epoxy application and the man power requirement should be taken into consideration.

7.2 Recommendations for Future Work

The present study evaluated the bond stresses, specifically the shear stresses, between ultra modulus CFRP laminates and steel in both tension and flexure. Field application of ultra high modulus CFRP laminates on an active bridge was also carried out and the effectiveness of the retrofit evaluated. During the course of the study numerous areas of research were identified which shall require future investigation.

- The shear strength of the adhesive epoxy was not directly tested in the study. While the tensile test coupons failed in a linear elastic brittle manner, it would be beneficial to experimentally validate the behavior of the epoxy in shear. This would also facilitate the identification of a suitable plastic strain value, to input in to the Hart-Smith model for bond strength calculation.
- The present tests showed that the bond failed in tensile failure of the adhesive epoxy rather than in shear. The factors affecting this type of failure, properties of the epoxy adhesive as well as the laminates should be both analytically and experimentally verified. Any advantages or disadvantages of this type of failure over a shear failure should be explored.
- The experiments undertaken in the present study used laminates that had a width smaller than the strengthened steel plate/flange to represent possible field application conditions. As most analytical solutions assume plane stress conditions, which in turn assume that the strengthened steel and laminate are the same width, the same tests should be carried out with the steel and laminates of the same width to compare results.
- The effect of thermal mismatch between the steel and the laminate was not considered in the study. The thermal coefficient for ultra high modulus laminates needs to be verified and possible strength reduction at the joint needs to be studied.

- The optimum laminate width for developing ultra high modulus strip panels should be investigated further. The 5 mm (0.2 in) strip panel was seen to have more stress along the strip at the middle compared to both the full width and 10 mm (0.4 in) strip panel. Different widths of strip panels should be evaluated and the possibility of field application assessed.
- As the strip panels were tested in four-point bending, with the finger joint within the constant moment region, shear forces on the beam were minimal. The effect of shear forces at the joint location due to distributed and off center point loads should be investigated for the effect of shear loads on the finger joint.
- Research has shown that tapering the laminate edge can significantly reduce the bond stresses. The applicability of tapered ends on strip panels should be investigated for possible increase in load carrying capacity.
- While the effects of shear stresses within the bond were studied, the peel stresses were not evaluated as they were expected to be small for the thin 1.2 mm (0.047 in) thick laminate. The behavior of peel stresses requires investigation as they might become a factor for thicker laminates and also for different adhesive thicknesses.
- The effect of fatigue and also environmental effects on the performance of the steel-laminate bond interface was not addressed in this study, and very few studies have been carried out in this area. More research should be performed on both of these areas to improve understanding of the bond interface.

APPENDIX A

A.1 Double Strap Joint Test

Normal modulus CFRP 10 mm (0.4 in) width specimens

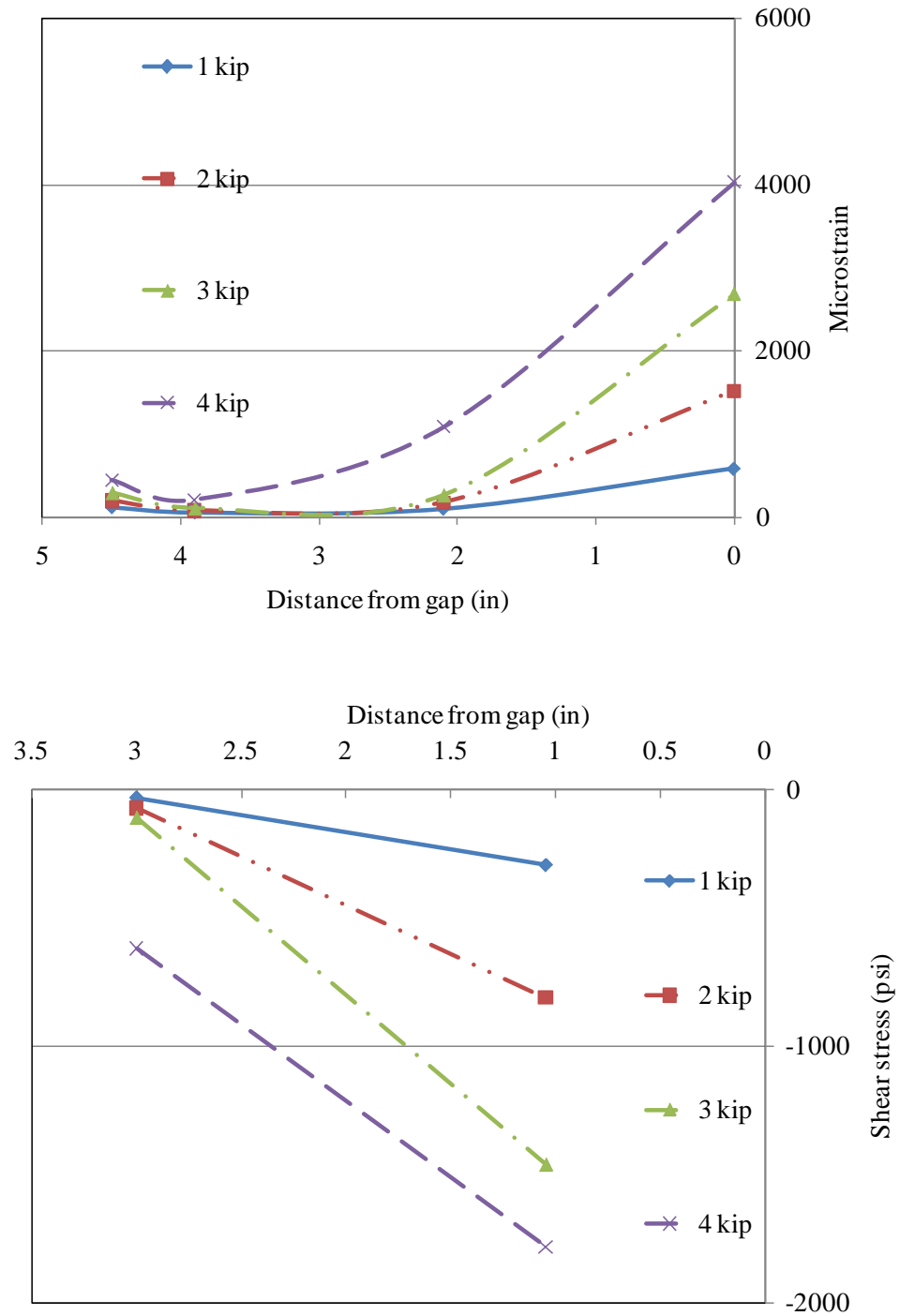


Fig. A1: 100 mm (4 in) bond length specimen strain and shear distribution

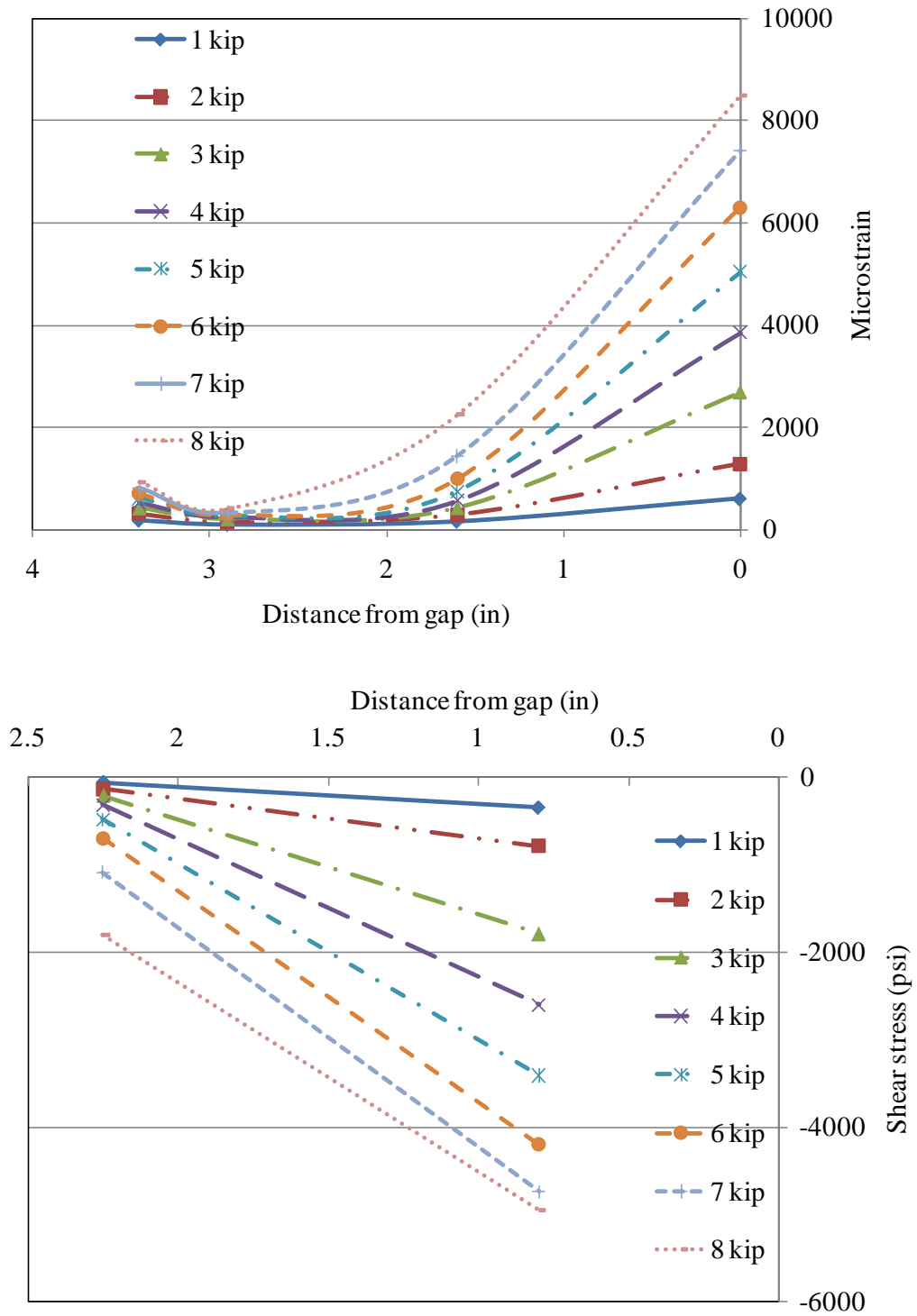


Fig. A2: 75 mm (3 in) bond length specimen strain and shear distribution

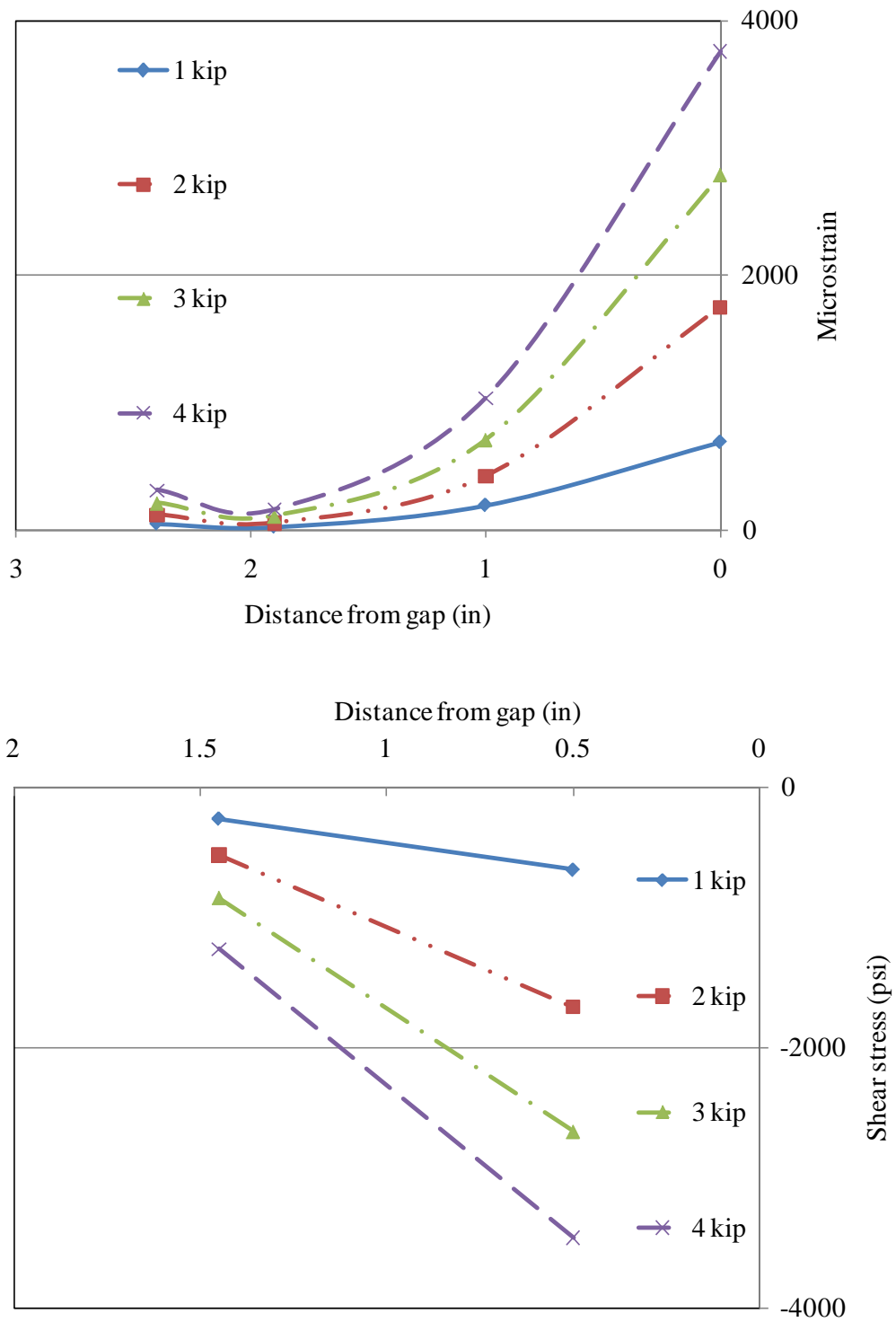


Fig. A3: 50 mm (2 in) bond length specimen strain and shear distribution

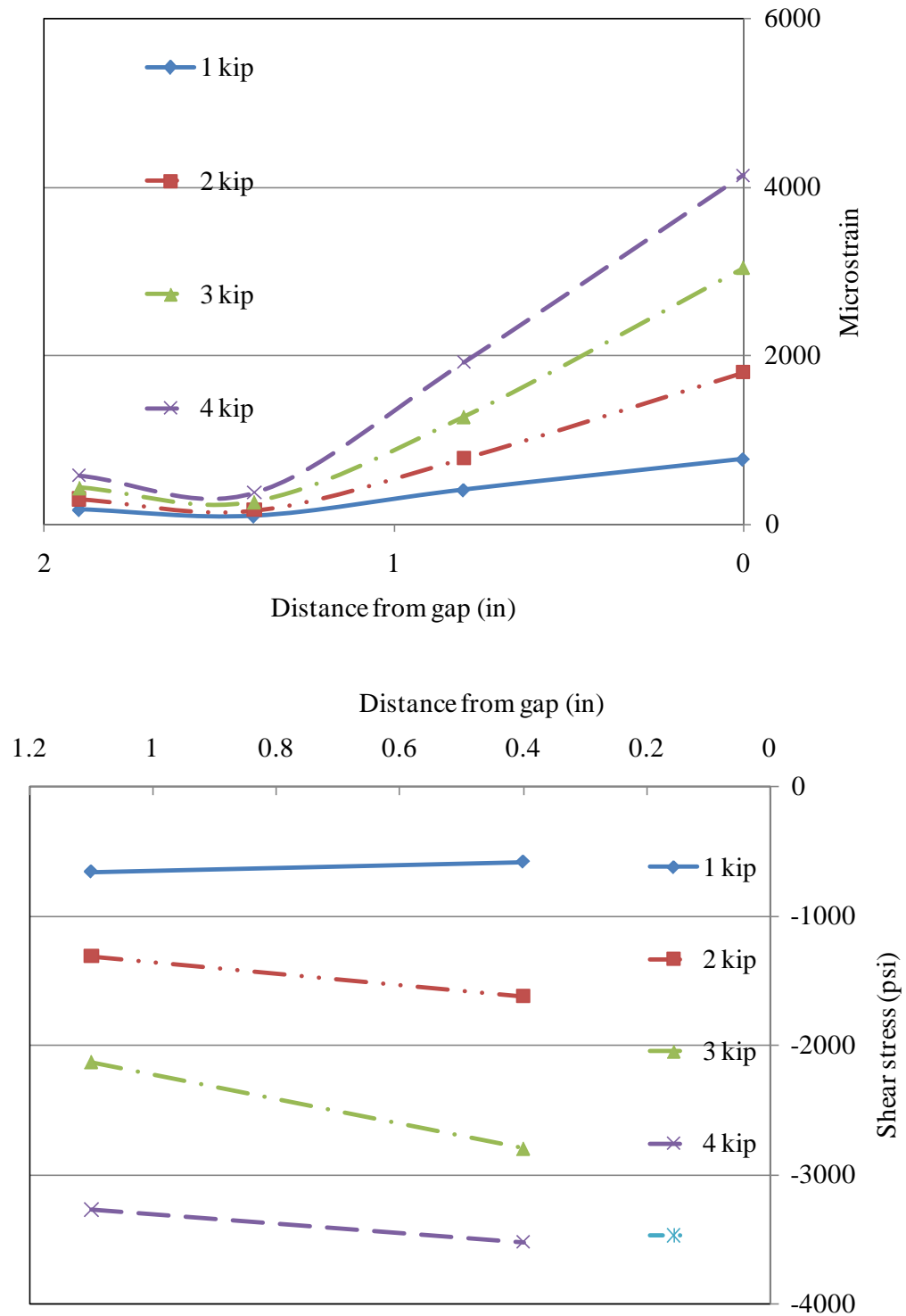


Fig. A4: 37.5 mm (1.5 in) bond length specimen strain and shear distribution

Normal modulus CFRP 5 mm (0.2 in) width specimens

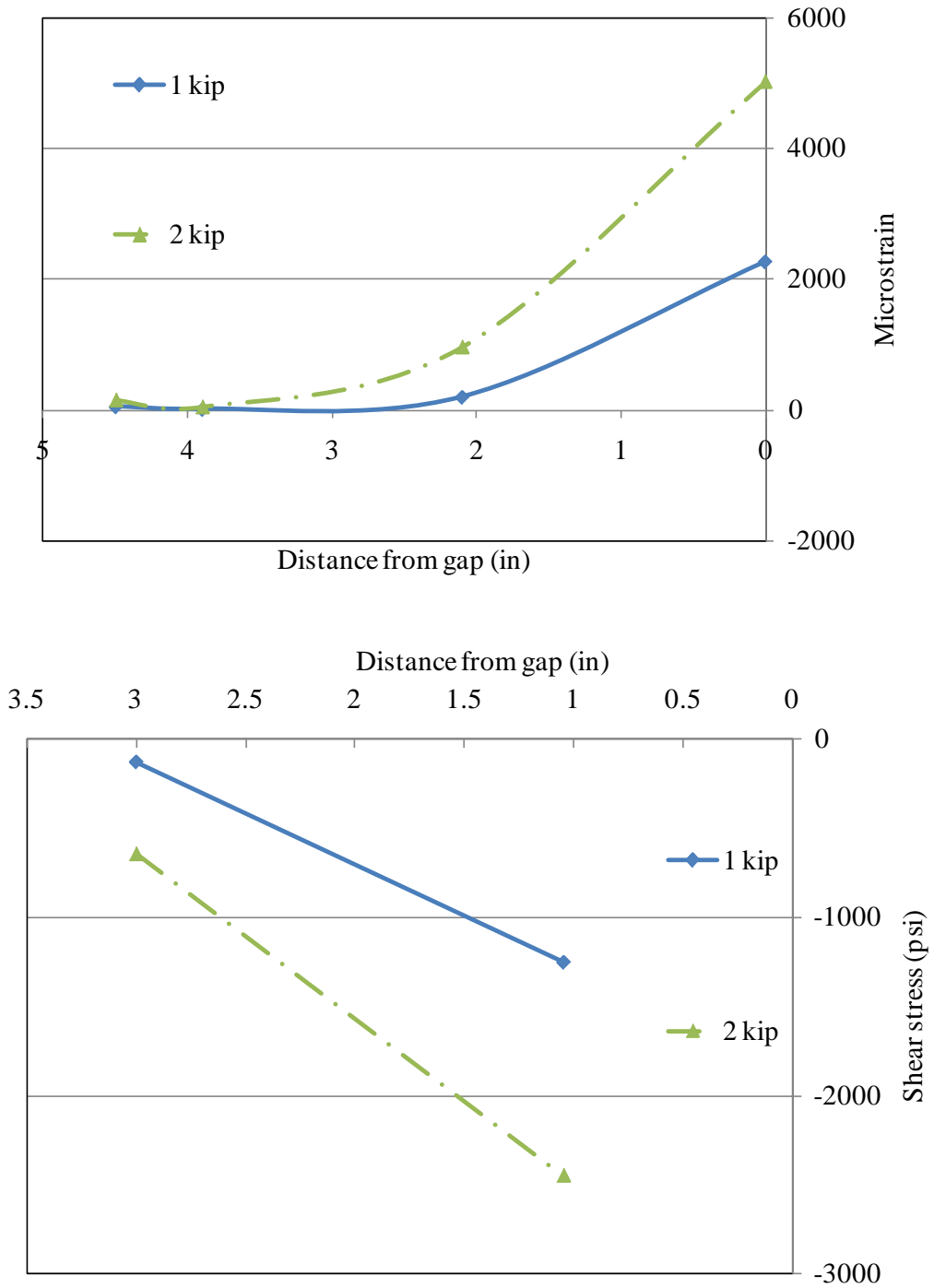


Fig. A5: 100 mm (4 in) bond length specimen strain and shear distribution

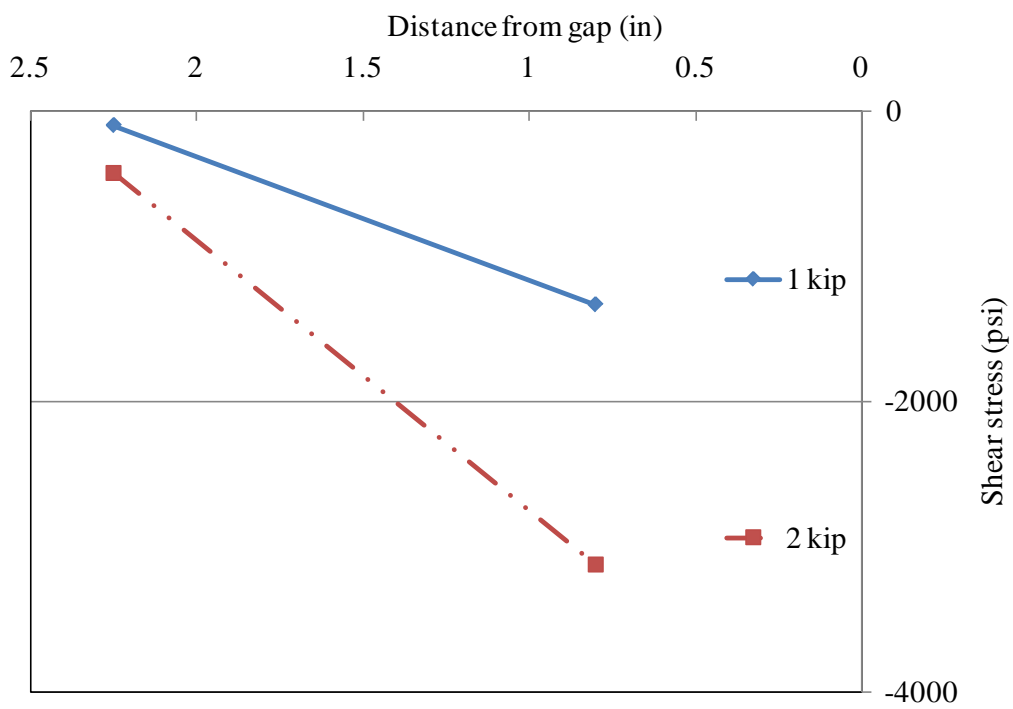
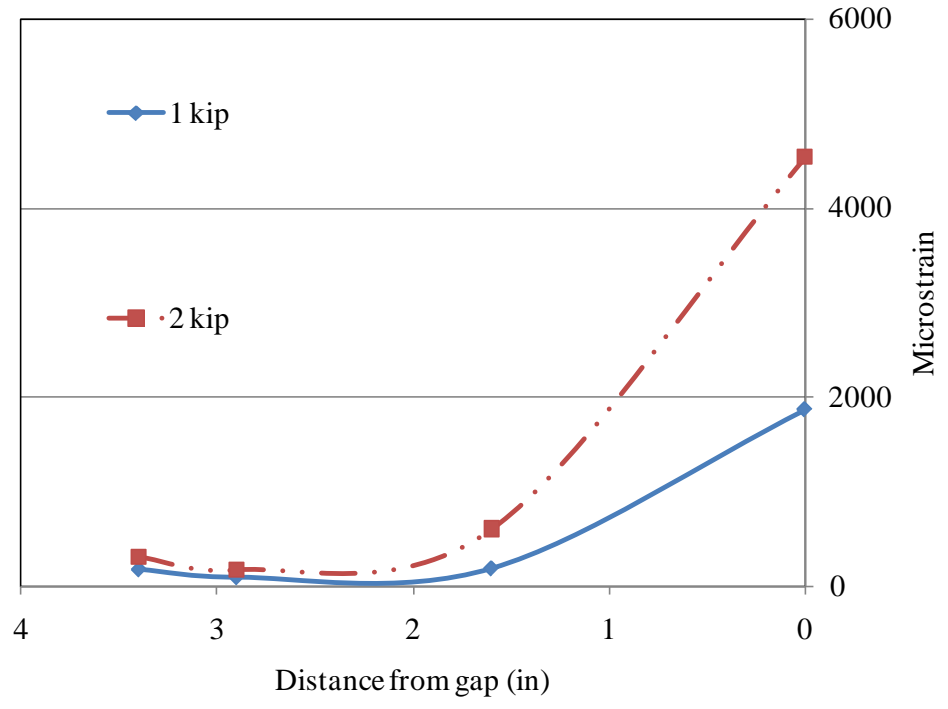


Fig. A6: 75 mm (3 in) bond length specimen strain and shear distribution

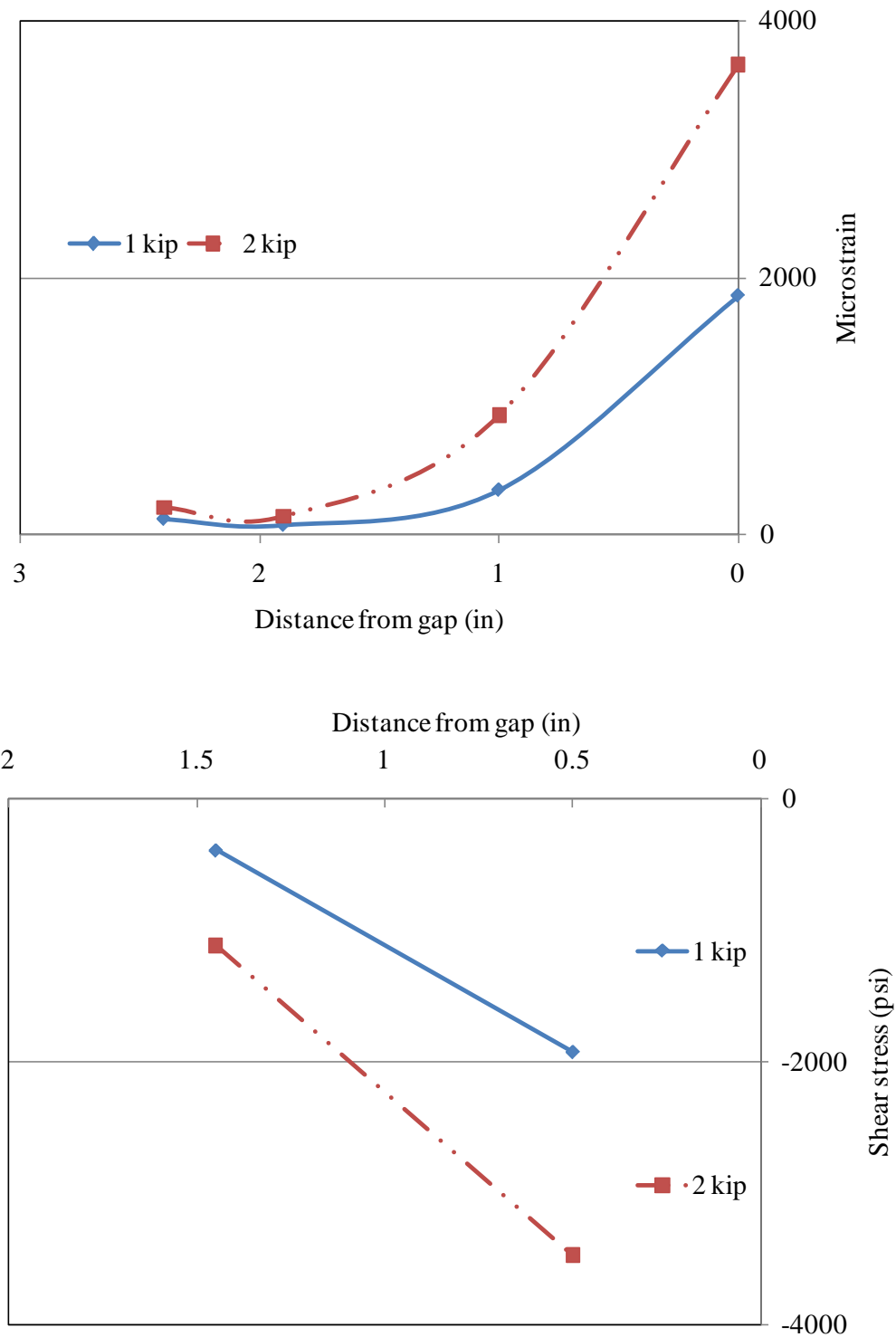


Fig. A7: 50 mm (2 in) bond length specimen strain and shear distribution

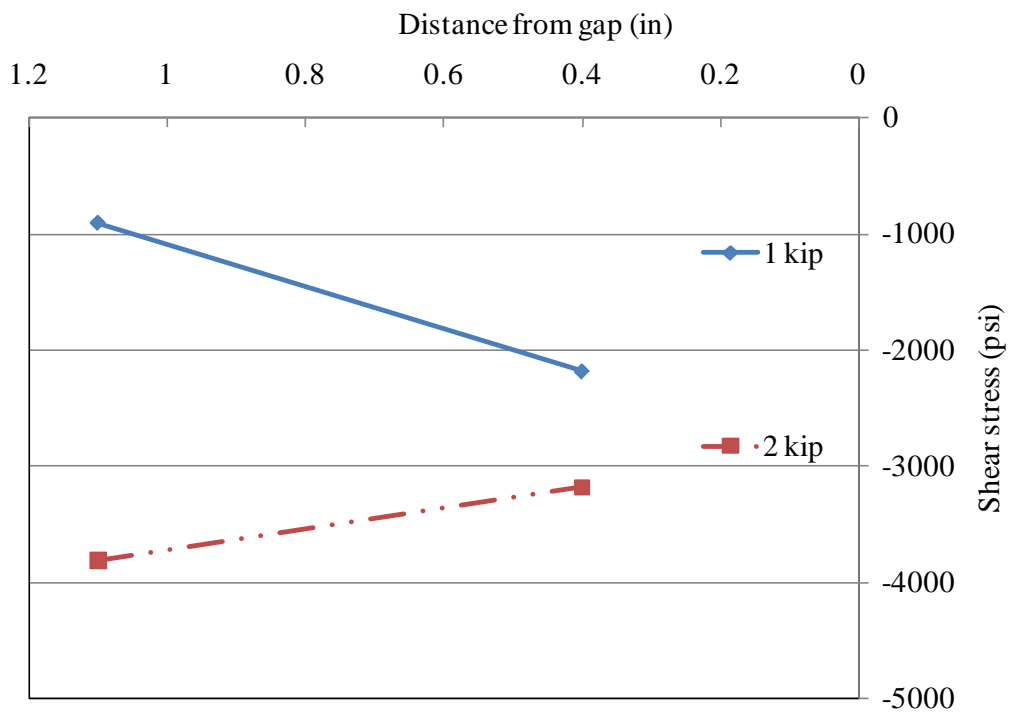
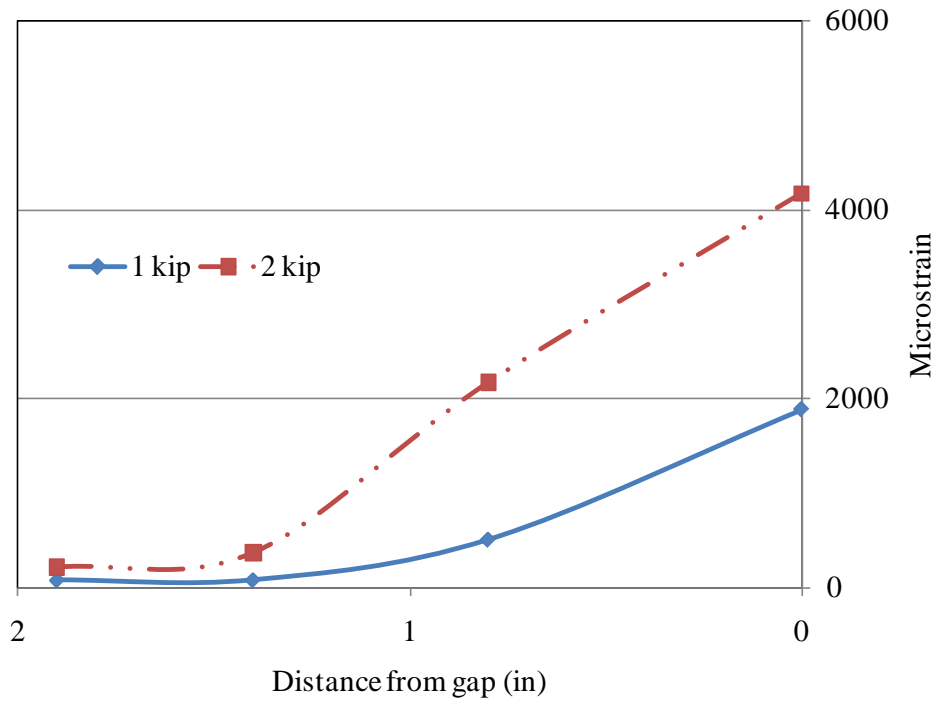


Fig. A8: 37.5 mm (1.5 in) bond length specimen strain and shear distribution

Ultra high modulus CFRP 10 mm (0.4 in) width specimens

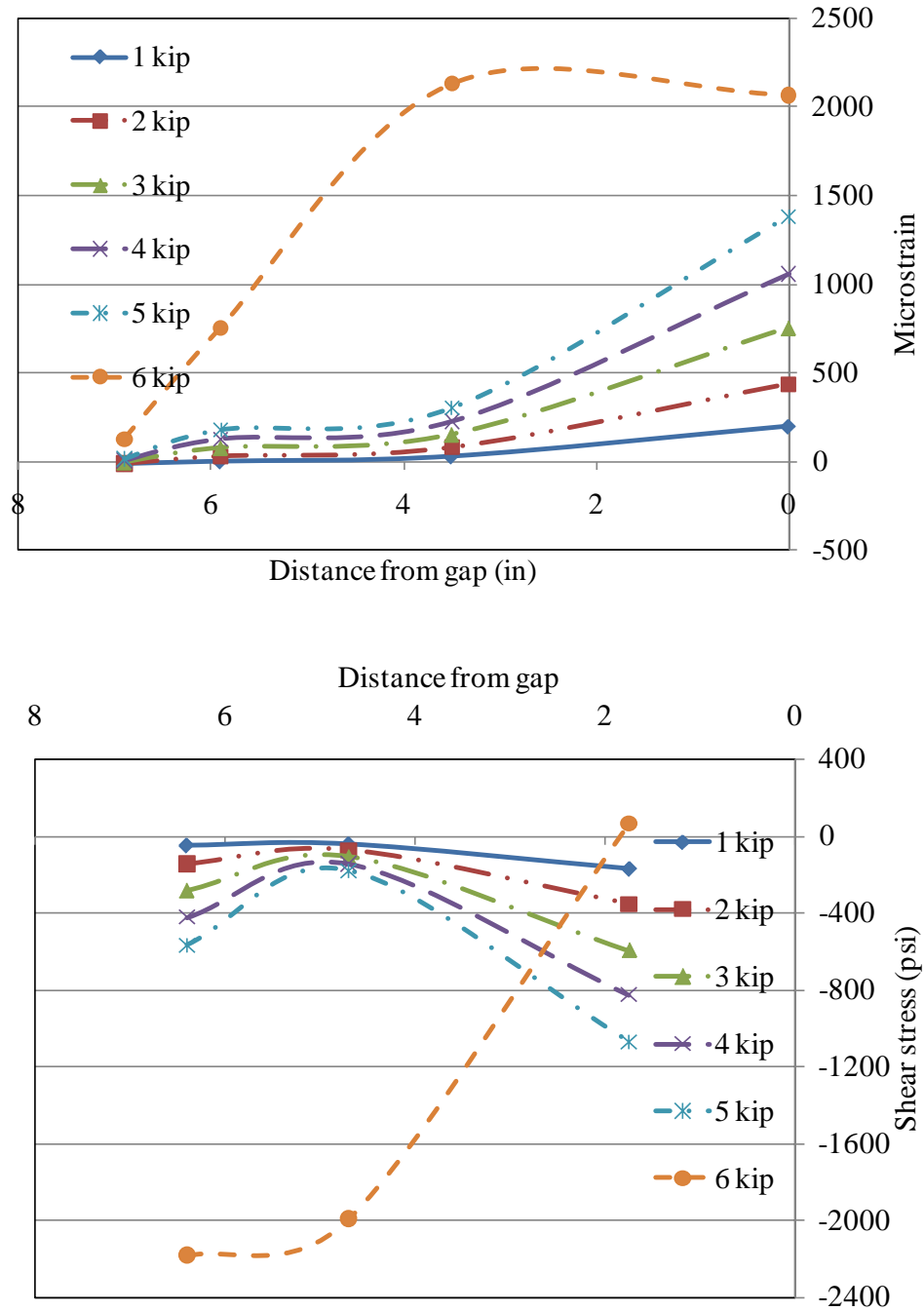


Fig. A9: 175 mm (7 in) bond length specimen strain and shear distribution

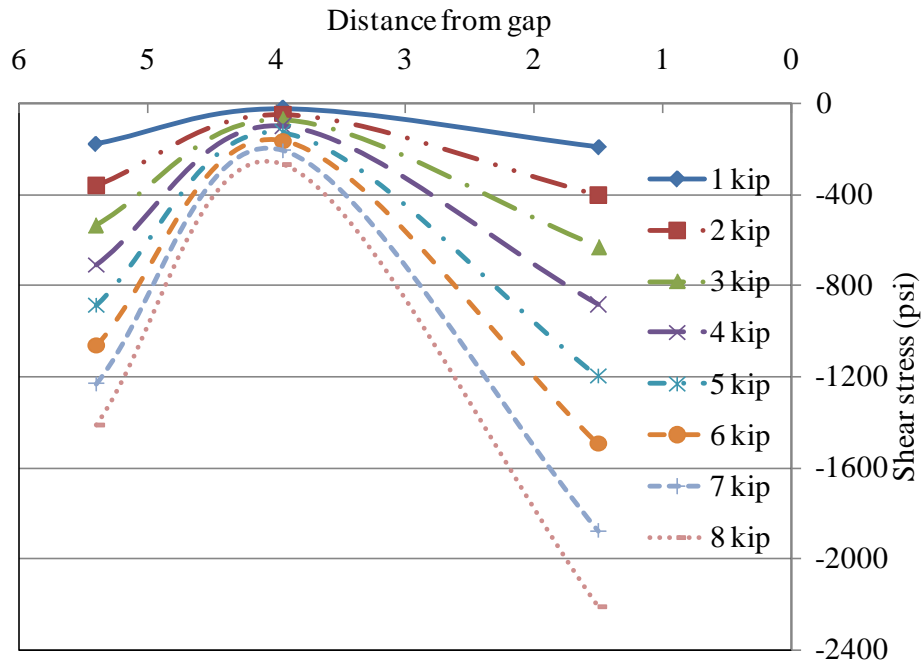
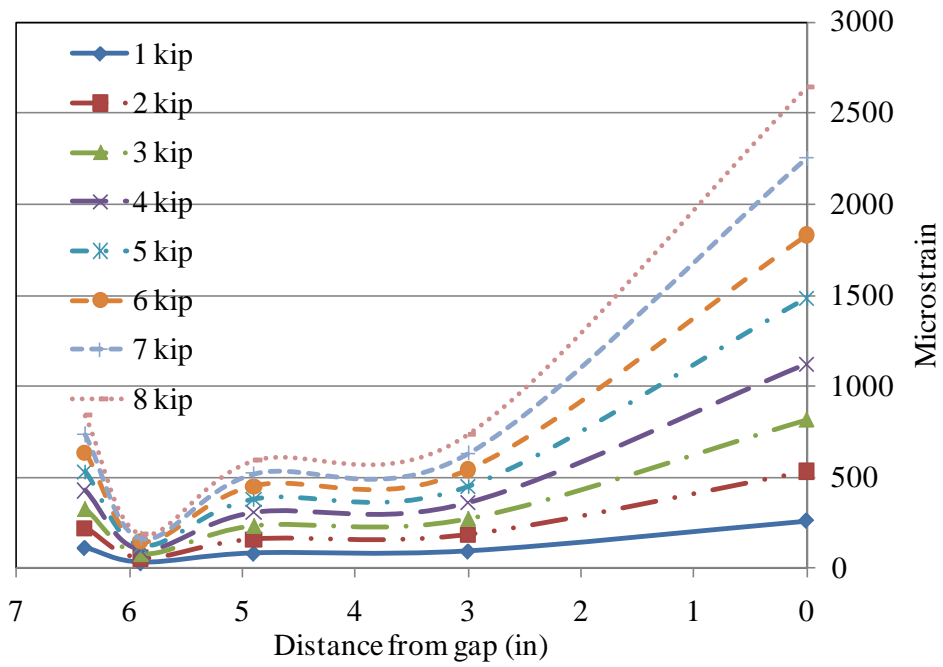


Fig. A10: 150 mm (6 in) bond length specimen strain and shear distribution

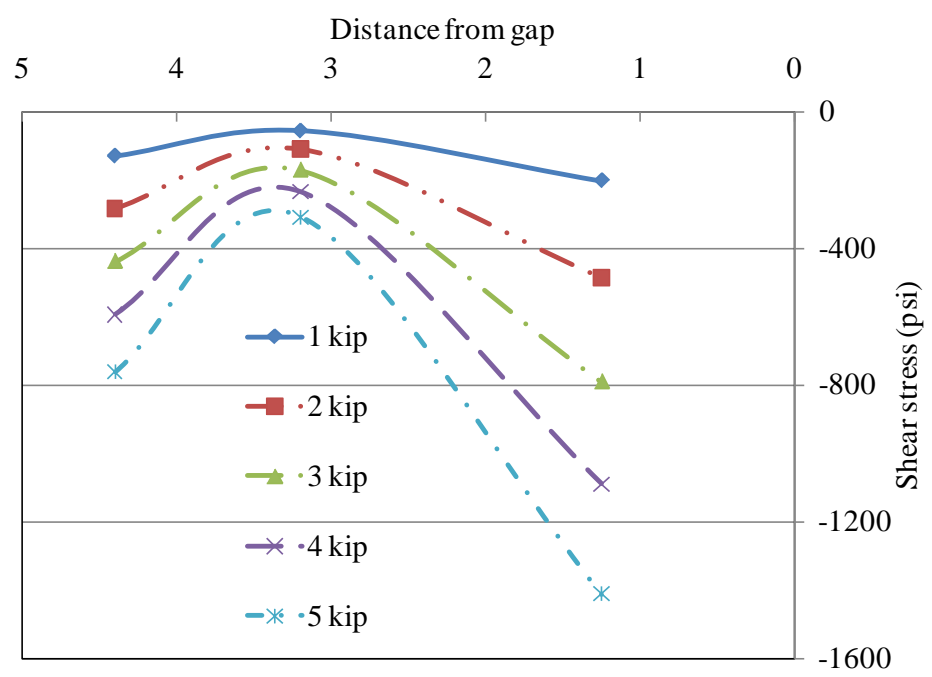
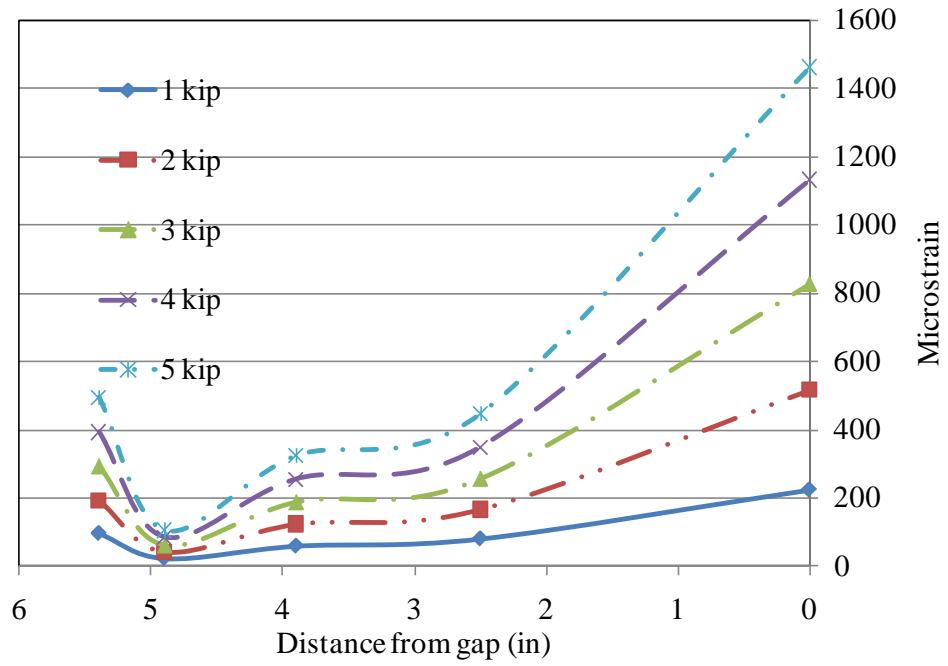


Fig. A11: 125 mm (5 in) bond length specimen strain and shear distribution

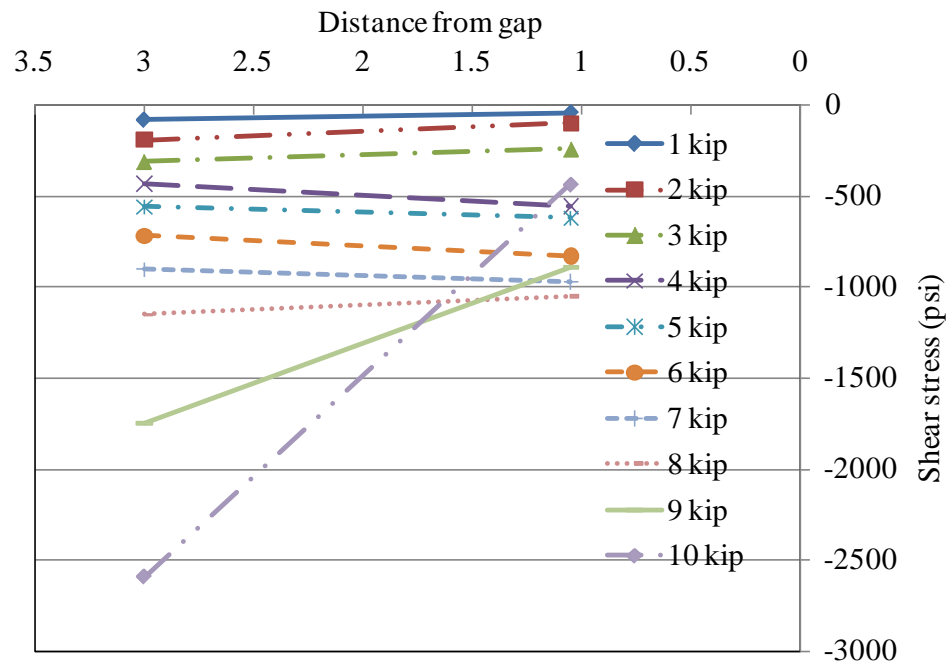
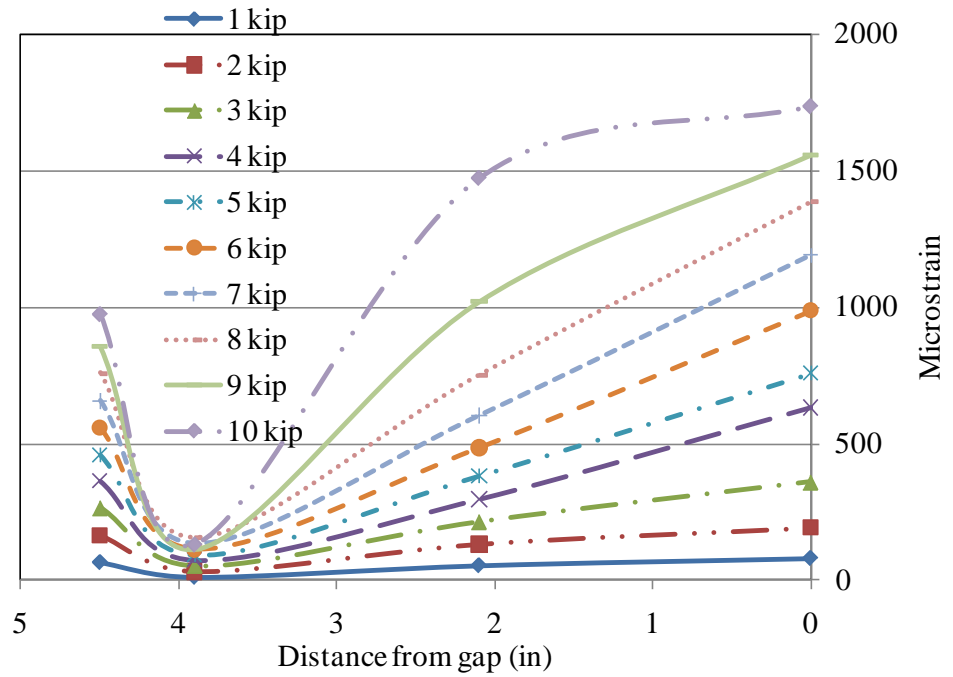


Fig. A12: 100 mm (4 in) bond length specimen strain and shear distribution

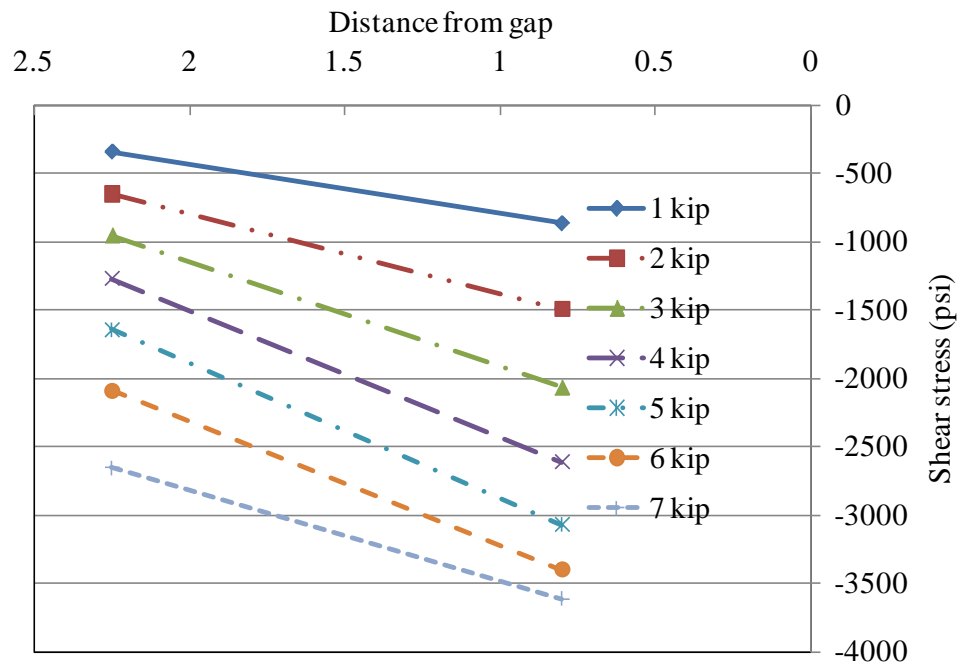
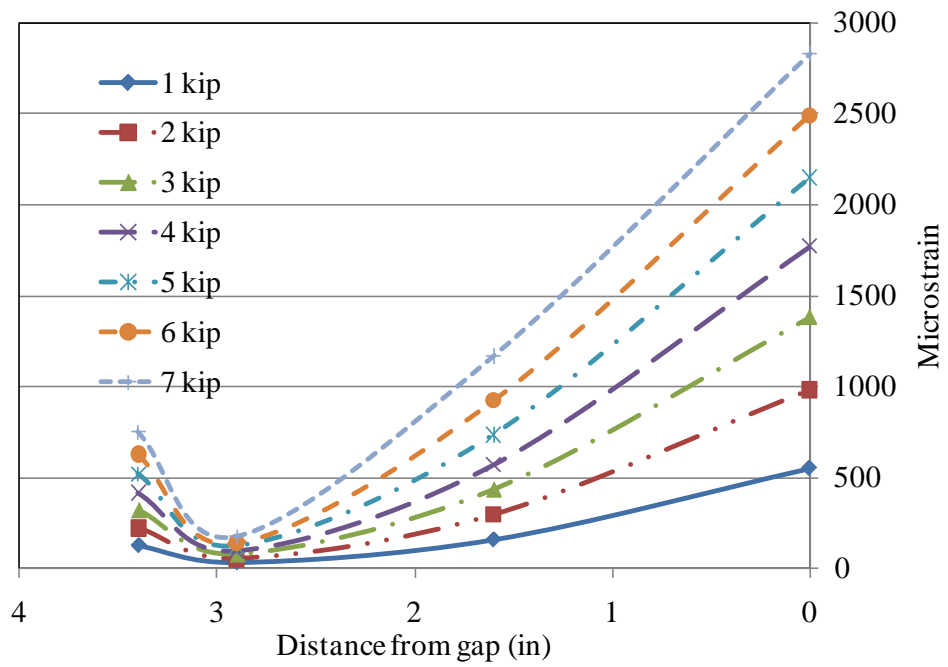


Fig. A13: 75 mm (3 in) bond length specimen strain and shear distribution

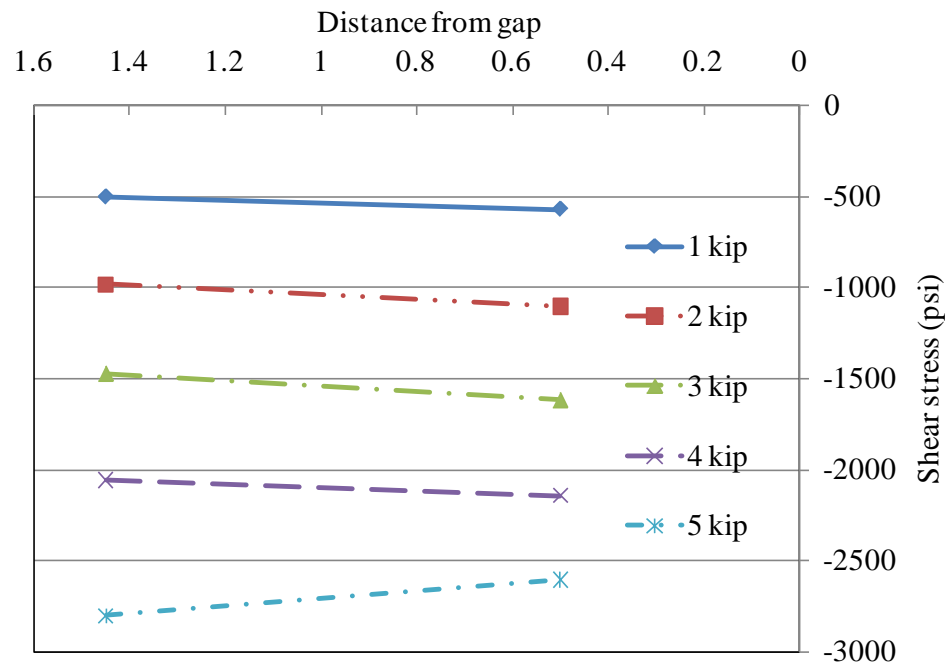
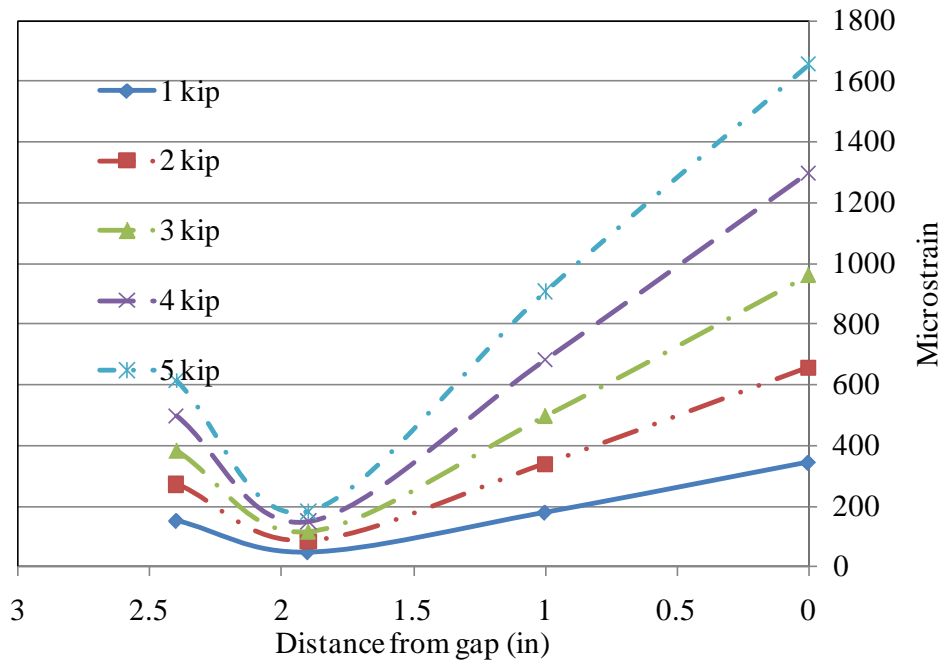


Fig. A14: 50 mm (2 in) bond length specimen strain and shear distribution

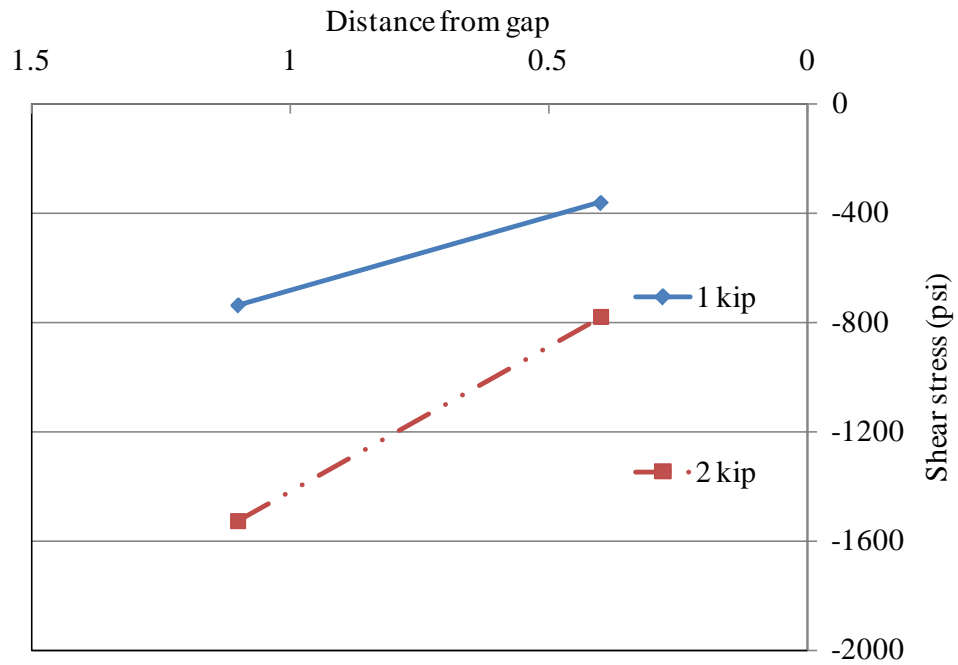
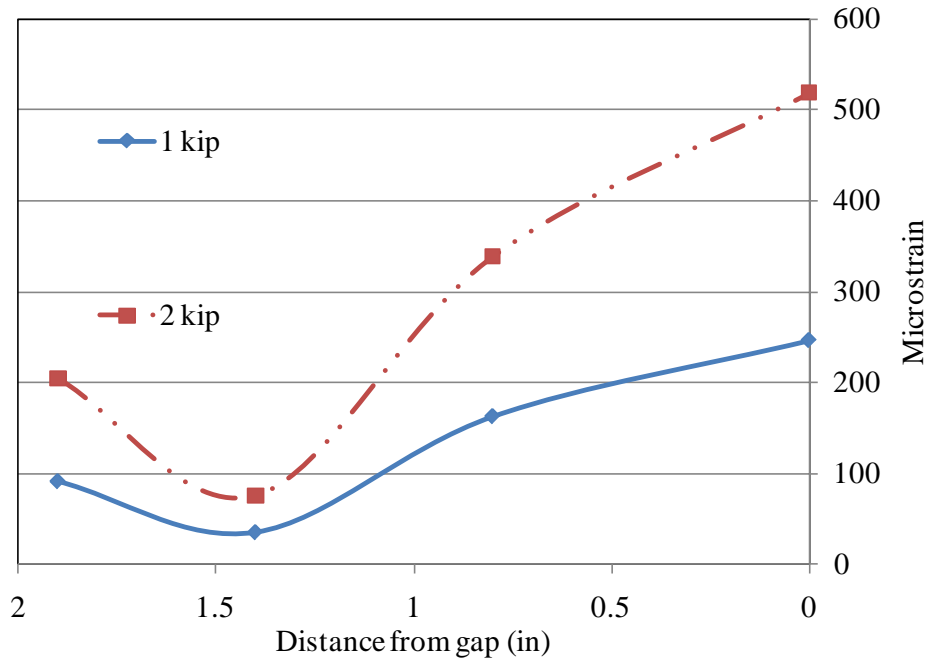


Fig. A15: 37.5 mm (1.5 in) bond length specimen strain and shear distribution

Ultra high modulus CFRP 5 mm (0.2 in) width specimens

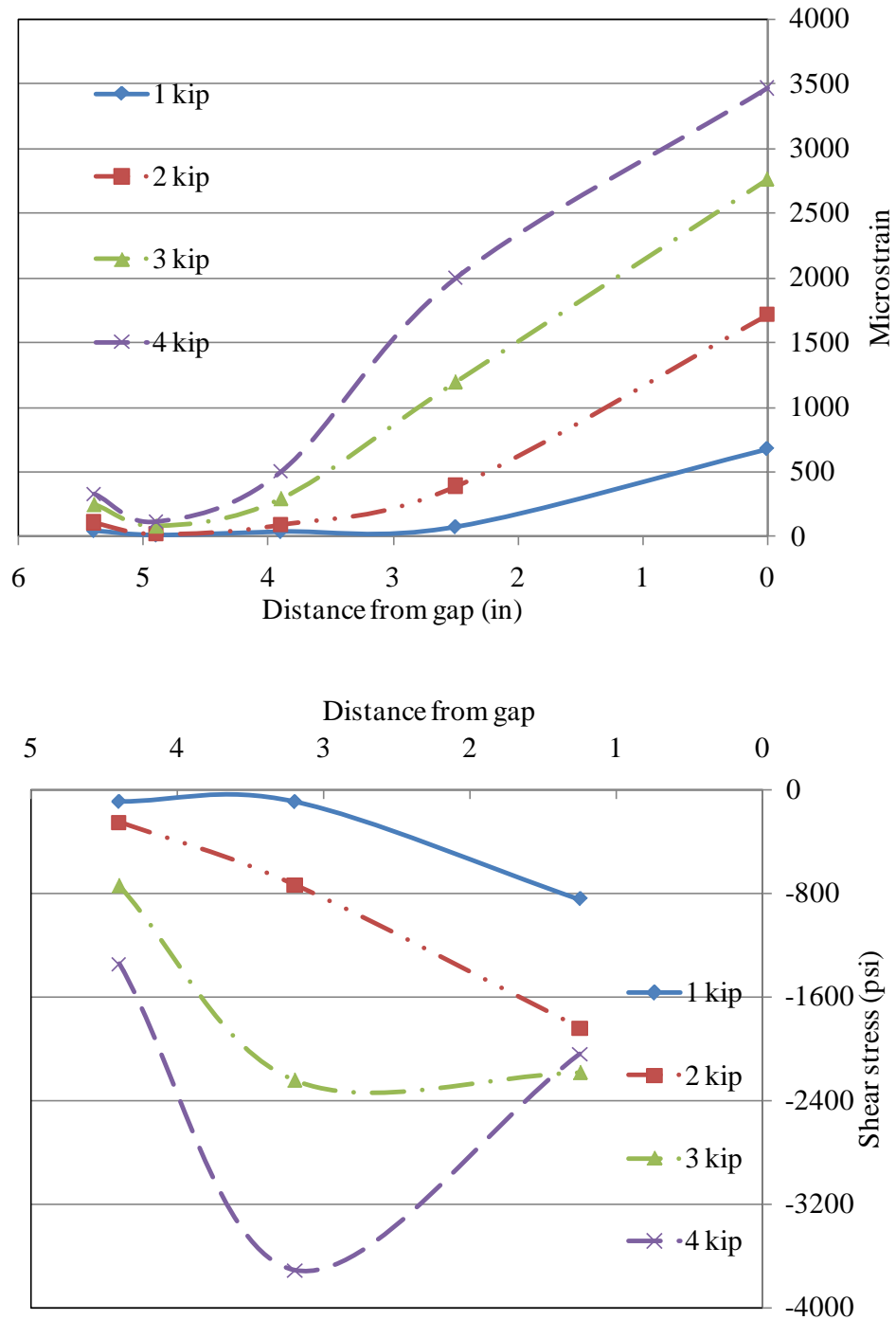


Fig. A16: 125 mm (5 in) bond length specimen strain and shear distribution

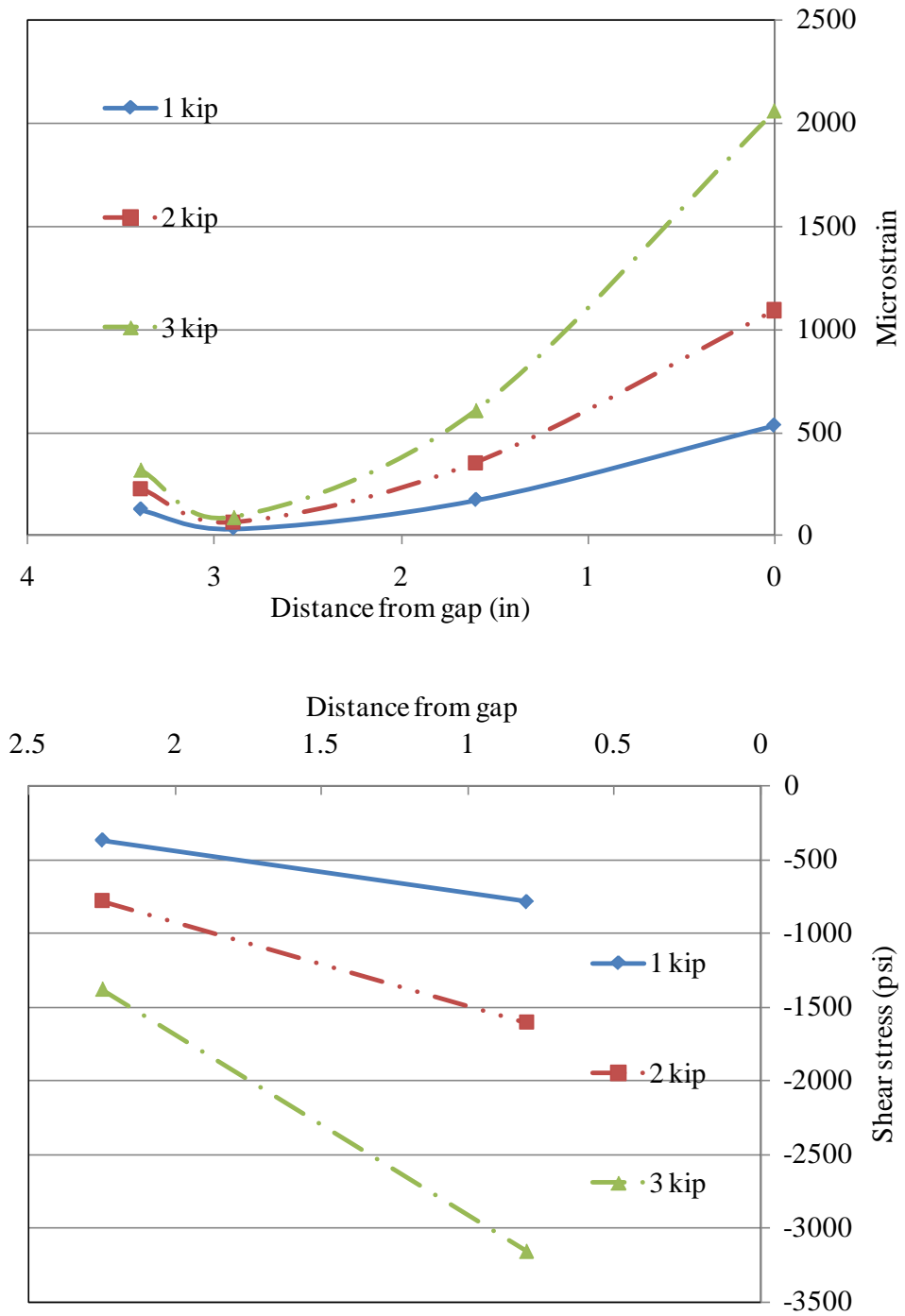


Fig. A17: 75 mm (3 in) bond length specimen strain and shear distribution

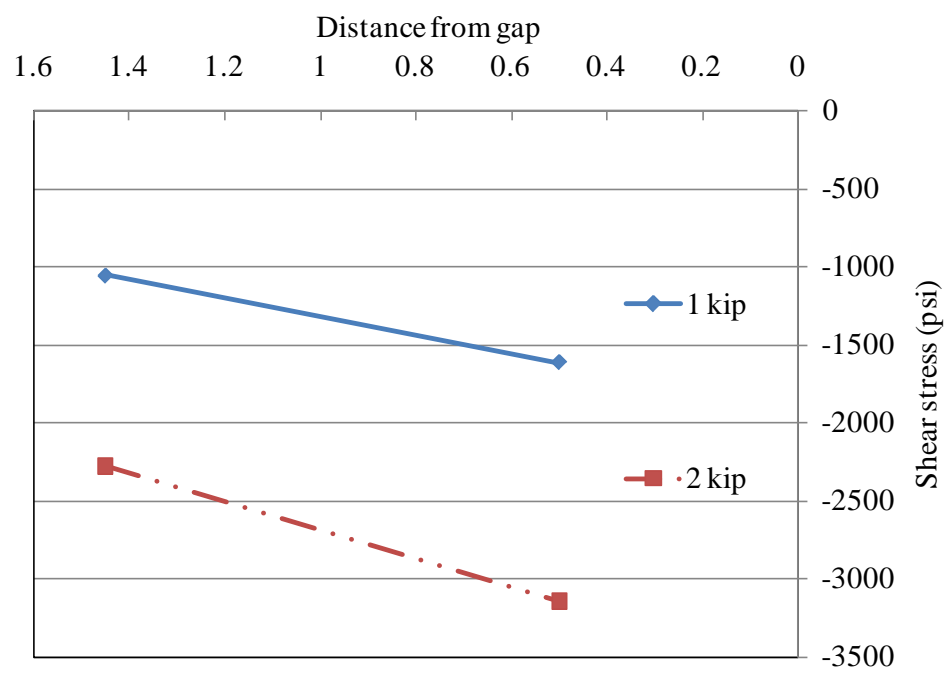
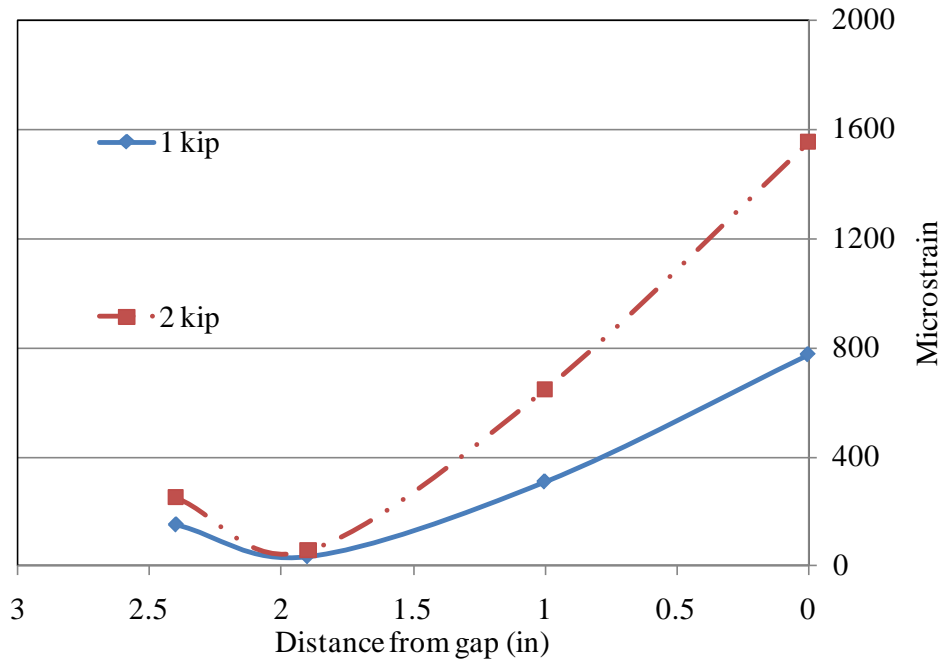


Fig. A18: 50 mm (2 in) bond length specimen strain and shear distribution

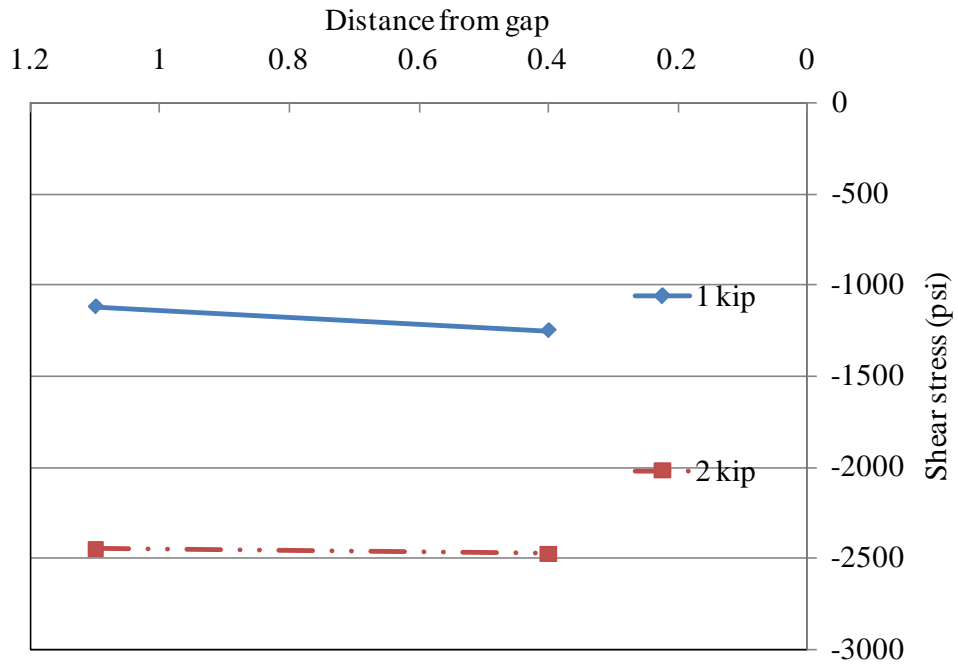
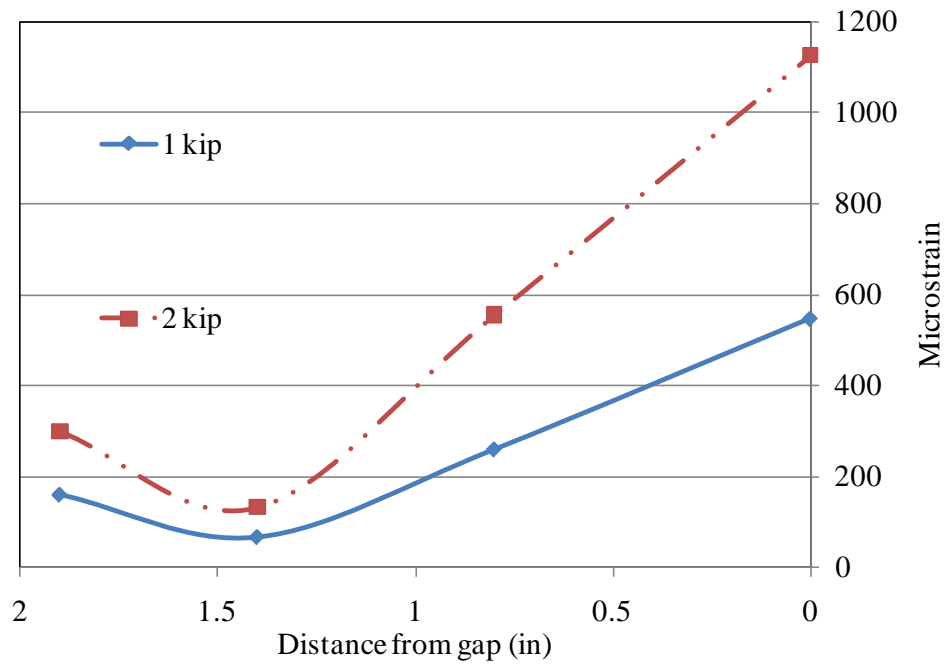


Fig. A19: 37.5 mm (1.2 in) bond length specimen strain and shear distribution

A.2 Doubly Reinforced Steel Plate Tests

Normal modulus CFRP Specimen #1

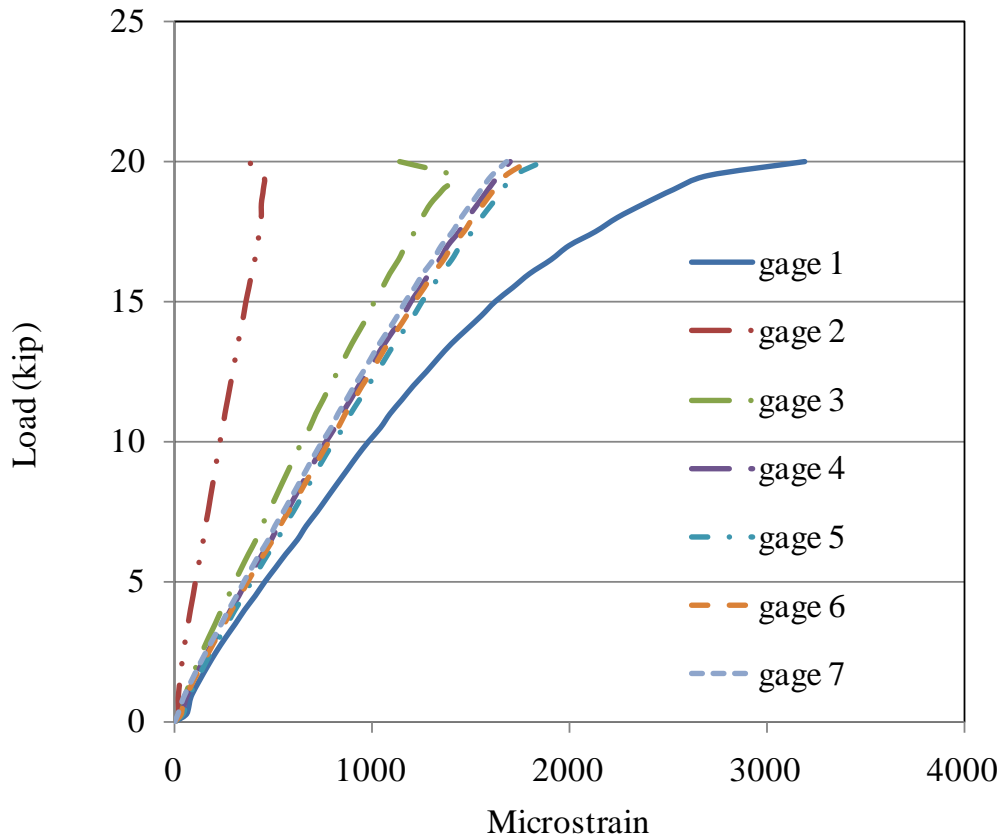
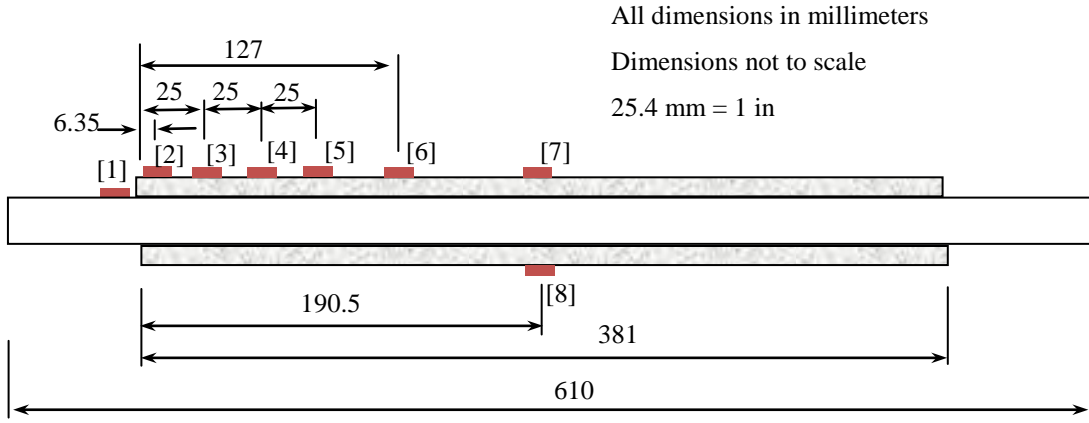


Fig. A20: Strain variation with increasing load

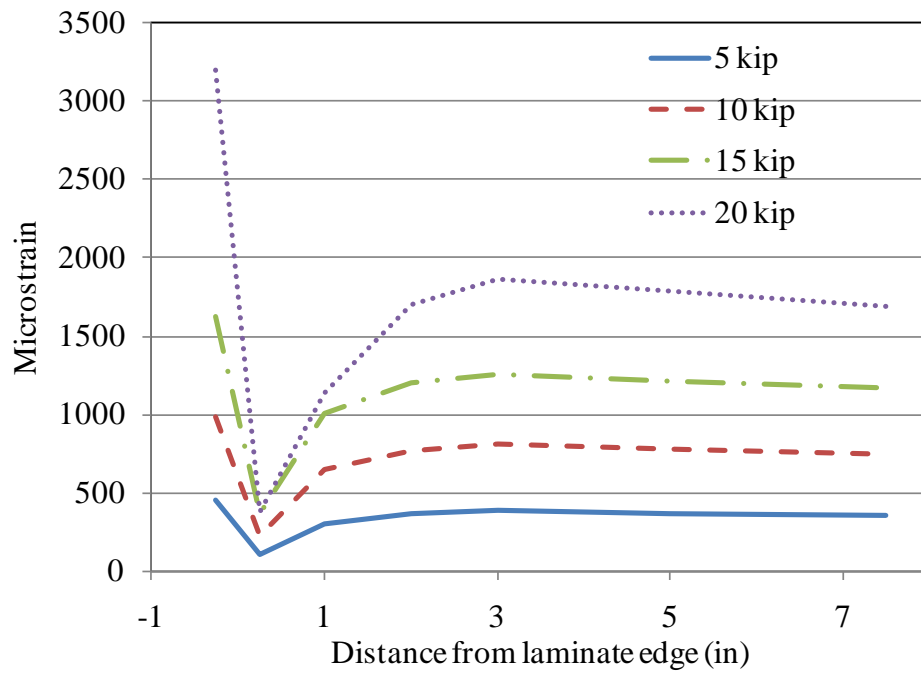


Fig. A21: Strain variation along laminate

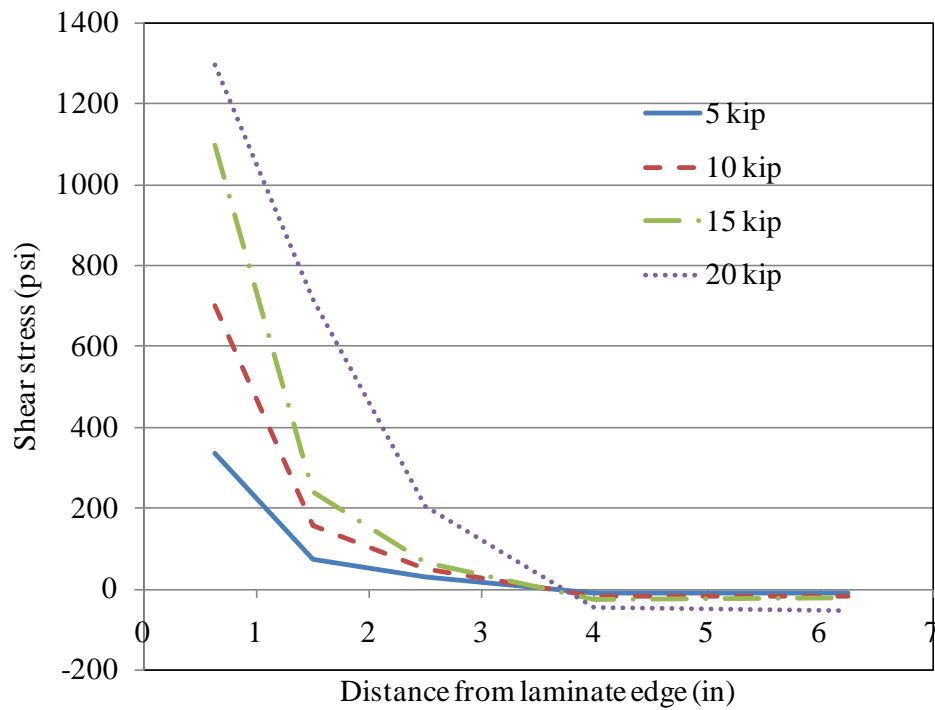


Fig. A22: Shear stress variation along laminate

Normal modulus CFRP Specimen #2

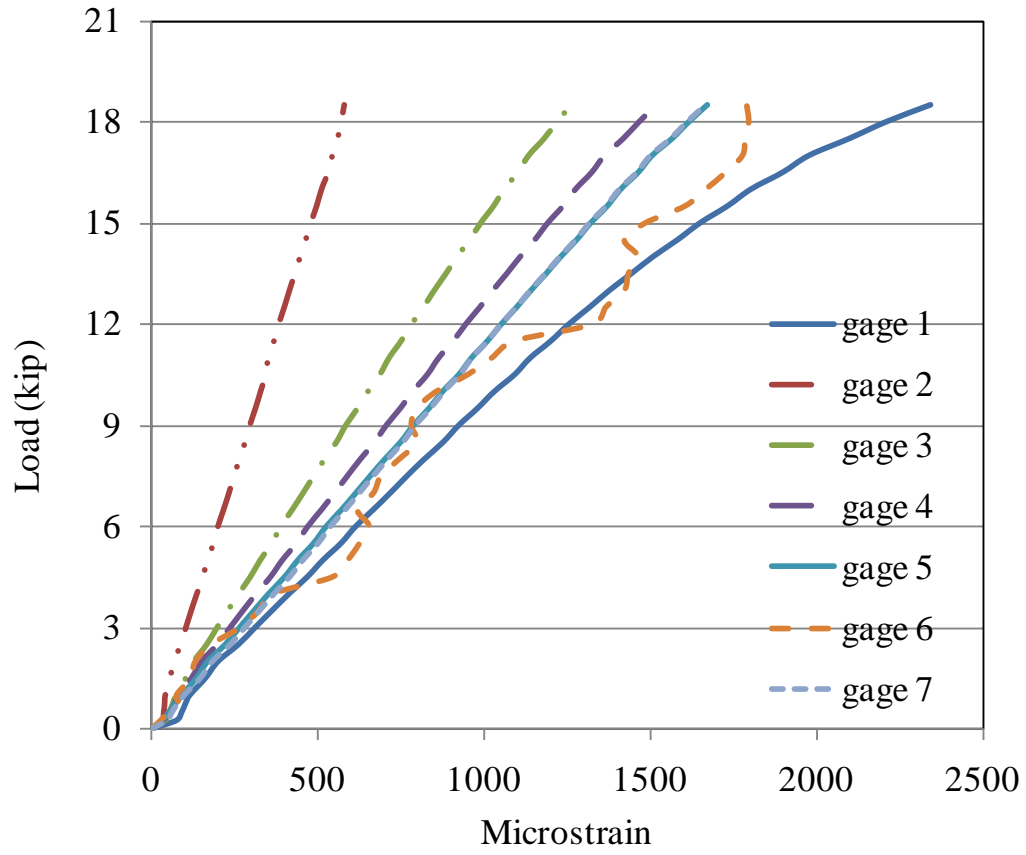


Fig. A23: Strain variation with increasing load

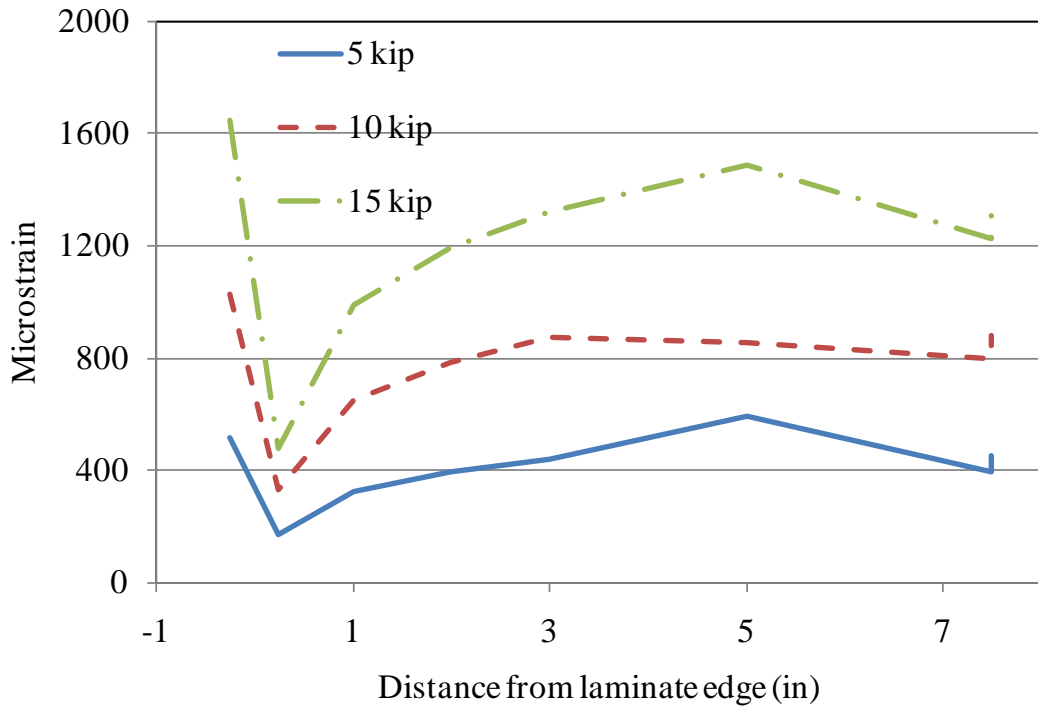


Fig. A24: Strain variation along laminate

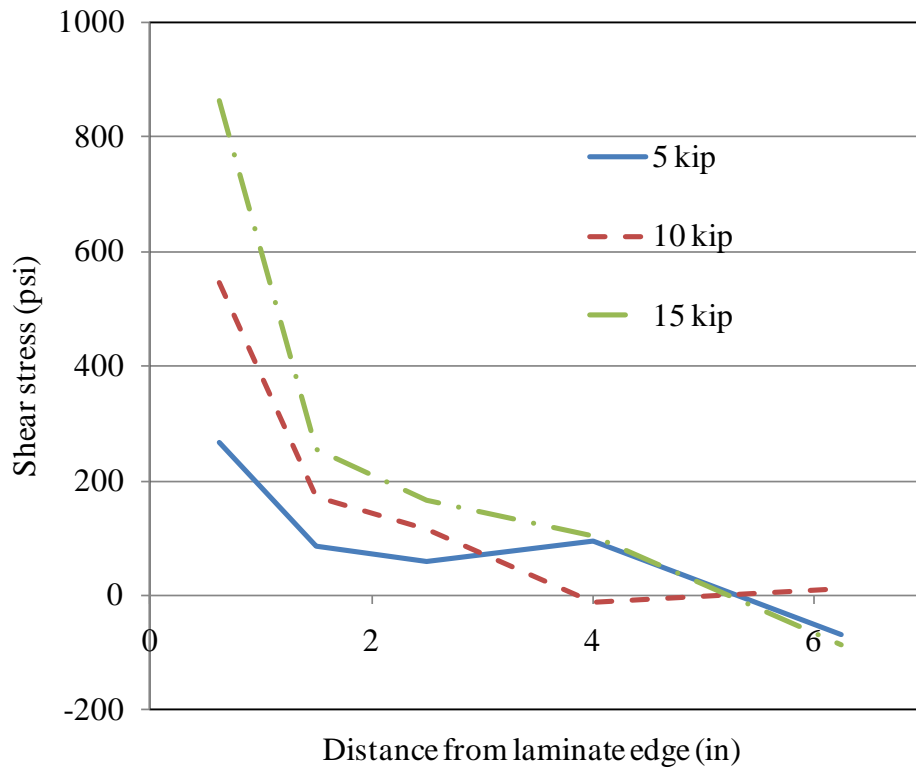


Fig. A25: Shear stress variation along laminate

Normal modulus CFRP Specimen #3

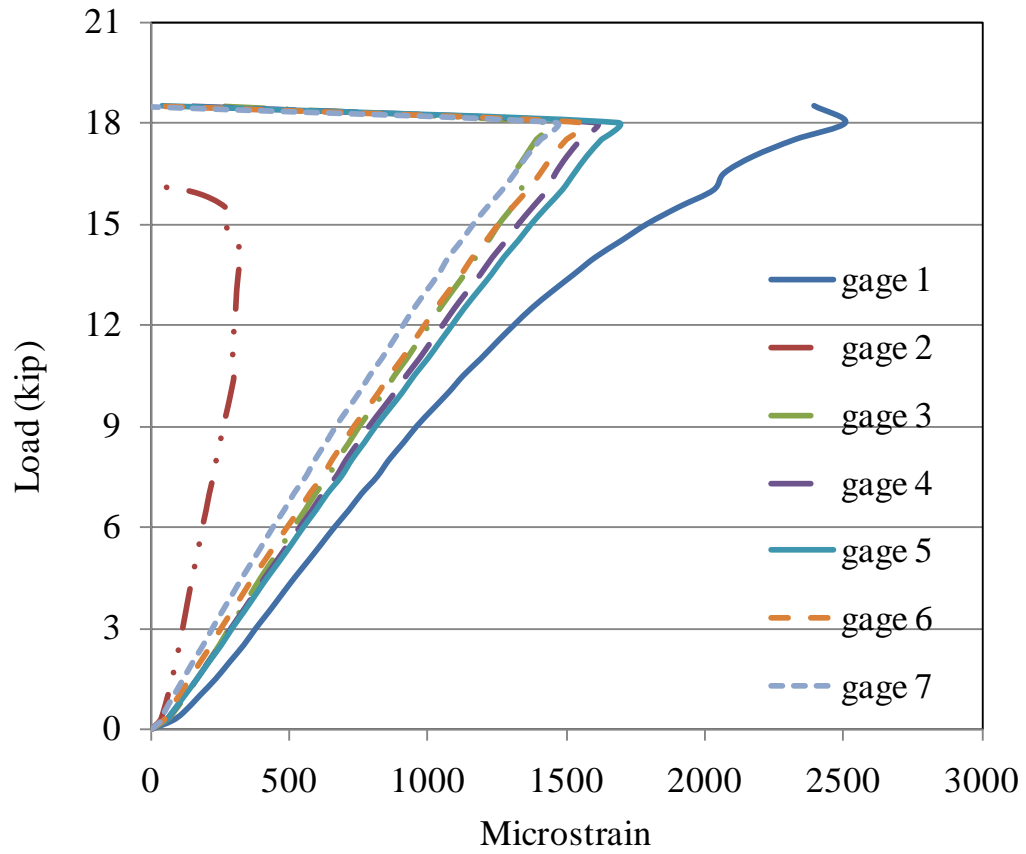


Fig. A26: Strain variation with increasing load

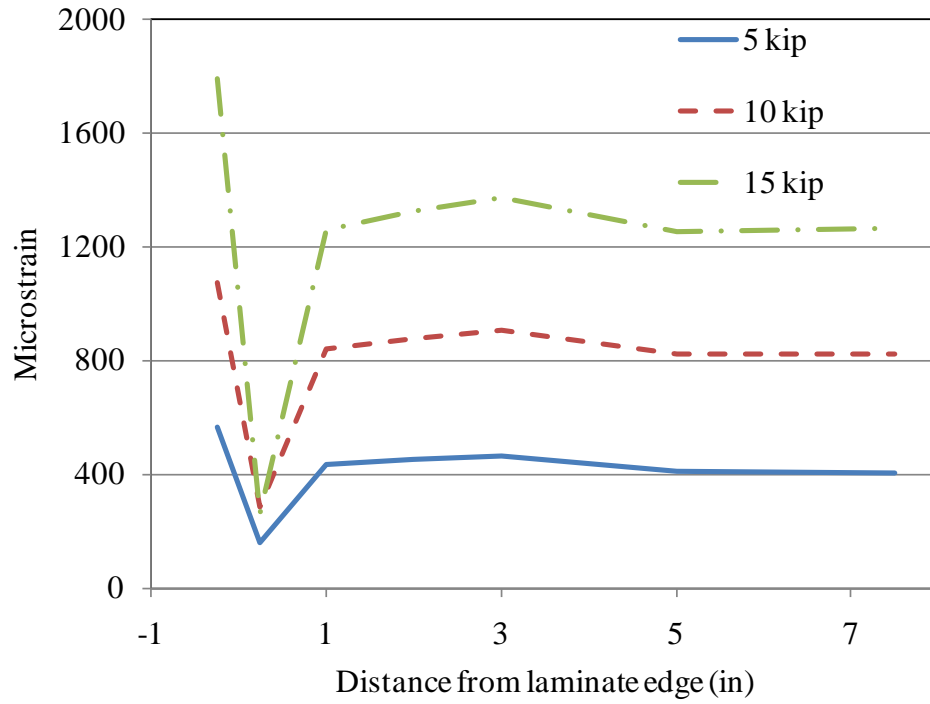


Fig. A27: Strain variation along laminate

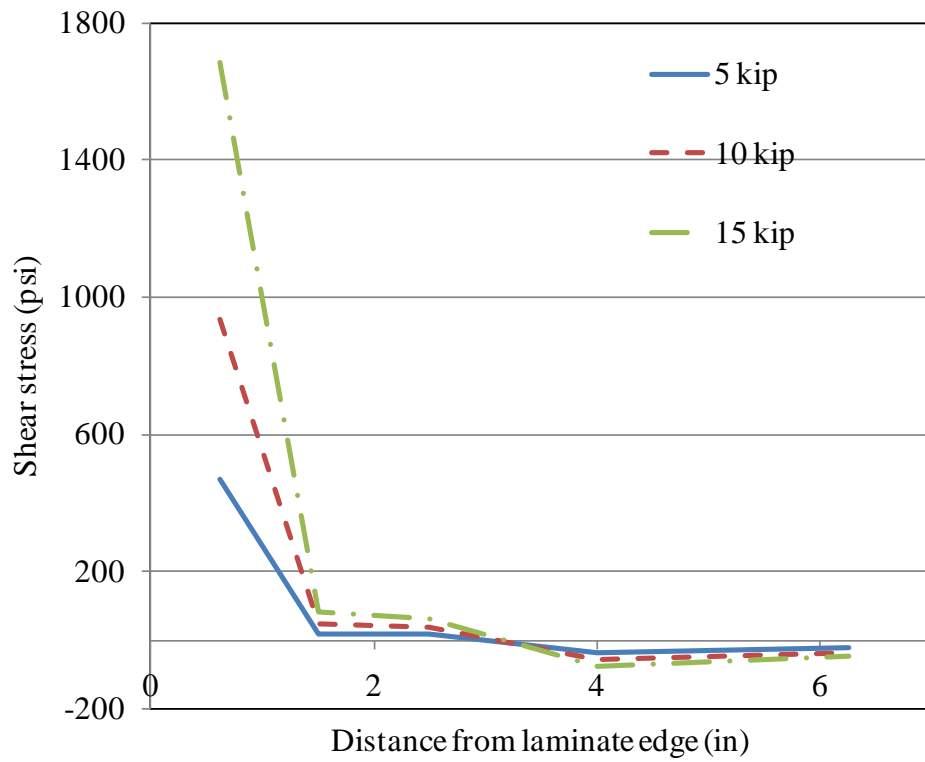


Fig. A28: Shear stress variation along laminate

Ultra high modulus CFRP Specimen #1

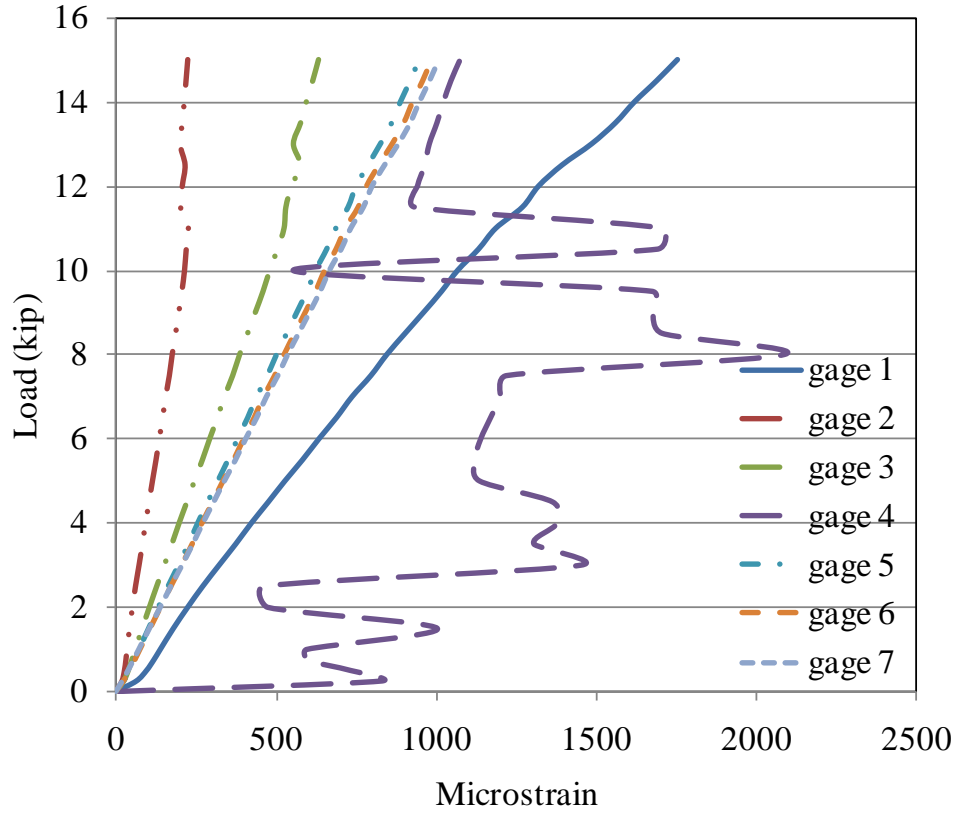


Fig. A29: Strain variation with increasing load

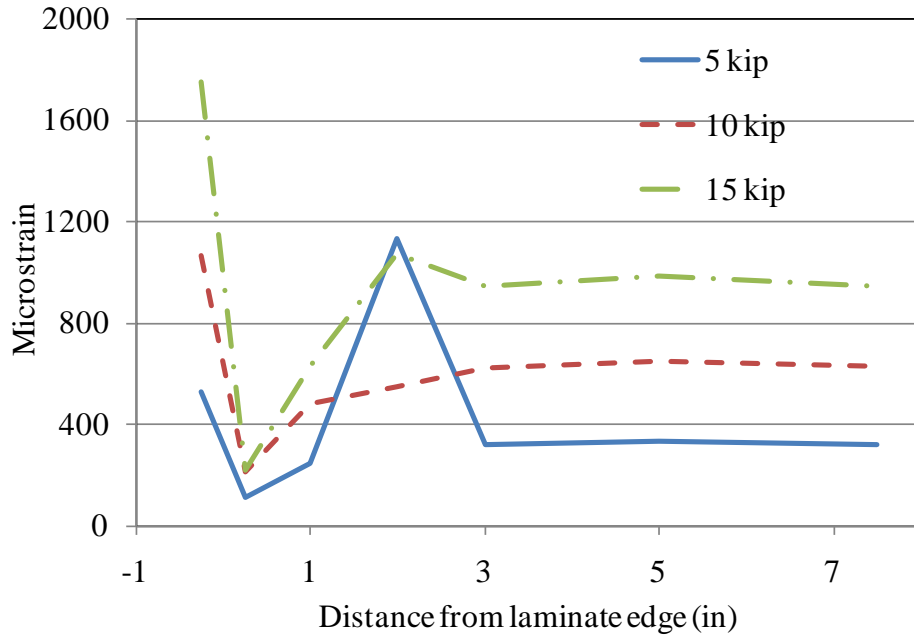


Fig. A30: Strain variation along laminate

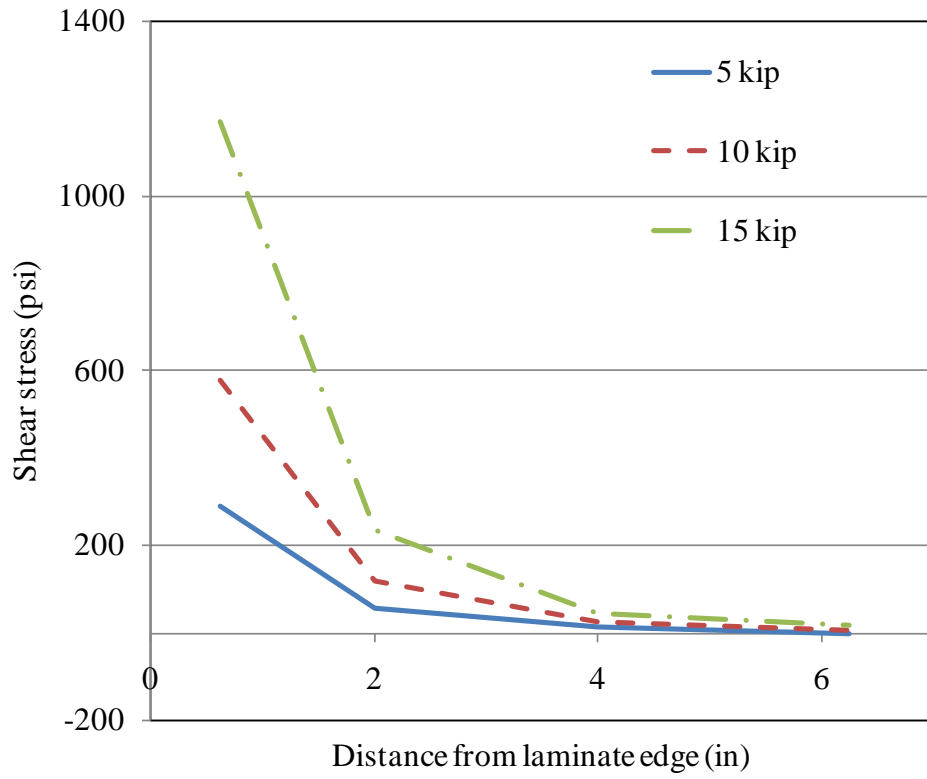


Fig. A31: Shear stress variation along laminate

Ultra high modulus CFRP Specimen #2

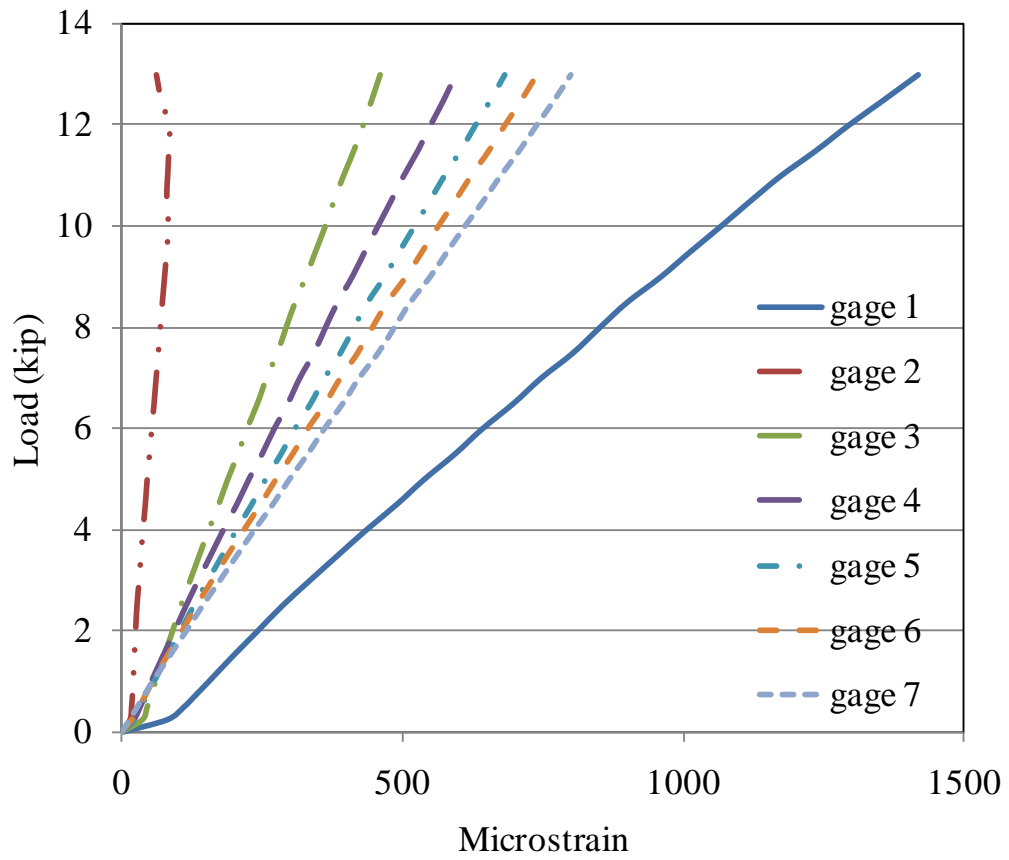


Fig. A32: Strain variation with increasing load

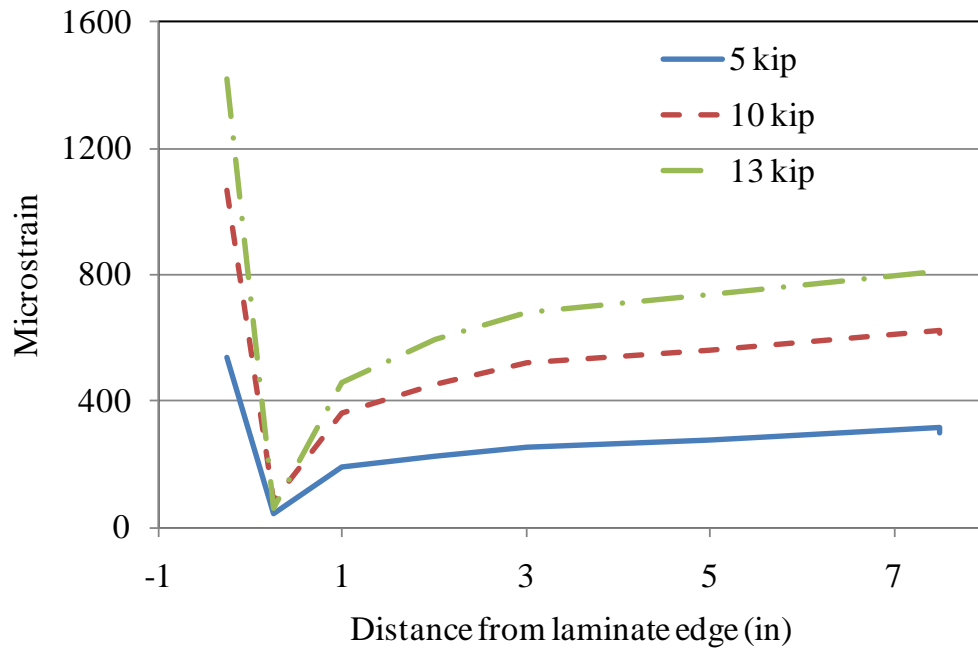


Fig. A33: Strain variation along laminate

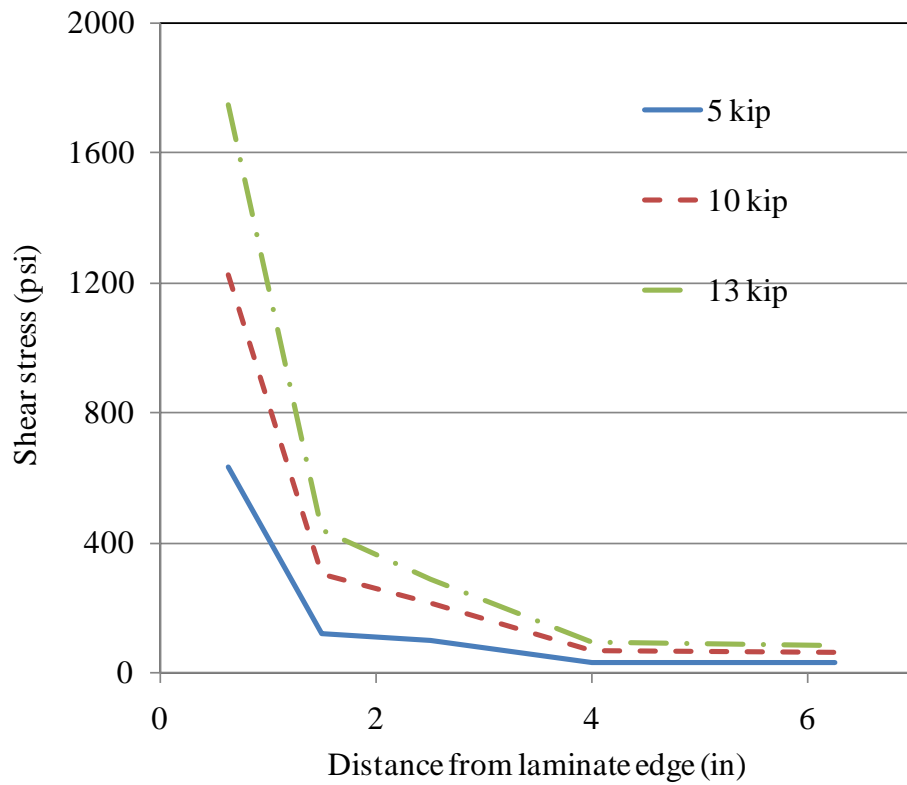


Fig. A34: Shear stress variation along laminate

Ultra high modulus CFRP Specimen #3

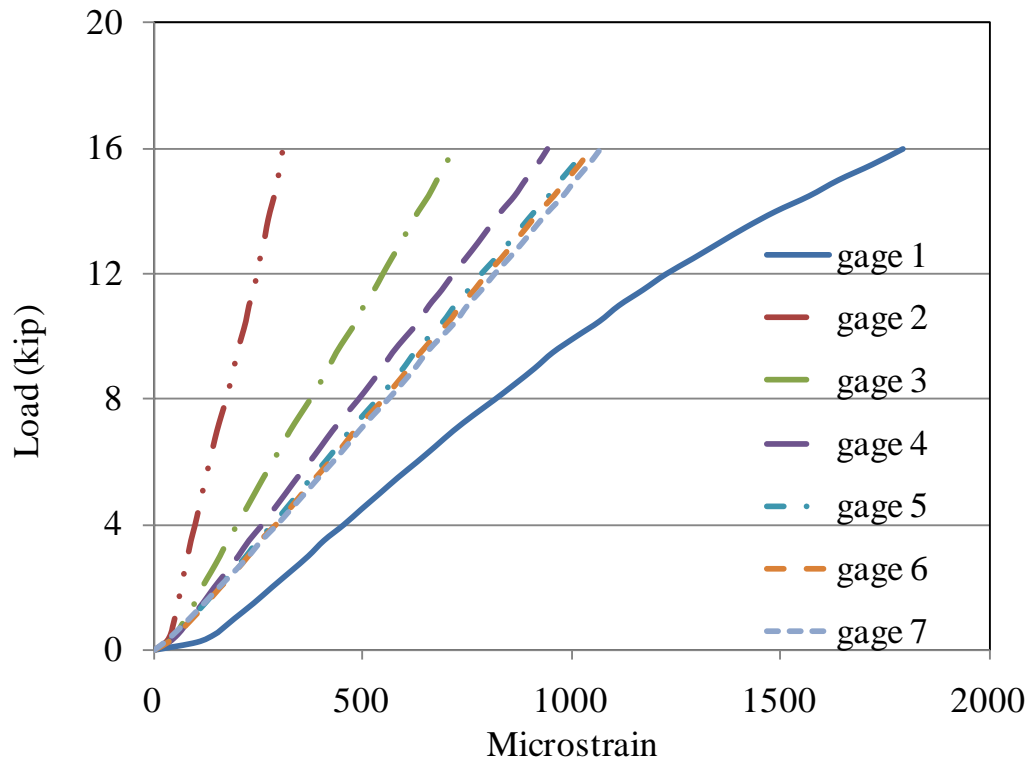


Fig. A35: Strain variation with increasing load

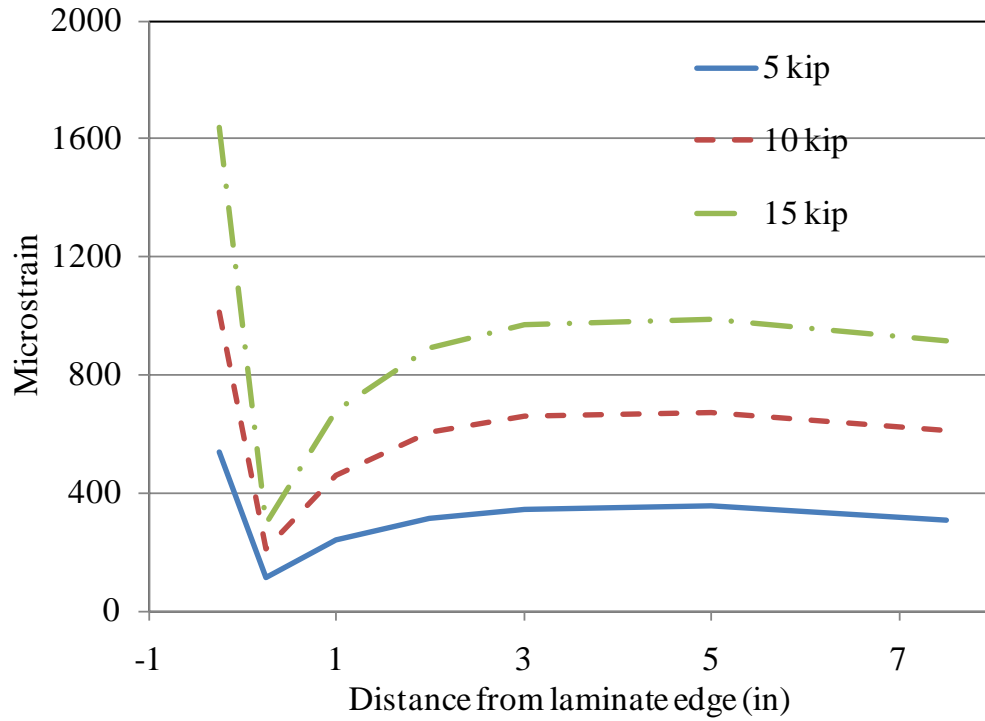


Fig. A36: Strain variation along laminate

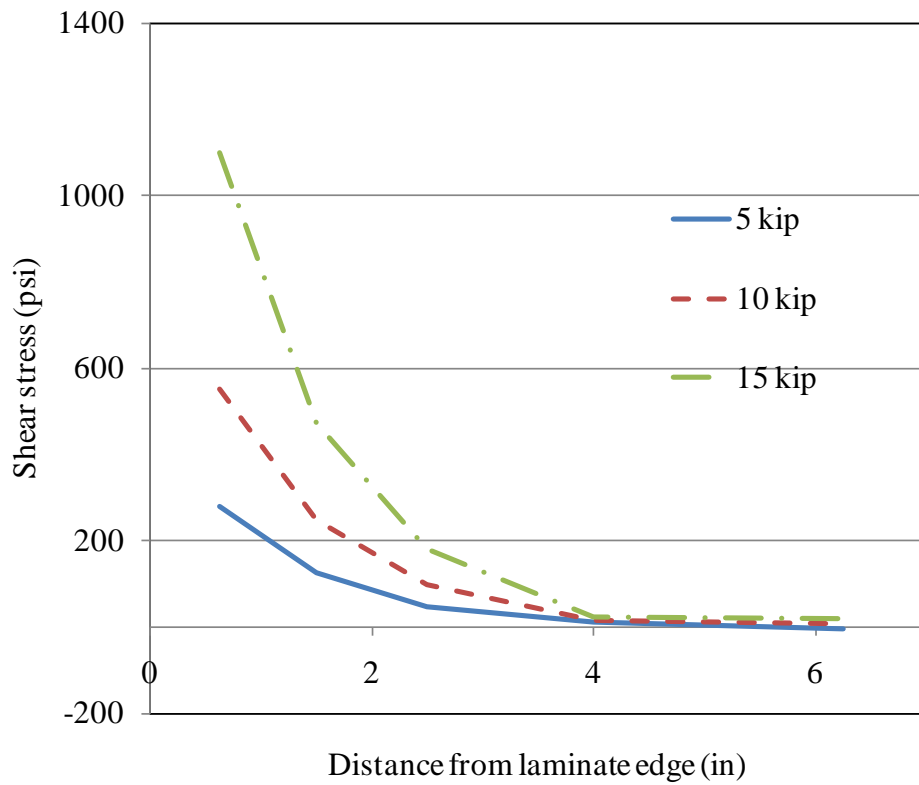


Fig. A37: Shear stress variation along laminate

A.3 Steel Beam Specimens

Control Steel Beam

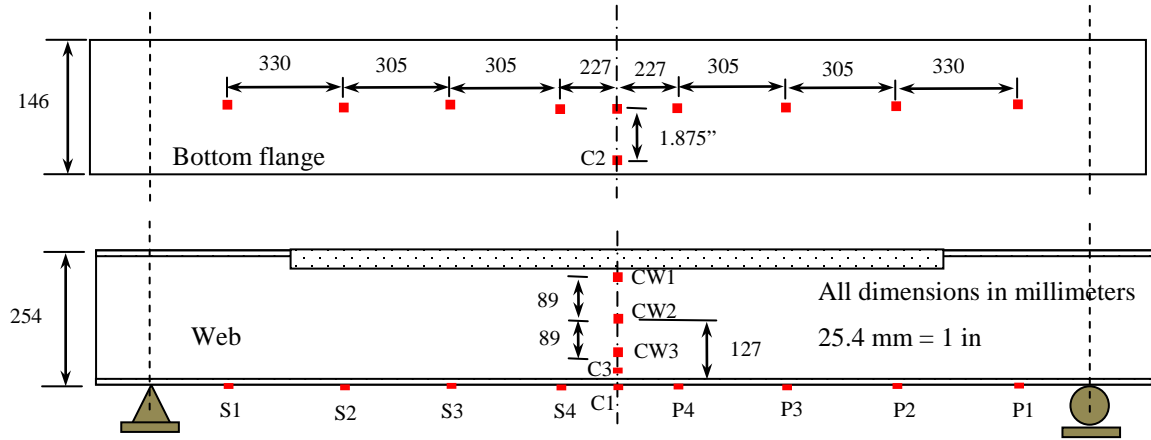


Fig. A38: Control steel beam gage layout

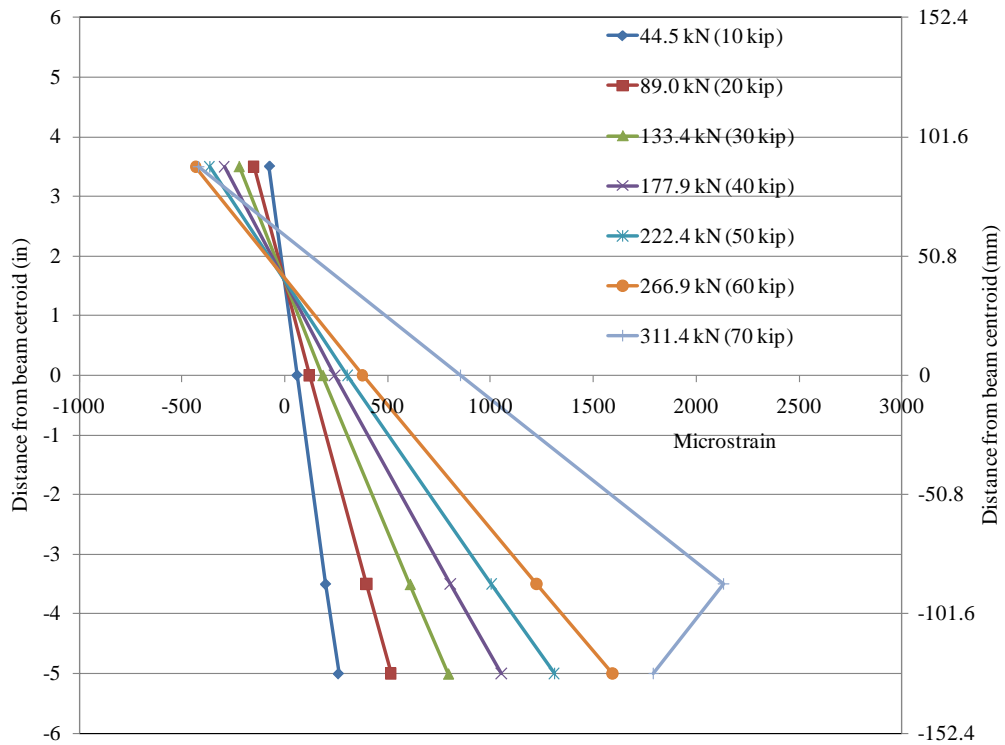


Fig. A39: Neutral axis change with load

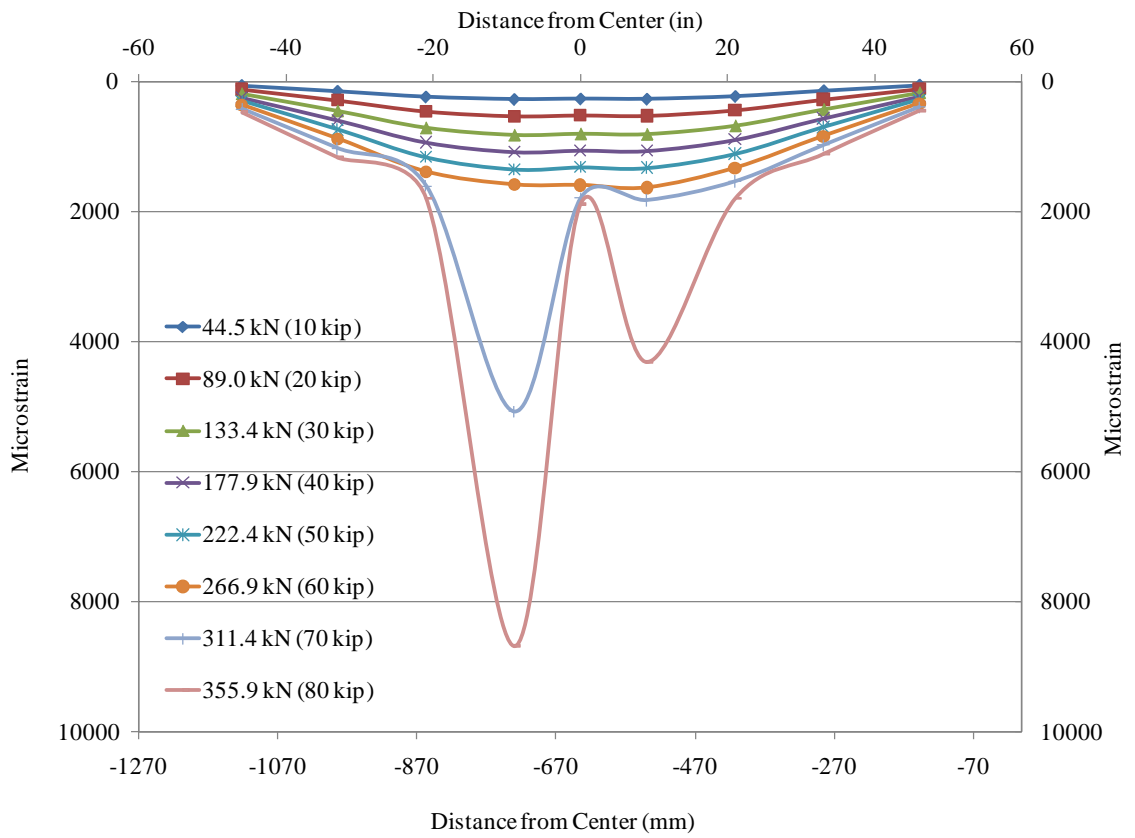


Fig. A40: Strain distribution along bottom flange

Full Width Laminate Strengthened Beam

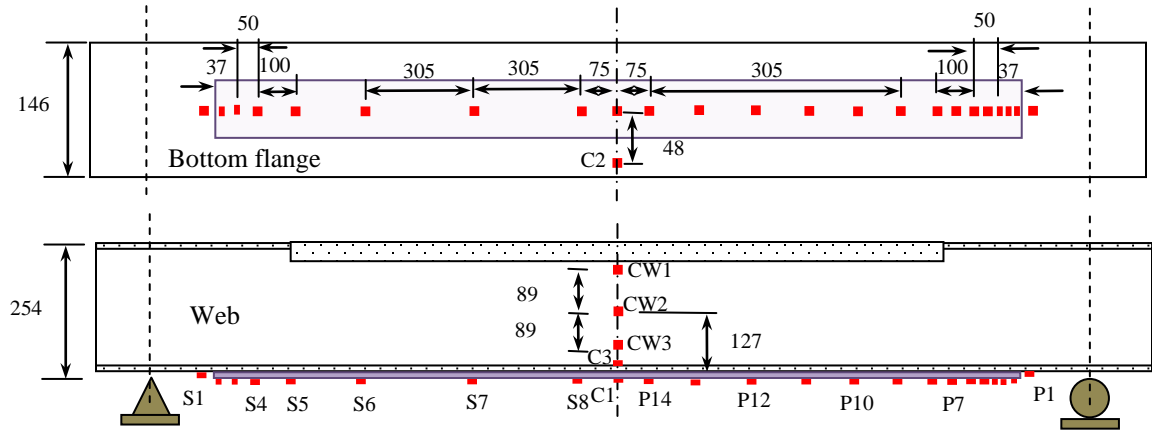


Fig. A41: Full width strengthened beam layout

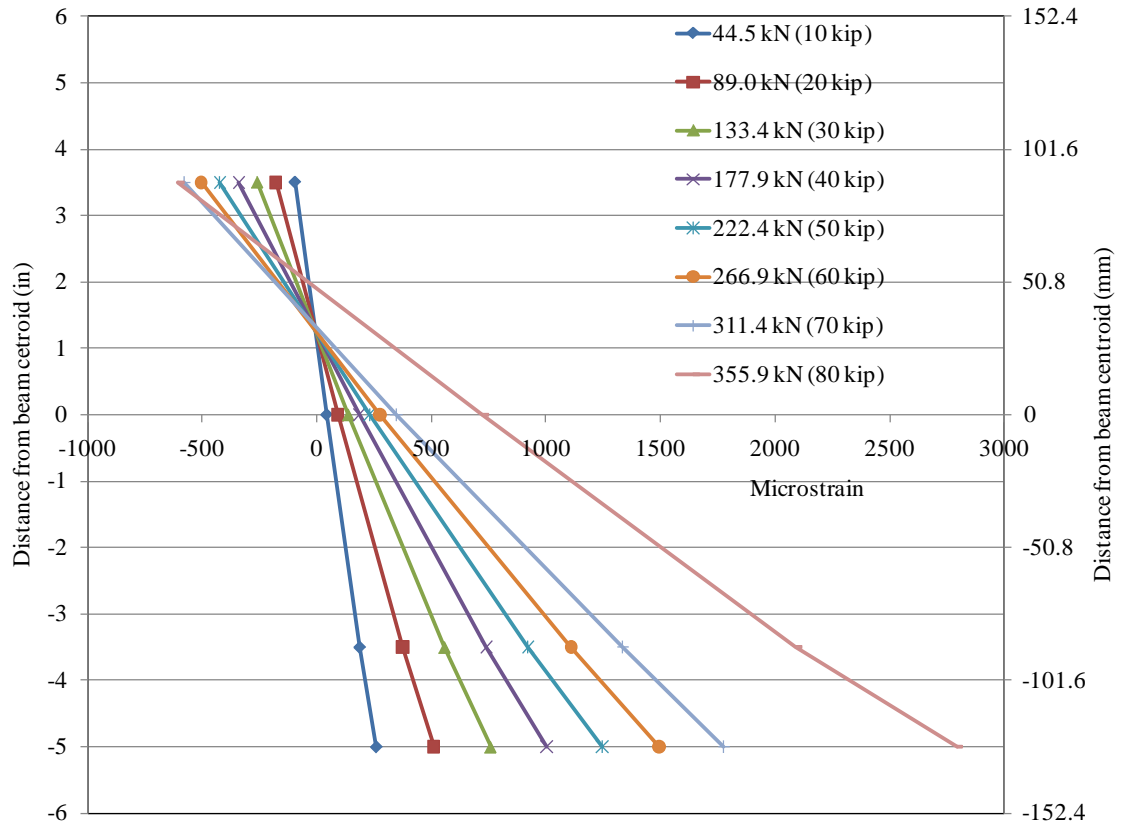


Fig. A42: Neutral axis change with load

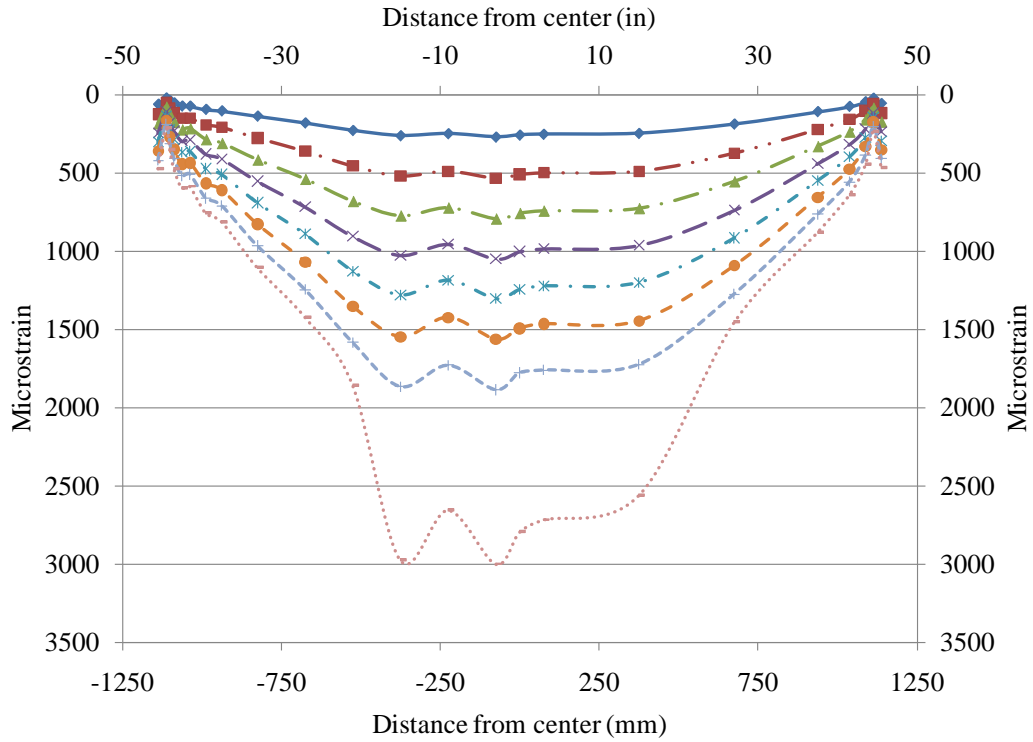


Fig. A43: Strain distribution along laminate

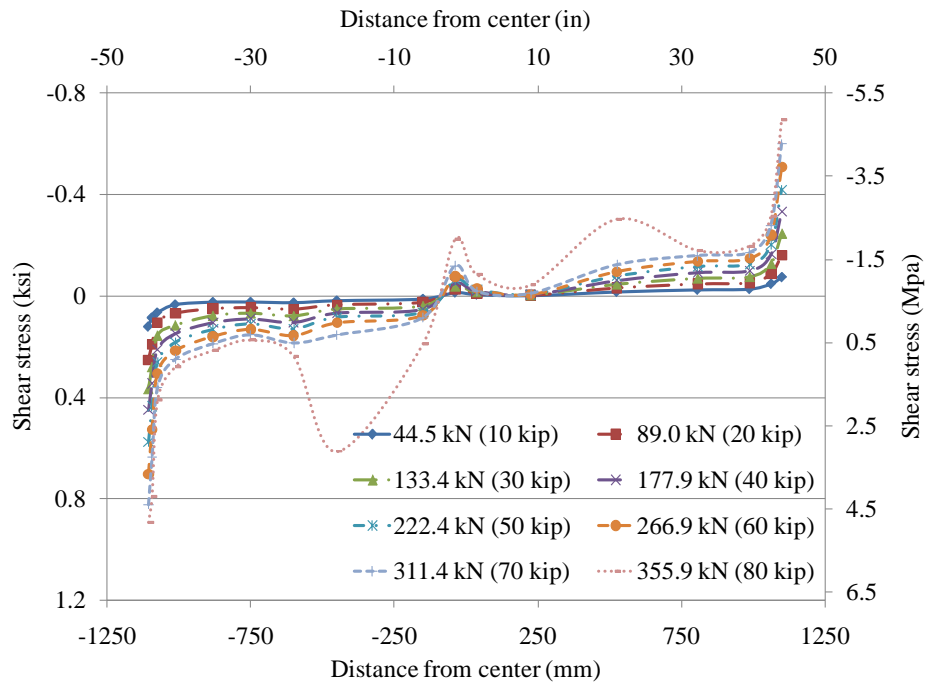


Fig. A44: Shear stress distribution along laminate

10 mm (0.4 in) Strip Panel Strengthened Beam

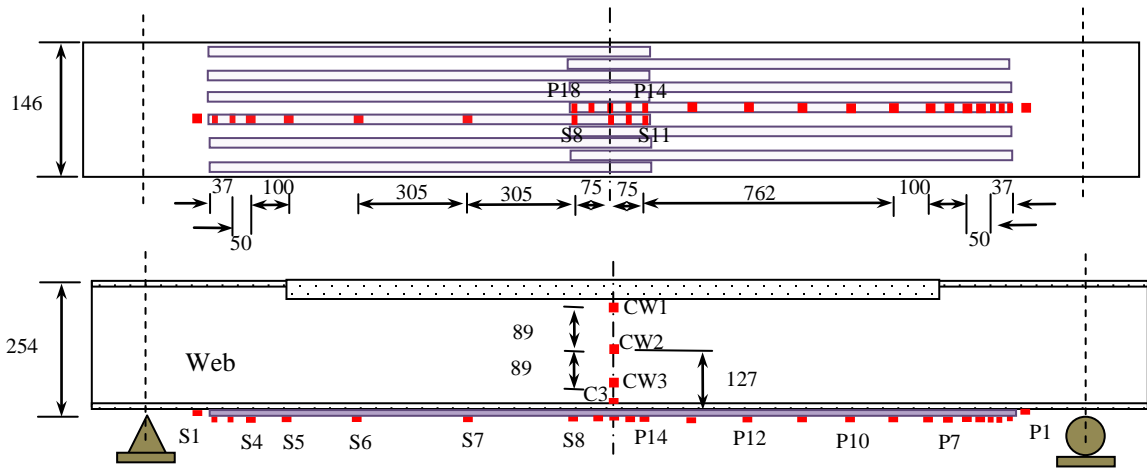


Fig. A45: Strip panel strengthened beam gage layout

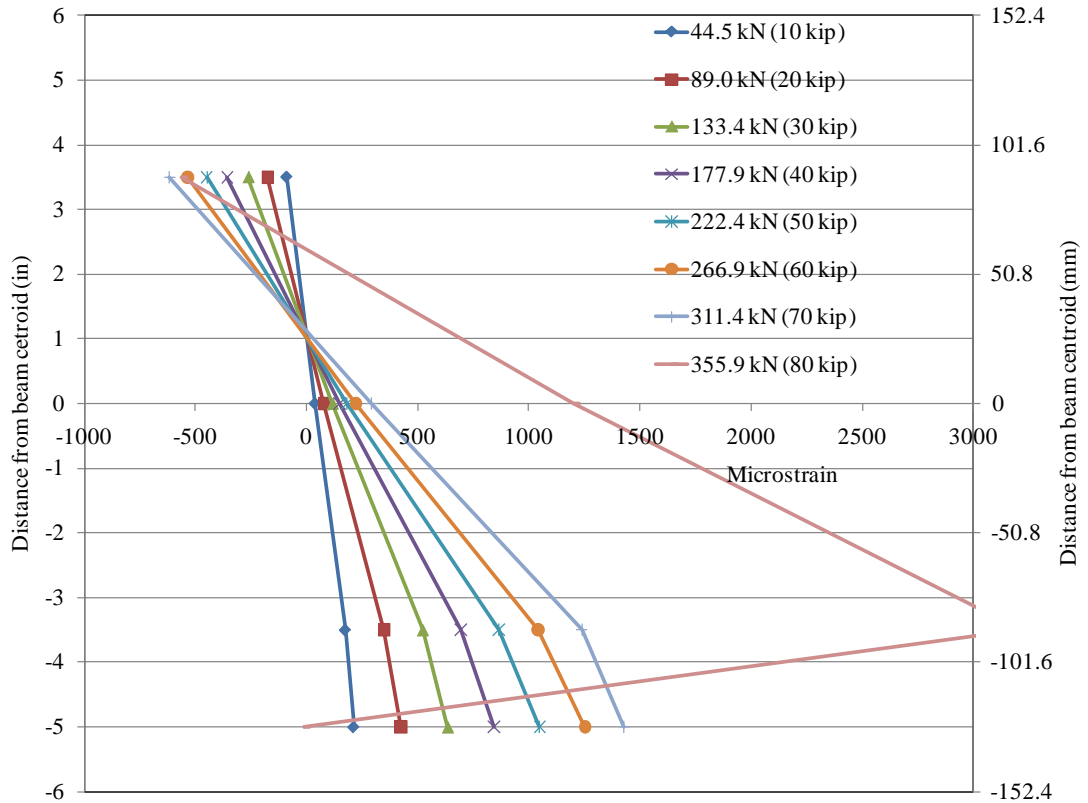
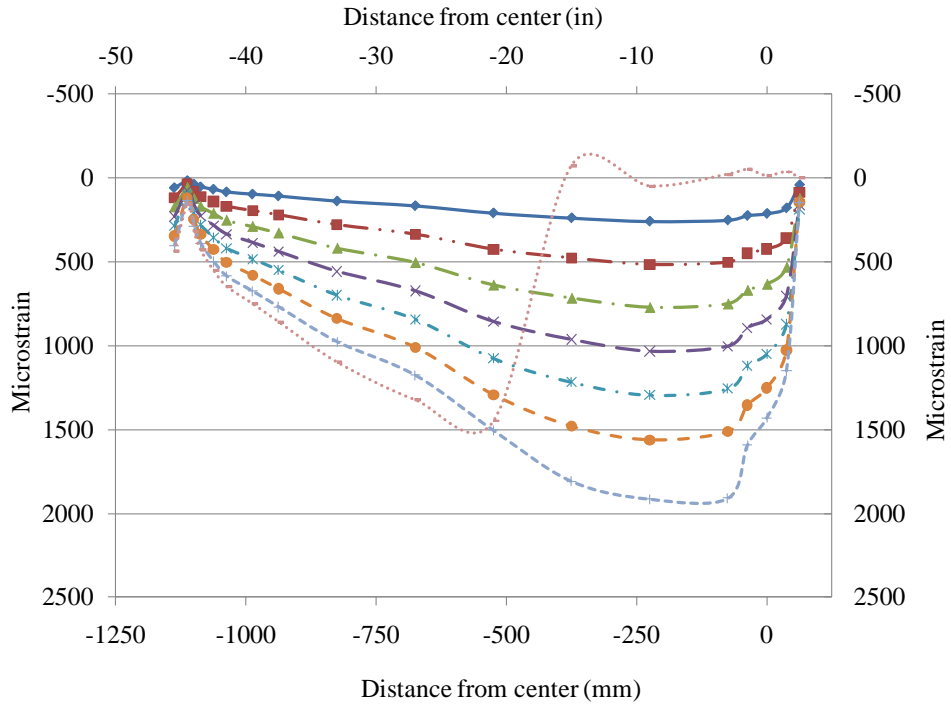
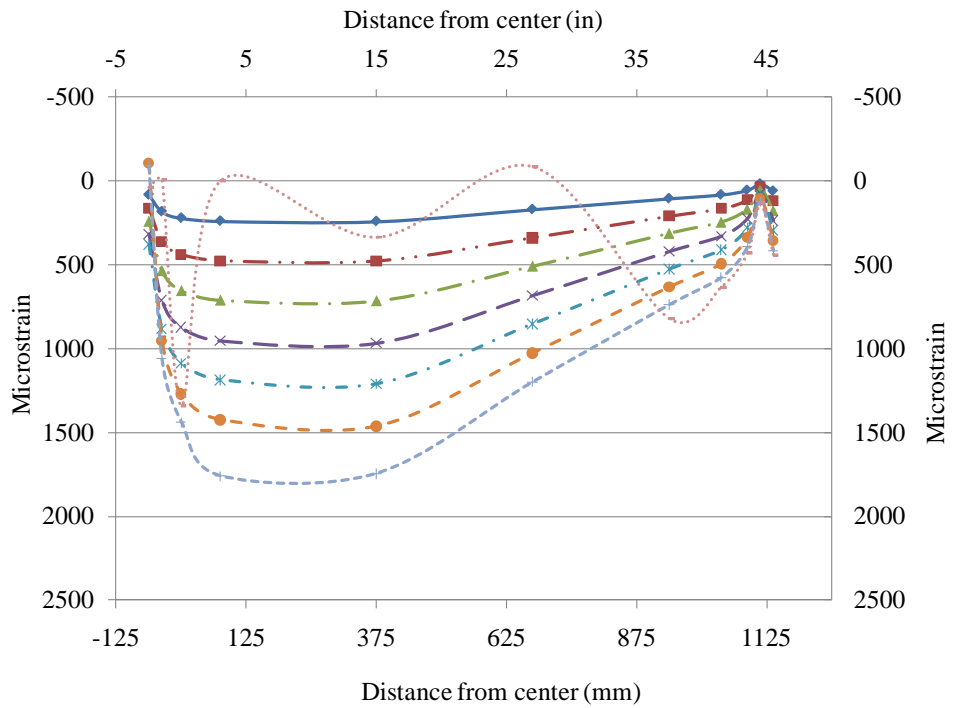


Fig. A46: Neutral axis change with load

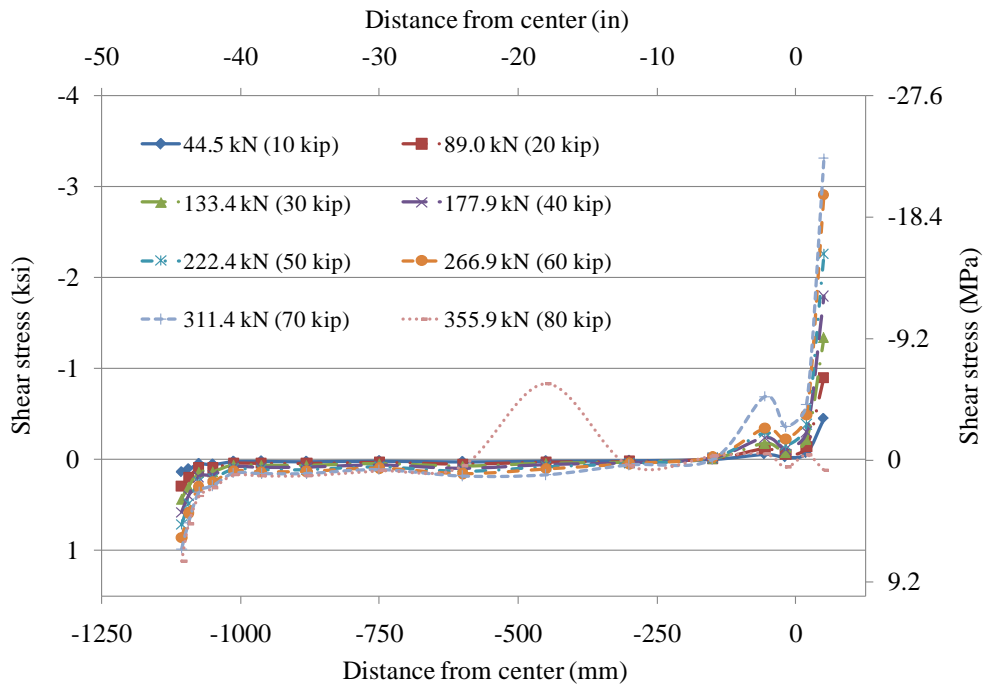


(a) Primary gages

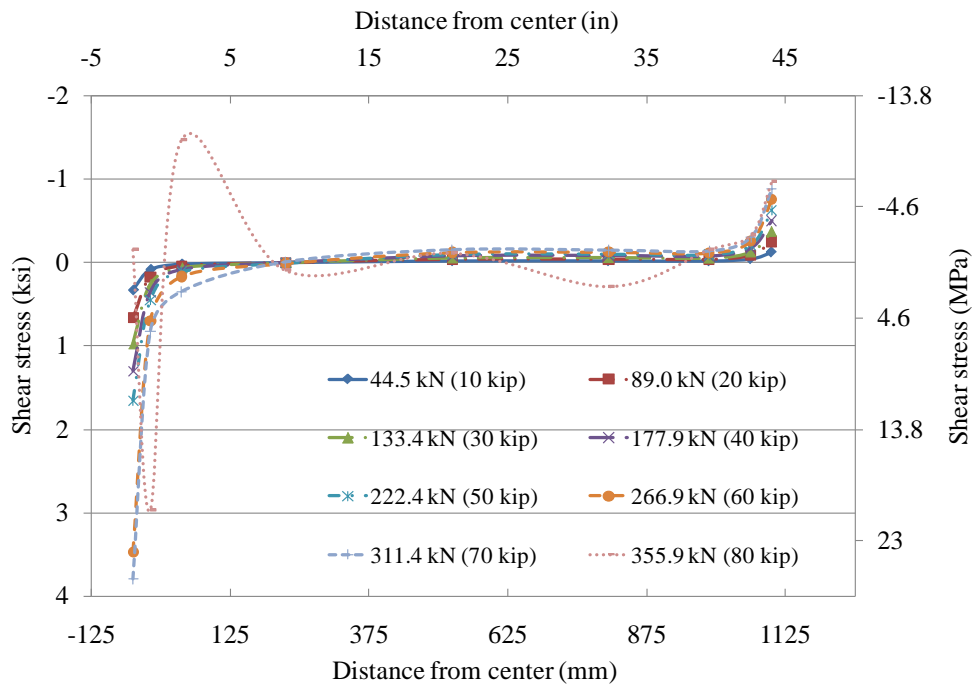


(b) Secondary gages

Fig. A47: Strain distribution along laminate



(a) Primary gages



(b) Secondary gages

Fig. A48: Shear stress distribution along laminate

5 mm (0.2 in) Strip Panel Strengthened Beam

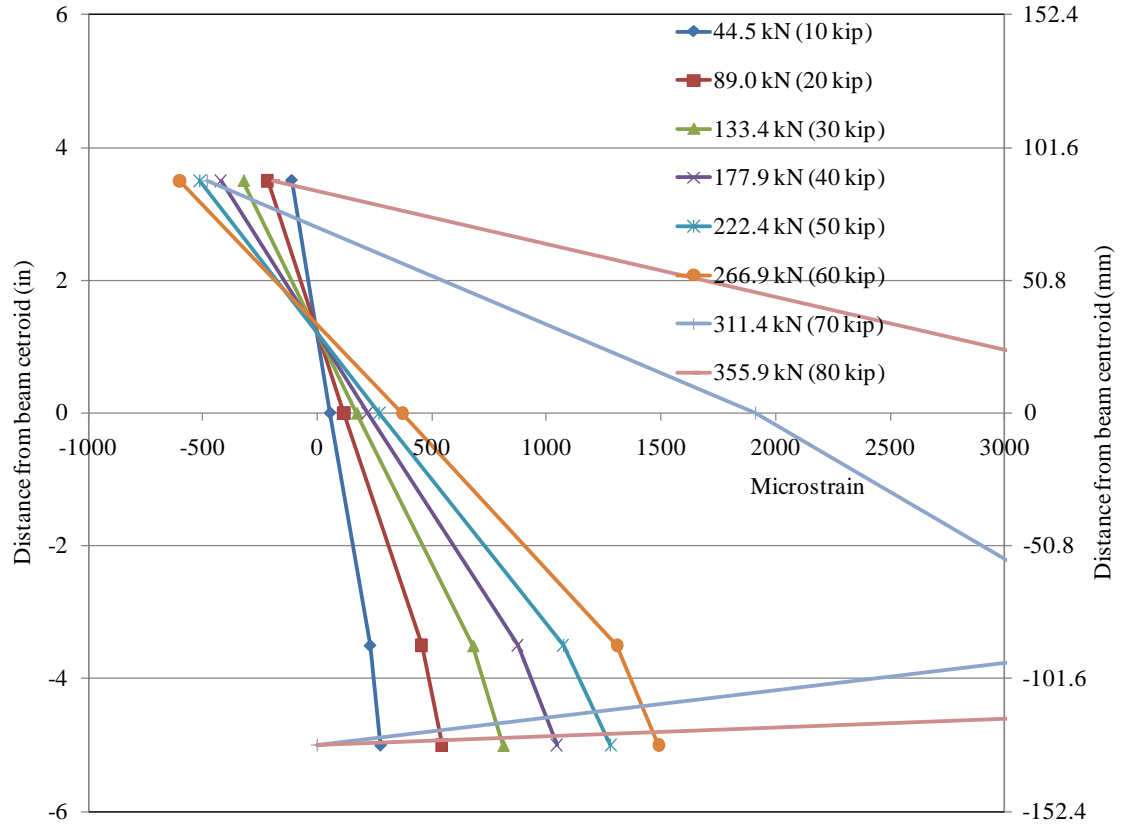
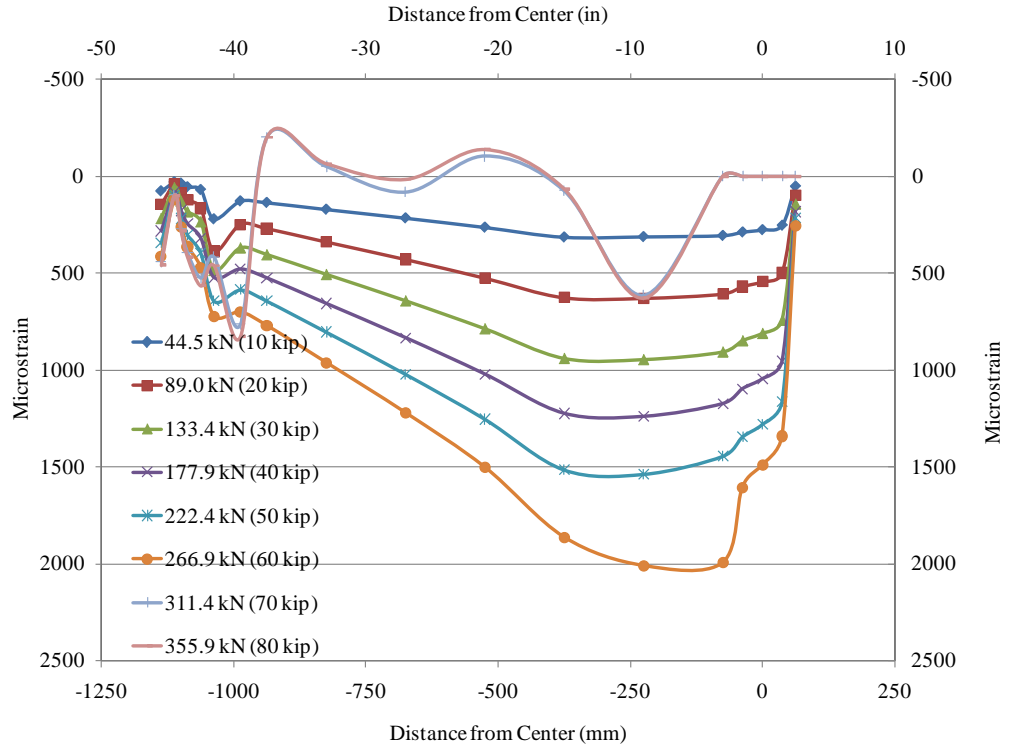
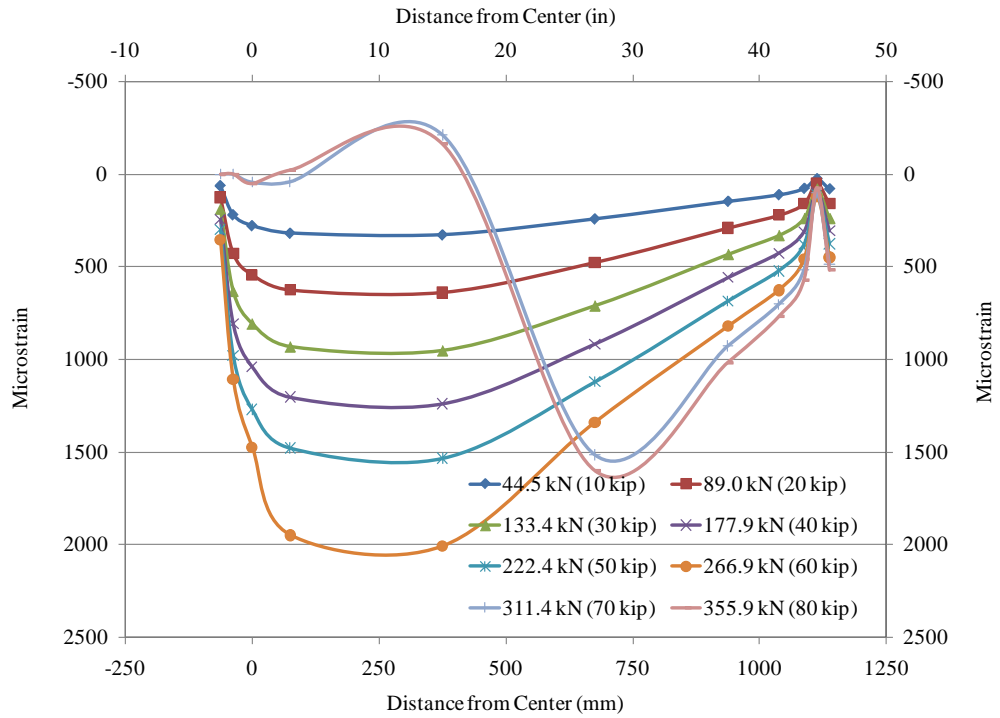


Fig. A49: Neutral axis change with load



(a) Primary gages



(b) Secondary gages

Fig. A50: Strain distribution along laminate

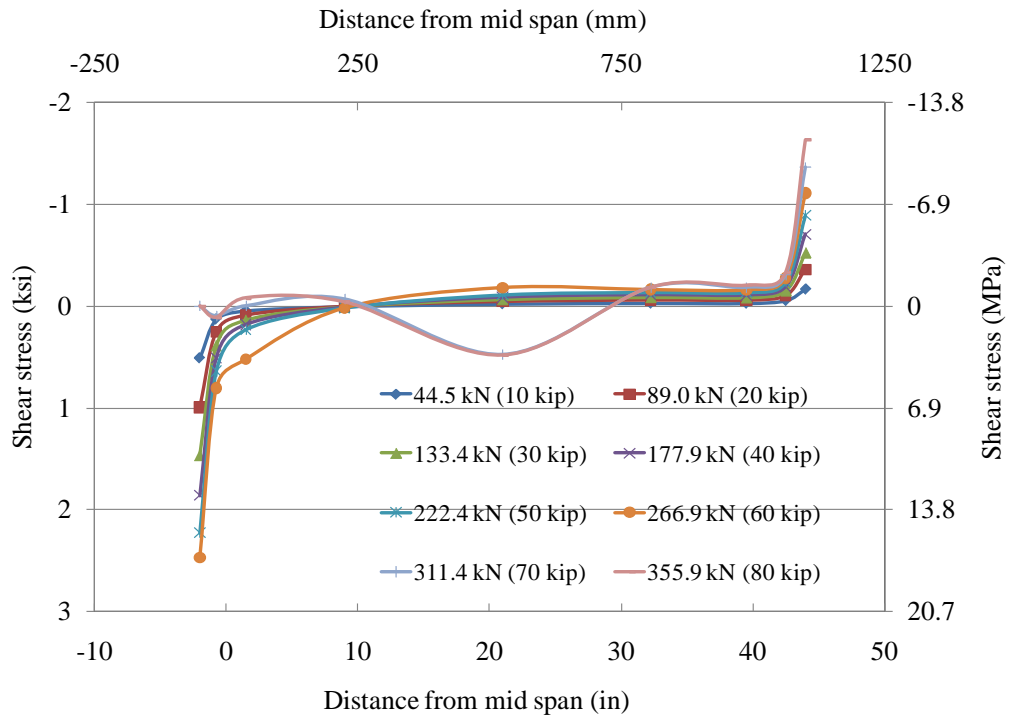
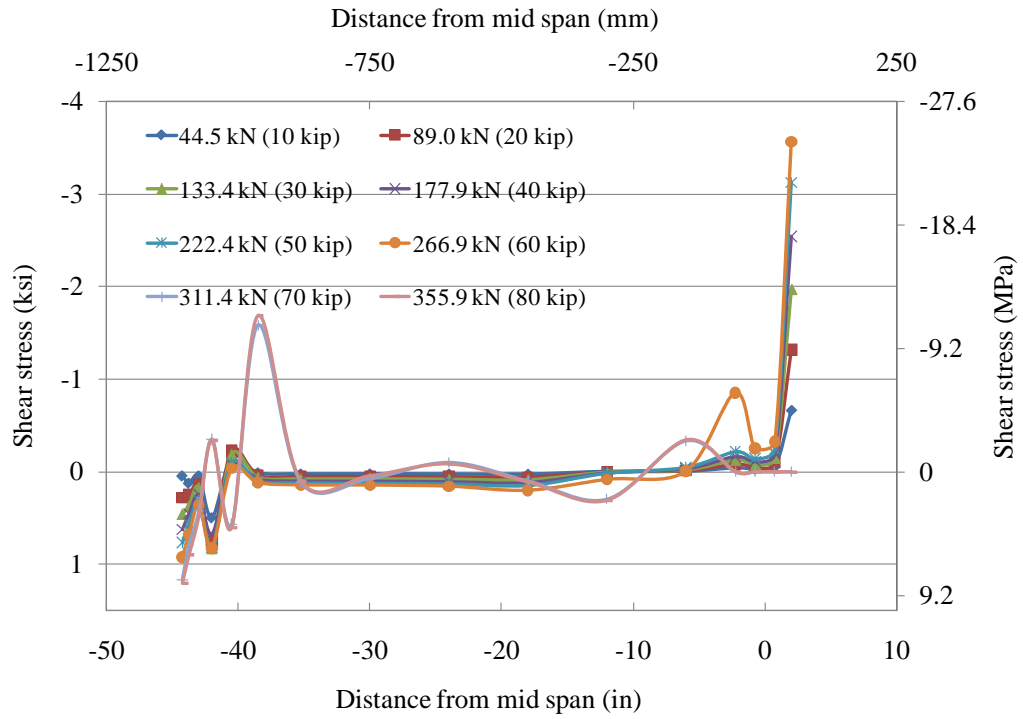


Fig. A51: Shear stress distribution along laminate

APPENDIX B

B.1 Simple Beam Strengthening Analysis

Strengthening of Non-composite Steel Girder

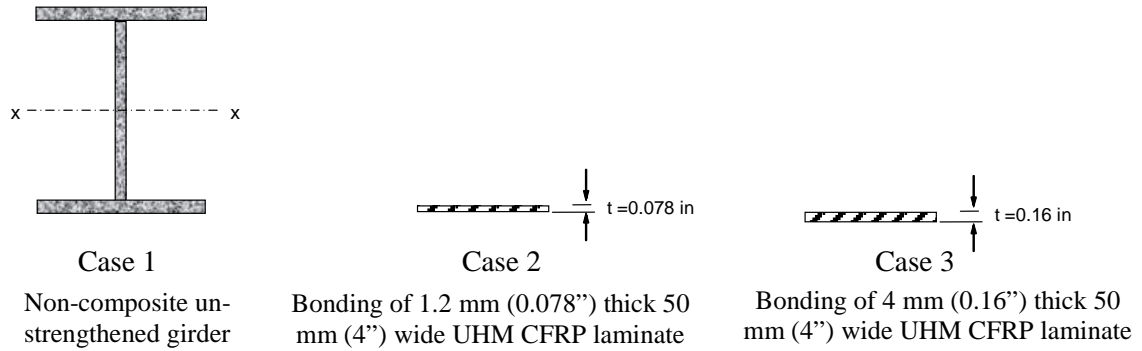


Fig. B1: Non-Composite Bridge Girder Types

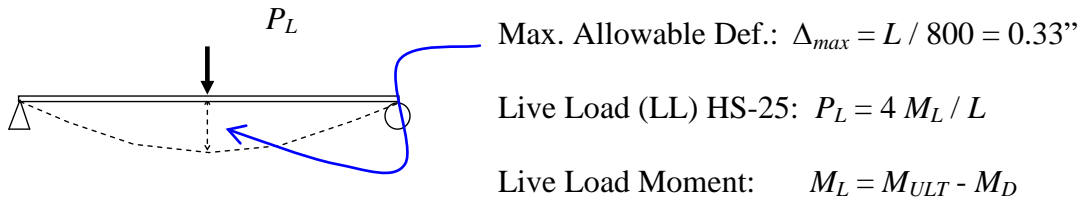


Fig. B2: Simple Support Beam

Table B1: Strengthening of Non-Composite Steel Bridge Girder

Girder Case	I_x in ⁴	Controlling Parameter			
		Top Flange Stress ^a		Live Load Deflection ^b	
		P_L kip	Increase in P_L Capacity	P_L kip	Increase in P_L Capacity
Case 1	291	24.83	-	7.26*	-
Case 2	322	25.80	3.9 ^c %	8.04*	10.7 %
Case 3	351	26.71	7.6 %	8.76*	20.7 %

*Controlling parameter for design

^a Controlling parameter 50ksi stress in top flange

^b Controlling parameter 0.33in Live Load deflection

^c % increase in P_L capacity = $(25.80 - 24.83) / 24.83 = 3.9\%$

1" = 25.4 mm

1 kip = 4.45 kN

Strengthening of Concrete –Steel Composite Girder

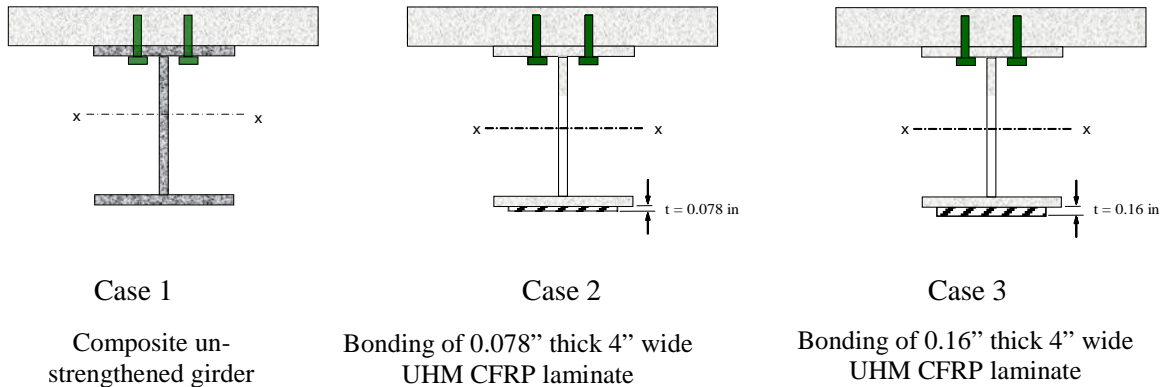


Fig. B3: Composite Bridge Girder Types

Table B2: Strengthening of Composite Steel Bridge Girder

Girder Case	I_x in ⁴	Controlling Parameter			
		Bottom Flange Stress ^a		Live Load Deflection ^b	
		P_L kip	Increase in P_L Capacity	P_L kip	Increase in P_L Capacity
Case 1	2392	61.13	-	59.72*	-
Case 2	2567	71.53	17.0 ^c %	64.09*	7.3 %
Case 3	2745	82.42	34.8 %	68.53*	14.8 %

*Controlling parameter for design

^a Controlling parameter 50ksi stress in bottom flange

^b Controlling parameter 0.33in Live Load deflection

^c % increase in P_L capacity = $(71.53-61.13) / 61.13 = 17.0\%$

1” = 25.4 mm

1 kip = 4.45 kN

1 psi = 6.89 kPa

Note:

The compressive strength of the concrete was taken as 3500 psi.

The strength of the steel was taken as 50,000 psi.

The second moment of area of the equivalent section (I_x) was calculated from a moment-curvature analysis with the tension strain in the bottom flange as the governing criteria. Top flange is assumed to be restrained against buckling and Whitney’s stress block is assumed for the concrete stress distribution.

B.2 AASHTO Shear Stud Ratio Calculation

Section Properties (W14x30^c)

Area	A_s	: 8.85	in ²
Depth	d	: 13.8	in
Web thickness	t_w	: 0.27	in
Flange width	b_f	: 6.73	in
Flange thickness	t_f	: 0.385	in
Nominal Weight	w_s	: 30	lb/ft
Moment of Inertia	I_{xx}	: 291	in ⁴
Elastic section modulus	S_{xx}	: 42	in ³
Plastic section modulus	Z_{xx}	: 47.3	in ³

Material Properties

Modulus of Steel	E_s	: 29000	ksi	(assumed)
Yield strength	F_y	: 50	ksi	(assumed)
Concrete density	w_c	: 145	pcf	(assumed)
Concrete strength	f'_c	: 3	ksi	(assumed)
Concrete modulus	E_c	: 3150	ksi	$(33w_c^{1.5}\sqrt{f'_c})$

Deck Properties

Span Length	L	: 22	ft
Deck height	h_d	: 8	in
Effective deck width	b_e	: 5	ft

Check for compact section

AASHTO Standard Specifications 10.48.1

(a) Compression Flange

$$\frac{b_f}{t_f} \leq \frac{4110}{\sqrt{F_y}} \Rightarrow 17.48 \leq 18.38 \quad \text{O.K}$$

(b) Web thickness

$$\frac{D}{t_w} \leq \frac{19230}{\sqrt{F_y}} \Rightarrow 48.26 \leq 86.0 \quad \text{O.K}$$

D= 13.03 in. is the clear distance between the flanges

Calculate Forces

AASHTO Standard Specifications 10.38.5.1.2

The compression force in the concrete slab will be the lesser of;

$$\begin{aligned} P_1 &= A_s F_y &= 8.85 \times 50 &= 442.5 \text{ kip} \\ P_2 &= 0.85 f'_c b_e h_d &= 0.85 \times 3 \times (60 \times 8) &= 1224.0 \text{ kip} \end{aligned}$$

The ultimate strength of welded shear studs is given by;

$$S_u = 0.4d^2(f'_c E_c)^{0.5} \leq 60,000 A_{sc}$$

Where; S_u = Ultimate strength of individual shear connector
 A_{sc} = Cross-section area of shear stud connector
 d = diameter of shear stud

$$\begin{aligned} A_{sc} &= \pi \times 0.75^2 / 4 &= 0.44 \text{ in}^2 \\ S_u &= 0.5 \times 0.6 \times (3000 \times 3.15 \times 10^6)^{0.5} &\leq 0.44 \times 60000 \text{ lbs} \\ S_u &= 21.49 \text{ kip} &\leq 26.4 \text{ kip} \end{aligned}$$

Calculate Number of Shear Studs

The number of shear studs is equal or greater than;

$$\begin{aligned} N_l &= P / (\phi S_u) \\ N_l &= \text{Number of connectors between points of maximum positive moment} \\ &\quad \text{and adjacent end supports} \\ \phi &= \text{reduction factor} = 0.85 \\ P &= \text{Lesser of } P_1 \text{ and } P_2 \end{aligned}$$

$$N_l = 442.5 / (0.85 \times 21.49) = 25 \text{ studs per half span}$$

Neglecting reduction factor:

$$N_l = 442.5 / 21.49 = 21 \text{ studs per half span}$$

B.3 Load Posting Analysis for the KY 32 Bridge Over Lytles Creek

This section analyzes the Bridge over Lytles creek on route KY32 in Scott County, KY to evaluate the maximum load carrying capacity under different Truck Types before and after the retrofit using post installed shear studs. The Truck Types are depicted in Figure B4. The axle placement, depending on the axle configuration of each truck, is given in Figure B5. Table B3 and Table B4 provide the AASHTO load rating evaluation assuming simple support conditions at the abutments. Table B5 and Table B6 provide the load rating before and after the retrofit utilizing stresses obtained through a finite element model calibrated using field measurements, but conservatively loaded under simple support conditions.

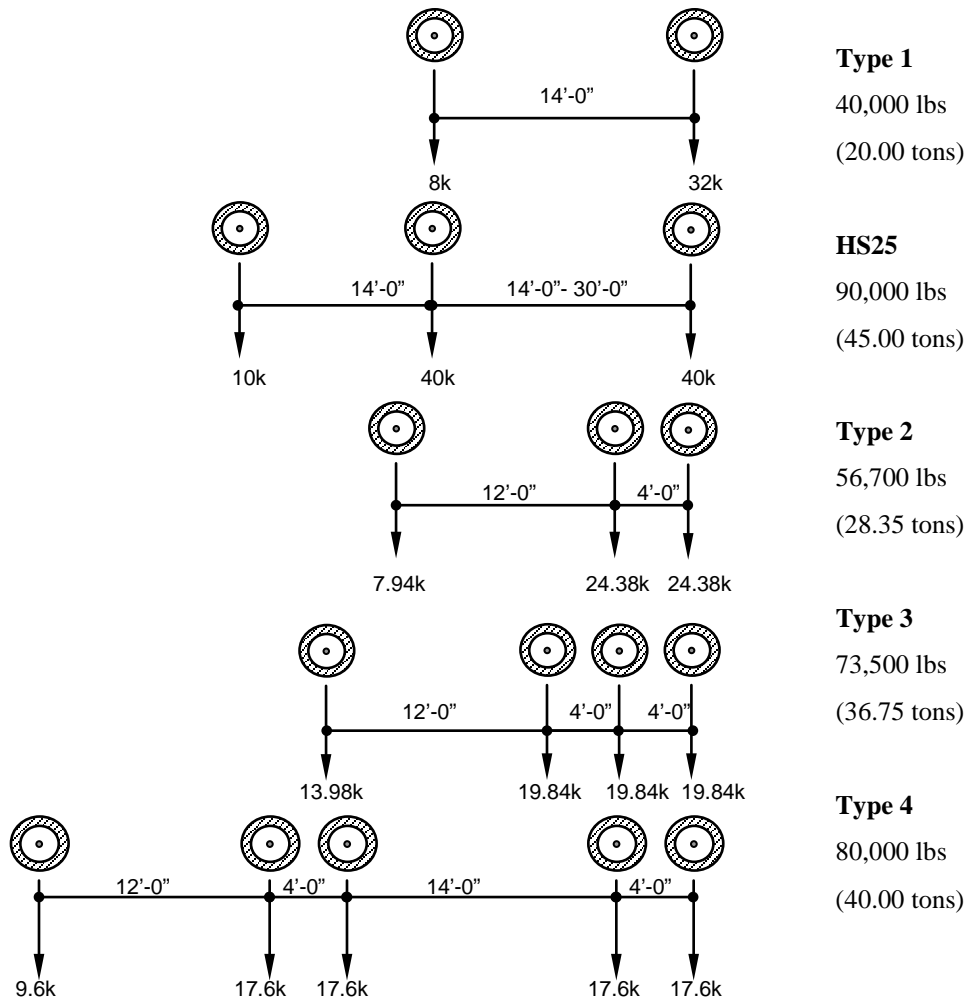
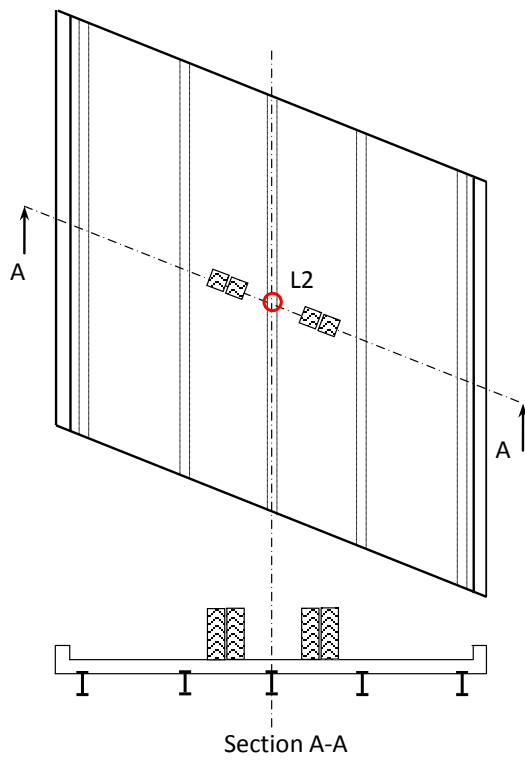
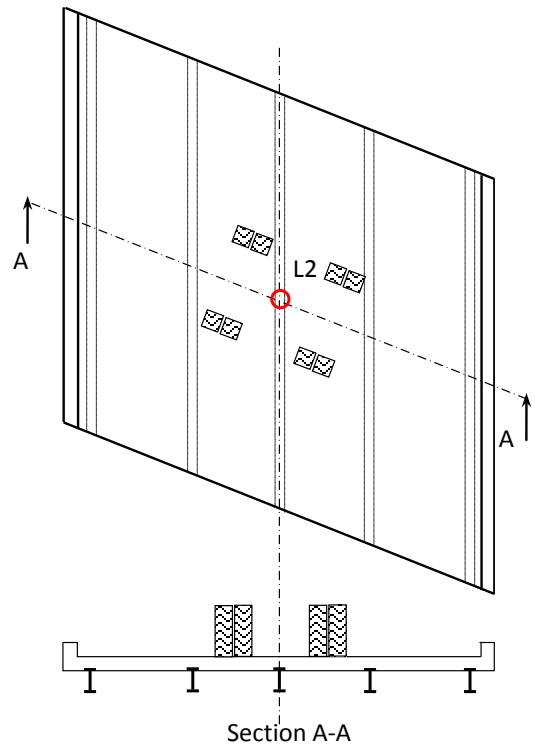


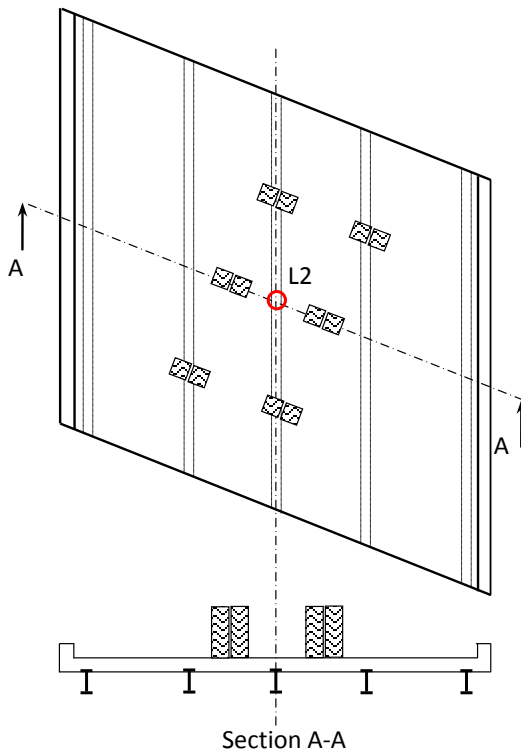
Fig. B4: Truck Types and their corresponding axle weights



**Truck Type 1 and HS25^a
Truck Type 3**



Truck Type 2 and Type 4^b



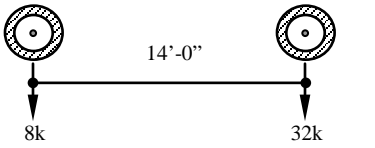
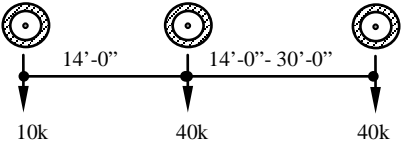
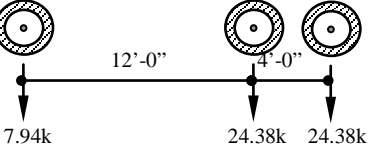
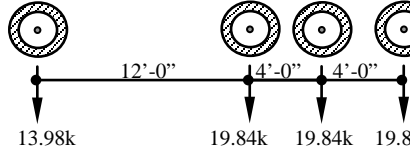
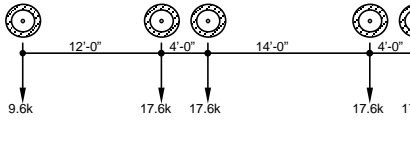
Note: The truck's rear axle placement in this figure is selected to produce the maximum deflection at point L2 and the maximum stress in the steel girder at point L2.

^a The single rear axle location and load for the HS25 truck is the same as the Type 1 truck.

^b The tandem rear axle location for Type 4 truck is similar to the Type 2 truck, but the Type 2 governs due to larger axle load

Fig. B5. Axle location on the KY 32 Bridge in Scott County for different Truck Types

Table B3. Truck Weight Analysis according to AASHTO guidelines (Non-Composite bridge – prior to retrofit)

Truck Type	Rear Axle Weight (kips)	Non-Composite Bridge					
		Dead Load (DL) Moment ^a (kip-ft)	Live Load (LL) Moment ^a (kip-ft)	Impact Load (IL) Moment ^b (kip-ft)	Total Applied Moment ^{c,d} (LL+IL) (kip-ft)	“Inventory Level” Truck Weight ^e (Tons)	“Operational Level” Truck Weight ^e (Tons)
	32	31.06	88.00	26.40	114.4	11.4	19.0
	40	31.06	110.00	33.0	143.0	20.7	34.2
	24.38	31.06	109.71	32.91	142.6	13.0	21.5
	19.84	31.06	123.75	37.12	160.9	15.1	25.0
	17.6	31.06	79.20	23.76	103.0	25.2	42.0

^a The moments determined at the center of a beam, assuming simple support conditions.

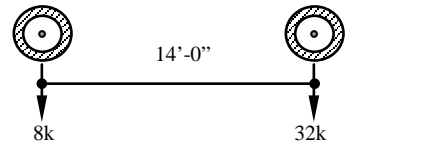
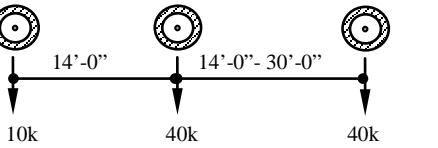
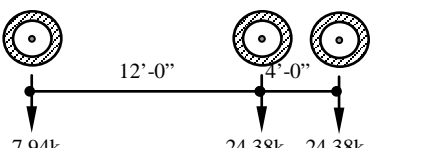
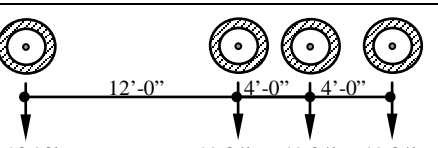
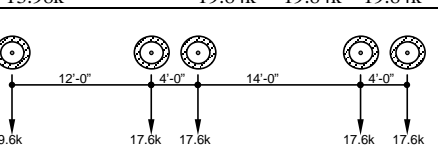
^b The Impact load is taken as 30% of Live load

^c Half the axle load/s are conservatively applied to a single girder without considering load distribution

^d The nominal moment capacity of the steel section is 197.1 kip-ft

^e The AASHTO load rating for the bridge

Table B4. Truck Weight Analysis according to AASHTO guidelines (Composite bridge-following retrofit)

Truck Type	Rear Axle Weight (kips)	Composite Bridge					
		Dead Load (DL) Moment ^a (kip-ft)	Live Load (LL) Moment ^a (kip-ft)	Impact Load (IL) Moment ^b (kip-ft)	Total Applied Moment ^{c,d} (LL+IL) (kip-ft)	“Inventory Level” Truck Weight ^e (Tons)	“Operational Level” Truck Weight ^e (Tons)
	32	31.06	88.00	26.40	114.4	26.8	44.6
	40	31.06	110.00	33.0	143.0	48.1	80.5
	24.38	31.06	109.71	32.91	142.6	30.3	50.5
	19.8	31.06	123.75	37.12	160.9	34.9	58.1
	17.6	31.06	79.20	23.76	103.0	59.6	99.2

^a The moments determined at the center of a beam, assuming simple support conditions.

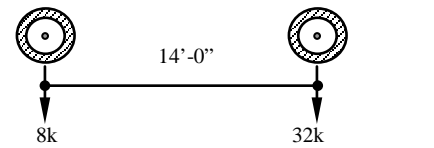
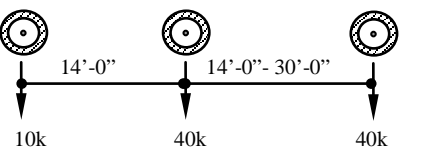
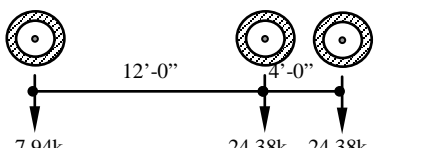
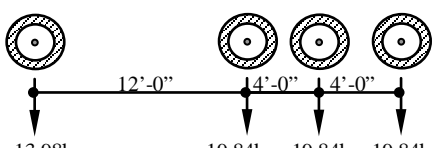
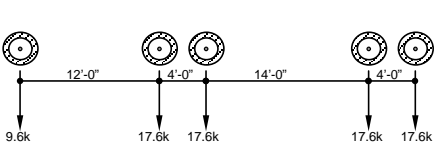
^b The Impact load is taken as 30% of Live load

^c Half the axle load/s are conservatively applied to a single girder without considering load distribution

^d The nominal moment capacity of the composite section is 480.7 kip-ft

^e The AASHTO load rating for the bridge

Table B5. Truck Weight Analysis using data from calibrated finite element model (Non-Composite bridge – prior to retrofit)

Truck Type	Rear Axle Weight (kips)	Non-Composite Bridge					
		Live Load (LL) Deflection ^a (kip-ft)	Live Load (LL) Stress ^b (psi)	Impact Load (IL) Stress ^{b,c} (psi)	Dead Load (DL) Stress ^b (psi)	“Inventory Level” Truck Weight ^d (Tons)	“Operational Level” Truck Weight ^d (Tons)
	32	0.089	4400	1320	2800	36.2	60.4
	40	0.111	5500	1650	2800	65.2	108.9
	24.38	0.131	6300	1890	2800	35.7	59.8
	19.84	0.149	6900	2070	2800	42.3	70.9
	17.6	0.095	4600	1380	2800	69.2	115.6

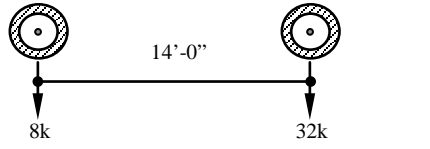
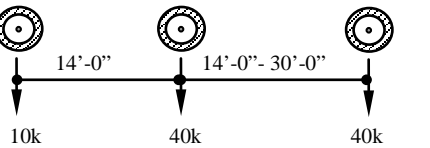
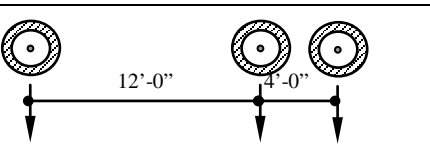
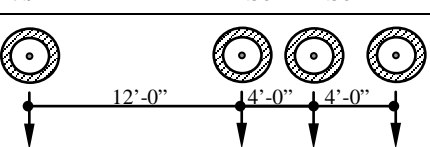
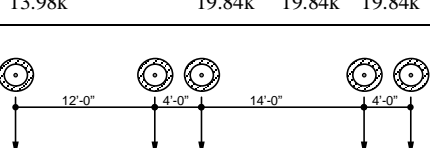
^a The deflections are determined at the center of the bridge at location L2 in Fig. B5.

^b The stresses are determined at the bottom flange in the girder at location L2 in Fig. B5

^c The Impact load is taken as 30% of Live load

^d The AASHTO Inventory level load rating for the bridge

Table B6. Truck Weight Analysis using data from calibrated finite element model (Composite bridge-following retrofit)

Truck Type	Rear Axle Weight (kips)	Composite Bridge					
		Live Load (LL) Deflection ^a (kip-ft)	Live Load (LL) Stress ^b (psi)	Impact Load (IL) Stress ^{b,c} (psi)	Dead Load (DL) Stress ^b (psi)	“Inventory Level” Truck Weight ^d (Tons)	“Operational Level” Truck Weight ^d (Tons)
	32	0.067	4600	1380	2800	74.6	124.4
	40	0.084	5800	1725	2800	133.2	221.8
	24.38	0.099	6500	1950	2800	74.8	124.7
	19.8	0.112	7100	2130	2800	88.9	148.1
	17.6	0.071	4700	1410	2800	146.0	243.6

^a The deflections are determined at the center of the bridge at location L2 in Fig. B5.

^b The stresses are determined at the bottom flange in the girder at location L2 in Fig. B5

^c The Impact load is taken as 30% of Live load

^d The AASHTO Inventory level load rating for the bridge

B.3.1 Non-Composite Bridge (prior to retrofit)

Section Properties (W14x30^c)

Area	A_s	: 8.85	in ²
Depth	d	: 13.8	in
Web thickness	t_w	: 0.27	in
Flange width	b_f	: 6.73	in
Flange thickness	t_f	: 0.385	in
Nominal Weight	w_s	: 30	lb/ft
Moment of Inertia	I_{xx}	: 291	in ⁴
Elastic section modulus	S_{xx}	: 42	in ³
Plastic section modulus	Z_{xx}	: 47.3	in ³

Material Properties

Modulus of Steel	E_s	: 29000	ksi	(assumed)
Yield strength	F_y	: 50	ksi	(assumed)
Concrete density	w_c	: 145	pcf	(assumed)
Concrete strength	f'_c	: 5	ksi	(rebound hammer tests)
Concrete modulus	E_c	: 4075	ksi	$(33w_c^{1.5}\sqrt{f'_c})$

Deck Properties

Span Length	L	: 22	ft
Deck height	h_d	: 8	in
Effective deck width	b_e	: 5	ft

Check for compact section

AASHTO Standard Specifications 10.48.1

(c) Compression Flange

$$\frac{b_f}{t_f} \leq \frac{4110}{\sqrt{F_y}} \Rightarrow 17.48 \leq 18.38 \quad \text{O.K}$$

(d) Web thickness

$$\frac{D}{t_w} \leq \frac{19230}{\sqrt{F_y}} \Rightarrow 48.26 \leq 86.0 \quad \text{O.K}$$

D= 13.03 in. is the clear distance between the flanges

$$\begin{aligned} \text{Nominal Flexural Strength } M_n &= F_y Z_{xx} \\ &= 50 \times 47.3 = \underline{\underline{197.1 \text{ kip-ft}}} \end{aligned}$$

Loads

$$\text{Deck weight} = 145 \times \left(\frac{8}{12} \right) \times 5 = 483.3 \text{ lb/ft}$$

$$\text{Steel Beam Weight} = 30 \text{ lb/ft}$$

Neglecting curb and railing weight;

$$\text{Total weight } w_T = 483.3 + 30 = 513.3 \text{ lb/ft}$$

$$\begin{aligned} \text{Dead load moment } M_{DL} &= \frac{w_T L^2}{8} = \frac{513.3 \times 22^2}{8} \\ &= 31.06 \text{ kip-ft} \end{aligned}$$

$$\text{Impact factor } I = \frac{50}{L+125} \leq 0.3$$

$$I = 0.3$$

Live and Impact load moments

- Truck Type 1

$$\text{Load per beam } P = 16 \text{ kips} \quad (\frac{1}{2} \text{ the rear axle weight})$$

$$\begin{aligned} \text{Live load } M_L &= \frac{PL}{4} = \frac{16 \times 22}{4} \\ &= 88 \text{ kip-ft} \end{aligned}$$

$$M_{L+I} = 1.3 \times 88 = 114.4 \text{ kip-ft} \quad (\text{no distribution factor})$$

- Truck Type HS25

$$\text{Load per beam } P = 20 \text{ kips} \quad (\frac{1}{2} \text{ the rear axle weight})$$

$$\begin{aligned} \text{Live load } M_L &= \frac{PL}{4} = \frac{20 \times 22}{4} \\ &= 110 \text{ kip-ft} \end{aligned}$$

$$M_{L+I} = 1.3 \times 110 = 143.0 \text{ kip-ft} \quad (\text{no distribution factor})$$

- Truck Type 2

Load per beam $P = 12.19$ kips/axle ($\frac{1}{2}$ the rear axle weight)

Distance from each axle to support $b = 9$ ft

Distance from mid-span to support $x = 11$ ft (location of maximum moment)

$$\text{Live load } M_L = 2 \frac{Pbx}{L} = 2 \times \frac{12.19 \times 9 \times 11}{22}$$

$$= 109.71 \text{ kip-ft}$$

$$M_{L+I} = 1.3 \times 109.71 = 142.6 \text{ kip-ft (no distribution factor)}$$

- Truck Type 3

Load per beam $P = 9.9$ kips/axle ($\frac{1}{2}$ the rear axle weight)

Distance from outer axles to support $b = 7$ ft

Distance from mid-span to support $x = 11$ ft (location of maximum moment)

$$\text{Live load } M_L = 2 \frac{Pbx}{L} + \frac{PL}{4} = 2 \times \frac{9.9 \times 7 \times 11}{22} + \frac{9.9 \times 22}{4}$$

$$= 123.75 \text{ kip-ft}$$

$$M_{L+I} = 1.3 \times 123.75 = 160.9 \text{ kip-ft (no distribution factor)}$$

- Truck Type 4

Load per beam $P = 8.8$ kips/axle ($\frac{1}{2}$ the rear axle weight)

Distance from each axle to support $b = 9$ ft

Distance from mid-span to support $x = 11$ ft (location of maximum moment)

$$\text{Live load } M_L = 2 \frac{Pbx}{L} = 2 \times \frac{8.8 \times 9 \times 11}{22}$$

$$= 79.2 \text{ kip-ft}$$

$$M_{L+I} = 1.3 \times 79.2 = 103.0 \text{ kip-ft (no distribution factor)}$$

AASHTO Load Rating for Non-composite bridge

AASHTO Manual for condition evaluation of bridges 6.5.1

$$RF = \frac{C - A_1 D}{A_2 L (1 + I)}$$

where; RF = Rating Factor for the live-load carrying capacity. The rating factor multiplied by the rating vehicle in tons gives the rating of the structure.

C = Capacity of member

D = Dead load effect on member

L = Live load effect on member

I = Impact factor to be used with the live load effect

A_1 = Factor for dead loads

A_2 = Factor for live loads

AASHTO Strength Criterion:

$A_1 = 1.3$ for Inventory and Operating levels

$A_2 = 2.17$ for Inventory and 1.3 for Operating levels (AASHTO Manual 6.5.3)

- Truck Type 1

$$\text{Inventory level } RF = \frac{197.1 - (1.3 \times 31.06)}{2.17 \times 88(1 + 0.3)} = 0.63$$

$$\text{Operating level } RF = \frac{197.1 - (1.3 \times 31.06)}{1.3 \times 88(1 + 0.3)} = 1.05$$

- Truck Type HS25

$$\text{Inventory level } RF = \frac{197.1 - (1.3 \times 31.06)}{2.17 \times 110(1 + 0.3)} = 0.50$$

$$\text{Operating level } RF = \frac{197.1 - (1.3 \times 31.06)}{1.3 \times 110(1 + 0.3)} = 0.84$$

- Truck Type 2

$$\text{Inventory level } RF = \frac{197.1 - (1.3 \times 31.06)}{2.17 \times 109.71(1 + 0.3)} = 0.51$$

$$\text{Operating level } RF = \frac{197.1 - (1.3 \times 31.06)}{1.3 \times 109.71(1 + 0.3)} = 0.85$$

- Truck Type 3

$$\text{Inventory level } RF = \frac{197.1 - (1.3 \times 31.06)}{2.17 \times 123.75(1 + 0.3)} = 0.45$$

$$\text{Operating level } RF = \frac{197.1 - (1.3 \times 31.06)}{1.3 \times 123.75(1 + 0.3)} = 0.75$$

- Truck Type 4

$$\text{Inventory level } RF = \frac{197.1 - (1.3 \times 31.06)}{2.17 \times 79.2(1 + 0.3)} = 0.70$$

$$\text{Operating level } RF = \frac{197.1 - (1.3 \times 31.06)}{1.3 \times 79.2(1 + 0.3)} = 1.17$$

AASHTO Serviceability Criterion:

AASHTO Design Specifications 10.57.1 stipulate that the maximum stress under overloaded conditions should be limited to $0.8F_y$ for non-composite sections

For AASHTO H and HS loadings the overload is defined as the un-factored dead load (D) + $5(1+I)/3$ times the live load (L). Where I is the Impact Factor.

- Truck Type 1

$$\text{Inventory level } RF = \frac{0.8 \times 50 \times \left(\frac{42}{12}\right) - 31.06}{5 \times 88(1 + 0.3)/3} = 0.57 \quad \text{Controls}^*$$

$$\text{Operating level } RF = 0.57 \times (5/3) = 0.95 \quad \text{Controls}^*$$

- Truck Type HS25

$$\text{Inventory level } RF = \frac{0.8 \times 50 \times \left(\frac{42}{12}\right) - 31.06}{5 \times 110(1+0.3)/3} = 0.46 \quad \text{Controls}^*$$

$$\text{Operating level } RF = 0.46 \times (5/3) = 0.76 \quad \text{Controls}^*$$

- Truck Type 2

$$\text{Inventory level } RF = \frac{0.8 \times 50 \times \left(\frac{42}{12}\right) - 31.06}{5 \times 109.71(1+0.3)/3} = 0.46 \quad \text{Controls}^*$$

$$\text{Operating level } RF = 0.46 \times (5/3) = 0.76 \quad \text{Controls}^*$$

- Truck Type 3

$$\text{Inventory level } RF = \frac{0.8 \times 50 \times \left(\frac{42}{12}\right) - 31.06}{5 \times 123.75(1+0.3)/3} = 0.41 \quad \text{Controls}^*$$

$$\text{Operating level } RF = 0.41 \times (5/3) = 0.68 \quad \text{Controls}^*$$

- Truck Type 4

$$\text{Inventory level } RF = \frac{0.8 \times 50 \times \left(\frac{42}{12}\right) - 31.06}{5 \times 79.2(1+0.3)/3} = 0.63 \quad \text{Controls}^*$$

$$\text{Operating level } RF = 0.63 \times (5/3) = 1.05 \quad \text{Controls}^*$$

* Note: The Non-Composite bridge AASHTO Load Rating is governed by the Serviceability Criterion

AASHTO Load Rating;

The rating of the bridge (RT) is given by;

$$RT = (RF) W \quad \text{(AASHTO Manual)}$$

Where; RT = bridge member rating in tons

W = weight (tons) of nominal truck used in determining the live load effect

- Truck Type 1

Inventory level bridge rating $RT = 0.57 \times 20.00 = 11.40$ tons

Operating level bridge rating $RT = 0.95 \times 20.00 = 19.00$ tons

- Truck Type HS25

Inventory level bridge rating $RT = 0.46 \times 45.00 = 20.70$ tons

Operating level bridge rating $RT = 0.76 \times 45.00 = 34.20$ tons

- Truck Type 2

Inventory level bridge rating $RT = 0.46 \times 28.35 = 13.04$ tons

Operating level bridge rating $RT = 0.76 \times 28.35 = 21.55$ tons

- Truck Type 3

Inventory level bridge rating $RT = 0.41 \times 36.75 = 15.07$ tons

Operating level bridge rating $RT = 0.68 \times 36.75 = 24.99$ tons

- Truck Type 4

Inventory level bridge rating $RT = 0.63 \times 40.00 = 25.20$ tons

Operating level bridge rating $RT = 1.05 \times 40.00 = 42.00$ tons

B.3.2 Load Rating from FEA (finite element analysis)

FEA Strength Criterion:

$A_1 = 1.3$ for Inventory and Operating levels

$A_2 = 2.17$ for Inventory and 1.3 for Operating levels (AASHTO Manual 6.5.3)

Note: The stresses were calculated using the calibrated finite element model at mid-span location L2 in Fig. B4.

Since the degree of composite action due to friction between the steel top flange and concrete deck is difficult to measure, the section modulus of the fully composite girder ($S_{tr} = 90.55 \text{ in}^3$) is used to obtain conservative Dead and Live load moments.

- Truck Type 1

$$\text{Inventory level } RF = \frac{197.1 - \left(1.3 \times 2.8 \times \frac{90.55}{12}\right)}{2.17 \times 4.4 \times \frac{90.55}{12} \times (1 + 0.3)} = 1.81 \quad \text{Controls}^*$$

$$\text{Operating level } RF = \frac{197.1 - \left(1.3 \times 2.8 \times \frac{90.55}{12}\right)}{1.3 \times 4.4 \times \frac{90.55}{12} \times (1 + 0.3)} = 3.02 \quad \text{Controls}^*$$

- Truck Type HS25

$$\text{Inventory level } RF = \frac{197.1 - \left(1.3 \times 2.8 \times \frac{90.55}{12}\right)}{2.17 \times 5.5 \times \frac{90.55}{12} \times (1 + 0.3)} = 1.45 \quad \text{Controls}^*$$

$$\text{Operating level } RF = \frac{197.1 - \left(1.3 \times 2.8 \times \frac{90.55}{12}\right)}{1.3 \times 5.5 \times \frac{90.55}{12} \times (1 + 0.3)} = 2.42 \quad \text{Controls}^*$$

- Truck Type 2

$$\text{Inventory level } RF = \frac{197.1 - \left(1.3 \times 2.8 \times \frac{90.55}{12}\right)}{2.17 \times 6.3 \times \frac{90.55}{12} \times (1 + 0.3)} = 1.26 \quad \text{Controls}^*$$

$$\text{Operating level } RF = \frac{197.1 - \left(1.3 \times 2.8 \times \frac{90.55}{12}\right)}{1.3 \times 6.3 \times \frac{90.55}{12} \times (1 + 0.3)} = 2.11 \quad \text{Controls}^*$$

- Truck Type 3

$$\text{Inventory level } RF = \frac{197.1 - \left(1.3 \times 2.8 \times \frac{90.55}{12}\right)}{2.17 \times 6.9 \times \frac{90.55}{12} \times (1 + 0.3)} = 1.15 \quad \text{Controls}^*$$

$$\text{Operating level } RF = \frac{197.1 - \left(1.3 \times 2.8 \times \frac{90.55}{12}\right)}{1.3 \times 6.9 \times \frac{90.55}{12} \times (1 + 0.3)} = 1.93 \quad \text{Controls}^*$$

- Truck Type 4

$$\text{Inventory level } RF = \frac{197.1 - \left(1.3 \times 2.8 \times \frac{90.55}{12}\right)}{2.17 \times 4.6 \times \frac{90.55}{12} \times (1 + 0.3)} = 1.73 \quad \text{Controls}^*$$

$$\text{Operating level } RF = \frac{197.1 - \left(1.3 \times 2.8 \times \frac{90.55}{12}\right)}{1.3 \times 4.6 \times \frac{90.55}{12} \times (1 + 0.3)} = 2.89 \quad \text{Controls}^*$$

* Note: The Non-Composite bridge FEA Load Rating is governed by the Strength Criterion

FEA Serviceability Criterion:

ASSHTO Design Specifications 10.57.1 stipulate that the maximum stress under overloaded conditions should be limited to $0.8F_y$ for non-composite sections.

For AASHTO H and HS loadings the overload is defined as the un-factored dead load (D) + $5(1+I)/3$ times the live load (L). Where I is the Impact Factor.

- Truck Type 1

$$\text{Inventory level } RF = \frac{0.8 \times 50 - 2.8}{5 \times 4.4 \times (1 + 0.3) / 3} = 3.90$$

$$\text{Operating level } RF = 3.90 \times (5/3) = 6.50$$

- Truck Type HS25

$$\text{Inventory level } RF = \frac{0.8 \times 50 - 2.8}{5 \times 5.5 \times (1 + 0.3) / 3} = 3.12$$

$$\text{Operating level } RF = 3.12 \times (5/3) = 5.20$$

- Truck Type 2

$$\text{Inventory level } RF = \frac{0.8 \times 50 - 2.8}{5 \times 6.3 \times (1 + 0.3) / 3} = 2.73$$

$$\text{Operating level } RF = 2.73 \times (5/3) = 4.54$$

- Truck Type 3

$$\text{Inventory level } RF = \frac{0.8 \times 50 - 2.8}{5 \times 6.9 \times (1 + 0.3) / 3} = 2.48$$

$$\text{Operating level } RF = 2.48 \times (5/3) = 4.14$$

- Truck Type 4

$$\text{Inventory level } RF = \frac{0.8 \times 50 - 2.8}{5 \times 4.6 \times (1 + 0.3) / 3} = 3.73$$

$$\text{Operating level } RF = 3.73 \times (5/3) = 6.22$$

FEA Load Rating (RT):

- Truck Type 1

Inventory level bridge rating $RT = 1.81 \times 20.00 = 36.2$ tons

Operating level bridge rating $RT = 3.02 \times 20.00 = 60.4$ tons

- Truck Type HS25

Inventory level bridge rating $RT = 1.45 \times 45.00 = 65.2$ tons

Operating level bridge rating $RT = 2.42 \times 45.00 = 108.9$ tons

- Truck Type 2

Inventory level bridge rating $RT = 1.26 \times 28.35 = 35.7$ tons

Operating level bridge rating $RT = 2.11 \times 28.35 = 59.8$ tons

- Truck Type 3

Inventory level bridge rating $RT = 1.15 \times 36.75 = 42.3$ tons

Operating level bridge rating $RT = 1.93 \times 36.75 = 70.9$ tons

- Truck Type 4

Inventory level bridge rating $RT = 1.73 \times 40.00 = 69.2$ tons

Operating level bridge rating $RT = 2.89 \times 40.00 = 115.6$ tons

B.3.3 Composite Bridge (following retrofit)

Composite Properties

The compression force C in the concrete slab will be the lesser of;

$$C_s = A_s F_y$$

$$C_c = 0.85 f'_c A_c$$

$$C_q = \sum Q_n$$

Where;

A_c = Area of concrete slab within effective width

$\sum Q_n$ = Sum of nominal strength of shear connectors between maximum positive moment and zero moment points

The depth of the concrete compression block a is obtained from;

$$a = C / 0.85 f'_c b_e$$

The nominal plastic moment capacity M_n is then obtained from;

$$M_n = C (d_1 + d_2) + P_y (d_3 - d_2)$$

P_y = Tensile strength of steel section $A_s F_y$

d_1 = Distance from centroid of compression force C to top of steel section

d_2 = Distance from centroid of compression force in steel to top of steel section, for no compression in steel $d_2 = 0$

d_3 = Distance from centroid of steel section to the top of Non-Composite steel section

The plastic stress distribution for positive bending for a composite section is shown below.

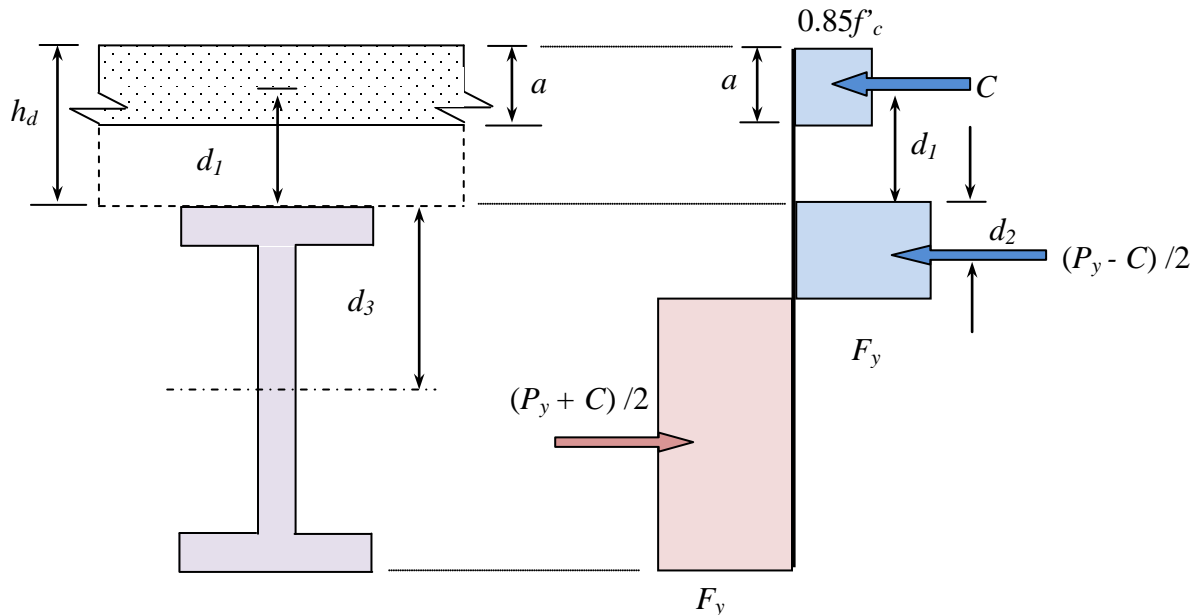


Fig. B.6: Plastic stress distribution for positive bending in composite section

The nominal strength of a shear connector Q_n according to AISC LRFD specifications is given by;

$$Q_n = 0.5A_{sc}(f'_c E_c)^{0.5} \leq A_{sc} F_u$$

$$A_{sc} = \text{Cross sectional area of shear stud}$$

$$E_c = \text{Modulus of elasticity of concrete (taken as } 33w_c^{1.5} \sqrt{f'_c} \text{)}$$

ASTM B7 threaded rods of 0.875 in. diameter were used in the KY32 bridge ($F_u = 125$ ksi). A total of 14 studs were used in each half span (conservatively neglecting the two studs at mid-span).

$$A_{sc} = \pi \times 0.875^2 / 4 = 0.6 \text{ in}^2$$

$$Q_n = 0.5 \times 0.6 \times (5000 \times 4.075 \times 10^6)^{0.5} \leq 0.6 \times 125000$$

$$= 42.82 \text{ ksi} \leq 75 \text{ ksi}$$

$$C_s = A_s F_y = 8.85 \times 50 = 442.5 \text{ kip}$$

$$C_c = 0.85 f'_c A_c = 0.85 \times 5 \times (60 \times 8) = 2040.0 \text{ kip}$$

$$C_q = \sum Q_n = 14 \times 42.82 = 599.5 \text{ kip}$$

Therefore $C = 442.5 \text{ kip}$

$$a = C / 0.85 f'_c b_e$$

$$= 442.5 / (0.85 \times 5 \times 60) = 1.74 \text{ in}$$

$$P_y = 442.5 \text{ kip}$$

$$d_1 = h_d - a/2 = 7.13 \text{ in}$$

Assume $d_2 < \text{flange thickness } t_f$

$$d_2 = [(P_y - C)/2] / 2b_f F_y = 0.0 \text{ in} \quad (< t_f = 0.385 \text{ in O.K.})$$

$$d_3 = d/2 = 6.9 \text{ in}$$

$$\begin{aligned}
 M_n &= 599.5 (7.13 + 0.0) + 442.5 (6.9 - 0.0) \\
 &= 7327 \text{ kip-in} \\
 M_n &= \underline{610.6 \text{ kip-ft}}
 \end{aligned}$$

AASHTO Load Rating

AASHTO Strength Criterion:

$A_1 = 1.3$ for Inventory and Operating levels

$A_2 = 2.17$ for Inventory and 1.3 for Operating levels (AASHTO Manual 6.5.3)

- Truck Type 1

$$\text{Inventory level } RF = \frac{610.6 - (1.3 \times 31.06)}{2.17 \times 88(1 + 0.3)} = 2.30$$

$$\text{Operating level } RF = \frac{610.6 - (1.3 \times 31.06)}{1.3 \times 88(1 + 0.3)} = 3.83$$

- Truck Type HS25

$$\text{Inventory level } RF = \frac{610.6 - (1.3 \times 31.06)}{2.17 \times 110(1 + 0.3)} = 1.84$$

$$\text{Operating level } RF = \frac{610.6 - (1.3 \times 31.06)}{1.3 \times 110(1 + 0.3)} = 3.07$$

- Truck Type 2

$$\text{Inventory level } RF = \frac{610.6 - (1.3 \times 31.06)}{2.17 \times 109.71(1 + 0.3)} = 1.84$$

$$\text{Operating level } RF = \frac{610.6 - (1.3 \times 31.06)}{1.3 \times 109.71(1 + 0.3)} = 3.08$$

- Truck Type 3

$$\text{Inventory level } RF = \frac{610.6 - (1.3 \times 31.06)}{2.17 \times 123.75(1 + 0.3)} = 1.63$$

$$\text{Operating level } RF = \frac{610.6 - (1.3 \times 31.06)}{1.3 \times 123.75(1 + 0.3)} = 2.74$$

- Truck Type 4

$$\text{Inventory level } RF = \frac{610.6 - (1.3 \times 31.06)}{2.17 \times 79.2(1 + 0.3)} = 2.55$$

$$\text{Operating level } RF = \frac{610.6 - (1.3 \times 31.06)}{1.3 \times 79.2(1 + 0.3)} = 4.26$$

AASHTO Serviceability Criterion:

AASHTO Design Specifications 10.57.1 stipulate that the maximum stress under overloaded conditions should be limited to $0.95F_y$ for composite sections and $0.8F_y$ for non-composite sections.

Conservatively since the beam is only partially composite the steel stress is limited to $f_s \leq 0.8F_y$;

For AASHTO H and HS loadings the overload is defined as the un-factored dead load (D) + $5(1+I)/3$ times the live load (L). Where I is the Impact Factor.

The effective section modulus (S_{eff}) is calculated according to commentary in the *AISC specifications*.

$$S_{eff} = S_s + \sqrt{(\sum Q_n / C_f)} (S_{tr} - S_s)$$

- where;
- S_{eff} = Effective section modulus
 - S_s = Section modulus for the structural steel section
 - S_{tr} = Section modulus for the fully composite uncracked transformed section
 - C_f = Compression force in concrete slab for fully composite beam; smaller of $A_s F_y$ and $0.85 f'_c A_c$
 - $\sum Q_n$ = Strength of shear connectors between point of maximum positive moment and point of zero moment

For an interior girder on the bridge;

$$S_s = S_{xx} = 42.00 \text{ in}^3$$

$$S_{tr} = 90.55 \text{ in}^3$$

$$C_f = 442.5 \text{ kip}$$

$$\sum Q_n = 599.5 \text{ kip}$$

$$S_{eff} = 42 + \sqrt{\left(\frac{599.5}{442.5}\right)}(90.55 - 42) = 98.51 \text{ in}^3$$

- Truck Type 1

$$\text{Inventory level } RF = \frac{0.8 \times 50 - \left(\frac{31.06 \times 12}{42}\right)}{(5/3) \times \left(\frac{114.4 \times 12}{98.51}\right)} = 1.34 \quad \text{Controls}^*$$

$$\text{Operating level } RF = 1.34 \times (5/3) = 2.23 \quad \text{Controls}^*$$

- Truck Type HS25

$$\text{Inventory level } RF = \frac{0.8 \times 50 - \left(\frac{31.06 \times 12}{42}\right)}{(5/3) \times \left(\frac{143.0 \times 12}{98.51}\right)} = 1.07 \quad \text{Controls}^*$$

$$\text{Operating level } RF = 1.07 \times (5/3) = 1.79 \quad \text{Controls}^*$$

- Truck Type 2

$$\text{Inventory level } RF = \frac{0.8 \times 50 - \left(\frac{31.06 \times 12}{42}\right)}{(5/3) \times \left(\frac{142.6 \times 12}{98.51}\right)} = 1.07 \quad \text{Controls}^*$$

$$\text{Operating level } RF = 1.07 \times (5/3) = 1.78 \quad \text{Controls}^*$$

- Truck Type 3

$$\text{Inventory level } RF = \frac{0.8 \times 50 - \left(\frac{31.06 \times 12}{42} \right)}{(5/3) \times \left(\frac{160.88 \times 12}{98.51} \right)} = 0.95 \quad \text{Controls}^*$$

$$\text{Operating level } RF = 0.95 \times (5/3) = 1.58 \quad \text{Controls}^*$$

- Truck Type 4

$$\text{Inventory level } RF = \frac{0.8 \times 50 - \left(\frac{31.06 \times 12}{42} \right)}{(5/3) \times \left(\frac{103.0 \times 12}{98.51} \right)} = 1.49 \quad \text{Controls}^*$$

$$\text{Operating level } RF = 1.49 \times (5/3) = 2.48 \quad \text{Controls}^*$$

* Note: The Composite bridge AASHTO Load Rating is governed by the Serviceability Criterion

AASHTO Load Rating (RT):

- Truck Type 1

$$\text{Inventory level bridge rating } RT = 1.34 \times 20.00 = 26.80$$

$$\text{Operating level bridge rating } RT = 2.23 \times 20.00 = 44.60$$

- Truck Type HS25

$$\text{Inventory level bridge rating } RT = 1.07 \times 45.00 = 48.15$$

$$\text{Operating level bridge rating } RT = 1.79 \times 45.00 = 80.55$$

- Truck Type 2

Inventory level bridge rating $RT = 1.07 \times 28.35 = 30.33$

Operating level bridge rating $RT = 1.78 \times 28.35 = 50.46$

- Truck Type 3

Inventory level bridge rating $RT = 0.95 \times 36.75 = 34.91$

Operating level bridge rating $RT = 1.58 \times 36.75 = 58.06$

- Truck Type 4

Inventory level bridge rating $RT = 1.49 \times 40.00 = 59.60$

Operating level bridge rating $RT = 2.48 \times 40.00 = 99.20$

B.3.4 Load Rating from FEA (finite element analysis)

FEA Strength Criterion:

$A_1 = 1.3$ for Inventory and Operating levels

$A_2 = 2.17$ for Inventory and 1.3 for Operating levels (AASHTO Manual 6.5.3)

Note: The stresses were calculated using the calibrated finite element model at mid-span location L2 in Fig. B4.

- Truck Type 1

$$\text{Inventory level } RF = \frac{610.6 - \left(1.3 \times 2.8 \times \frac{90.55}{12}\right)}{2.17 \times 4.6 \times \frac{90.55}{12} \times (1 + 0.3)} = 5.96$$

$$\text{Operating level } RF = \frac{610.6 - \left(1.3 \times 2.8 \times \frac{90.55}{12}\right)}{1.3 \times 4.6 \times \frac{90.55}{12} \times (1 + 0.3)} = 9.94$$

- Truck Type HS25

$$\text{Inventory level } RF = \frac{610.6 - \left(1.3 \times 2.8 \times \frac{90.55}{12}\right)}{2.17 \times 5.8 \times \frac{90.55}{12} \times (1 + 0.3)} = 4.72$$

$$\text{Operating level } RF = \frac{610.6 - \left(1.3 \times 2.8 \times \frac{90.55}{12}\right)}{1.3 \times 5.8 \times \frac{90.55}{12} \times (1 + 0.3)} = 7.88$$

- Truck Type 2

$$\text{Inventory level } RF = \frac{610.6 - \left(1.3 \times 2.8 \times \frac{90.55}{12}\right)}{2.17 \times 6.5 \times \frac{90.55}{12} \times (1 + 0.3)} = 4.21$$

$$\text{Operating level } RF = \frac{610.6 - \left(1.3 \times 2.8 \times \frac{90.55}{12}\right)}{1.3 \times 6.5 \times \frac{90.55}{12} \times (1 + 0.3)} = 7.03$$

- Truck Type 3

$$\text{Inventory level } RF = \frac{610.6 - \left(1.3 \times 2.8 \times \frac{90.55}{12}\right)}{2.17 \times 7.1 \times \frac{90.55}{12} \times (1 + 0.3)} = 3.86$$

$$\text{Operating level } RF = \frac{610.6 - \left(1.3 \times 2.8 \times \frac{90.55}{12}\right)}{1.3 \times 7.1 \times \frac{90.55}{12} \times (1 + 0.3)} = 6.44$$

- Truck Type 4

$$\text{Inventory level } RF = \frac{610.6 - \left(1.3 \times 2.8 \times \frac{90.55}{12}\right)}{2.17 \times 4.7 \times \frac{90.55}{12} \times (1 + 0.3)} = 5.83$$

$$\text{Operating level } RF = \frac{610.6 - \left(1.3 \times 2.8 \times \frac{90.55}{12}\right)}{1.3 \times 4.7 \times \frac{90.55}{12} \times (1 + 0.3)} = 9.73$$

FEA Serviceability Criterion:

ASSHTO Design Specifications 10.57.1 stipulate that the maximum stress under overloaded conditions should be limited to $0.8F_y$ for non-composite sections.

For AASHTO H and HS loadings the overload is defined as the un-factored dead load (D) + $5(1+I)/3$ times the live load (L). Where I is the Impact Factor.

- Truck Type 1

$$\text{Inventory level } RF = \frac{0.8 \times 50 - 2.8}{5 \times 4.6 \times (1 + 0.3) / 3} = 3.73 \quad \text{Controls}$$

$$\text{Operating level } RF = 3.73 \times (5/3) = 6.22 \quad \text{Controls}$$

- Truck Type HS25

$$\text{Inventory level } RF = \frac{0.8 \times 50 - 2.8}{5 \times 5.8 \times (1 + 0.3) / 3} = 2.96 \quad \text{Controls}$$

$$\text{Operating level } RF = 2.96 \times (5/3) = 4.93 \quad \text{Controls}$$

- Truck Type 2

$$\text{Inventory level } RF = \frac{0.8 \times 50 - 2.8}{5 \times 6.5 \times (1 + 0.3) / 3} = 2.64 \quad \text{Controls}$$

$$\text{Operating level } RF = 2.64 \times (5/3) = 4.40 \quad \text{Controls}$$

- Truck Type 3

$$\text{Inventory level } RF = \frac{0.8 \times 50 - 2.8}{5 \times 7.1 \times (1 + 0.3) / 3} = 2.42 \quad \text{Controls}$$

$$\text{Operating level } RF = 2.42 \times (5/3) = 4.03 \quad \text{Controls}$$

- Truck Type 4

$$\text{Inventory level } RF = \frac{0.8 \times 50 - 2.8}{5 \times 4.7 \times (1 + 0.3) / 3} = 3.65 \quad \text{Controls}$$

$$\text{Operating level } RF = 3.65 \times (5/3) = 6.09 \quad \text{Controls}$$

* Note: The Composite bridge FEA Load Rating is governed by the Serviceability Criterion

FEA Load Rating (RT):

- Truck Type 1

Inventory level bridge rating $RT = 3.73 \times 20.00 = 74.6$ tons

Operating level bridge rating $RT = 6.22 \times 20.00 = 124.4$ tons

- Truck Type HS25

Inventory level bridge rating $RT = 2.96 \times 45.00 = 133.2$ tons

Operating level bridge rating $RT = 4.93 \times 45.00 = 221.8$ tons

- Truck Type 2

Inventory level bridge rating $RT = 2.64 \times 28.35 = 74.8$ tons

Operating level bridge rating $RT = 4.40 \times 28.35 = 124.7$ tons

- Truck Type 3

Inventory level bridge rating $RT = 2.42 \times 36.75 = 88.9$ tons

Operating level bridge rating $RT = 4.03 \times 36.75 = 148.1$ tons

- Truck Type 4

Inventory level bridge rating $RT = 3.65 \times 40.00 = 146.0$ tons

Operating level bridge rating $RT = 6.09 \times 40.00 = 243.6$ tons

REFERENCES

- ACI Committee 440. (2002). "Guide to the Design and Construction of Externally Bonded FRP Systems for Strengthening Concrete Structures, ACI 440.2R-02, American Concrete Institute, Farmington Hills, MI.
- Albat, A.M. and Romilly, D.P. (1999). "A direct linear-elastic analysis of double symmetric bonded joints and reinforcements." *Composites Science and Technology*, 59, 1127-1137.
- Al-Emrani, M. and Kliger, R. (2006). "Experimental and Numerical Investigation of the Behaviour and Strength of Composite Steel-CFRP Members." *Advances in Structural Engineering*, 9(6), 819-831.
- Al-Saidy, A.H., Klaiber, F.W. and Wipf, T.J. (2004). "Repair of Steel Composite Beams with Carbon Fibre-Reinforced Polymer Plates." *Journal of Composites for Construction*, 8(2), 163-172.
- Aly, M. and El-Hacha, R. (2007). "Strengthening Steel-Concrete Composite Girders using Prestressed FRP." *Proceedings of the 8th International Symposium on Fibre-Reinforced Polymer Reinforcement for Concrete Structures (FRPRCS-8)*, Patras, Greece, 16-18.
- American Association of State Highway and Transportation Officials. (2002). *AASHTO Standard Specifications for highway Bridges*, 17th Edition, AASHTO, Washington, D.C.
- American Association of State Highway and Transportation Officials. (2003). *AASHTO Manual for Condition Evaluation of Bridges*, AASHTO, Washington, D.C.
- American Institute of Steel Construction. (2005). *Steel Construction Manual*, 13th Edition, AISC, Chicago, Illinois.
- ANSYS. (2009). ANSYS Academic Research, Release 12.0, ANSYS, Inc., Canonsburg, Pennsylvania.
- Benachour, A., Benyoucef, S., Tounsi, A., and Adda bedia, E.A. (2008). "Interfacial stress analysis of steel beams reinforced with bonded prestressed FRP plate," *Engineering Structures*, 30, 3305-3315.

Bocciarelli, M., Colombi, P., Fava, G. and Poggi, C. (2009(a)). "Prediction of debonding strength of tensile steel/CFRP joints using fracture mechanics and stress based criteria." *Engineering Fracture Mechanics*, 76(2), 299-313.

Bocciarelli, M., Colombi, P., Fava, G. and Poggi, C. (2009(b)). "Fatigue performance of tensile steel members strengthened with CFRP plates." *Composite Structures*, 87(4), 334-343.

Budiansky, B. and Fleck, N.A. (1993). "Compressive Failure of Fibre Composites." *J. Mech. Phys. Solids*, 41(1), 183-211.

Cadei, J.M.C. and Stratford, T.J. (2004). "Elastic analysis of adhesion stresses between a beam and a bonded strengthening plate." *Advanced Composites in Construction (ACIC-2004)*, Guildford, 20-22 April, 235-244.

Chacon, A., Chajes, M., Swinehart, M., Richardson, D. and Wenzel, G. (2004). "Application of Advanced Composites to Steel Bridges: A Case Study on the Ashland Bridge (Delaware-USA)." *Proceedings, Advanced Composite Materials in Bridges and Structures*, Calgary.

Colombi, P. and Poggi, C. (2005). "Strengthening of tensile steel members and bolted joints using adhesively bonded CFRP plates." *Construction and Building Materials*, 20, 22-33.

Colombi, P. and Poggi, C. (2006). "An experimental, analytical and numerical study of the static behavior of steel beams reinforced by pultruded CFRP strips." *Composites Part B: Engineering*, 37 (1), 64-73.

Dawood, M.M.R. (2005). "Fundamental behavior of steel-concrete composite beams Strengthened with high modulus carbon fiber Reinforced polymer (CFRP) materials." M.Sc. Thesis, Department of Civil Engineering, North Carolina State University, Raleigh NC.

Dawood, M., Guddati, M. and Rizkalla, S. (2009). "Effective splices for a CFRP strengthening system for steel bridges and structures." *Transportation Research Record: Journal of the Transportation Research Board*, 2131, 125-133.

Dawood, M., Rizkalla, S. and Sumner, E. (2007). "Fatigue and overloading behavior of steel-concrete composite flexural members strengthened with high modulus CFRP materials." *Journal of Composites for Construction*, 11(6), 659-669.

Deng, J., Lee, M. and Moy, S. (2004). "Stress analysis of steel beams reinforced with a bonded CFRP plate." *Composite Structures*, 65(2), 205-215.

Diaz Diaz, A., Hadj-Ahmed, R., Foret, G. and Ehrlacher A. (2009). "Stress analysis in a classical double lap, adhesively bonded joint with layerwise model." *International Journal of Adhesion & Adhesives*, 29, 67-76.

El Damatty, A.A. and Abushagur, M. (2003). "Testing and modeling of shear and peel behavior for bonded steel/FRP connections." *Thin-Walled Structures*, 41(11), 987-1003.

Fam, A., MacDougall, C. and Shaat, A. (2009). "Upgrading Steel-Concrete Composite Girders and Repair of Damaged Steel Beams using Bonded CFRP Laminates." *Thin-Walled Structures*, 47(10), 1122-1135.

Fawzia, S., Zhao, X.L., Al-Mahaidi, R. and Rizkalla, S. (2005). "Bond Characteristics between CFRP and Steel Plates in Double Strap Joints." *Advances in Steel Construction – An International Journal*, 1 (2), 17-28.

Fawzia, S., Al-Mahaidi, R. and Zhao, X.L. (2006). "Experimental and Finite Element Analysis of a Double Strap Joint between Steel Plates and Normal Modulus CFRP." *Composite Structures*, 75, 156-162.

Federal Highway Administration: National Bridge Inventory, United State Department of Transportation, Federal Highway Administration (2007)

fib Task Group 9.3. (2001). "Externally bonded FRP reinforcement for RC structures." fib Bulletin 14, Lausanne: Federation International du Beton.

Goland, M. and Reissner, E. (1944). "The stresses in cemented joints." *J. Appl. Mech.*, 11, A17-A27.

Greco, F., Lonetti, P., and Blasi, P.N. (2007). "An analytical investigation of debonding problems in beams strengthened using composite plates." *Engineering Fracture Mechanics*, 74, 346-372.

Hart-Smith, L.J. (1973(a)). "Adhesive-bonded double-lap joints." NASA CR-112235, National Aeronautics and Space Administration.

Hart-Smith, L.J. (1973(b)). "Adhesive-bonded single-lap joints." NASA CR-112236, National Aeronautics and Space Administration.

Hart-Smith, L.J. (1973(c)). "Adhesive-bonded scarf and stepped-lap joints." NASA CR-112237, National Aeronautics and Space Administration.

Hart-Smith, L.J. (1994). "The key to designing durable adhesive bonded joints." *Composites*, 25 (9), 895-898.

Hognestad, E. (1951). "A Study of Combined Bending and Axial Load in Reinforced Concrete Members." Bulletin Series No.399, University of Illinois Engineering Experiment Station.

Hollaway, L.C. and Cadei, J. (2002). "Progress in the Technique of Upgrading Metallic Structures with Advanced Polymer Composites." *Progress in Structural Engineering and Materials*, 4(2), 131-148.

Hildebrand, M. (1994). "Non-linear analysis and optimization of adhesively bonded single lap joints between fibre-reinforced plastics and metals," *International Journal of Adhesion and Adhesives*, 14, 261-267.

Hollaway, L.C. and Cadei, J. (2002). "Progress in the Technique of Upgrading Metallic Structures with Advanced Polymer Composites." *Progress in Structural Engineering and Materials*, 4(2), 131-148.

Kwon, G., Hungerford, B., Kayir, H., Schaap, B., Ju, Y.K., Klingner, R., Engelhardt, M. (2007). "Strengthening Existing Non-Composite Steel Bridge Girders Using Post-Installed Shear Connectors." FHWA/TX-07/0-4124-1, Center for Transportation Research, University of Texas at Austin.

Kwon, G. (2008). "Strengthening existing steel bridge girders by the use of post-installed shear connectors." Ph.D. dissertation, Department of Civil, Architectural and Environmental Engineering, University of Texas at Austin.

Kwon, G., Engelhardt, M.D., Klingner, R.E. (2009). "Implementation project: Strengthening of a bridge near Hondo, Texas using post-installed shear connectors." FHWA/TX-09/5-4124-01-1, Center for Transportation Research, University of Texas at Austin.

Kwon, G., Engelhardt, M.D., Klingner, R.E. (2010). "Behavior of post-installed shear connectors under static and fatigue loading." *Journal of Constructional Steel Research*, 66, 532-541.

Lenwari, A. and Thepchatri, T. (2002). "Predicting of premature separation of bonded CFRP plates from strengthened steel beams using a fracture criterion." *Structural Engineering and Mechanics*, 14(5), 565-574.

Lenwari, A., Thepchatri, T. and Watanabe, E. (2005). "Flexural Response of Steel Beams Strengthened With Partial-length CFRP Plates." *Journal of Composites for Construction*, 9 (4), 296-303.

Lenwari, A., Thepchatri, T., and Albrecht, P. (2006). "Debonding Strength of Steel Beams Strengthened with CFRP Plates." *Journal of Composites for Construction*, 10(1), 69-78.

Linghoff, D., Al-Emrani, M. and Kliger, R. (2009). "Performance of steel beams strengthened with CFRP laminate – Part1: laboratory tests." *Composites Part B: Engineering*, 41(7), 516-522.

Liu, H.B., Zhao, X.L. and Al-Mahaidi, R. (2005(a)). "The Effect of Fatigue Loading on Bond Strength of CFRP Bonded Steel Plate Joints." In *Proceedings of the International Symposium on Bond Behaviour of FRP in Structures (BBFS 2005)*, edited by Chen, J.F. and Teng, J.G, (Hong Kong:International Institute for FRP in Construction), 459-464.

Liu, H.B., Zhao, X.L., Al-Mahaidi, R. and Rizkalla, S. (2005(b)). "Analytical Bond Models Between Steel and Normal Modulus CFRP." 4th International Conference on Advances in Steel Structures, Shanghai, 13-15 June.

Malek, A.M., Saadatamanesh, H., and Ehsani, M. (1998). "Prediction of failure load of R/C beams strengthened with FRP plate due to stress concentration at the plate end." *ACI Structural journal*, 95(1), 142-152.

Miller, T.C., Chajes, M.J., Mertz, D.R. and Hastings, J.N. (2001). "Strengthening of a Steel Bridge Girder using CFRP Plates." *Journal of Bridge Engineering*, 6(6), 514-522.

Moy S.S.J. and Bloodworth, A.G. (2007). "Strengthening a steel bridge with CFRP composites." *ICE Proceedings - Structures and Buildings*, 160, (2), 81-93.

Moy, S. (2001). *ICE Design and Practice Guides – FRP Composites Life Extension and Strengthening of Metallic Structures*, (London: Thomas Telford Publishing).

National Research Council: Advisory Committee on Technical Recommendations for Construction (CNR). "Guidelines for the Design and Construction of Externally Bonded FRP System for Strengthening Existing Structures." CNR-DT 202/2005, Rome, 2007.

Nozaka, K., Shield, C. K. and Hajjar, J.F. (2005(a)). "Effective bond length of carbon-fiber-reinforced polymer strips bonded to fatigued steel bridge I-girders." *Journal of Bridge Engineering*, 10(2), 195-205.

Nozaka, K., Shield, C.K., and Hajjar, J.F. (2005(b)). "Design of a test specimen to assess the effective bond length of carbon fiber-reinforced polymer strips bonded to fatigued steel bridge girders." *Journal of Composites for Construction*, 9(4), 304-312.

Ollgaard, J.G., Slutter, R.G. and Fisher, J.W. (1971). "Shear Strength of Stud Shear Connectors in Lightweight and Normal-weight Concrete." *AISC Engineering Journal*, 8, 55-64.

Pellegrino, C., Maiorana, E. and Modena, C. (2009). "FRP strengthening of steel and steel-concrete composite structures: An analytical approach." *Materials and Structures/Materiaux et Constructions*, 42 (3), 353-363.

Phares, B. M., Wipf T.J., Klaiber F.W., Abu-Hawash A., Lee Y-S. (2003). "Strengthening of Steel girder bridges using FRP." *Proceedings of the 2003 Mid-Continent Transportation Research Symposium*, Ames, Iowa, August.

Photiou, N.K., Hollaway, L.C. and Chryssanthopoulos, M.C. (2006). "Selection of CFRP systems for structural upgrading." *Journal of Materials in Civil Engineering*, 18 (5), 641-649.

Pickett, A.K. and Hollaway, L. (1985). "The analysis of elastic-plastic adhesive stress in bonded lap joint in FRP structures." *Composite Structures*, 4, 135-160.

Rabinovich, O. And Frostig, Y. (2000). "Closed-form high-order analysis of RC beams strengthened with FRP strips." *Journal of Composites for Construction*, 4 (2), 65-74.

Schnerch, D.A. (2005). "Strengthening of Steel Structures with High Modulus Carbon Fiber Reinforced Polymer (CFRP) Materials." Ph.D. Dissertation, Department of Civil Engineering, North Carolina State University, Raleigh NC.

Schnerch, D., Dawood, M., Rizkalla, S., Sumner, E. and Stanford, K. (2006). "Bond Behavior of CFRP Strengthened Steel Structures." *Advances in Structural Engineering*, 9(6), 805-817.

Schnerch, D., Dawood, M., Rizkalla, S. and Sumner, E. (2007). "Proposed design guidelines for strengthening of steel bridges with FRP materials." *Construction and Building Materials*, 21(5), 1001-1010.

Schnerch, D. and Rizkalla, S. (2008). "Flexural Strengthening of Steel Bridges with High Modulus CFRP Strips." *Journal of Bridge Engineering*, 13(2), 192-201.

Schnerch, D., Stanford, K., Sumner, E. and Rizkalla, S. (2004). "Strengthening steel structures and bridges with high modulus carbon fiber reinforced polymers: Resin selection and scaled monopole behaviour." *Transportation Research Record*, 1892, 237-245.

Shen, H-S., Teng, J.G. and Yang, J. (2001). "Interfacial stresses in beams and slabs bonded with thin plate." *Journal of Engineering Mechanics*, 127 (4), 399-406.

Smith, S.T. and Teng, J.G. (2001). "Interfacial stresses in plated beams," *Engineering Structures*, 23, 857-871.

Stallings, J.M. and Porter, N.M. (2003). Experimental investigation of lap splices in externally bonded carbon fiber-reinforced plastic plates. *ACI Structural Journal*, 100 (1), 3-10.

Stratford, T.J. and Cadei, J.M.C. (2006). "Elastic analysis of adhesion stresses for the design of a strengthening plate bonded to a beam." *Construction and Building Materials*, 20, 34-45.

Taljsten, B. (1997). "Strengthening of beams by plate bonding." *Journal of Materials in Civil Engineering*, 9(4), 206-212.

Tavakkolizadeh, M. and Saadatmanesh, H. (2003(a)). "Fatigue Strength of Steel Girders Strengthened with Carbon Fiber Reinforced Polymer Patch." *Journal of Structural Engineering*, 129(2), 186-196.

Tavakkolizadeh, M. and Saadatmanesh, H. (2003(b)). "Strengthening of Steel-Concrete Composite Girders using Carbon Fibre Reinforced Polymer Sheets." *Journal of Structural Engineering*, 129(1), 30-40.

Teng, J.G. and Zhang, L. (2005). "Finite element predictions of interfacial stresses in beams bonded with a thin plate." *Proceedings of the International Symposium on Bond Behavior of FRP in Structures (BBFS 2005)*, Hong Kong, 189-195.

Tsai, M.Y., Oplinger, D.W. and Morton, J. (1998). "Improved theoretical solutions for adhesive lap joints." *Int. J. Solids Structures*, 35 (12), 1163-1185.

Vilnay, O. (1988). "The analysis of reinforced concrete beams strengthened by epoxy bonded steel plates." *The International journal of Cement Composites and Lightweight Concrete*, 10(2), 73-78.

Volkersen, O. (1938). "Die nietkraftverteilung in zugbeanspruchten nietverbindungen mit konstanten laschen-querschnitten." *Luftfahrtforschung*, 15, 4-47.

Whitney, C.S. (1942). "Plastic theory in reinforced concrete design." *Transactions ASCE*, 7, 251-326.

Wu, Z., Yuan, H. and Niu, H. (2002). "Stress transfer and fracture propagation in different kinds of adhesive joints." *Journal of Engineering Mechanics*, 128 (5), 562-573.

Xia, S.H. and Teng, J.G. (2005). "Behaviour of FRP-to-steel bonded joints." *Proceedings of the International Symposium on Bond Behavior of FRP in Structures*, Hong Kong, 411-418.

Yang, X., and Nanni, A. (2002). "Lap Splice Length and Fatigue Performance of FRP Laminates." *Materials Journal*, American Concrete Institute, 99(4), 386-392.

Zhao, X.L. and Zhang, L. (2007). "State of the Art Review on FRP Strengthened Steel Structures." *Engineering Structures*, 29(8), 1808-1823.

VITA

Name: Nisal Abheetha Peiris
Date of Birth: May 8, 1977
Place of Birth (City, State, Country): Colombo, Sri Lanka

Education: B.Sc. (Hons.), Civil Engineering,
University of Peradeniya, Sri Lanka
(July 1998 - Dec. 2002)

M.Eng., Civil Engineering (Structures),
Osaka University, Japan
(April 2004 - March 2006)

Nisal Abheetha Peiris
June 27, 2011